Time and Position-sensitive Foil-MCP Detector for Mass Measurements at the Rare-RI Ring

Zhuang GE

Supervisor: Prof. Tomohiro UESAKA

Advisor: Sarah NAIMI & Daisuke NAGAE

Department of Physics
Saitama University

This dissertation is submitted for the degree of
Doctor of Science

Material Sciences September 2018

I would like to dedicate this thesis:

To my loving parents and friends who always support my scientific research career.

To my heart and souls of the beauty of science.

To the giants in every fields that guide me moving on.

To the beauty of the world: the music, the sound, the poetry, the beautiful scenery, the blue sea, the white cloud, the shooting star, the nebula, everything that calms the heart and soul.

To the bright future: be ambitious, be creative and it is what the life means, to be great and believe in yourself.

To everything that makes you stronger.

"The eyes, thanks to flows the multi-tears, became more bright and clear; the heart, because of suffering much hard experience and lots of tenderest sorrow, is good nurturing and softened. " Modified from Louisa May Alcott

"I am not afraid of storms, for I am learning how to sail my ship." From Louisa May Alcott

"Be worthy love, and love will come." From Louisa May Alcott

Declaration

I hereby declare that except where specific reference is made to the work of others, the contents of this dissertation are original.This dissertation is my own work and contains nothing which is the outcome of work done in collaboration with others, except as specified in the text and Acknowledgements. This dissertation contains fewer than 100,000 words including appendices, bibliography, footnotes, tables and equations and has fewer than 310 figures.

Zhuang GE
September 2018

Acknowledgements

I would like to thank all the people for their help during my years at RIKEN. Without your helps and contributions in different ways, from RIKEN, Saitama University , University of Tsukuba, CNS, University of Tokyo, in Japan, and IMP in China, this work would not have been possible.

I would like to express my sincere gratitude to my supervisor Prof. Dr. Tomohiro Uesaka for his guidance and support. His encouragements and supports give me lots of motivations for physics and will always let me be ambitious to be succeeded in doing things.

In particular, I am grateful to Prof. Dr. Yuhu ZHANG, Prof. Dr. Hushan XU, Prof. Dr. Meng WANG for the contact and care in IMP and giving me the chance to work at RIKEN.

Special thanks should give to Dr. Sarah Naimi for her many helps and instructions as a tutor when I come to Japan. It will be not forgettable memory to be together with her, who acted as not only a senior partner but a most kind and warm friend, when I am abroad as student.

My warm thanks go also to Dr. Daisuki Nagae as a senior tutor, for his help with the preparation of experiments in RIBF and also HIMAC. I am grateful for a lot of his outstanding help like assisting me to correct the technical drawing of the designed Masks and detector, ordering of instruments from manufacturers who speaks Japanese.

It gives me pleasure to acknowledge Dr. Yasushi Abe for his unfailing help and support in construction of electronics for offline test and instruction for online test at RIBF. Thanks should also be given to Dr. Fumi SUZAKI due to her helps and kindness all the time.

Thanks for the discussions with Dr. Shinji SUZUKI and I am grateful for the all kinds of suggestions in my research work.

I sincerely acknowledge Mr. Syunichiro OMIKA who is always ready to help with lots of daily issues of mine with his kindness during my stay in Japan, many thanks to his hard work during the detector test in HIMAC.

I am grateful to Prof. Dr. Takayuki YAMAGUCHI for his lots of helps, kindness as a friend most of the time, and training about nuclear experimental physics to instruct me in HIMAC to get familiar with analysis code and electronics system.

I appreciate and enjoy the time with Mr. Hiroshi MIURA, Miss Natsuki TADANO, Mr. Kiyoshi WAKAYAMA, Hiroki ARAKAWA, Miss Kumi INOMATA, Mr. Kunimits NISHIMURO, Mr. Takaaki KOBAYASHI, Mr. Hongfu LI, Mr. Yushiyuki TAJIRI, Dr. Tetsuaki MORIGUCHI, Mr. Masamichi AMANO, Mr. Daiki KAMIOKA, Mr. Yukina ICHIKAWA, Mr. Kentaro HIRAISHI, Mr. Takuya MATSUMOTO, Mr. HOSOI, Mr. SAKAUE for experiments at HIMAC and also in RIKEN. It is very nice time to meet you all, who I will remember for my life long. Anywhere you go, I will treat you all as good friends and hope to meet you again. I express my sincerest gratitude to Dr. Yoshitaka YAMAGUCHI, Dr. Masanori WAKASUGI, Pro. Dr. Akira OZAWA, Pro. Dr. Takeshi SUZUKI for your all kinds of helps and contributions to help me finish my PhD.

I am grateful to Prof. Dr. Hideki Yamaguchi, Mr. SHIMIZU, Dr. Seiya HAYAKAWA and Dr. Lei YANG for their invitation for their experiments at CRIB in CNS, University of Tokyo for study and have fun for physics. It is one of the most great and happy time for experiments for study.

Thanks so much for Dr. Yasushige YANO, and warm-hearted talks from him let me know there are ones that looking forward to the young to make big things, and make me calm down for the years to go through the difficulties and see far and beyond to the bright future. It is also unforgettable time to have experiments in RIBF B3F with Dr. Yuri LITVINOV for several times and have Sushi together. Thanks for Dr. Yuri LITVINOV's kindness and support for my research in a planned proposal to cover my most interested area of nuclei for mass measurements and the suggestions for further extension.

I would also like to thank RIKEN for the financial support throughout my studies in Japan as an International Program Associate (IPA) student. It also gives me pleasure to acknowledge the co-workers in IMP and thanks for help in advance.

Many thanks goes to the members of the RIBF, CNS, HIMAC for their providing stable and high quality beams for this work and applying training chances for my study in experimental physics.

I am grateful to all the ones in support with my research and my future career in different ways, and myself, my heart and soul for so long time of silence, and grateful for the good moods to move me going on and make the bright sun always in the heart. You can do it all and more, even thunders and storms in front, just believe in yourself.

Abstract

High accuracy and precise mass measurements of exotic nuclei are very important for the study of nuclear physics and nuclear astrophysics. To increase the accuracy and extend the capability of now existing storage ring techniques for mass measurements, a newly constructed storage ring, the Rare-RI Ring, operating as an isochronous Mass Spectrometry (IMS) in RIKEN Nishina center to measure the mass of rare radioactive ions with a target precision of 10^{-6} for even one event during a time of flight (TOF) less than 1 millisecond, has been commissioned and studied experimently. To satisfy the requirements of high resolution, good accuracy, very fast and efficient mass measurements with the Rare RI Ring as an IMS, the TOF and extra velocity/magnetic-rigidity (for TOF correction) have to be measured with required accuracy and high resolution. Therefore, a high efficiency, good resolution for both timing and position, large effective area and low energy loss detector are dispensable. For these reasons, the study of the principle of mass measurements via the new obit-IMS method (IMS TOF with extra velocity/magnetic-rigidity correction) by the Rare-RI Ring and the development of the high performance detector described are carried out in this thesis.

An experiment aimed to study the performance of the Rare RI Ring performing as an Isochronous mass spectroscopy (IMS) and the principle of IMS mass measurements with additional velocity or momentum measurements has been carried out at RIBF. In-flight fission fragments, created by ^{238}U projectiles in a beryllium target at the entrance of the BigRIPS focus F_0, were spatially separated by the BigRIPS-HA-SHARAQ beam-lines and injected into the Rare-RI Ring. In the experiment, we succeeded in selection, injection, accumulation and extraction of 5 different nuclei to R3 for mass determination and the isochronism $\sim$5x10^{-6} was achieved by checking the TOF spectrum of ^{78}Ge. A two stage selection and particle identification method has been carried out with the $B\rho$-TOF-ΔE-E method based on individual injection technique, and with this new method, all the ions have be well separated and identified for mass deduction analysis. The analysis of the data was done to investigate and verify that the IMS method with extra velocity or magnetic-rigidity correction can increase the mass accuracy and precision with a large momentum acceptance other than only using the IMS method without extra correction. It is proved that to achieve a high resolu-

tion, the revolution time measurement of the storied ions and the magnetic rigidity or the velocity for correction of the in ring TOF should be simultaneously measured, thus we can achieve higher resolution with small systematic error to cover relative large range of $\delta m/m$ relative to reference ion in isochronous condition for the IMS method. From the analysis, it is also confirmed that from one experiment run, two complementary mass measurements methods (IMS and $B\rho$-TOF) can be employed simultaneously to deduce masses and benefit each other, in which it is very suitable to save beam time and cover large area of nuclide of chart and large momentum area of secondary products from experiment of very exotic nuclei. Besides, the first new mass of ^{74}Ni which is not included in the newest atomic mass evolution (2016) is deduced in this work by $B\rho$-TOF method at the Rare-RI-Ring. The mass of ^{74}Ni is very important for the research of nuclear shell effect and also shows importance of the impact on the r-process modeling. The pioneering mass measurements experiment by using two complementary time-of-flight methods (Bρ-TOF and IMS) simultaneously in one experiment run for mass determination in the world has been realized and verified within this work.

In the in-flight fission experiment, there is large energy loss in the PPAC at F6 dispersive focus, which is for position measurement to deduce the momentum have large influence to the mass accuracy. At the same time the timing resolution of MCP detector of about 200 ps can not satisfy the high resolution mass measurements form the TOF. For these reasons, a electrostatic large-area thin-foil MCP detector was developed at the RIBF, which possess a higher timing resolution and has a capability to measure the position (to deduce velocity and magnetic-rigidity) at the same time with low energy loss and a large active area.

The specification and performance of different position-sensitive anode that can be coupled with MCPs for position measurements have been studied systematically. A 2-dimentional delay-line type anode with dual wires for each coordinate are been chosen and utilized for our final design. The secondary electrons (SEs) electro-magnetic motion and trajectory in the detector are studied theoretically and by simulation. To calibrate the delay-line MCP detector (DLD120) system, a higher order calibration method is carried out and the precision and accuracy of the DLD120 system is discussed for different calibration methods. An isochronous condition for the operation of the electrostatic detector was calculated and studied by simulation. To characterize and optimize the timing and position resolution of the detector, the position resolution dependence of high voltage supplies has been studied both in the isochronous and non-isochronous condition by simulation and experimentally with ^{241}Am alpha source. The detection efficiency and position resolution by using a carbon foil with thickness of 60 μg/cm^2 or 2 μmm mylar foil coated with aluminium as SEs emitters are studied with variations of HV supplies of the detector potential plates. Two ex-

periments aimed at studying the performance (efficiency, timing and position resolution) of the position-sensitive timing detector were conducted at HIMAC (Heavy Ion Medical Accelerator in Chiba) with heavy ion beam for the detector with different grid pitch of 1mm and 3mm for the outer mirror. The performance of the detector have been optimized and the best achieved timing resolution and position is ≤ 50 ps and 1 mm in σ respectively, for which the detection efficiency is $\sim$95 %. The performance of another same type of mirror detector coupled with timing anode which is dedicated for TOF measurement has been studied by heavy ions at HIMAC . The best achieved timing resolution is $\sim$ 40 ps (in σ) and detection efficiency is $\sim$ 96 % for heavy ion beams. This timing detector will be used for revolution time measurement inside R3, start TOF detector of the total TOF for in-ring circulation, beam-line TOF measurement for beam-line mass determination and velocity reconstruction for in-ring mass correction.

Prospects of mass measurements at the Rare RI Ring employing the two complementary time-of-flight methods (Bρ-TOF and Orbit-IMS) have been demonstrated and the versatility of the fast low-energy-loss position-sensitive timing detector developed within this work in use for in-ring and on beam-line are discussed and summarized. Other next generation facilities with storage rings which are in plan to perform IMS mass measurements and possible new methods are summarized.

Table of contents

Chapter 1

Introduction

1.1 The history and present of mass spectrometry

The history of nuclear masses and the history of its most important contributor, namely mass spectrometry with improvement of the resolving power closely related to increasing insight in the structure of the atomic nucleus, have continuously fed nuclear physics with major discoveries [1, 2]. Each progress in building new spectrometers, increasing resolving power or sensitivity or both, has led to important new physics: the nature of canal rays; the discovery of isotopism; the restoration of the whole number rule; the explanation of the age of the Sun; the discovery of mass defect and the experimental proof of the equivalence of mass and energy; the discovery of the magic numbers; the discovery of deformations; the discovery of a sub-shell closure; the discovery that magic numbers might disappear; much more on recent breakthroughs brought about by mass measurements could be said, and the history of mass measurements is still to be written [1–5].In 1913, J.J. Thomson constructed a positive-ray parabola mass spectrometry at Cambridge and discovered two isotopes of neon (^{20}N and ^{22}N) after his discovery of the electron [6–8]. Thomson was awarded the Nobel Prize for physics in 1906 for his studies. His student F. W. Aston extended this work by constructing a mass spectrometer with an increased resolving power and contributed significantly to our first glimpses into the binding energy of the nucleus, which leads to the discovery of "mass defect" of atomic nuclei. The mass spectrograph he built was employed for systematic studies of more than 200 nuclides and he received the Nobel Prize for chemistry in 1922 for his work [9–13]. Mass spectrometers were used to measure isotopic abundances that time and Aston tabulated the isotopic distributions and abundances of the stable elements. The precision mass measurements started by Aston laid the basis for the development of Weizsäcker mass formula, a fundamental contribution to the understanding of nuclear binding. At the same time, The first magnetic focusing was achieved by Dempster in a 180° spectrometer

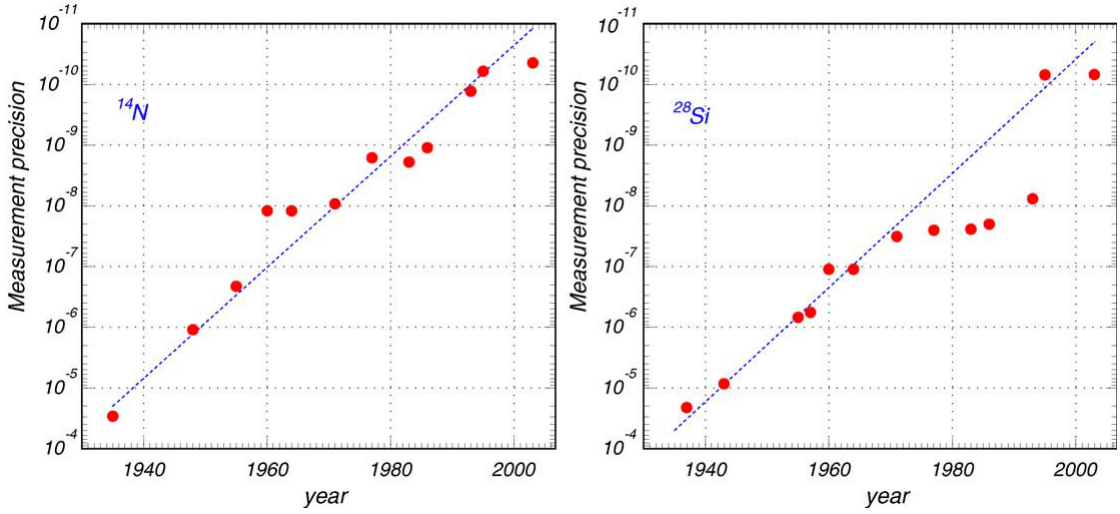

Fig. 1.1 The graph demonstrates for the exemplary case of ^{14}N and ^{28}Si how the relative mass uncertainty decreased over the years due to the continuous improvement of existing and the advent of new experimental techniques. Figure from [1].

[16, 17], and the double-focussing spectrograph was developed by Mattauch and Herzog [18], which is still in use for precision instruments. Meanwhile, a Mattauch-Herzog type mass spectrograph with a resolution of more than 30000 for high precision mass measurements was constructed by H. Ewald [19]. H. Matsuda developed and built a double focusing spectrometer of the highest resolution in 1968 with a measurement of the atomic mass difference of ^{40}Ca and ^{40}Ar with a resolving power of 700000 to 1000000 [20]. The modern mass spectrometry of isotopes off stability, such as ion traps and storage rings, with advantage of time and/or frequency measurements are being operated or in construction to achieve a much higher precision of 10^{-6} or higher and sensitivity to single atom with cheaper and lighter instruments [14]. The pioneering works of sir Thomson and Aston in parallel with other scientists boosted the interests to atomic mass measurements, and more and more mass spectrometry methods were invented and refined after their endeavor to have brought a great increase in precision. Fig. 1.1 demonstrates the increase of precision obtained from the year of 1937 to 2003 in the determination of the masses of ^{14}N and ^{28}Si [1]. On the average, relative uncertainty was decreased due to major technical advances by about one order of magnitude every decade, which results in a significant expansion of the fields of physics that can be accessed to (see table 1.1). Dependent on the physics being investigated, mass uncertainties ranges from 10^{-5} up to 10^{-8} can be required [23] for short-lived nuclei considerably less than a second, and even down to 10^{-11} for stable nuclides as shown in table 1.1. Newly measured accurate mass values, together with other information of nuclides, can be employed for numerous studies in nuclear structure and nuclear astrophysics. Beside nuclear

Table 1.1 The generally required relative uncertainty on the measured mass ($\delta m/m$) to probe the associated physics fields of application [23].

Fields	Mass uncertainty
Chemistry: identification of molecules	$10^{-5} - 10^{-6}$
Nuclear physics: shells, sub-shells, pairing	10^{-6}
Nuclear fine structure: deformation, halos	$10^{-7} - 10^{-8}$
Astrophysics: r-process, rp-process, waiting points	10^{-7}
Nuclear models and formulas: IMME	$10^{-7} - 10^{-8}$
Weak interaction studies: CVC hypothesis, CKM unitarity	10^{-8}
Atomic physics: binding energies, QED	$10^{-9} - 10^{-11}$
Metrology: fundamental constants, CPT	$\leq 10^{-10}$

physics and nuclear astrophysics, a number of new domains, such as the particle physics, neutrino physics, and metrology can also be addressed with the required uncertainty with the determination of atomic or nuclear masses [23].

The requirements of the techniques applied to the study of unstable nuclei: ultra-fast investigation of exotic radioactive nuclides with half-lives in order of milliseconds or below, very accurate with statistical uncertainties only, extremely sensitive and efficient so that only a single ion or atom would be sufficient for the entire experiment, and extreme resolving power exceeding 1 million in order to resolve hyperfine structure splittings by optical spectroscopy or ground and isomeric states by mass spectrometry, are challenging dreams of atomic and nuclear physicist. Today, the highest accuracy in measurements of any quantity in all field of science, is achieved when the measurement can be converted into frequency [23]. Penning trap and storage ring are among those which take advantage of frequency or revolution time measurements for mass measurements to achieve much high precision of 10^{-6} or higher and sensitivity to single atom or ion with cheaper and lighter instruments. The time-of-flight (TOF) spectrometers are also promising technique to determine masses due to its high efficiency and capability of measurements in less than even $1\mu s$ with a relative precision of $\sim 10^{-4} - 10^{-6}$.

As the first running next generation facility around the world, the Radioactive Isotope Beam Factory (RIBF) [21], at RIKEN Nishina center, has shown its extraordinary capabilities and advancing techniques to be devoted to the determination of properties of extremely short-lived nuclei far from the valley of stability, such as masses and half-lives. With the highest intensity of the radioactive ion beam of interest, the goal of studying nuclei on the limits of existence and nuclear masses will trigger foreseeing productive and fruitful new physics results in the near future.

In this work, emphasis is given to the development of low-energy-loss fast detection instrument possessing both high timing resolution and good position sensitivity, application of a storage ring for high-accuracy mass determination of short-lived nuclides, for which the typical uncertainty $\delta m/m$ is $\sim 10^{-6} - 10^{-7}$ [23, 48], and study of the possibility of combination of the isochronous mass spectrometer (IMS) with the high resolution beam-line for complementary mass measurements in one same experimental run.

1.2 Nuclear masses and mass models

Nuclear and atomic masses

Nuclear masses have a character that the mass $M_N(N, Z)$ of a nucleus with N neutrons and Z protons is measurably less than the sum of the masses of its constituent free nucleons [5], and are usually converted in terms of the mass excess defined by

$$\Delta M_N(N, Z) = M_N(N, Z) - A\mu, \tag{1.1}$$

where μ [1] is the Atomic Mass Unit,

$$\mu = M(^{12}C)/12 = 931.4940954(57)\, MeV/c^2. \tag{1.2}$$

The nucleon masses of proton and neutron are

$$\begin{aligned} M_p &= 938.27203(8) MeV/c^2 = 1.00727646693(9)\, \mu; \\ M_n &= 939.56536(8) MeV/c^2 = 1.0086649158(5)\, \mu, \end{aligned} \tag{1.3}$$

The difference between the atomic mass and the nuclear mass is the atomic binding energy of the electrons, plus the rest mass of the electron. The relation between the atomic and nuclear masses is given by:

$$M_A(Z, N) = M_N(Z, N) + Z \cdot M_e - B_e(Z), \tag{1.4}$$

where $M_A(N, Z)$ is the atomic mass, M_e the electron mass, and $B_e(Z)$ is the total binding energy of the electrons. An approximation [5] by using

$$B_e(Z) = 14.4381 \cdot Z^{2.39} + 1.55468 \cdot 10^{-6} \cdot Z^{5.35}\, eV, \tag{1.5}$$

provides a root mean square (rms) error of 150 eV over the entire range of tabulated masses.

The missing mass of the bound system compared to the sum of all masses of the constituent protons ZM_p and neutrons NM_n is explained by the nuclear binding energy. In terms of the atomic masses $M_A(N, Z)$, the binding energy is defined by

$$B(Z, N) = [NM_n + ZM_H - M_N(Z, N)]c^2 \tag{1.6}$$

[1] From the AME2012 [4] the $\mu = M(^{12}C)/12 = 931.494061(21)\, MeV/c^2$ get evaluated to $\mu = M(^{12}C)/12 = 931.4940954\, MeV/c^2$ in AME2016 [3].

where M_n is the mass of the neutron and $M_H = 1.00782503224(9)\,\mu$ is the mass of the hydrogen atom. The binding energy represents the sum of all the nucleonic interactions that give rise to correlations in many-body systems. Nuclei with larger binding energies per nucleon tend to be stabler. ^{56}Fe is the most bound common nucleus, ^{56}Ni is the most bound nucleus for symmetric (N = Z) nuclei, and ^{62}Ni is the most bound nucleus of all. Notice that all these "most bound nuclei" are at the "iron peak." In terms of the mass excess, the binding energy is given by

$$B(Z,N) = Z\Delta_H c^2 + \Delta_n c^2 - \Delta(N,Z)c^2, \tag{1.7}$$

$\Delta_H c^2 = 7.28897061(9)$ MeV, $\Delta_n c^2 = 8.0713171(5)$ MeV and $M_n - M_H = 839883.59(51)\,n\mu$.

Mass differences

Differences of masses give separation energies [5] (the energy needed to separate some nucleons from the nucleus), providing clues to shell structure and phase transitions. The one-proton Sp and one-neutron Sn separation energies have also a very interesting practical meaning: they determine the corresponding drip-lines. The drip-lines are defined by the conditions of Sp = 0 or Sn = 0. The neutron separation energy is defined as

$$S_n(Z,N) = M(Z,N-1) + M_n - M(Z,N) = BE(N,Z) - BE(N-1,Z), \tag{1.8}$$

and the proton separation energy reads

$$S_p(Z,N) = M(Z-1,N) + M_p - M(Z,N) = BE(N,Z) - BE(N,Z-1), \tag{1.9}$$

Because of pairing effect, the single-nucleon separation energy is a less clear-cut indicator. There is an example figure of the one-neutron separation energy in a long isotopic chain of Sn nuclei (Z = 50) as a function of neutron number shown in Fig. 1.3 and illustrating most impressively how masses give a first glimpse of nuclear structure. The most striking way in which shell structure manifests itself in mass systematics is through the two-neutron separation energy

$$S_{2n}(Z,N) = M(Z,N-2) + 2M_n - M(Z,N) = BE(N,Z) - BE(N-2,Z), \tag{1.10}$$

in the case of neutron shells, and the two-proton separation energy:

$$S_{2p}(Z,N) = M(Z-2,N) + 2M_p - M(Z,N) = BE(N,Z) - BE(N,Z-2), \tag{1.11}$$

in the case of proton shells. Here, specific classes of interactions can be isolated. An example figure of the two-neutron separation energy in a long isotopic chain as a function of neutron number is demonstrated in Fig. 1.4.

We can define the so-called energy gap for neutrons as:

$$\Delta S_n = 2BE(N,Z) - BE(N-1,Z) - BE(N+1,Z), \tag{1.12}$$

this quantity can in turn be used to determine which nuclei are magic or not. For protons we would have:

$$\Delta S_p = 2BE(N,Z) - BE(N-1,Z) - BE(N+1,Z). \tag{1.13}$$

Specifically, one would like to know whether there is any quenching, in the sense of either a weakening or a total extinction, of the shell gaps. The two-neutron or two-proton gaps defined by

$$\Delta_{2n}(N_0,Z) = S_{2n}(N_0,Z) - S_{2n}(N_0+2,Z) \tag{1.14}$$

and

$$\Delta_{2p}(N,Z_0) = 2BE(N,Z) - BE(N,Z-1) - BE(N,Z+1). \tag{1.15}$$

The study of energy differences, such as mirror displacement energy, triplet displacement energy between analogue states in isobaric multiplets allows to verify the validity of isospin symmetry and independence as a function of the angular momentum [22]. Mirror displacement energy definition:

$$CDE(A,T) = BE(T,T_{z<}) - BE(T,T_{z>}), \tag{1.16}$$

where $z <$ and $z >$ indicate proton less or neutron less than N =Z nuclei. ΔCDE definition:

$$\Delta CDE(A,T) = CDE(A+2,T) - CDE(A,T). \tag{1.17}$$

$T = 1, T_z = 0, \pm 1$, Triplet displacement energy definition:

$$TDE(A,T) = BE(T,T_{z<}) + BE(T,T_{z>}) - 2BE(T,T_z = 0). \tag{1.18}$$

Another interaction of high interest is that of the last proton(s) with the last neutron(s) and is called δV_{pn} [27–29]. For even–even nuclei, δV_{pn} value refers to the interaction of the (Z − 1) and Zth protons with the (N−1) and Nth neutrons and is defined by

$$\delta V_{pn}^{ee}(Z,N) = \frac{1}{4}\left[B(Z,N) + B(Z-2,N-2) - B(Z,N-2) - B(Z-2,N)\right]. \tag{1.19}$$

and for odd-odd nuclei:

$$\delta V_{pn}^{oo}(Z,N) = B(Z,N) + B(Z-1,N-1) - B(Z,N-1) - B(Z-1,N). \quad (1.20)$$

δV_{pn} values can help to explain the shell structure and orbit occupations near the Fermi surface, for example in the ^{208}Pb region. It can also show striking singularities for nuclei with $N = Z$, reflecting the isospin $T = 0$ interaction [5].

The mass of an atomic nucleus is its fundamental property which reflects the total interactions through the strong, weak and electro-magnetic forces within a many-body quantum system composed of two kinds of fermions, protons and neutrons. As listed in the recent Atomic-Mass Evaluation (AME2016) [3], about 7000 nuclides are expected to be existing in nature and the masses of 3436 nuclides are known or estimated, while masses of 2497 nuclides are known experimentally at present and other known nuclides are predicted by extrapolation as shown in Fig. 1.2. The nuclides with still unknown masses are difficult to measure due to extremely low production cross sections and short life-times. Most of them are barely within reach at present and will remain inaccessible at the presently in construction next-generation radioactive beam facilities. As the lack of an exact description of the strong interaction and the complexity of the many-body nucleonic system, the binding energy of nucleus is difficult be described by ab-initio theories. Due to these difficulties, mass predictions by models (with the aim of a quantitative prediction of the total binding energy of a nucleus) and formulas (with the aim of a numerical calculation of masses on a physical basis) are relied on [23]. Mass formulas are typically based on a set of free parameters up to several hundreds and have to be constrained by local [24] or empirical [25] comparison to experimental data. In particular, data far from the valley of stability represent well-suited test cases for the predictive power of models. Various modern mass formulas are being used to extrapolate from the experimental data towards the drip-lines and explain the interplay between experiment and theory.

Isobaric multiplet mass equation

Besides the global mass formulas, there exist also a number of local mass formulas, which can be used to address the problem for the requirement to predict the mass of an unmeasured nucleus that lies fairly close to an area of a considerable number of nuclei of known masses. Detailed overview can be found in [5]. Here, one test of the most powerful local mass formula, the isobaric multiplet mass equation (IMME) [34, 38], is presented. In light nuclei, isobaric analog states (IAS) have nearly identical wave functions, i.e. same mass number (A), angular momentum (spin), parity, and isospin (T). The charge dependent energy dif-

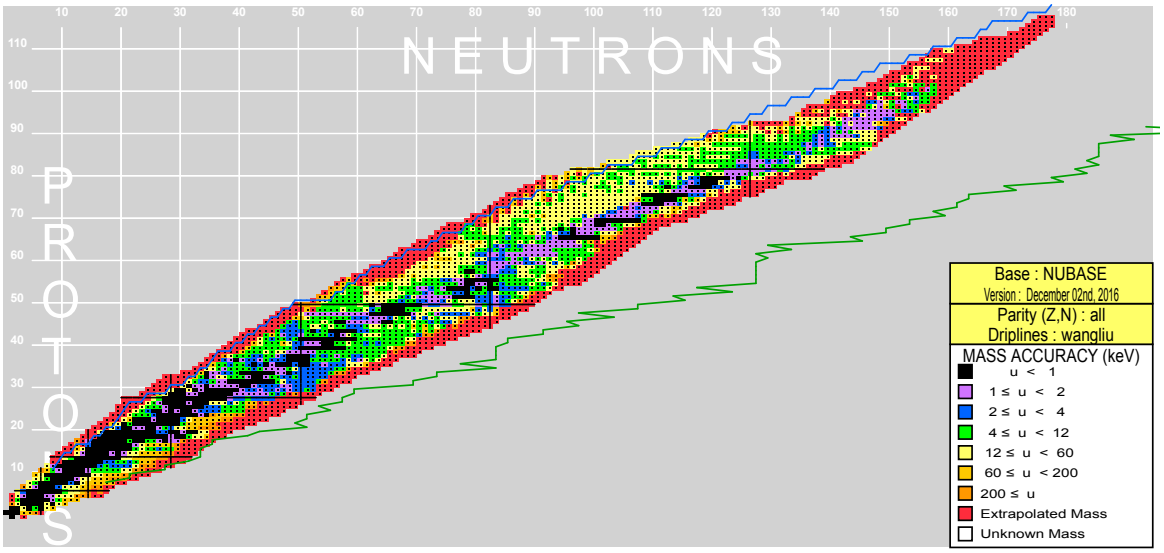

Fig. 1.2 Nuclear chart showing the regions with certain mass precision (in keV) coded in different colors, where measurements have been made by the various dedicated mass programs using direct techniques and those determined by indirect measurements [3]. Stable nuclides are shown as well as the drip lines calculated by the finite-range droplet model (Moller et al., 1995 [26]). The masses unknown experimentally for the nuclei which are discovered at present are predicted by extrapolation as shown in red. Data from [3].

ference of these states can be calculated using first-order perturbation theory assuming only two-body Coulomb forces. Noted first by Wigner, Weinberg and Treiman [35–37], a simple equation, is given as the mass M(A,T,Z) of a member of an isospin multiplet as a function of its isospin projection $T_Z = (N - Z)/2$:

$$M(A,T,Z) = a(A,T) + b(A,T)T_Z + c(A,T)T_Z^2 \tag{1.21}$$

As of fundamental importance in isospin symmetry in nuclear physics, the quadratic relation of IMME worked has been extremely successful and only failed in light multiplets with an unbound member. Due to the success of IMME and lack of newer experimental data for very exotic nuclides, IMME is widely used to predict masses as well as level energies, for instance, to map the proton drip line over a wide mass range, which is important for determining the rp-process path [39, 40]. To test the validation of IMME, an additional cubic term $d(A,T)T_Z^3$ in Eq. 1.21 can be utilized for fit. If the quadratic form of IMME is correct, the results should fit with $d(A,T) \sim 0$, and the experiment yields the $d(A,T)$ coefficient is consistent with zero within the error bars.

1.3 Physics motivation for mass measurements at storage rings

Mass and half-life of a nucleus are fundamental properties which result from the complex interaction of strong, weak and electro-magnetic interactions acting between all nucleons [5]. New phenomena in nuclear physics such as shell structure, pairing correlations, and decay and reaction properties have been discovered via nuclear mass measurements. Separation energies and Q-values for reactions can be deduced from atomic masses. The drip-lines (Sn = 0 or Sp =0), which are defined as the borders of nuclear existence, are determined from the mass differences of neighboring nuclei. The final pathways of the nucleosynthesis in cosmos are also governed by the masses and life-times.Strong interest in high-accuracy mass measurements on super-allowed β-emitters and their daughters can be utilized to test two fundamental postulates of the Standard Model, namely, the unitarity of the Cabibbo-Kobayashi-Maskawa (CKM) quark-mixing matrix and the conserved-vector-current hypothesis of the weak interaction [23].

Another very important motivation for measuring new masses of exotic nuclides is the test and improvement of nuclear theories and models (see also section. 1.2). Although the progress of the theories has been enormous, especially when concerning the microscopic calculations, their predictive power is usually more than one order of magnitude worse compared to the presently achieved experimental accuracy [23, 3]. Today the most challenging issue to measure the masses and lifetimes of exotic nuclei is to measure the ones close to the borders of their existence. These nuclides have the properties of strong asymmetry of their proton-to-neutron ratio for the neutron rich side or special symmetry at the higher Z of the proton rich side, like the N = Z nuclei. However, they are difficult to investigate due to their tiny production cross-sections and extremely short lifetimes. Two methods for direct mass and life-time measurements of stored projectile fragments were pioneered at GSI [43–46], namely Schottky mass spectrometry (SMS) and isochronous mass spectrometry (IMS). The time-resolved SMS ideally enables the simultaneous mass and half-life measurements down to intensities of a single particle. As a one of the first running next generation beam factory RIBF, many new isotopes have been discovered at RIKEN, which demonstrate the chance for the Rare-RI Ring (apparatus used in the work) to perform its great potential in mass measurements and life-time measurements in the near future. New mass and life-time measurements techniques are being tested and developed. The access to exotic nuclides allows us to contribute to a large variety of physics applications. In this section, several topics of physical motivation of mass measurements are discussed briefly below corresponding to the future possible prospects for physics cases at the Rare-RI Ring.

1.3.1 Nuclear Structure Studies

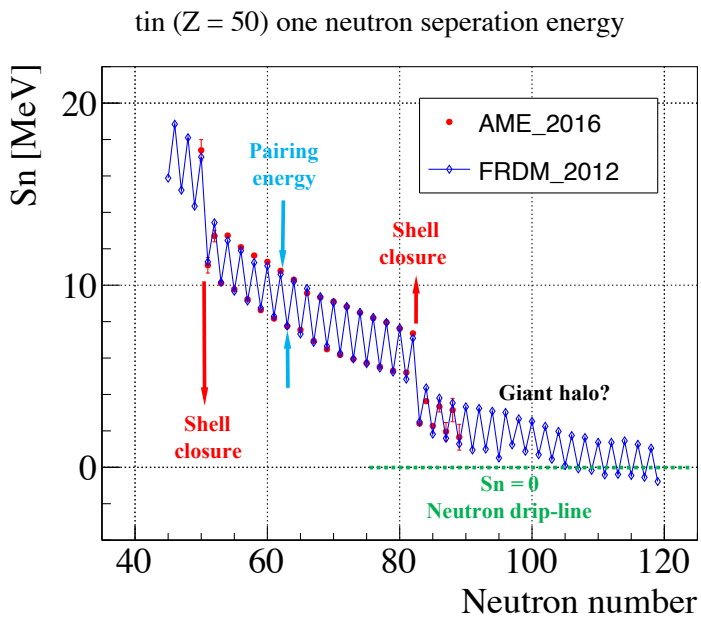

Fig. 1.3 Neutron-separation energy Sn for tin (Z=50) isotopes versus neutron number N. Full dots represent experimental data (from AME2016 [3]) while the open symbols are from FRDM2012 [49]. The neutron drip-line is indicated by the horizontal dashed line in blue and shell closures at N = 50 and N = 82 by arrows. The pairing effect can be clear seen as tagged in blue arrows and near the most neutron rich side, the predicted halo nuclei may appear.

Differences of masses give separation energies (the energy needed to separate certain nucleons from the nucleus), providing clues to shell structure and phase transitions. The most striking way, in which shell structure manifests itself in mass systematics, is through the double differences of masses of nulcei, i.e. the two-neutron separation energy as discussed in section 1.2. With the highest intensity of the primary beams all around the world at RIBF now, the Rare-RI Ring coupled with high resolution beam-lines, possess a feature of mapping studies of the chart of nuclides in a systematic manner. Masses of neighbouring nuclides plotted together form the nuclear mass surface, which is in general a smooth trend, and new structure effects may be seen from irregularities of the surface. Masses of heavy atomic nuclei are in the range up to 100 GeV (A $\sim$ 100), while the binding of individual valence nucleons is on the order of 10 MeV. Specific localized (in isotopic or isotonic chains) structure-related effects are in the range from a few MeV to 10s of keV, making it difficult to distinguish subtle shell or correlation effects. Therefore one normally looks at difference of binding energies, i.e., separation energies, either one-nucleon or two-nucleon. Fig. 1.3

and Fig. 1.4 illustrate the typical behavior of one- and two-neutron separation energies (see section 1.2) as a function of neutron number in a large region of nuclei. The revealed new nuclear structure effects are demonstrated from the irregularities on the figures. The local deviations from a smooth linear trend indicate the nucleon-nucleon pairing correlations, shell structure, sub-shell structure, and deformations, which illustrates impressively how masses give a first glimpse of nuclear structure [23].

One also would use the energy gap (one/two-neutron or one/two-proton) defined in section 1.2 to determine which nuclei are magic, or whether there is any quenching. A three-point odd-even mass staggering formula [41, 42]: $\Delta_3(N) = (-1)^N[ME(Z,N+1) - 2ME(Z,N) + ME(Z,N-1)]/2$ can be used to study pairing in nuclei as well. The one proton or neutron drip-line which indicates the limits of bound nuclear systems can be mapped by drawing the one proton or neutron separation energies (S_p or S_n) though measuring the masses of exotic nuclei. The proton or neutron halos, and the meta-stability island in the superheavy-element region can be addressed by related to mass models and formula. δV_{pn} values can be used to explain and describe shell structure and orbit occupations near the Fermi surface, for example, near the ^{208}Pb region. δV_{pn} values are usually extracted from experimental masses to indicate the variations of the $p-n$ interaction and to interpret the very characteristic behavior like the shell effect. Another important motivation of direct mass measurements with respect to nuclear structure studies is to resolve isomeric from ground states since nearly one third of the nuclides in the chart of nuclides have long-lived isomeric states with unknown excitation energies in many cases. [2]

1.3.2 Test of nuclear mass models and mass formulas

Masses, as a fundamental property of nuclei, are among the most critical nuclear parameters in nucleosynthesis calculations in astrophysics. However, many nuclei involved in these processes are still not available in sufficient amounts of production at RI beam facilities to perform a high-accuracy mass measurement. One has to rely on mass predictions by models with the aim of a quantitative prediction of the total binding energy of a nucleus and formulas with the aim of a numerical calculation of masses on a physical basis. The experimental data far from the valley of stability where masses are accurately known represent well-suited test cases for the predictive power of these models and formula.

The differences in mass predictions between the WS4-RBF model (the recent Weizsäcker-Skyrme WS4+ radial basis function (RBF) method [54]), which obtains the best accuracy of description of mass and other different mass formulae or experimental data as a function

[2] Isomers are excited states of atomic nuclides with half-lives range from nanoseconds to beyond the age of the Universe (10^{15} $years$, ^{180m}Ta) at excitation energies ranging from 100 keV up to a few MeV [23].

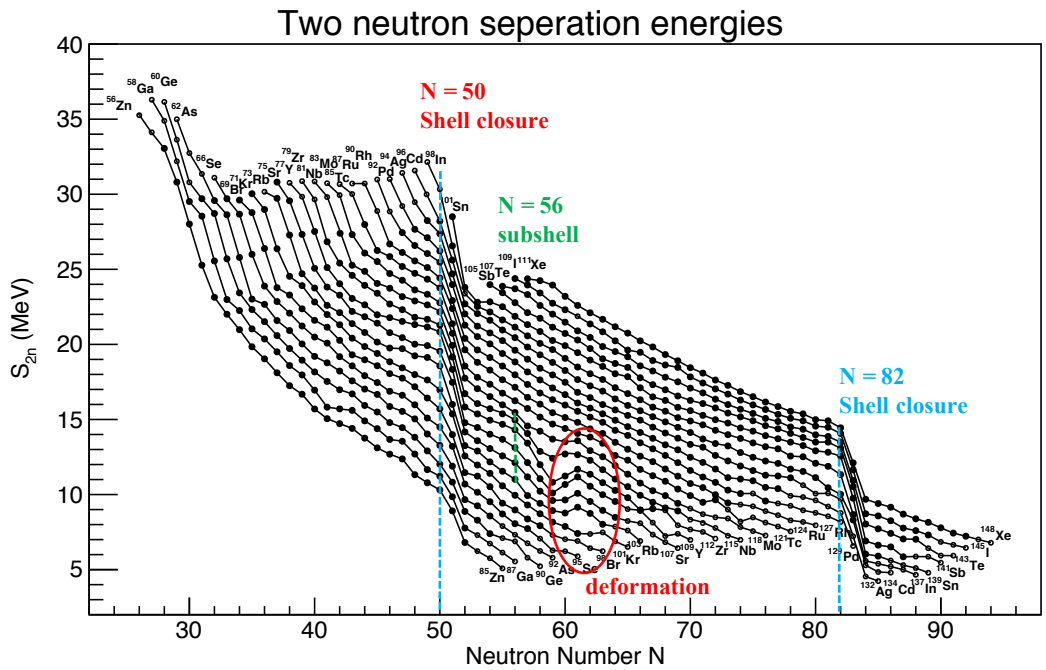

Fig. 1.4 Two-neutron separation energy of several elements in the range $Z \sim 30 - 54$, as a function of neutron number N. Data are taken from AME2016 [3]. Generally, a tendency for the two-neutron separation energy S_{2n} to fall steadily appears as the neutron number N increases with the proton number Z being a constant. However, at the magic numbers marking shell closure there comes out a sudden drop. The magic number $N = 50$ and 82 are conspicuous, corresponding to a sudden drop in the energy necessary to remove neutrons after a closed shell. Proton shell structure can likewise be displayed by plotting the two-proton separation energy S_{2p} as a function of Z for isotonic chains.

of atomic mass number (A) for tin isotopes are illustrated in Fig. 1.5. While the various nuclear mass models agree quite well with the known nuclear masses, they diverge quickly (not shaded area in Fig. 1.5) among each other in their predictions for the nuclei far-off stability which are not yet measured. The mass models have normally a number of free parameters fitted to experimental data, and mass measurements of exotic nuclei will give a strict constrain and a further development of nuclear mass models.

1.3.3 Nuclear astrophysics

Nuclear physics plays an important role in the cosmos and nearly everything that is visible in the night sky is powered by nuclear reactions. The final fate of the evolution of stars from their birth are governed by nuclear physics. Due to the significance that nuclear physics plays in the cosmos, nuclear astrophysics is not simply a project that provides nuclear physics

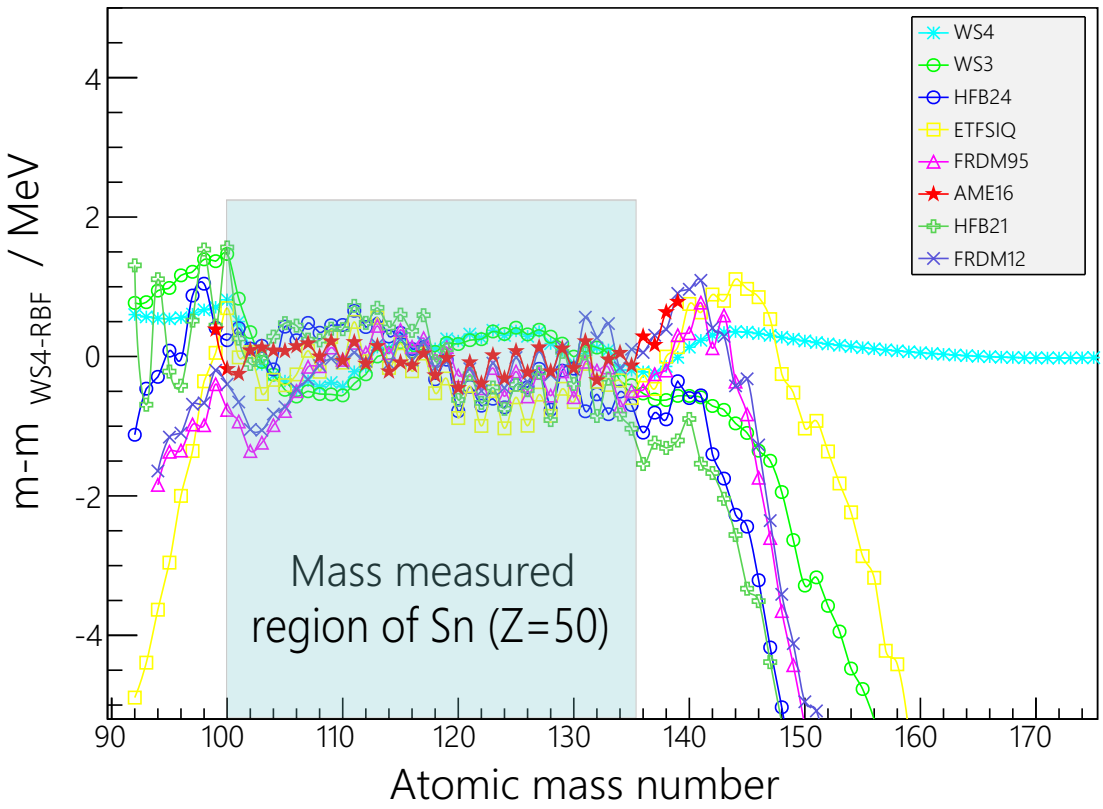

Fig. 1.5 Comparison in mass predictions of various theoretical mass models and experimental data from predictions to the WS4-RBF mass model [54] as a function of atomic mass number (A) for tin isotopes (Sn, Z = 50). Since the model parameters are adjusted to measured masses, the agreement is very good where masses are known, but large deviations appear at the unknown mass region for different mass models. The experimental data are taken from AME2016 [3] and the measured mass area are shaded in blue color. Seven widely used mass models including the microscopic self-consistent mean-field Hartree-Fock-Bogoliubov (HFB) mass models (HFB21 [51], HFB24 [52]), Hartree-Fock approach (ETFSI-Q [50]), the macroscopic-microscopic approach finite-range droplet model (FRDM95 [26], FRDM12 [49]), and a newly developed mass formula: Weizsäcker– Skyrme model (WS3 [53], WS4 [54], which includes many corrections, such as isospin and mass dependence, deformation influence to the macroscopic energy, mirror nuclei constraint, and some residual corrections) are selected for comparison to the the macroscopic-microscopic mass formula WS4-RBF model (Weizsäcker–Skyrme WS4+ radial basis function (RBF) method [54]), which is with the highest accuracy of prediction for the known masses now.

data for astrophysics research, but is a field on its own at the forefront of science, solving the fundamental questions concerning the cosmic evolution of matter and synthesis of the elements.

Today, the nuclear masses of the stable or nearly stable isotopes which are necessary to understand the energy production and nucleosynthesis in stars are known with extraordinary precision. However, this is not the case for many unstable nuclei that play a role in stellar explosions or neutron stars, which are not known with sufficient precision, or even not known at all. Boost of the nuclear astrophysics requires the development of hypotheses, and models to describe the processes inside stars and stellar explosions. Theoretical mass models currently do not reach the precision needed for nuclear astrophysics models, and even if theory would indicate that such accuracy can be achieved, experimental data are required to check the predictions. Therefore, mass measurements continue to be of highest importance for nuclear astrophysics to judge the models whether they can reproduce the real natural conditions. Several nuclear processes are summarized in a schematic way in Fig.1.6.

Difference of nuclear masses of the involved nuclei in the corresponding nuclear reactions provides the Q values. In equilibrium situations, binding energy differences become the major quantities defining the reaction flow. This can have a strong influence on nucleosynthesis and on energy generation rates. The r- and the rp-process are both characterized by quasi nuclear statistical equilibrium within isotopic or isotonic chains of isotopes: In such an equilibrium, the abundance distribution along the chain of isotopes is entirely determined by the chemical potentials which are then required to be equal. In an isotonic or isotopic equilibrium, the abundance ratio of two neighboring nuclei indexed by n and $n+1$ with increasing Z or N can then be expressed by the Saha equation [57, 70]:

$$\frac{Y_{n+1}}{Y_n} = \rho_n \frac{G_{n+1}}{2G_n}\left(\frac{A_{n+1}}{A_n}\frac{2\pi\hbar^2}{m_\mu kT}\right)^{3/2} e^{\left(\frac{S_{n+1}}{kT}\right)} \tag{1.22}$$

where Y_n and Y_{n+1} are the abundances of an initial and final nucleus of a single proton or neutron capture reaction in the chain, A is atomic mass number, T is the temperature, G the partition function, ρ_n the proton or neutron density, m_μ is the atomic mass unit, k the Boltzmann constant, and S_n is the proton or neutron separation energy. The maximum abundance in a chain and therefore the path of the process for a given density and temperature occurs at a fixed separation energy. Because of the exponential dependence on binding energy differences nuclear masses are among the most important quantities for modeling the r- and rp-processes. The partition functions are defined as

$$G = \sum_i (2J_i + 1) e^{(-E_i/kT)}, \tag{1.23}$$

summing over all states with spin J and excitation energy E. The ratio is primarily determined by Sn and therefore the nuclear masses, which enter exponentially.

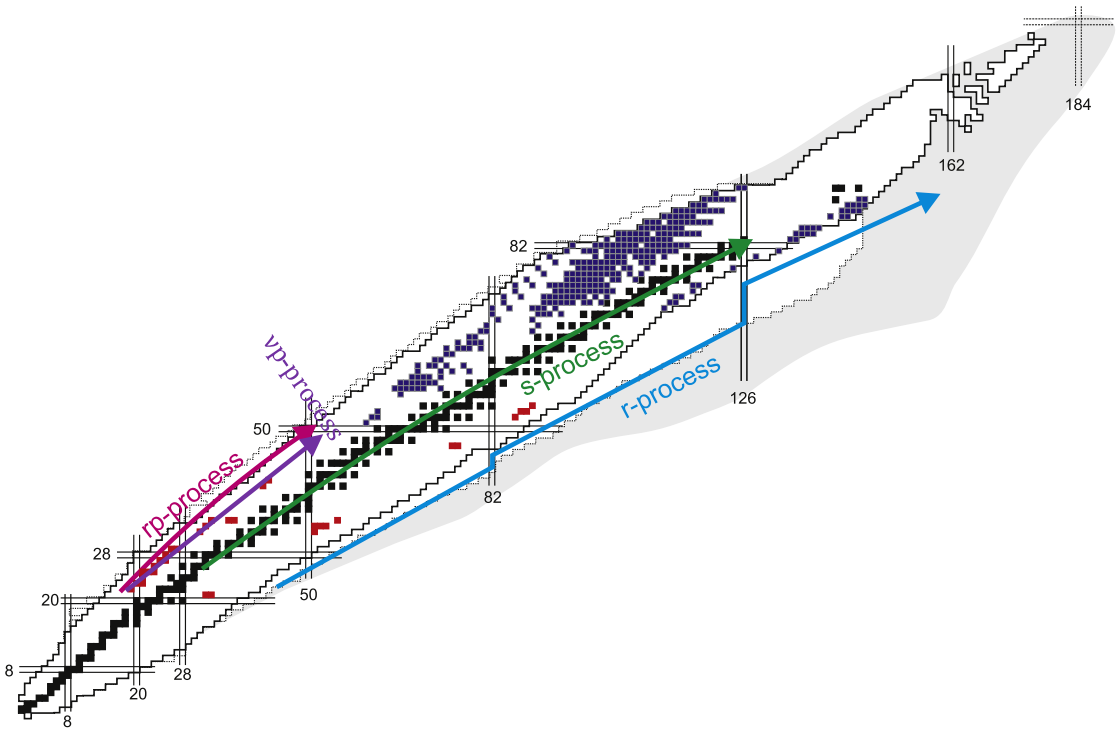

Fig. 1.6 Schematic overview of the nuclear processes in the Universe on the chart of nuclides. Locations of slow neutron capture (s-process), rapid proton (rp-process), neutrino-proton (νp-process), and rapid neutron (r-process) processes of nucleosynthesis are schematically illustrated by arrows with different colors. Stable nuclides are shown with black color. White region of nuclei with solid black borders represents the nuclei which were synthesised in laboratory. Blocks in grey are the expected region of existence of bound nuclei. Nuclei whose masses were determined with help of the storage ring mass spectrometry are indicated with red and blue color, respectively, for Isochronous and Schottky mass spectrometry. Masses obtained indirectly by using the data from α and proton decay spectroscopy on the measured ^{209}Bi projectiles are also indicated with blue color. The white region with dotted boundary reflects the nuclei which will be accessible at the next generation radioactive-ion beam facilities like RIKEN, HIAF or FAIR. Figure modified from [55].

With an exponentially depend on the Q values of the reaction rates as explained in the Saha equation and reaction rates depending on the adopted Q values in theoretical predictions, the mass is among the most important input parameters for the reaction paths of nucleosynthesis.

Some of the most important scenarios of matter creation in stars are discussed below:

s-process

The site of the slow neutron capture process (s-process) is estimated to have produce about half of the heavy elements beyond germanium by a sequence of slow neutron captures. The process is slow (the defined name) in the sense that there is sufficient time for radioactive decay to occur before another neutron is captured. A series of these reactions produces stable isotopes by moving along the valley of β-decay stable isobars in the chart of nuclides.

The s-process is mainly responsible for the creation of nuclei close to the valley of β-stability. The s-process is relatively well studied and the now important information needed are neutron capture rates. Measurements of neutron capture rates on the related isotopes are difficult and many of the shorter-lived cases have not been determined experimentally. To maximize the validation potential of stellar models through s-process nucleosynthesis: measurements of neutron capture rates on these radioactive species are important for the future new generation RI facilities [58].

r-process

The r-process is the second major nucleosynthesis process nearly producing another half of the heavy elements beyond iron ($Z > 26$) [59, 60]. This process proceeds via rapid neutron captures (n,γ) and β-decays, possibly including (γ, n) photo-disintegration reactions and fission processes postulated to occur in high temperature and neutron density environments. Unlike the s-process, the r-process resorts have not been determined with certainty.

The future observational constraints may distinguish the sites between supernovae and neutron star mergers, and first hints in favor of neutron star mergers are being obtained from the observations of optical afterglows of short γ-ray bursts (kilo-novae [61]) and the r-process enrichments observed in some dwarf galaxies [62]. However, nuclear physics seems to be the only possible way to validate individual sites and mechanisms within these various scenarios for r-process.

The abundant supply of neutrons and high temperature in stellar events within the scenarios of r-process is sufficient to produce neutron-rich nuclides through a series of rapid neutron-capture reactions upon seed nuclei that is counterbalanced by photodissociation.

Elements of higher Z nuclei are created when isotopes for each element subsequently decay, which occurs on a much slower timescale than the neutron-capture and photodissociation reactions. As the event ends, the temperature and neutron density decrease, and the nuclides created decay back towards stability with increasing proton number by keeping the atomic number and populate the observed elements today.

The observed abundances of the elements peaks at A $\sim$ 80 (zinc,) , 130 (tellurium), and 195 (platinum) correspond to magic numbers N = 50, 82, 126 due to the sudden transition of the neutron-separation energy across the closed shell and the corresponding long β-decay lifetimes. Establishment of the r-process path requires knowledge of the masses of a large number of neutron-rich nuclei, and r-process models indicate that a mass precision of $\sim$ 250 keV is generally sufficient for these purposes. However, for some key waiting-point nuclei, a mass precision from experiments on the order of 25 keV may be necessary. The other nuclides whose masses are of most importance to the accuracy of r-process models are those that are involved during freeze-out, when the assumption of (n,γ) - (γ,n) equilibrium begins to fail and may be responsible for the creation of the rare-earth peak in the abundance distribution at $A \sim 160$. At this time in the r-process event, photodissociation (γ,n) and neutron-capture (n,γ) rates become more important in the distribution of the elements produced. Since photodissociation rates are exponentially dependent on the neutron-separation energies, the mass uncertainties of the relevant nuclides can also affect the final abundances. The long-standing challenge for study of this field is to produce the extremely unstable nuclei along the r-process path to enable measurements of the critical nuclear physics quantities. This is one of the primary motivations for a next generation radioactive beam facilities such as RIBF, FAIR, and FRIB, HIAF and more. Despite these difficulties, some experiments have succeeded to reach the r-process examples include the mass measurements of $^{129-131}Cd$ at ISOLDE/CERN [65], the half-life measurement of ^{78}Ni at NSCL/MSU [66], recent measurements near $N = 126$ at FRS/GSI [67], and some results from the first next generation radioactive beam facility at RIBF/RIKEN where a broad range of new half-lives in the r-process has been determined [68]. β-decay endpoint measurements on ^{130}Cd gave hints that the N = 82 shell closure might be quenched at Z = 48 thus leading to the conclusion that ^{130}Cd is not a waiting point. However, isomeric decay studies on ^{130}Cd conclude in contrast that $N = 82$ is not quenched at Z = 48. To resolve this controversy, the masses of $^{129-131}Cd$ were determined with high precision via the Penning-trap mass spectrometer ISOLTRAP [69] and new masses show a significant reduction of the N = 82 shell gap for Z $<$ 50. The Rare-RI Ring was originally proposed to measured the r-process masses and the first two motivations for these area are focus on the masses of $^{74-78}Ni$ isotopes and $A \sim 130$ r-process second peak area. The next steps are approaching the heavier nuclei near the rare-

earth peak at $A \sim 160$ area and other important masses related to the r-process. It should be emphasized that the biggest uncertainties when using mass models do not come from their rms performance measured with known masses (that often have been used to determine the parameters of the mass model), but from deviations of predicted systematic mass trends over many isotopes from the true mass surface. Such deviations can be caused for example by over or under prediction of shell gaps, or by failing to correctly predict the evolution of deformation with neutron number. It would be important to find ways to account for such highly correlated systematic uncertainties in sensitivity studies.

rp-process and νp-process

X-ray bursts occur on the surface of neutron stars that accrete matter from a companion star, powered by the rp-process [70–72], a sequence of rapid proton captures and β^+-decays reaching up to a SnSbTe cycle for bursts with large amounts of hydrogen to burn [71]. The hydrogen rich material often accumulates on the neutron star surface for a few hours before a thermonuclear runaway triggers an explosion that gives rise to a bright $10-100s$ long X-ray burst. The ashes of the burst remain on the neutron star surface and the process repeats with a new fuel layer accumulating. Nuclear physics determines the shape of the observed burst light-curve and the composition of the ashes of X-ray burst, which sequentially defines the composition of the underlying neutron star crust. The latter is important as heat generated in the crust will affect burst recurrence times and also observations of cooling crusts in systems where the accretion has shut off. The rp-process in type I x-ray bursts starts, for example, from a breakout of the hot CNO cycle by a sequence of β-induced reactions and proceeds then via rapid proton-capture reactions and subsequent β^+ decays close to the $N = Z$ line on the chart of nuclides. The importance of the nuclear mass in rp-process lies mainly in the balance between the forward (p, γ) reaction and its inverse. Particularly, at the so called waiting points, i.e. nuclei with even $N = Z$, these two processes compete with each other. A small positive or a negative Sp usually ensures that the inverse process dominates. In such a scenario, the rp-process may get stalled and wait for β-decay of the waiting point nucleus. Of course, it is well known that at certain temperature range, depending on the Q-value of the reaction, two proton capture can bridge the waiting point enabling the rp-process to continue without any hindrance. In particular in hydrogen-rich bursts, it can reach up to tellurium, where the predominant α-instability, ^{107}Te and ^{108}Te, returns the flow into the closed $SnSbTe$ cycles, although recent mass results have shown that the branching into the closed $SnSbTe$ cycle is weaker than expected. In the Ge to Kr mass region mass excesses of short-lived $A = 2Z - 1$ nuclei have been addressed for the first time with the CSRe storage ring employing isochronous mass measurements [81]. Mass uncertainties of a few

keV allowed to deduce the proton-separation energy of ^{65}As to be $S_p = -90(85)\,keV$, thus being slightly proton unbound. Including the new data into $x-ray$ burst model calculations showed that the majority of the reaction flow passes through ^{64}Ge via proton capture for most relevant temperature-density conditions, thus, removing ^{64}Ge from the list of prominent rp-process waiting points. The possibility for the existence of the ZrNb cycle for the low α separation energies predicted for ^{84}Mo by the Finite Range Droplet Mass Model in the rp process, would impose an upper temperature limit for the rp process to synthesize elements beyond Nb, including the light p nuclei in the A = 92-98 mass region [39]. The most recent mass measurements of the ^{82}Zr, ^{84}Nb by storage ring CSRe/IMP and the extrapolated masses of ^{78}Y, ^{80}Zr, ^{82}Nb, ^{84}Mo are used for type I X-ray burst model calculations and indicates a reduced $^{84}Mo(\gamma,\alpha)^{80}Zr$ and $^{83}Nb(p,\alpha)^{80}Zr$ reaction rate, which leads to a weakening or even disappearance of the Zr– Nb cycle in the rp-process in type I X-ray bursts [80]. In order to finally quantify the temperature limit and to explore to which degree such a cycle poses a limitation to current models of the rp process, precise mass measurements of ^{80}Zr, ^{84}Mo are still called for. It would be of great significance for future mass measurements to address the ZrNb cycle problem in the future.

In the nearly same mass region, the νp-process [73–76] occurs as a sequence of (p,γ) and (n,p) or β^+ reactions which produce neutron-deficient nuclei with A > 64. It is estimated to occur in proton-rich core-collapse supernova ejecta with the influence of strong neutrino and antineutrino flux producing neutrons via antineutrino absorption on free protons: $\overline{\nu}_e + p \rightleftharpoons n + e^+$. The (n,p) reactions being a source of neutrons allow the long β-decay half-lives to be overcome. After the temperature drops, the proton-capture reactions freeze out, and matter decays back to the valley of β stability. In this way, neutron-deficient nuclei are produced and ejected in the supernova explosion. This process allows for the nucleosynthesis of nuclei with mass numbers $A \leq 64$, making itself a possible candidate to explain the origin of the solar abundances of light p-process nuclei $^{92;94}Mo$ and $^{96;98}Ru$ which could not be well produced by other process [78, 79]. It offers a natural explanation for the large abundance of Sr observed in a hyper-metal-poor star as well.

Besides nuclear astrophysics processes like $rp, \nu p, r$ processes, the mass data as inputs for modeling neutron crust process, i-process and EC processes are strong interests to continue with high-accuracy mass measurements. The precision masses of exotic nuclei also contribute to constrain the nuclear matter equation of state (EOS), which might be important for the understanding of the structure of neutron stars.

1.4 Techniques for mass measurements

Mass measurement techniques are often divided into "indirect", i.e. radioactive decay or nuclear reaction, and "direct" techniques, e.g time-of-flight (TOF) or frequency measurements based on mass spectrometry to determine masses, due to the fact that the former yields mass differences and the latter generally makes measurements with respect to a reference with well-known mass value eliminating error accumulation. Absolute measurements are impracticable due to the fact that it would be somehow impossible to determine the magnetic field values to anywhere near the desired precision.

Several experimental techniques currently dedicated to the mass measurements of radioactive nuclei by mass spectrometry are briefly described below.

1.4.1 Indirect techniques

Radioactive decay Q values can provide relatively accurate mass differences between parent and daughter nuclides [5]. However, in order to derive mass values, these differences must be linked to a known mass which can be quite far away sometimes, which will induce cumulative error. Besides, it is usually very difficult to get the complete spectroscopic information, and errors can occur if a decay branch, particularly high-lying, has not been detected. This is especially true in the case of beta decay, for which the additional determination of the detector response function, required to correctly unfold the end-point energy, can also render such mass determinations risky.

Indirect methods to deduce mass values are based on the determination of the Q value in a reaction or decay taking advantage of the energy-conservation law $E = mc^2$.The Q value of a nuclear reaction is defined as the difference between the sum of the masses of the initial reactants and the sum of the masses of the final products, in energy units (usually in MeV):

$$Q = \Delta mc^2 = (M_f - M_i)c^2. \tag{1.24}$$

A nuclear reaction $A(a, b)B$ can be used to determine the mass of the unknown product B if the masses of the incoming particle a, outgoing particle b and the target A are known. Additionally, the kinematics of the unknown mass or the reaction Q value must be determined by a relatively precise mass spectrometer and well-calibrated. Due to these requirements, the applicability of reaction studies is somewhat limited. Since product B does not need to be bound, it is possible to take this advantage to study nuclei that would otherwise not be accessible by other methods. Missing mass and invariant mass methods are generally used for this technique.

The mass of a radioactive nuclide can also be derived from its decay Q value which can provide relatively accurate mass differences between parent and daughter nuclides. This, however, will only yield a mass difference; obtaining the mass of the parent requires linking this mass difference to a known mass, which can be quite far away, thus leading to cumulative errors along a decay chain. Additional uncertainties arise from an insufficient knowledge of the decay scheme, where high-lying decay branches might not be detected. β decay is especially complicated in that it is a three-body process, with a neutrino being emitted along with the β particle carrying away part of the decay energy:

$$\beta^- : A(Z, N) \rightarrow A(Z+1, N-1) + e^- + \nu_e \tag{1.25}$$

It is therefore necessary to determine the maximum energy of the β particle, the endpoint of the β spectrum.

1.4.2 Direct techniques

Although many different methods are employed for mass measurements, nearly all presently running experiments for direct mass measurements are based on TOF or frequency measurements.

Penning-Trap Mass Spectrometer

In a Penning trap, a superposition of a strong homogeneous magnetic field B on the radial confinement with a weak electrostatic quadrupolar field E on the axial one is employed to confine the stored ions three-dimensionally in space (see Fig. 1.7). An ion with a charge-to-mass ratio m/q is exposed to the electric and magnetic forces and the resulting net effect is a cyclotron motion, which is composed of three Eigen-motions [23]. These are the axial motion (up and down along the magnetic field axis) with axial oscillation frequency ω_z, and two rotational motions, the magnetron frequency ω_- and reduced cyclotron frequency ω_+ [23, 82]. The latter are both perpendicular to the axial motion. Figure 1.7 shows on the right a calculated trajectory of an ion in a Penning trap and the deconvolution projection of the Eigen-motions. The ions with charge-to-mass ratio q/m perform a radial circular motion with the mass-characteristic cyclotron frequency of revolution ω_c (pure cyclotron frequency). Besides, ω_c can be expressed as the square root of the quadratic sum of all Eigen-motion:

$$\omega_c = \left(\frac{q}{m}\right) B = \omega_+ + \omega_- = \sqrt{\omega_+^2 + \omega_-^2 + \omega_z^2}, \tag{1.26}$$

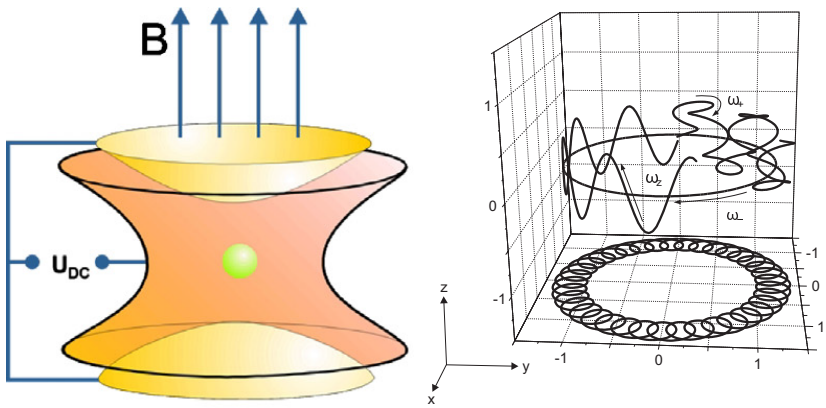

(a) Schematic configuration of a Penning trap system.

(b) Schematic trajectory with ideally three independent eigen-motions of an ion in a Penning trap.

Fig. 1.7 Penning trap structure and motion of trapped ions. Figures from [23, 83]

For an ideal electric quadrupole field, the three eigen-frequencies are:

$$\omega_+ = \frac{\omega_c}{2} + \sqrt{\frac{\omega_c^2}{4} - \frac{\omega_z^2}{2}}, \tag{1.27}$$

$$\omega_- = \frac{\omega_c}{2} - \sqrt{\frac{\omega_c^2}{4} - \frac{\omega_z^2}{2}}, \tag{1.28}$$

$$\omega_z = \sqrt{\frac{qU}{md^2}}. \tag{1.29}$$

Penning traps have been used to measure the masses of nuclides with half-lives down to about several tens of millisecond, and relative precisions of $\leq 10^{-8}$ can be achieved. The resolving power:

$$R = \frac{m}{\Delta m} = \frac{\nu_c}{\Delta \nu} \approx \nu_c T_{rf}, \tag{1.30}$$

where, $\nu_c = \omega_c/(2\pi)$, is directly proportional to the observation time T_{rf}. R together with the number of ions N_{tot} of a radionuclide being confined and accumulated in the trap determine the statistical uncertainty by:

$$\frac{\delta m}{m} = \frac{1}{RN^{1/2}} \tag{1.31}$$

Multi-reflection time-of-flight mass spectrometer (MR-TOF MS)

At present several MR-TOF MS around the world are in operation or under construction [84]. Here, the MR-TOF MS (Fig. 1.8) in recently upgraded ISOLTRAP at ISOLDE/CERN is taken as an example for introduction. In ISOLDE, MR-TOF MS can be operated as a mass spectrometer, either to analyze the ISOLDE ion beam or for precision mass measurements of nuclides. The MR-ToF device, as an electrostatic time-of-flight mass spectrometer with multiple folded trajectories, has improved significantly ISOLTRAP's capability of purification of contaminated RI beams. Due to its extended flight path, which is no longer limited by the dimension of the device, long flight times could be achieved, leading to mass resolving powers several times higher than obtained up to now with conventional table-top mass spectrometers. This property, combined with a fast operation cycle, single-shot measurement of several ion species (although of a limited mass range) and single-ion detection made the MR-ToF device appear as a promising mass spectrometer for short-lived RI species or that have lower yields than those accessible for Penning-trap mass spectrometry. Furthermore, in connection with a fast ion selector, it can supply highly-resolved mass-over-charge selected bunches for subsequent experiments.

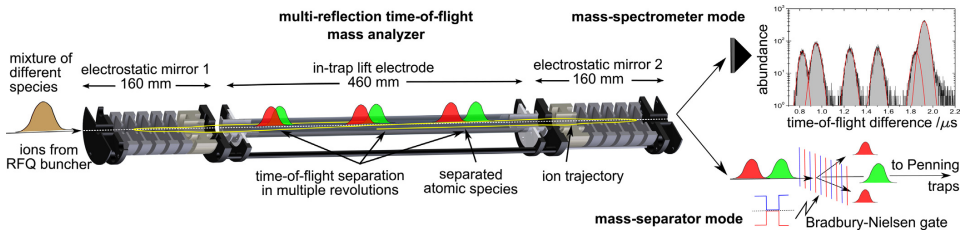

Fig. 1.8 Sectional view of the MR-ToF device. Through two mass-sepectrometer mode, the mass-separated ions can be either detected by a MCP detector to record a TOF spectrum (right top) or selected by a Bradbury-Nielsen gate (BNG) as a fast ion selector (right bottom). Figure adopted from [84].

Fig. 1.8 shows the ISOLTRAP's MR-TOF mass analyzer. It consists of two 160 mm long electrostatic ion optical mirrors, each incorporating six electrodes, with inner and outer shielding electrodes surrounded. The mirrors are separated by an 460 mm long in-trap lift, a drift electrode whose electric potential can be pulsed to facilitate ion injection, ejection and control of the TOF focus plane [84]. High mass resolving power can be achieved by either increasing the TOF in MR-TOF MS or decreasing the signal width at the detector plane. The operation period for maximum mass resolving power of $\approx$ 200,000 (in FWHM) is about 30 ms for this MR-TOF MS.

Bρ-TOF method

Many fruitful combinations of high energy projectile fragmentation and high resolution spectrometers have been utilized to deliver a wide range of isotopes allowing for simultaneous measurement of nuclei of interest and nuclei of known mass via Bρ-TOF method [87]. Particle identification (PID) is usually performed with time of flight and energy loss measurements in the spectrometer. The Bρ-TOF technique for mass measurements of exotic nuclei is based on measurement of the magnetic rigidity and the corresponding time-of-flight of the ion:

$$B\rho = \frac{\gamma M_0}{q}\frac{L}{TOF}. \tag{1.32}$$

The mass-to-charge ratio M/q is derived from Eq. 1.32:

$$M_0/q = \frac{B\rho}{\gamma L/TOF} = B\rho\sqrt{(\frac{TOF}{L})^2 - (\frac{1}{c})^2} \tag{1.33}$$

where c is the speed of light, and γ is the Lorentz factor. TOF can usually be determined with very high precision, while the measurements of magnetic rigidity Bρ and flight length L would severely limit the precision of the resultant mass. Thus in practice nuclei with well-known masses are measured along with nuclei of unknown mass in order to calibrate the relationship between time of flight, rigidity, and mass. Consequently one yields a simple relationship between time of flight and mass of the nuclei of interest. The method will be discuss in detail in chapter 3. The mass uncertainty can be deduced from Eq. 1.33:

$$\frac{\delta M_0}{M_0} = \frac{\delta(B\rho)}{B\rho} + \frac{1}{1-(\frac{1}{c}\frac{L}{TOF})^2}(\frac{\delta(TOF)}{TOF} - \frac{\delta L}{L}) \tag{1.34}$$

The analysis and calculation of the mass resolving power of this technique depending on detector resolutions in this work have been shown in Appendix D.

Till now, Bρ-TOF mass measurement experiments have primarily been performed at four facilities. The Ganil (SPEG) [85] at the Grand Accélérateur National d'Ions Lourds (GANIL) performed the first Bρ-TOF experiment in 1986, shortly followed by measurements using TOF Isochronous Spectrometer (TOFI) [86] at Los Alamos National Laboratory (LANL) that same year. The recent Bρ-TOF mass measurement (2006) started to use the S800 Spectrograph at the National Superconducting Cyclotron Laboratory (NSCL) [89]. Each facility employs beam optics settings which result in a TOF that is only dependent on the mass to charge ratio (m/q). Measurements at SPEG and NSCL have additionally employed mid-TOF position measurement to correct for the momentum spread of the ion beam. Most recent Bρ-TOF mass measurement were conducted at RIKEN by the BigRIPS-ZeroDegree

beam-line, BigRIPS-SHARAQ combination with dispersive focus position and in this work as a by-product of in-ring mass measurement by applying the conjugation of the BigRIPS with the high resolution beam-line in RIKEN as discussed in chapter 2. Recently, the results of neutron-rich calcium isotopes beyond neutron number 34 at the RIKEN Radioactive Isotope Beam Factory by using the Bρ-TOF method have been published [90]. The atomic masses of the neutron-rich calcium isotopes $^{55-57}$Ca were measured and determined for the first time. By observation of the mass evolution in Ca isotopes beyond N = 34, the magic nature at N = 34 in the neutron-rich Ca region became evident by showing the energy gap of the single-neutron spectrum.

Bρ-TOF mass measurement with typical TOF $\sim$ 1μs provides mass data with an accuracy from 10^{-4} up to the level of 10^{-6} which is usually depending on the statistics and allow simultaneous measurements of many nuclides, reference isotopes as well as isotopes of interest. Experiments via this technique have generally focused on the most proton and neutron-rich nuclei very far from stability as shown in Fig.1.13 corresponding to the nuclei with lowest half-lives, benefiting from its single-ion sensitivity and the short measurement time. Bρ-TOF method would be a perfect marriage with multi-physics pursue experiments in next generation rare isotope facility like RIBF in RIKEN, as each has the goal of studying nuclei on the limits of existence and obtain several fruitful results from different experimental purpose in one experiment run. The combination of two mass techniques (Bρ-TOF via beam-line and isochronous mass spectrometer by storage ring) in one experiment is realized in this work.

Cyclotron mass spectrometry

In order to improve the resolution of a time-of-flight measurement, a longer flight path is needed. This can be achieved by using a cyclotron, where the ion path increases to ~1 km, as is developed using the GANIL coupled cyclotrons, which uses a cyclotron CSS2 as a high resolution mass spectrometer for fast secondary ions [91]. The previous TOF is measured over ~116 m flight path at SPEG/GANIL via Bρ-TOF method. A mass resolution of 3 x 10^{-5} can be reached for nuclides with half-lives down to a few tens of µs. This method has already been used successfully for the mass measurement of doubly magic ^{100}Sn [92] to a precision of 10^{-5}. In the ^{100}Sn experimental setup, residues are produced by fusion-evaporation reactions between a primary beam delivered by the first cyclotron (CSS1) of GANIL, and a target placed between the two cyclotrons. Secondary ions produced in the target are injected into CSS2 tuned with the magnetic rigidity. Different nuclides can be simultaneously accelerated in CSS2, making it possible to accelerate known and unknown masses at the same time. The unknown mass can be determined from a well-known reference

mass after the same number of turns inside CSS2 by measuring their time-of-flight (or phase) relative to the high frequency signal of CSS2. The total time-of-flight of the beam could be measured between the micro-channel plate detector and the plastic scintillator.

Storage ring mass spectrometry

Dimensions of Paul and Penning traps are typically only of the order of a few centimeters, while heavy ion storage rings, which are also widely used as large ion traps, have diameters of a few meters to tens of meters.

There are presently three laboratories where a combination of a radioactive-ion-beam fragment separator with a storage-ring facilities is realized. Storage ring mass spectrometry was pioneered at GSI at Darmstadt in 1990 [44, 93, 94, 97]. The GSI facility is schematically illustrated in Fig. 1.9.

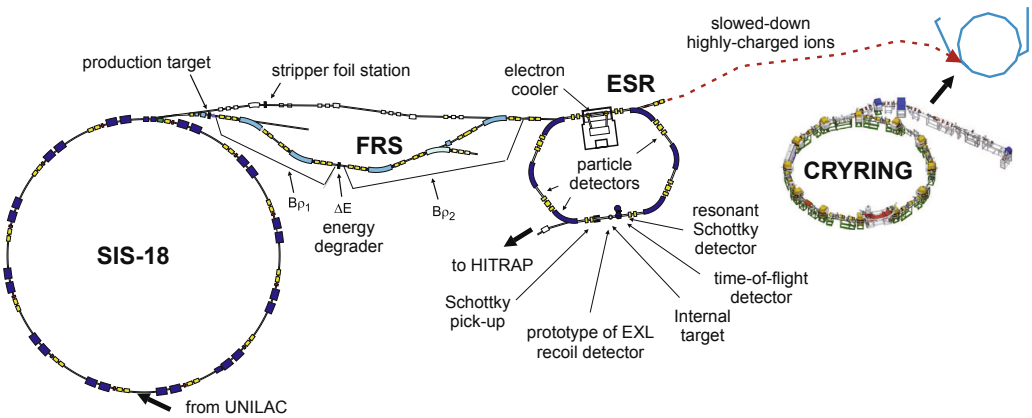

Fig. 1.9 Schematic demonstration of the SIS-FRS-ESR facility at GSI. Locations of important installations and detectors are indicated. Primary beams provided from the linear accelerator UNILAC are injected into the heavy-ion synchrotron SIS, then accelerated in the SIS to several hundred MeV/u and bombarded on the production target in front of the fragment separator FRS. After separation in flight in the FRS, reaction products are injected into the storage ring ESR for experimental investigations. IMS and SMS have been both utilized for mass measurements in ESR. The low-energy storage ring, CRYRING, which was until recently in operation at Stockholm university, is being presently installed right after the ESR. Figure modified from [95, 96].

The second storage ring facility is located at the Institute of Modern Physics in Lanzhou (IMP), Chinese Academy of Sciences [98–100]. Its high energy part is based on a similar principle as the GSI facility as shown Fig. 1.10 . Selected parameters of the GSI and IMP storage ring facilities are listed in table 1.2. Although the decay studies of Radioactive highly charged ions (R-HCIs) are possible in CSRe, it was commissioned only recently and all

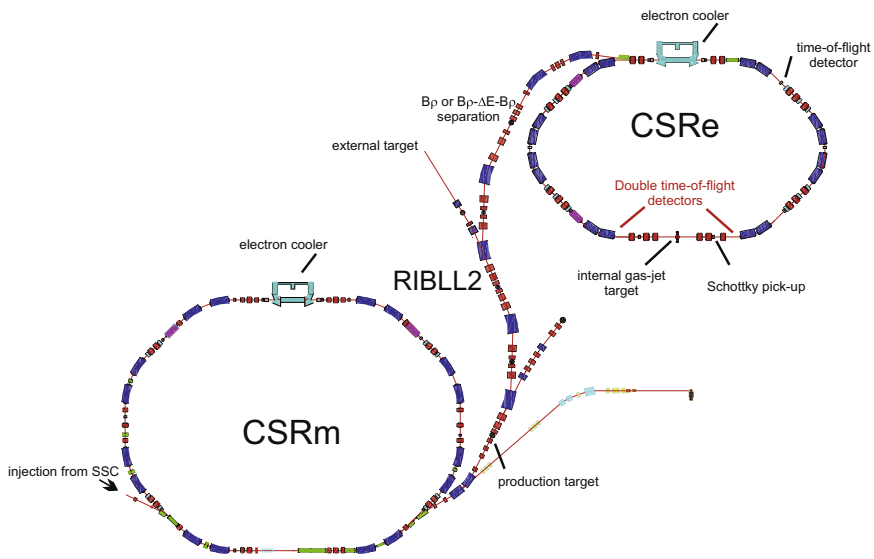

Fig. 1.10 Schematic view of the radioactive beam facility at the IMP in Lanzhou. Primary beams from the superconducting cyclotron SSC are accelerated by the synchrotron CSRm, which are then fast extracted and impinge on the production target in front of the in-flight fragment separator RIBLL2. Projectile fragments are separated in the RIBLL2, then injected and stored in the CSRe. Revolution frequencies of the electron-cooled ions can be measured using the Schottky pick-up (SMS is not yet used till now). If the CSRe is tuned into the isochronous ion-optical mode as an Isochronous Mass Spectrometry (IMS) then the revolution frequencies can be obtained also for uncooled particles by using dedicated time-of-flight detectors. Adopted from [100].

Table 1.2 Selected major parameters of the ESR/CRYRING, CSRe, R3 storage rings. This table is modified from [96].

Parameters	ESR	CSRe	R3	CRYRING
Circumference (m)	108.36	128.80	60.3507	54.17
Maximal magnetic rigidity Bρ (Tm)	10.0	8.4	4.045	1.44 Tm (ions)
Electron cooling (ion energy) (MeV/μ)	4–430	25–400	-	
Stochastic cooling (ion energy) (MeV/μ)	400	-	-	-
Transition point γt (isochronous mode)	1.39–1.41	1.395	1.2147	-
Transition point γt (standard mode)	2.29	2.629	-	-
Acceptance in isochronous mode $\delta(B\rho)/(B\rho)$	±0.2%	±0.2%	±0.5%	-
location	GSI/Germany	IMP/China	RIKEN/Japan	GSI/Germany

studies to date were performed at the ESR. A schematic few of the Rare-RI Ring is shown in Fig. 1.11.

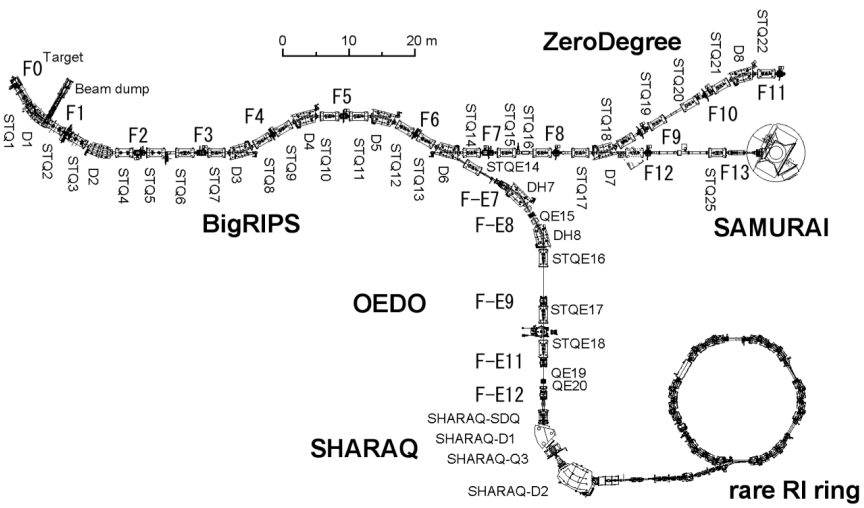

Fig. 1.11 Schematic layout of the latest RI Beam Factory (RIBF) with the Optimized Energy Degrading Optics (OEDO) beam-line and the Rare-RI Ring included at RIKEN Nishina Center. The layout illustrates the BigRIPS separator and the ZeroDegree spectrometer along with the OEDO beam-line and the SHARAQ, the Rare-RI Ring and SAMURAI spectrometers. The RIBF cyclotrons can accelerate all heavy ions up to approximately 345 MeV/nucleon, including very heavy elements such as uranium. The goal beam intensity is as high as 1 $p\mu A$, corresponding to 6×10^{12} particles/s.

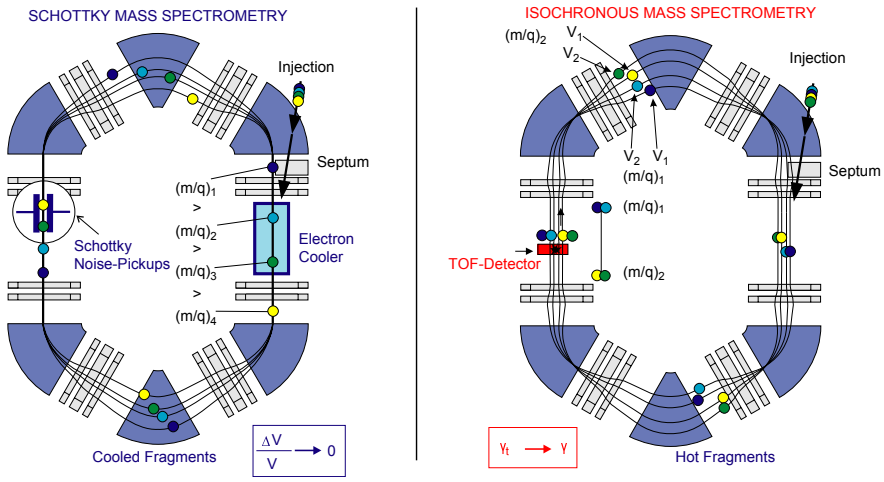

Fig. 1.12 Schematic overview of the IMS and SMS methods. Left hand side: Schottky mass-spectrometry. After electron-cooling [104], velocity spread of the ions gets negligibly small. Their revolution frequencies or times are measured by Schottky pick-up [112] mounted in the ring aperture. This technique has been successfully applied at longer-lived exotic nuclei. Right hand side: Isochronous mass-spectrometry. Uncooled ions circulate at the transition energy $\gamma = \gamma_t$, and their revolution times are measured by a time-of-flight technique [113, 114]. This method is in particular suited for short-lived nuclei with half-lives in the millisecond or even microsecond range. Figure adopted from [101]

The revolution time, T, for an ion circulating in the storage ring, is related with its mass-over-charge ratio, m/q, via the following expression:

$$T = \frac{L}{c}\sqrt{1 + (\frac{mc}{q})^2 \frac{1}{(B\rho)^2}}, \tag{1.35}$$

where L is the orbit length of the ion, c the speed of light, and $B\rho$ the magnetic rigidity. Within a certain magnetic rigidity acceptance, $\delta(B\rho)$, orbit lengths of ions are not constant.

The basic principle for storage ring mass spectrometry describing the relationship between mass-over-charge ratio (m/q) and revolution period (T) or revolution frequency (f) can be quantitatively expressed in first order approximation [43–46]:

$$\frac{dT}{T} = -\frac{df}{f} = \frac{1}{{\gamma_t}^2}\frac{d(m/q)}{m/q} - \left(1 - \frac{\gamma^2}{\gamma_t^2}\right)\frac{dv}{v} = \frac{1}{\gamma^2}\frac{d(m/q)}{m/q} + \left(\frac{1}{\gamma_t^2} - \frac{1}{\gamma^2}\right)\frac{d(B\rho)}{B\rho},$$

where γ is the relativistic Lorentz factor, v the velocity of the ion. γ_t is the so-called transition energy of the ring [18] For more details of the equation deduction (see chapter 2). The

momentum compaction factor α_p is defined as:

$$\alpha_p = -\frac{1}{\gamma_t^2} = -\frac{(\Delta C/C)}{(\Delta(B\rho)/B\rho)} = \frac{1}{C_0}\oint \frac{D(s)}{\rho}\, ds, \tag{1.36}$$

α_p characterize the ratio between the relative change in the orbital length C and the relative change in the magnetic rigidity $B\rho$ of the stored ions, which is nearly constant over the entire revolution frequency acceptance of the storage ring. The α_p can also be deduced from the dispersion function $D(s)$ of the ring. Here s denotes the coordinate along the reference orbit C_0, while ρ is the radius of the curvature of this reference orbit in the bending sections.

The mass resolving power of IMS:

$$R = \frac{m}{\Delta m} = \frac{1}{{\gamma_t}^2}\frac{T}{\Delta T}, \tag{1.37}$$

which is inversely proportional to the uncertainty of measured revolution time T. In order to determine m/q-values with the measured revolution frequencies or alternatively revolution times of the ions, the second term of Eq. (1.4.2) right hand side has to be made negligibly small:

$$(1 - \frac{\gamma^2}{\gamma_t^2})\frac{dv}{v} \rightarrow 0. \tag{1.38}$$

Based on this principle, two complementary experimental methods to satisfy Eq. 1.38, namely Schottky (SMS) [101–103] and isochronous (IMS) mass spectrometry [101, 105, 106] as shown in Fig. 1.12, have been developed for accurate mass measurements.

1. **Schottky mass spectrometry** One way is to cool the ions by stochastic and electron cooling [104], which forces all stored ions toward the same mean velocity and thereby reducing the velocity spread to roughly 5×10^{-7} at low intensities. The revolution frequency of the ions can be measured by sampling the induced signal by the Schottky noise spectroscopy [112]. The stored ions revolve in the storage ring more than a million times per second. Revolution frequencies at typically employed ion energies of 300-400 MeV/μ are about 2 MHz in the ESR, 1.5 MHz in the CSRe, and 3 MHz for the R3 with ion energy ~170 MeV/μ. Each ion induces at each revolution a mirror charge on the detectors which is added to the thermal noise. The Fourier transform of the amplified signal from the detector yields a spectrum of revolution frequencies. The charges induced on the pick-ups are tiny compared to the thermal noise of the pick-ups and electronics. Therefore, many thousands of revolutions of the ions in the ring are required to detect a single stored ion. With this method many different ion species can be studied simultaneously with single-ion sensitivity. However, the

relatively long cooling times set a limit on the half-life of the nuclide of about a second. Till now, only ESR has successfully conducted SMS experiments for mass and lifetime measurements. R3 has no electron cooler to only use IMS for mass measurements and the SMS is being tested at CSRe [115].

2. **Isochronous mass spectrometry**

   Another way to is to use a special ion-optical setting of the ring and inject the ions with $\gamma = \gamma_t$, which is the basis of the isochronous mass spectrometry (IMS). Exotic nuclei with half-lives shorter than the cooling time can be studied by operating the storage ring in the isochronous ion-optical mode. The principle of this ion-optical mode is to send a faster ion of a given ion species onto a longer orbit while a slower ion of the same ion species onto on a shorter orbit, so that the velocity spread is compensated by the lengths of the closed orbits. This means that the revolution time of the circulating fragments does not depend (in first order) on their velocity spread. In the case the ESR or CSRe, when ions of interest are injected into the ring, revolution times are measured by a dedicated TOF detector inside the storage. The detector is equipped with a thin ($10 - 20\mu g/cm^2$) carbon foil. Secondary electrons are released from the foil when it is penetrated by the fast highly charged ions. These electrons are detected giving a time stamp for each ion passing at each revolution through the detector. The ions perform several hundreds of revolutions before they are lost from the ring mainly due to the energy loss in the foil. The fragments do not require cooling and the nuclei with half-lives as short as 10 μs, about 20 revolutions in the ring, can in principle be measured with this method. This is the basis for the IMS, with which a number of successful mass measurements were conducted at ESR and CSRe.

   In the case of Rare-RI Ring, the revolution time is deduced from start TOF detector before injection and Stop TOF detector at the extraction line. The TOF detector at the injection as a start usually utilize a electrostatic (E) foil mirror-type MCP detector, electrostatic-magnetic field cross arranged (B-E) foil MCP which is the same type used in ESR and CSRe or thin plastic scintillator (0.1mm in thickness). By this way, no destructive detector is used inside the ring. With a long pass length after $\sim$ 2000 turns, which corresponds to circulating time of about 700 μs, the uncertainty brought from the TOF detector ($\leq 100ps$) can be neglected to reach a TOF precision of better than 10^{-6}. By the way, we can also use foil detector inside the Rare-RI Ring for revolution time measurement, which can be used for Shottky setting and mass deduction directly like ESR and CSRe.

Obviously, from Eq. 1.4.2, we can know that only one species of nucleus fulfill isochronous condition $\gamma = \gamma_t$ in one isochronous optics setting of storage ring. To measure the masses in the so-called isochronous condition, only within a small mass-to-charge region, which is called the isochronous window, can be used to deduce the masses with the required high resolving power. While for other ion species far away from the isochronous window, or even for the ions of other species within the isochronous window, the isochronous condition is not strictly fulfilled. Inevitable momentum spread due to the acceptance of the storage ring will broaden the distribution of revolution time period, which will result in a worse mass resolving power. Therefore, IMS with additional Bρ determination to correct the revolution time of stored ions is crucial to increase the mass resolving power of IMS. In conventional IMS method at GSI and CSRe, one TOF detector is installed in the ring for particle identification by measuring the in-ring TOF spectrum and deduce mass without extra $B\rho$ or velocity measurements of ions. Some possible ways for extra $B\rho$ or velocity measurements in IMS are overviewed below.

New concepts of TOF methods at storage ring

To decrease the spread of revolution period, additional magnetic rigidity or velocity measurements of stored ions should be precisely measured. It is assumed that, ions with the same magnetic rigidity will move around the same closed orbit, regardless of their species. Therefore, the correction of magnetic rigidity can be established via the correction of the corresponding orbit. By employing this additional information, the mass resolving power of IMS will be significantly improved. In conclusion, all these methods for magnetic rigidity or velocity correction can be called orbit confinement method.

(a) **$B\rho$-tagging IMS** Experiments at GSI where the high resolution of the FRS is used to determine the $B\rho$ of the injected fragments within $\sim 10^{-4}$ at the second dispersive focal plane via a modified slit system. The mass resolution achieved with this $B\rho$-tagging is significantly improved together with the time spectra resolution [109]. Of course, this achievement also improves the identification and separation of isomers compared to previous IMS measurements at ESR. A drawback of this method is the slit dramatically constrain the injected ions by the selected narrow $B\rho$ range and will result in lost of large amount of statistics.

(b) **IMS with Double-TOF** One method for $B\rho$-tagging is to measure velocity of heavy ion circulating in storage rings event by event, by using two time-of-flight

detectors installed at the straight section of the storage rings. The original idea is firstly proposed at GSI [110], and was recently realized with on-line IMS experiments at IMP [111] and shows good consistence with simulation results. Because of ions penetrating though the double TOF detectors for hundreds of times when setting a circulation hundreds of *um*s, which effectively increase the flight path to tens of thousands of meters. The precision measurement of velocity can be realized at the straight section of CSRe. Collector Ring (CR) at the next generation facility FAIR and the SRing at HIAF will both be equipped with double TOF detectors.

(c) **In-ring TOF-$B\rho$-IMS** To realize the correction by velocity or magnetic rigidity, measurement of the ion's position in the dispersive arc section of a storage ring by using a position-sensitive foil MCP detector or position-sensitive cavity doublet to determine the ion position event-by-event. Different from the Double-TOF method, in principle , only one foil MCP detector with lower energy or non-destructive cavity doublet can realize the same correction effect. Actually, the double TOF detector can be replaced by one compact detector with both good timing performance and high position resolution to reduce energy losses due to the passing through of the foil for hundreds or thousands of turns.

(d) **orbit-IMS method** The Rare-RI Ring is proposed to measure the exotic nuclei in IMS mode with additional velocity or magnetic rigidity measurement for mass correction, which is depend on the hypothesis that ions with the same magnetic-rigidity ($B\rho$) will move around the same closed orbit, regardless of their species. Therefore, the correction of the in-ring revolution time by $B\rho$ (equivalent to velocity for a certain close orbit) measurements can be carried out. Here, the name 'orbit-IMS' will be used for this method.

(e) **TOF-$B\rho$ at beam-line and orbit-IMS by ring** To reach the most exotic area of the chart of nuclides and to have an effective use of the precious beam time, two complementary direct Time-of-flight mass measurements techniques can be used at RIBF in one experiment run. One is the well developed $B\rho$-TOF method by BIGRIPS beam-line coupling with High resolution beam Line (OEDO) and another is the Isochronous TOF method IMS with velocity and $B\rho$ measurements event by event, the Rare-RI Ring at RIBF.

This method is specially suited for $N = Z$ nuclei with the mass-to-charge ratio relative difference on the order of $\sim 10^{-5}$, thus resulting in a foreseen ever better resolution in IMS mass measurements. Besides, after $\sim 700\,\mu s$ circulation in time of flight the $N = Z$ nuclei can all be extracted in the same setting with the

extraction TOF difference during 100 ns range, which means we can save a large amount of turning time for extraction of different circulating target nucleus.

In summary, all the upper new concept methods consider the TOF measurements with an additional $B\rho$ (equivalent with velocity) measurement. The future mass measurements in storage rings will be the one with relative long path length with stabilized magnetic field and $B\rho$ measurements in normal optical mode of the ring, at which the ring possess large acceptance of hot RIs.

Comparison of different techniques

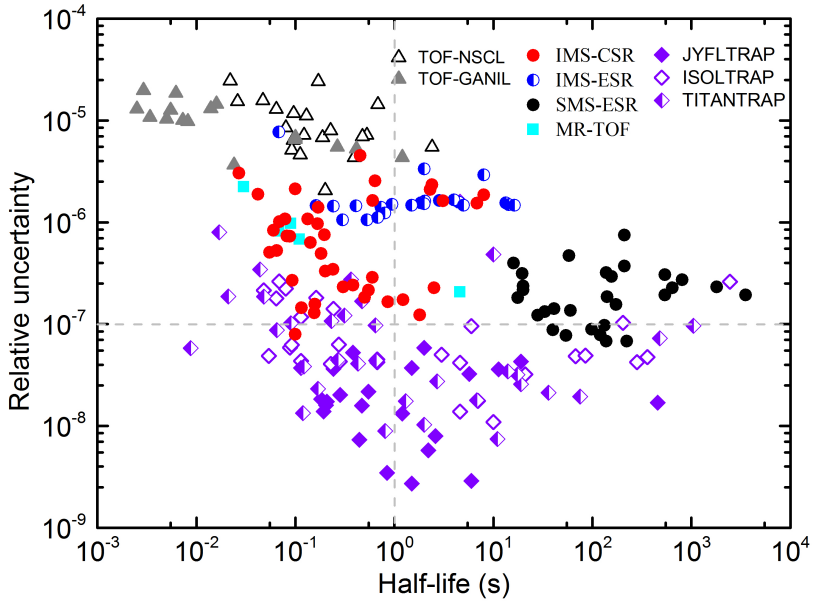

Fig. 1.13 Uncertainties of mass values from various dedicated mass programs using direct techniques as a function of half-lives of the measured nuclei since 2010, data taken from [3].

The precisions that can be reached by different direct mass measurement techniques as a function of life-times of nuclei are compared in Fig. 1.13. As can be seen, the farther one goes from stability which corresponds to lower life-times of measured nuclei, the lower the achieved precision. The highest precisions are currently reached in Penning trap measurements, whereas the Bρ-TOF mass spectrometer can access nuclides the farthest from stability for radioactive ions with a half-life $\leq 1\mu s$.

Chapter 2

TOF Mass measurements at the Rare-RI Ring and high resolution beam-line

2.1 Rare-RI Ring at RIBF

Since 2007, RI Beam Factory (RIBF) [21] as illustrated in Fig. 2.1, at RIKEN Nishina center in Japan, one of the new generation facilities, has been in operation to enhance RI beam intensities to enlarge our territory of advancing experimental studies on the nuclear chart as well as to explore nuclear astrophysical processes. Although the capability of RI-beam production is yet to be optimized to its final target values, its performance is already intriguing and its capability has already trigger tremendous fruitful results and much more on the way. The RIBF accelerator complex, consisting of linacs and cyclotrons, can accelerate all kinds of heavy ions (from proton to uranium) up to 345 MeV/nucleon, and the goal beam intensity is as high as 1 pμA, corresponding to 6.24 x10^{12} particles/s. Since the commissioning, a variety of radioactive isotopes (RI) beams has been produced at the superconducting in-flight separator BigRIPS by using in-flight fission of a $238U$ beam as well as projectile fragmentation of several heavy ion beams such as ^{18}O, ^{48}Ca, ^{70}Zn, $^{78,86}Kr$, and ^{124}Xe. Thanks to the advantageous features of the BigRIPS separator and continuous increase of primary-beam intensities at RIBF, the regions of accessible rare RIs are expanding significantly.

There are many experimental apparatus following the BigRIPS separator, the main experimental instrumentation utilized in this thesis is the Rare-RI ring. Fig. 2.1 shows the placement of the Rare-RI ring in a red square at RIBF. A combination of the High resolution beam-line (updated to be newly constructed OEDO beam-line in the year 2017), SHARAQ spectrometer, injection-line of Rare-RI ring, the Rare-RI Ring mass spectrometer to the Bi-

gRIPS separator makes the mass measurements by two complementary TOF methods possible in one experimental setup.

A schematic view of the Rare-RI Ring (R3) [174–176] structure is shown in Fig. 2.2. The Rare-RI Ring was constructed in B3F of the RIBF and it was located in the down stream of the SHARAQ spectrometer [178]. R3 consists of there parts: injection-line, cyclotron-like storage ring, and the ejection-line. The injection-line consists of 10 quadrupole magnets, which are reused from the KEK 12 GeV proton synchrotron, and one bending magnet used in a heavy-ion storage ring, TARN II (Institute of Nuclear Study, University of Tokyo). Two quadrupole magnets are arranged in the E20 room, where the SHARAQ spectrometer locates, in order to transport particles from the SHARAQ efficiently. The phase advance from the septum2 end to the kicker center is about $3\pi/2$. The injected particle is transported to the kicker with a betatron oscillation, and it is subsequently kicked into the equilibrium orbit of the ring. The specifications of the septum magnets for extraction of the particles are the same as those for injection. The ejection area is a open space area for installation of the detector for particle identification. The cyclotron-like storage ring is main part of the Rare-RI Ring. It consists of six sectors and six straight lines, which looks like hexagonal shape. Each of the six sectors consists of four rectangular bending magnets. In order to make an isochronous field, ten one-turn trim coils in the two outer bending magnets of each sector are installed. The circumference of the ring is $\sim$ 60.3 m, which corresponds to a revolution time of 377 ns for rare-RI beams with 168 MeV/nucleon ($\gamma = 1.18$). The exotic RI is transported to the ring via BigRIPS, the high-resolution beam-line (updated to be newly constructed OEDO beam-line in the year 2017), the SHARAQ spectrometer, and the injection beam-line, and introduced into the ring through septum magnets and brought to the kicker magnet to kick RI to the center orbit of R3. Two septum magnets are operated as DC magnets, and each are divided into two magnets (septum1 and septum2) with bending angles of 12.7° and 5.3° were installed at injection and ejection area. The injection orbit at the exit of the septum magnets is off-centered by 90 mm and parallel to an accumulation orbit. The rare-RI is kicked with angle of about 11 mrad and put into the accumulation orbit. After about 2000 turns, the rare-RI is kicked out through the extraction septum magnets. The basic parameters of the Rare-RI Ring were summarized in Tab. 2.1.

Table 2.1 Specifications of the Rare-RI Ring

parameters	For the beam with energy of 170 MeV/μ
Circumference	60.3507 m
Length of straight section	4.02 m
Momentum acceptance	1% (designed) and 0.6% (tested IMS mode)
Max. injection energy	170 MeV/μ
Revolution frequency	2.65 MHz
Transition point γ_{tr}	1.18
Betatron tune	Q_x =1.18 , Q_y = 0.93
Max. Beta function	β_x = 8.4 m , β_y = 11.9 m
Dispersion of straight section	7.0 m

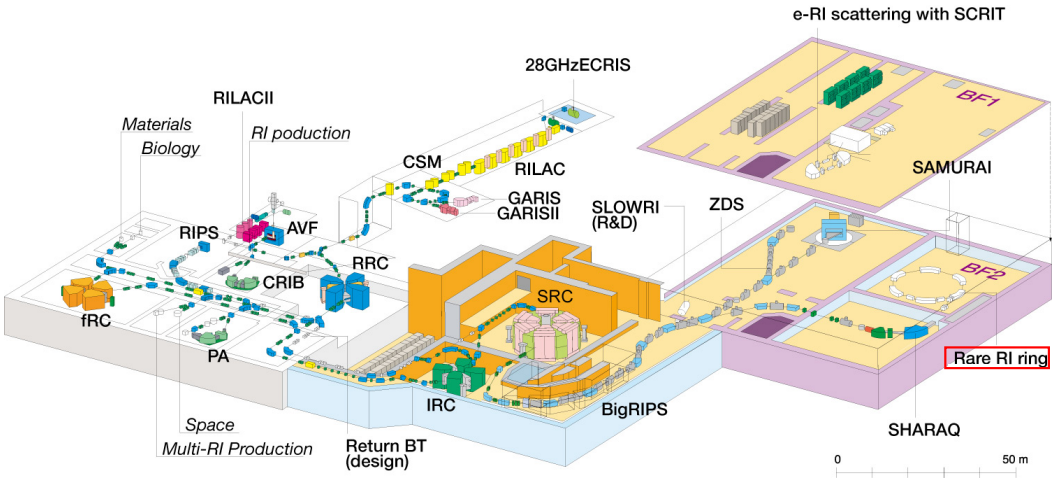

Fig. 2.1 Bird's eye view of the RI Beam Factory (RIBF) at RIKEN Nishina Center.

2.2 Overview of present machine study experiments at the Rare-RI Ring

The basic performance of the Rare-RI Ring (injection line, septum magnets, dipole magnets with trim- coils, and fast-kicker system) is examined , by using α-source in 2014. During the experiment, an α-particle was injected into the ring individually by using self-trigger mechanism and circulated several turns after the injection inside R3. Besides, it is confirmed that the isochronous condition of the ring can be adjusted by the trim-coils installed on the outer magnets of every sector. In June 2015, a first commissioning run using a ^{78}Kr beam was performed and basic performances of the Rare-RI Ring were verified. Fully stripped ^{78}Kr ion, which was randomly produced from a DC beam using cyclotrons, was successfully injected into the ring individually with the fast-kicker system, and then extracted from the ring in less than 1 ms with same kicker system. Time- of-flight (TOF) of the 78Kr particles be-

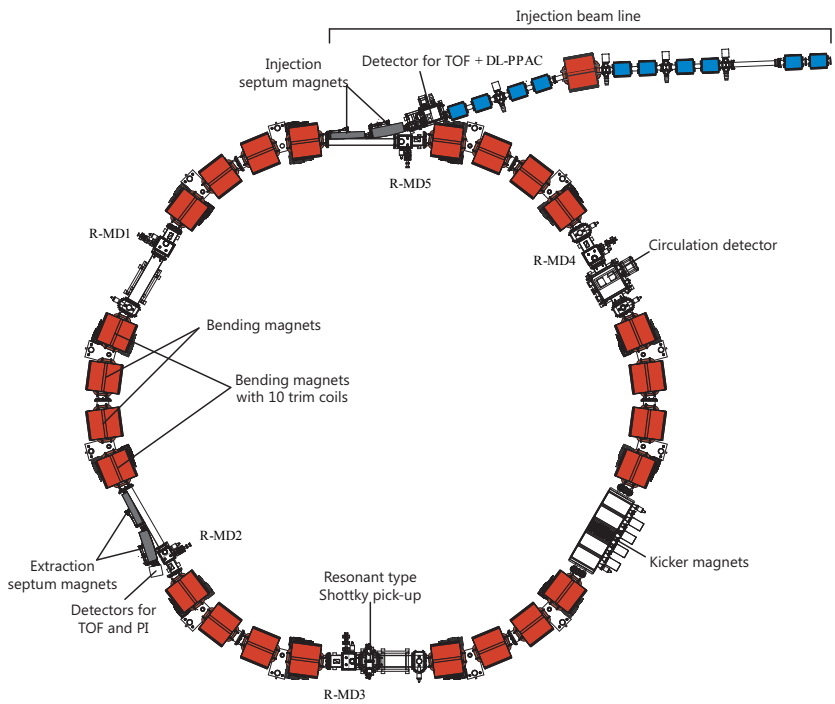

Fig. 2.2 Schematic view of the Rare-RI Ring structure. The magnets with red colors are dipoles and quadrupoles in blue. In each straight sections, plastic scintillation counters as Ring monitor detectors (R-MDs1-4) are installed to check the injection trajectory and a $\delta - raydetector$ as R-MD5 for checking circulation of ions. A Carbon-foil MCP detector and a resonant Schottky pick-up [177] are used to get the revolution frequency information from a circulating RI with and without destruction.

tween the entrance and the exit of the ring was measured to check the isochronism. Through the first-order adjustment with trim-coils, the isochronism on the 10 ppm order was achieved for the momentum spread of ± 0.3 %. In December 2015, the first experiment conducted to study the IMS performance of R3 was conducted, the secondary particles were produced via projectile fragmentation of primary beam ^{48}Ca colliding with a ^{9}Be production target. Two particles of ^{36}Ar and ^{35}Cl on proton-rich side along the N=Z line are identified and extracted successfully to deduce masses by IMS method, resulting of mass uncertainty of less than 300 keV. In November of the year 2016, the third machine study was conducted. The secondary beams were produced by the in-flight fission of a 345 MeV/nucleon ^{238}U primary beam bombarding on a ^{9}Be target. ^{78}Ge with a momentum spread of $\sim \pm 0.3\%$. was injected into R3 at an energy of ~175 MeV/nucleon in isochronous condition as a reference particle together with 7 other non-isochronous nuclei: ^{79}As, $^{77,79}Ge$, $^{76,77}Ga$, ^{76}Zn,

^{75}Cu, ^{76}Ga. The achieved isochronism for ^{78}Ge is ~5 x 10^{-6} with an efficiency of 0.2 % at a wide momentum spread of ±0.2 %. Besides, with the high momentum resolution of the high-resolution (HA) beam-line before the SHARAQ spectrometer, we are successfully to deduce the mass of the ^{74}Ni which is not included in the newest atomic mass evolution (AME2016) via the complementary method of $B\rho$-TOF. In 2017 November, the fourth machine study is done to inject in-flight fission fragments of a 345 MeV/nucleon ^{238}U to confirm the new optics for the OEDO beam-line, and an emittance matching method is performed to achieve an extraction efficiency of 1.9 % for the ^{78}Ge with an improved isochronism of 4 x 10^{-6}.

For this work, the third machine study experiment will be discussed in detail.

2.3 In-flight fission for mass measurements at the Rare-RI Ring

2.3.1 Primary beam production

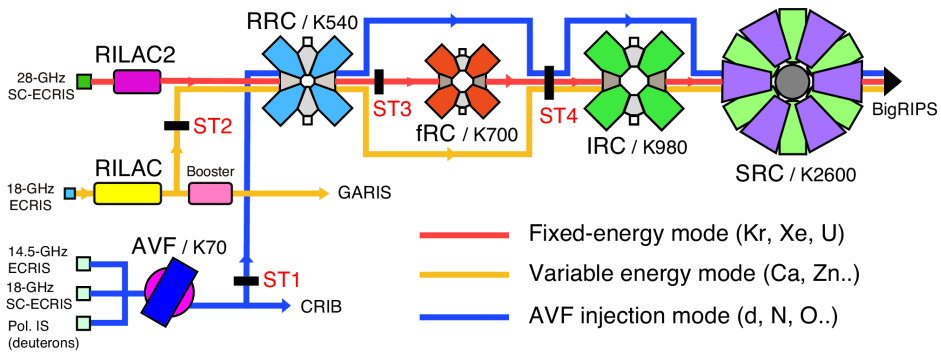

Fig. 2.3 Schematic view of RIBF accelerator chain at RIKEN. Three injectors—the AVF cyclotron, RILAC, and RILAC2, are followed by the four booster cyclotrons—the RIKEN Ring Cyclotron (RRC), fixed-frequency Ring Cyclotron (fRC), Intermediate-stage Ring Cyclotron (IRC), Superconducting Ring Cyclotron (SRC). The charge strippers are illustrated by labels in red text (ST1–ST4). Different modes and processes are labeled in different colors. The red line "Fixed-energy mode"displays the production process of the primary beam of uranium. Figure from [187].

As shown in Fig. 2.3, the $^{238}U^{35+}$ beam extracted from the superconducting electron cyclotron resonance (SC-ECR) ion source, was accelerated in a multistage accelerator complex at RIBF. The following accelerators are employed in sequence to increase ^{238}U beam energy step by step: RIKEN Heavy Ion LINAC 2 (RILAC2), RIKEN Ring Cyclotron (RRC),

Fixed-frequency Ring Cyclotron (fRC), Intermediate-stage Ring Cyclotron (IRC), and Superconducting Ring Cyclotron (SRC). The $^{238}U^{35}$ beam are stripped by two strippers made of carbon-foil placed before and after fRC respectively to increase the charge states for the further acceleration ($^{238}U^{35+}$ to $^{238}U^{71+}$, then to $^{238}U^{86+}$). At the extracted from SRC, the $^{238}U^{86+}$ beam finally reached an energy of 345 MeV/nucleon corresponding to $\sim$ 70 percent the speed of light.

2.3.2 Secondary beam production, separation and particle identification

The experimental setup starting from F0 secondary beam production target is schematically shown in Fig. 2.4. A thin ^{9}Be target was employed as the production target located at F0 of the BigRIPS separator and was bombarded by $^{238}U^{86+}$ primary beam from SRC [173]. The BigRIPS separator combined with High-resolution beam-line of SHARAQ (BigRIPS-HA) as a complex accelerator is served as a two-stage separator: the first stage from F0 to F2 is used for separation of the nuclei of interest through a $B\rho$-ΔE-$B\rho$ selection and the second stage from F3 to S0 for identification of the beam with a $B\rho$-ΔE-TOF method. The second state is also used to deduce velocity of RIs and momentum dispersion event-by-event. Alternatively, during the beam tuning for BigRIPS, ΔE-TOF method is utilized for particle identification (PID) from F2 to F3. The trajectory of an ion in magnetic field B depends on its mass number A, charge Q = Ze (Z is proton number and e is the charge of electron) and its momentum P can be described by the equation:

$$B\rho = \frac{P}{Q} = \frac{mv\gamma}{Q} = \frac{A}{Z}\frac{c\mu}{e}\gamma\beta, \tag{2.1}$$

where $\mu \approx 931.494$ MeV is the atomic mass unit, c the speed of light, ρ the radius of curvature, $\beta = v/c$ and $\gamma = (1-\beta^2)^{-1/2}$. The secondary nuclei are produced by fragmentation at F0, the velocity is nearly constant. The selection in $B\rho$ with the first dipole D1 is then equivalent to a selection in A/Z. A beam dump located at the opening of the dipole to stop the fragments away from the central trajectory, corresponds to the nuclei with relative large different A/Q from the nuclei of interest. The finally selected nuclei by D1 and the beam dump are then transported to the F1 dispersive focus with the achromatic wedge-shaped degrader whose thickness varies with the horizontal plane position. The momentum and energy lost by a nucleus (A, Z) in the degrader material are approximately:

$$\Delta P \propto \frac{Z}{v},\ \Delta E \propto \frac{AZ^2}{E} \propto (\frac{Z}{v})^2 \tag{2.2}$$

The dipole D2 with a constant magnetic field is utilized to center the nuclei of interest and disperse the nuclei possessing a different charge of Z to slits in the F2 focus to stop them. Thus, nuclei with different A/Z and Z are separated by the momentum achromatic separator.

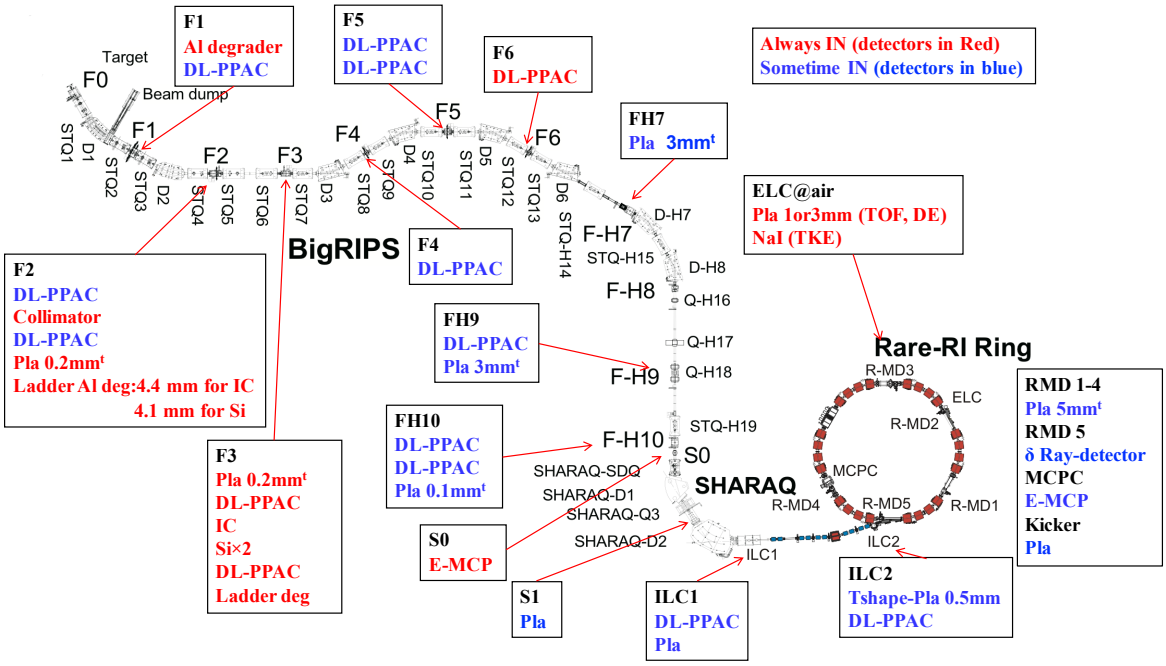

Fig. 2.4 Experimental setup for in-flight fission experiment at RIBF performing the Rare-RI Ring as an Isochronous Mass Spectrometer (IMS). The detectors tagged in red at the focal planes of beam-line or installed R3 are the final detectors using for mass measurements and are permanently installed. While the ones in blue are temporarily installed for beam tuning or other purposes, which is un-installed during the final mass measurement beam time.

The identification of the resulting secondary cocktail beam on a event-by-event basis is performed in the second part of the BigRIPS-HA beam-line (F3-S0). The doubly-achromatic high-resolution beam-line BigRIPS-HA is composed of ten Superconducting Triplet Quadrupoles (STQ7-13, STQ-H14-H15,STQ-H19), 4 quadrupoles (Q-H16-17, Q-H18a and Q-H18b) and six dipoles (D3-D6, D-H7-8), with the F4, F5, F6 as momentum dispersive planes and F3, S0 as doubly-achromatic foci. The nuclei of interest are transmitted up to the doubly-achromatic S0 focal plane (a beam focused in both the horizontal and vertical planes with no dependence of angle and momentum). The particle identification of the secondary cocktail beams is achieved by the $B\rho$-ΔE-TOF method in the BigRIPS-HA spectrometer, which ensures tagging of every particle delivered in the form of a cocktail beam from projectile fragments or in-flight fission.

The stand-alone BigRIPS separator is usually employed as a two-stage functional beam-line, with F0 to F2 as the first stage and F3 to F7 as the second stage. The TOF-$B\rho$-ΔE is performed in the second stage for high-resolution PID. Gamma ray for isomer tagging at F7 anchor is used to ensure the PID.

The identification method of the nuclei in detail will be discussed at the analysis part.

Introduction of multi-sampling ionization chamber (IC)

The ionization chamber (IC), shown in Fig. 2.2 installed at F3, before the trigger plastic scintillator, was dedicated to measure the velocity-dependent energy loss (ΔE) for PID of a heavy RI before being transported the the F3 focal plane. The structure inside a IC, designed by RIKEN, is schematically shown in Fig. 2.5 in a cross-sectional view, from Ref. [179]. It possesses a simple structure and twelve anode planes and thirteen cathode planes are alternately placed in 20-mm steps. Twenty-four parallel plate ionization chambers are tacked together back to back, resulting a 48-cm-thick chamber. In order to avoid the recombination of electrons and positive ions liberated from the gas, along the particle trajectories, the electrode planes are tilted 30 degrees towards the center axis. The tilted electrode gas ionization chamber obtained a high counting rate capability by reducing the drifting distance and, hence, drifting time of electrons and ions produced by charged particles. A gas mixture of Ar–CH_4 (90%, 10%, purity> 99%) was employed as the counter gas. The whole assembly of the electrodes is housed in an aluminum vessel, of which the entrance and exit windows are attached by a 50-μm-thick kapton sheet, respectively. Pairs of anode electrodes are connected together electrically inside the chamber to reduce the number of output connectors, and the summed anode signals of each set of four ionization chamber units are connected out through six separate feedthroughs, which are measured using a peak-sensitive ADC. For the description of the PPAC, plastic scintillator, and NaI, explanations can be found in the experimental test part of the foil-MCP detectors.

2.3.3 Setup of beam-lines in conjunction with the Rare-RI-Ring as IMS

The IMS mass measurement setup by using the Rare-RI Ring is demonstrated in Fig. 2.4 as well. When a produced secondary particle passes through the timing detector (Plastic) at F3 focal plane of the BigRIPS separator, a trigger signal will be generated and transmitted to a fast-kicker system via a high speed coaxial tube. Kicker magnets are then immediately excited by thyratrons. In the meanwhile, the particle that arrives at the entrance of the ring is injected into an equilibrium orbit of the ring using septum and kicker magnets. After the particle revolves in the ring about 700 μs, it will be extracted using another septum and the

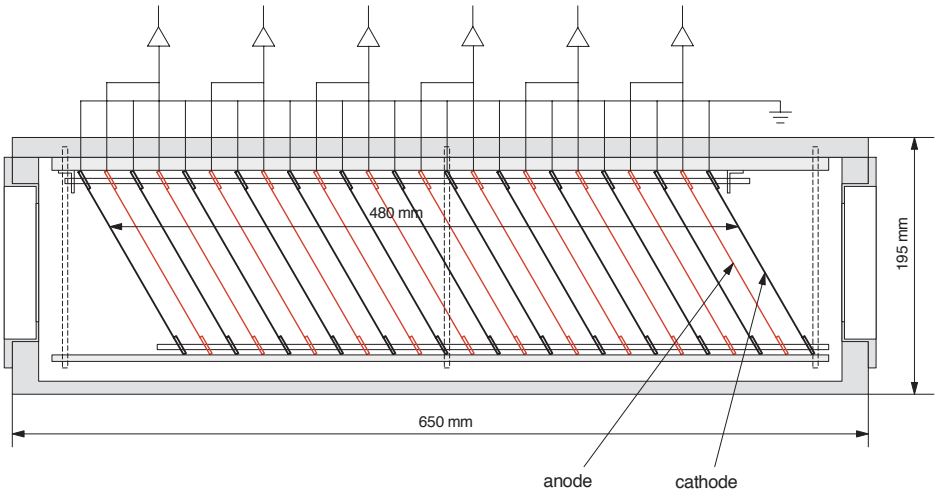

Fig. 2.5 Cross-sectional view of the tilted electrode gas ionization chamber (IC) at RIKEN. Figure from [179].

same kicker magnets. The start of total TOF for IMS is set at doubly-achromatic focus S0 of SHARAQ beam-line by using foil-MCP detector, and stop of total TOF is measured at the extraction line of R3 by using extraction-line course (ELC) plastic. In addition, the extracted ion can be identified by $\Delta E - E$ detectors (Ionization Chamber and NaI) located at the end of extraction line. Thus we can combine the PID of beam-lines and R3 to perform a $B\rho - TOF - \Delta E - E$ method for PID. The β or $B\rho$ measurement is necessary to correct the revolution time of non-isochronous condition particles if extracted from R3. The measurement of $B\rho$ at dispersive focal plane F6 by delay-line PPAC with the TOF measured from F3 to S0 can be employed to deduce the β (velocity) of each RI. In addition to the short measurement time (~700 μs), this method enables us to measure the mass of even one ion which is extracted with the same setting as the reference nuclei.

2.3.4 Setup of BigRIPS and High-resolution beam-line as Bρ-TOF Mass Spectrometer

The equation of motion of ions in beam line correlate the nuclear mass, TOF and magnetic rigidity (Bρ, or momentum per unit charge) of the ions: Bρ=(m/q)(L/TOF), Where is the relativistic Lorentz factor, L is the path length between the timing detectors at F3 and S0, and q is the charge of the ion (equal to Z for most of the beam particles that are fully-stripped ions). Figure 2.4 also includes the setup for Bρ-TOF mass measurements in the same experimental run in parallel and complementary. The time of flight for Bρ-TOF method is measured from F3 with plastic scintillator as TOF start to S0 with foil-MCP timing detector as TOF stop.

The beam position is measured at F6 for Bρ determination, and at F3 with PPAC detectors for emittance measurement. The timing resolution of the foil-MCP detector is worse than 130 ps (tested original resolution) for this experiment, which is now optimized to $\sim$ 40 ps, and the F3 plastic scintillator is about 30 ps. Because of the absolute path length of the beam line and the magnetic field of the dipoles can not be measured with the required precision. The relationship between TOF and m/q has to be calibrated with reference nuclei with precisely known masses. From this experiment, about 14 nuclei with counts more than 10000 are used as reference accumulated in the TOF (F3 to S0) spectrum by the BigRIPS-HA beam-line.

2.3.5 Introduction of the SHARAQ spectrometry

The SHARAQ spectrometer, shown in Fig. 2.2, is designed to achieve a high momentum resolution of $\delta P/P$=1/14700 and a high angular resolution of $\delta\theta$ $\sim$1 mrad for RIs with a magnetic rigidity of 1.8-6.8 Tm [178]. It consists of a Q-Q-D-Q-D configuration: The first quadrupole doublet (SDQ) consists of two superconducting magnets (Q1 and Q2) with effective lengths of 1000 mm and 500 mm. The D1 and D2 dipoles are normal-conducting magnets with bending angles of 32.7 and 60 degrees, respectively. The entrance edge of D2 is shaped to be a 3rd order polynomial type to minimize higher-order aberrations. The third quadrupole magnet (Q3) between the two dipoles is employed to achieve a zero vertical magnification (y|y), for which is essential in obtaining a vertical angular resolution better than 1 mrad for a large emittance beam. Though the high-resolution beam line can be designed to enable a dispersion-matched operation with the SHARAQ spectrometer, as the dispersion-matching for the R3 and the high-resolution beam line is under first consideration, the high resolution capability of SHARAQ spectrometer is not made into full use. In the future, a dispersion-matched OEDO with SHARAQ beam-line should be design to make another dispersion matching with the kicker part of R3 to librate the resolving power of the SHARAQ spectrometer to provide higher momentum resolution for each ion, thus benefits the resolution of momentum and velocity measurement for both IMS and $B\rho$-TOF mass measurements.

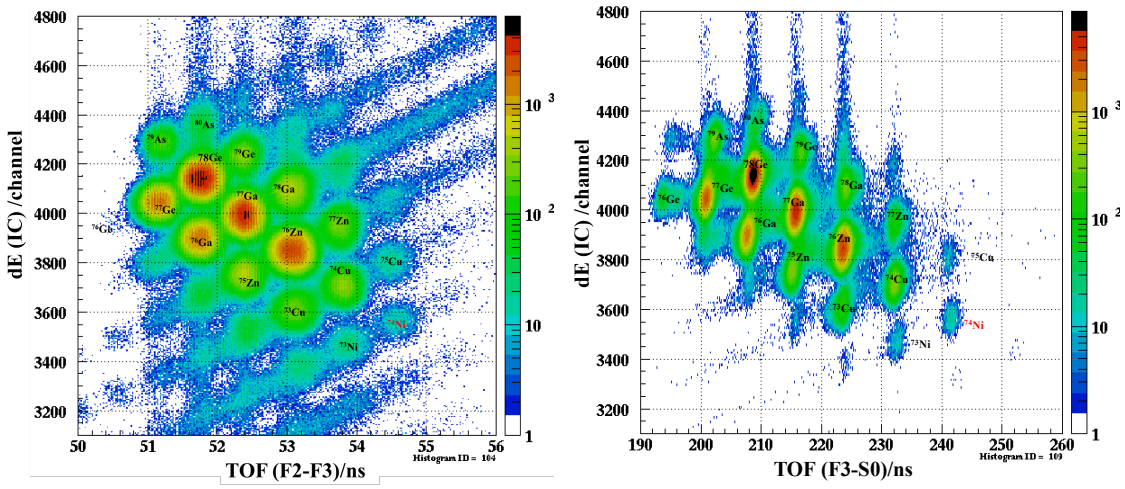

(a) ΔE (IC at F3) -TOF (F2 to F3) 2D histogram (b) ΔE (IC at F3) -TOF (F3 to S0) 2D histogram

Fig. 2.6 ΔE-TOF 2D histograms for PID

2.4 Analysis of mass measurements experiment of ^{238}U fission fragments

2.4.1 Particle identification (PID)

Neutron-rich nuclei were produced via relativistic in-flight fission of ^{238}U fission fragmentation from the SRC with an energy E = 345 AMeV, incident on a rotating beryllium target with a thickness (10 mm for IMS mass measurement setting). The particle identification of the incident nuclei transported at BigRIPS-HA then injected into R3 is performed event by event [173]. The initial conditions of the beam at F3 focus are illustrated in Fig. 2.7 for all ions at the arrival of F3 and the ones extracted form R3. The doubly-focus plane at F3 have a small imaging for X and Y with a relative large angular distribution for both horizontal and vertical direction along the beam. The basic 2D histogram of ΔE-TOF (ΔE by F3 IC and F2, F3 plastic to measure TOF) for PID, as shown in Fig. 2.6a, can be used for online beam tuning and offline analysis as well.

The PID at secondary stage from F3 to S0 provided the atomic number Z and mass-to-charge ratio A/Q of a fragment by measuring the energy loss, magnetic rigidity and time-of-flight (ΔE-Bρ-TOF) with the corresponding beam-line detectors. A typical ΔE-TOF 2D histogram for PID from F3 focus to S0 focus is shown in Fig. 2.6b.

The time of flight between two foci is measured by two timing detectors (F2-F3 by two plastic, and F3-S0 by plastic and foil-MCP detector): $TOF = L/(\beta c)$ can be used for velocity (β) measurements. The TOF is from F3 to S0 measured by plastic and foil-MCP detector.

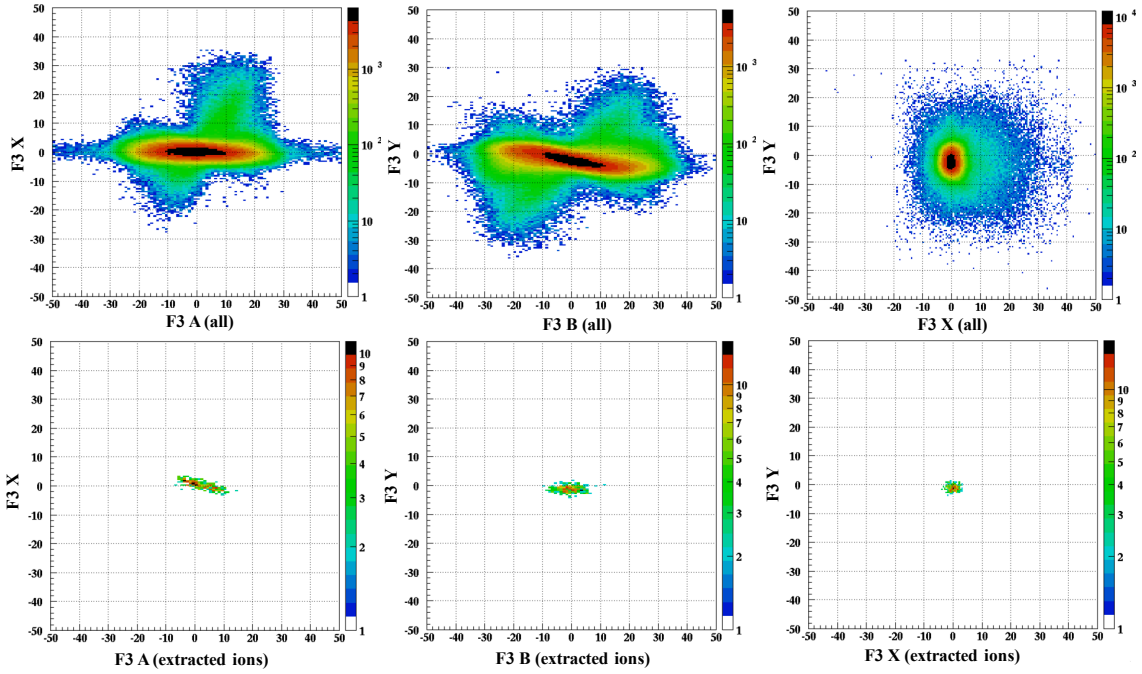

(a) 2D histograms of the initial condition of the RIs

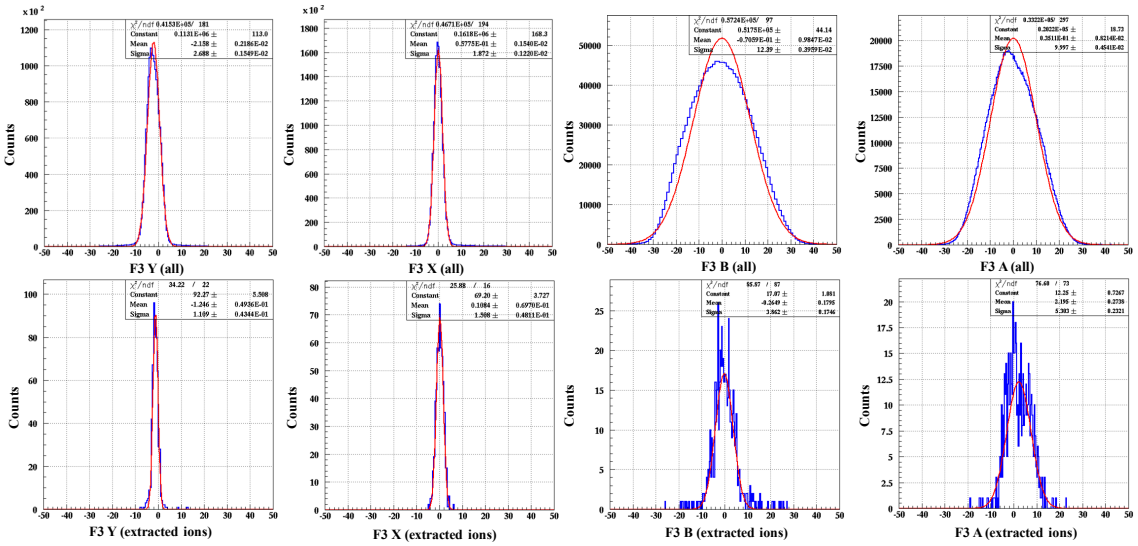

(b) 1D histograms of the initial condition of the RIs

Fig. 2.7 The initial condition of the RIs at F3 for all ions arriving at F3 (upper panel figures in (a) and (b)) and the extracted ions from R3 (lower panel figures in (a) and (b)).

From $B\rho = \frac{P}{Q} = \frac{mv\gamma}{Q} = \frac{A}{Q}\frac{cm_\mu}{e}\gamma\beta$, we can get :

$$\frac{A}{Q} = \frac{B\rho}{\beta\gamma}\frac{e}{m_\mu c}, \tag{2.3}$$

The Atomic number Z of a heavy ion was deduced based on the energy loss of the charged particle in the F3 IC. The energy loss of a heavy ion in an unit thickness of material can be described by the Bethe-Block formula [123, 124] as described as:

$$-\frac{dE}{dX} = \frac{4\pi Z^2 e^4 N Z_m}{m_e c^2 \beta^2}[ln\frac{m_e c^2 \beta^2}{I} - ln(1-\beta^2) - \beta^2], \tag{2.4}$$

and then the formula calculating the atomic number Z can be written as:

$$Z = a_1\beta\sqrt{\frac{\Delta E}{ln(\frac{2m_e c^2\beta^2}{I}) - ln(1-\beta^2) - \beta^2}} + a_2, \tag{2.5}$$

where a_1 and a_2 are parameters to be calibrated from the experiment to reconstruct the Z value each ion. I is the mean excitation potential of the counter gas; Z_m , atomic number of the counter gas; Z, atomic number of heavy ion; β, velocity (v/c) of heavy ion; m_e, electron mass. The variable ΔE in Eq. 2.5 is from the energy losses in the F3 IC while the velocity β of the heavy ion in the IC could be derived from the TOF between the F3 and S0 focal planes.

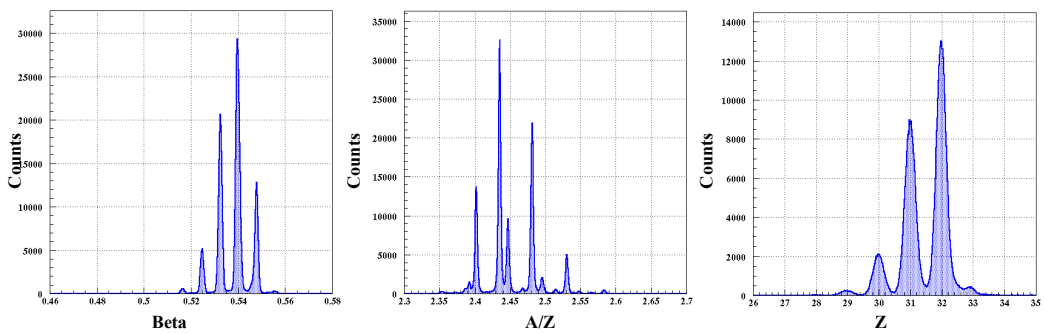

Fig. 2.8 Calculated β, A/Z, Z for all ions in 1D histograms.

The $B\rho$ value of a in-fission fragment, written as:

$$B\rho = (1+\delta)B\rho_0, \tag{2.6}$$

can be derived from the $B\rho_0$, which is the magnetic rigidity along the central trajectory plus the momentum dispersion $B\rho\delta$ of the fragment. The relative momentum dispersion

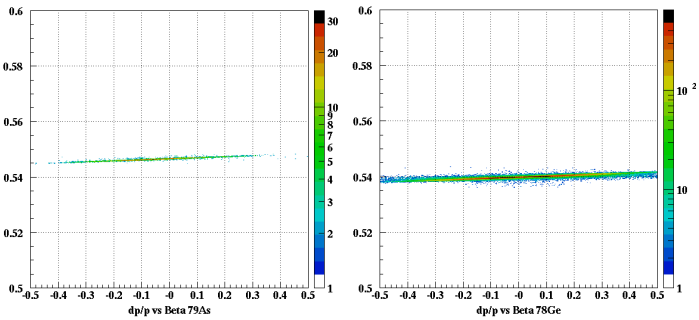

Fig. 2.9 2D spectra of calculated β as a function of the relative momentum dispersion for the ions of ^{79}As and ^{78}Ge.

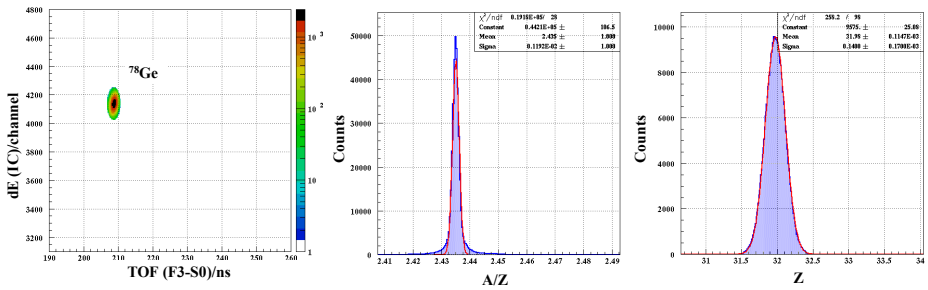

Fig. 2.10 ΔE-TOF 2D histogram (left) of ^{78}Ge using a 3σ gates of TOF and ΔE. Calculated A/Z (middle) and Z (right) for ^{78}Ge ions are displayed in form of 1D histogram.

$\delta = (B\rho - B\rho_0)/B\rho_0$, is proportional to the measured horizontal position of the RI at a momentum dispersive focal plane such as F6.

The position measurement of a heavy RIs can be carried out by the PPACs or Position-sensitive foil detectors placed at the F3, F4, F5, and F6, S0 focal planes to determine the momentum dispersion of the particle. A general expression considering the relationship between the horizontal positions at two successive focal planes, in which one is momentum achromatic and the other is momentum dispersive, can be written as:

$$x_{F6} = (x|x)x_{F3} + (x|a)a_{F3} + (x|\delta)\delta \tag{2.7}$$

where the transmission optical matrices parameters $(x|x)$, $(x|a)$, and $(x|\delta)$ can be obtained from the online reconstruction. The variables x and a represent the horizontal position and angle of a RI at the focal plane denoted by the subscript. Two position-sensitive detector can be employed to extrapolate the horizontal position and scattering angle of a fragment at the real focal plane based on the measurements at the measured positions. Here, the effects from the vertical (y) direction is neglected for the sake of simplicity. By substituting the derived

δ from Eq. 2.7 into Eq. 2.6, the $B\rho$ value can be expressed as:

$$B\rho = \frac{x_{F6} - (x|x)x_{F3} - (x|a)a_{F3}}{(x|\delta)} B\rho_0 \tag{2.8}$$

With substitution of Eq. 2.9 in Eq. 2.3, we can obtain:

$$\frac{A}{Q} = \frac{x_{F6} - (x|x)x_{F3} - (x|a)a_{F3}}{(x|\delta)} B\rho_0 \frac{e}{m_\mu c \beta_{36}\gamma_{36}}, \tag{2.9}$$

Three 1D histograms as shown in Fig. 2.8 demonstrate the calculated β, A/Z, Z. A 2D histogram of β as a function of the calculated $B\rho$ is shown in Fig. 2.9. The gated PID of ^{78}Ge using a 3σ gates of TOF and ΔE is shown in Fig. 2.10 and calculated A/Z and Z for ^{78}Ge ions are displayed in form of 1D histogram in the same figure event by event. The resolving power of (A/Z)/Δ(A/Z) is about 2045 for ^{78}Ge and Z resolution for ^{78}Ge is about 0.33 (FWHM).

As for mass measurements, the energy loss inside the PPAC located at F6 focal plane in the order of $10^{-3} - 10^{-4}$, which is still relatively large for β measurement to the order of 10^{-4}, the TOF between the F3 and S0 can be divided into two parts:

$$TOF_{3S0} = \frac{L_{36}}{\beta_{36}c} + \frac{L_{6S0}}{\beta_{6s0}c}, \tag{2.10}$$

where L_{36} is the flight path between the F3 and F6 focal planes, $L6s0$ flight path between the F3,S0 focal planes, β_{36} the velocity (v/c) between the F3 and F6 focal planes; β_{6s0} : velocity (v/c) between the F6 and S0 focal planes. Using a parameter $k = \beta_{6S0}/\beta_{36}$ and $1/k = k' = \beta_{36}/\beta_{6S0}$, the total TOF:

$$TOF_{3S0} = \frac{1}{\beta_{6S0}}\frac{L_{36}}{k} + \frac{L_{6S0}}{\beta_{6S0}} = \frac{1}{\beta_{6S0}}(L_{36}(1+k') + L_{6S0}) = \frac{1}{\beta_{6S0}}(L_{3S0} + k'L_{36}), \tag{2.11}$$

can be used to deduce the second stage β of RIs with unknown masses directly by reference particles with well-known masses. If the RI has no charge change during the transmission from F3 focal plane to S0 focal plane, the equation below holds:

$$\frac{A}{Q} = \beta_{36}\frac{e}{uc}\frac{1}{\beta_{36}\gamma_{36}} = \beta_{6S0}\frac{e}{uc}\frac{1}{\beta_{6S0}\gamma_{6S0}}, \tag{2.12}$$

where, $B\rho_{36}$ is the $B\rho$ value of the RI between the F3 and F6 focal planes, $B\rho_{3s0}$ the $B\rho$ of the RI between the F6 and S0 focal planes, $\gamma_{36} = \frac{1}{\sqrt{1-\beta_{36}^2}}$ and $\gamma_{6S0} = \frac{1}{\sqrt{1-\beta_{6S0}^2}}$. From Eq. 2.5

and Eq. 2.12, we can obtain that:

$$\beta_{6S0} = \frac{2L_{6S0}(TOF_{3S0})c + \sqrt{4(TOF_{3S0})^2c^2 + (P_{21}^2 - 1)L_{3S0}^2 L_{6S0}^2 - P_{21}^2 L_{36}^2}}{2((TOF_{3S0})^2c^2 + (P_{21}^2 - 1)L_{3S0}^2)} \tag{2.13}$$

and

$$\beta_{36} = \frac{2L_{36}(TOF_{3S0})c + \sqrt{4(TOF_{3S0})^2c^2 + (P_{21}^2 - 1)L_{3S0}^2 L_{6S0}^2 - P_{21}^2 L_{36}^2}}{2((TOF_{3S0})^2c^2 + (P_{21}^2 - 1)L_{3S0}^2)} \tag{2.14}$$

Where $P_{21} = B\rho_{6S0}/B\rho_{36}$ and $P_{12} = B\rho_{36}/B\rho_{6S0}$. If we install the position-sensitive timing

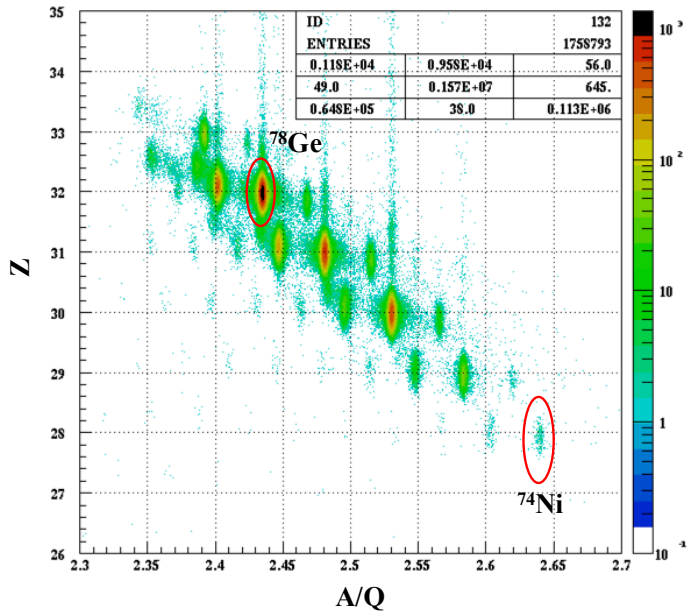

Fig. 2.11 2D correlation histogram of A/Z and Z for particle identification of in-flight fission fragments. Reference nucleus of ^{78}Ge for IMS mass measurements and the unknown mass ^{74}Ni are marked in red circles.

foil-MCP detector at the dispersive focal plan F6 (or F5) , we can acquire the TOF of F3-F6 and F6-S0 separately. Besides, with a 1-2 μm-thickness Mylar foil or carbon foil, the energy loss is in the order of $10^{-4} - 10^{-6}$, thus resulting a better accuracy of the beta and $B\rho$ measurements. Though the middle focal plan TOF, the charge change events after the detector will easier to be identified. The final reconstructed A/Q-Z 2D histogram for PID is shown in Fig. 2.11 with the reference nucleus of ^{78}Ge for IMS mass measurements and ^{74}Ni marked in red circles. As shown in Fig. 2.11, due to the excellent resolving power of

the BigRIPS-HA beam-line, the resolution of A/Z is good enough to resolve all the highly charged RIs with a relative good performance IC.

The next chapter will be mainly talking about the analysis results of TOF mass measurements by Obit-IMS method and $B\rho - TOF$ approach for these same experimental runs.

Chapter 3

Results of in-flight fission mass measurement experiment

3.1 Analysis results of Obit-IMS mass measurements

The layout of the experimental setup for mass measurements by employing the Rare-RI Ring as an isochronous mass spectrometer (IMS) is shown in Fig. 2.4 and has been explained in Chapter 2.

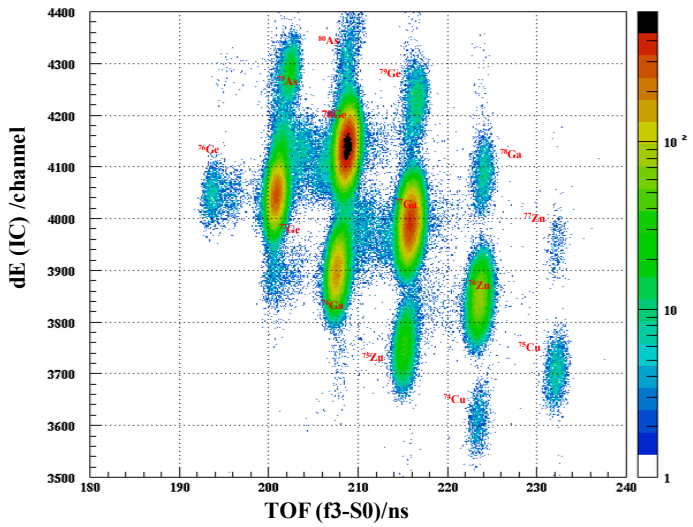

Fig. 3.1 2D correlation histogram of TOF-ΔE (TOF of F3 to S0 and ΔE at F3 IC) for PID of IMS mass measurements experiment runs.

The particle identification figure by using TOF-ΔE (TOF of F3 to S0 and ΔE at F3 IC) of the IMS mass measurements experimental runs is illustrated in Fig. 3.1. The nuclei that

have been extracted from the experiment are shown in Fig. 3.2 which are marked with blue points (left) or red points (right). The main extracted ions are the N = 46 isotonic chain with a total counts of about 600 for the machine study experiment, and the most intense ion is the ^{78}Ge as shown in Fig. 3.2, which is used for the reference nucleus. In this experiment, all the nuclei extracted from R3 are well-known masses to be used for principle of mass determination confirmation of the IMS mass measurements with additional velocity (β) or momentum (Bρ) measurements.

During the experiment, the beam are precisely transported depending on a fast optical matrix responding method. The precise ion-optical settings for beam tuning of both the transport beam-lines and the SHARAQ spectrometer is necessary to realize a high-resolution measurement. Typically, the interesting fragments from projectile or in-flight fission have a large longitudinal and transverse emittance with low intensity will enlarge the difficulty to select them to inject into the Rare-RI-Ring. To solve the problem, a fast tuning of the RI beam based on: 1. Measured beam trajectories at different focal planes for beam-optical matrix deduction and compared to simulation by COSY INFINITY; 2. Cancellation of momentum-spread effects by combining data at dispersive focal planes; 3. Response functions of each quadrupole magnet obtained via ion-optical calculations by COSY INFINITY, is employed. During the beam time, calculated transfer matrix elements by COSY INFINITY were compared to experimental ones, and then to fix the magnet excitations accordingly. The beam-line tracking detectors shown in Fig. 2.4 at each focal plane are utilized both to diagnosing of the ion transport optics and to tag particles event-by-event in the experiment. In addition, during the test experiment, a ΔE-TOF method for particle selection has been tested and were used for choosing the nuclei for individual injection, in which only the RI arriving at a certain time can be used as a trigger signal by employing the relationship between the timing of the RF signal and the arrival time of the RI beam.

After beam tuning and the ions were transported to inject into R3 by the individual injection method with the fast kicker system. The Ring Monitor detectors (RMDs) employing plastic scintillation counter are used to check the circulation of the injected ions at each sector. The PID of the particles were confirmed by using the ΔE-TOF information eventually. After removing the plastic scintillation counter from the central orbit of the ring, the periodic signals of the circulated particle in R3 were checked using a carbon-foil MCP detector. The total TOF of the particles between the entrance (S0) and the exit (ELC) of the ring to check the isochronism of the ring. By adjusting the first and then second-order isochronous magnetic field using trim-coils, which were installed into the outer dipole magnets of one

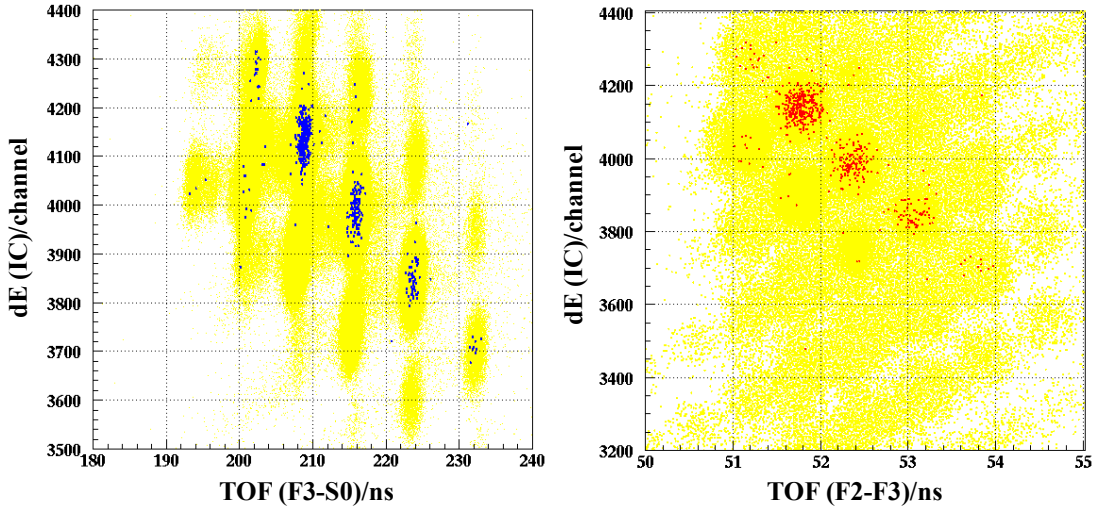

Fig. 3.2 (Left) Identified particles in 2D correlation histogram of TOF-ΔE (TOF of F3 to S0 and ΔE at F3 IC) for experimental run of IMS mass measurements, in which the blue corresponds to the extracted. (Right) 2D correlation histogram of TOF-ΔE (TOF of F2 to F3 and ΔE at F3 IC) and red points represent the extracted ions from R3. The yellow backgrounds are all the ions that arrival at F3 focal plane.

sector of the ring, the isochronism of around 5 parts per million (ppm)[1] was achieved for the momentum spread of $\pm 0.3\%$. In addition, a resonance-type Schottky pick-up were used to acquire the revolution frequency information of one particle with a resolution of approximately 1.3×10^{-6} in a storage mode. Alternatively, a δ-ray detector was used to check the circulation of ions in R3 as RMD5.

3.1.1 Confirmation of circulation of RIs in the Rare-RI Ring

The circulation of ions in R3 is confirmed by the foil-MCP detector located at micro-channel-plate chamber (MCPC), shown in Fig. 2.2, and revolution time of the ions is fitting with the timing spectrum by a first order polynomial function. An example of the injected ion of ^{78}Ge is shown in Fig. 3.3. The second order polynomial function should be employed when there is energy loss from destructive effect like foil or bad vacuum conditions. The revolution time at certain turn number n can be calculated form: $T(n) = \frac{dTime_{total}}{dn} = c_1 + 2c_2 \cdot n$, where c_1 and c_2 are fitting parameters from the quadratic fit.

[1] One ppm is equivalent to 1 milligram of something per liter of water (mg/l) or 1 milligram of something per kilogram soil (mg/kg).

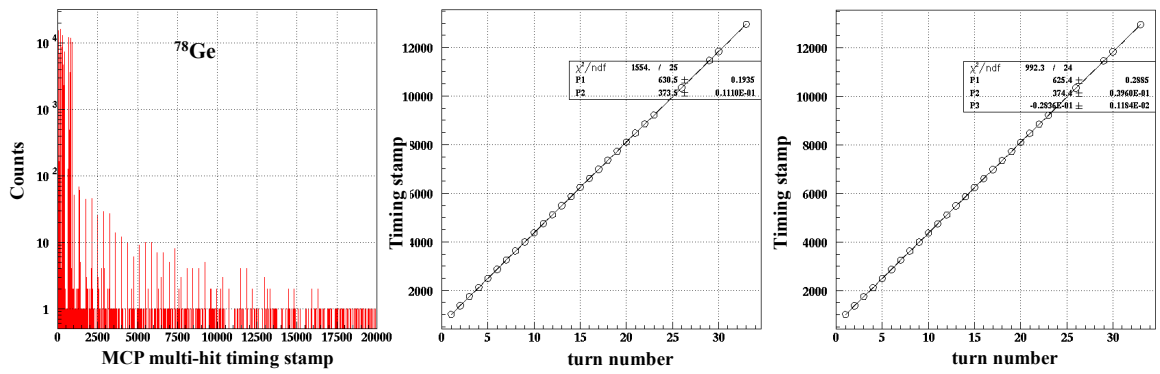

Fig. 3.3 (Left) Revolution timing spectrum of injected ^{78}Ge at R3. (Middle) Spectrum of the revolution time of 78^{Ge} with first order fitting. (Right) Spectrum of the revolution time of ^{Ge} with second order fitting.

3.1.2 Isochronicity curve

Before performing any isochronous mass measurements experiment in the IMS mode, the isochronisity of the ring has to be varified. The isochronisity is turned with a trim coil. After fine turning, small change and uncertainty in the revolution time is observed from spetrum of the revolution time as a function of the momentum dispersion of the isochronous nucleus. When the revolution time of the ions of the reference species is independent on their momentum, a flat trend appears for the curve and it is defined as " isochronicity curve". An isochronous curve after isochronous tuning by the trim coils are shown in the left side of Fig. 3.4. The TOF spectrum of ^{78}Ge at right of Fig. 3.4 indicted the isochronism of Rare-RI Ring of the value of 4.83 x 10^{-6}. In such an ion-optical mode of the ring, that a faster ion of certain species (^{78}Ge) circulates in a longer orbit and a slower ion moves on a shorter orbit. So all reference ions for mass calibration with the same m_0/q_0 will travel on the same trajectory and have the same revolution time. Consequently, measurements of the revolution times of RIs of non-isochronous species give the possibility to determine the m_1/q_1 ratio of the non-isochronous circulating RIs.

3.1.3 Extraction of RIs from the Rare-RI Ring

After isochronisity tuning, checking the revolution of the RIs injected and identification of them, the RIs were extracted by the same kicker magnet after a circulation time of $\sim$ 700 μs. The 2D extraction spectrum of the total TOF from S0 focus to ELC as a funtion of the relative momentum dispersion is displayed in Fig. 3.5. In the figure, different extracted ions are identified firstly and tagged with different colors in the histogram. The isochronicity curve is validated only for one ion species and in this IMS mass measurement experiment the

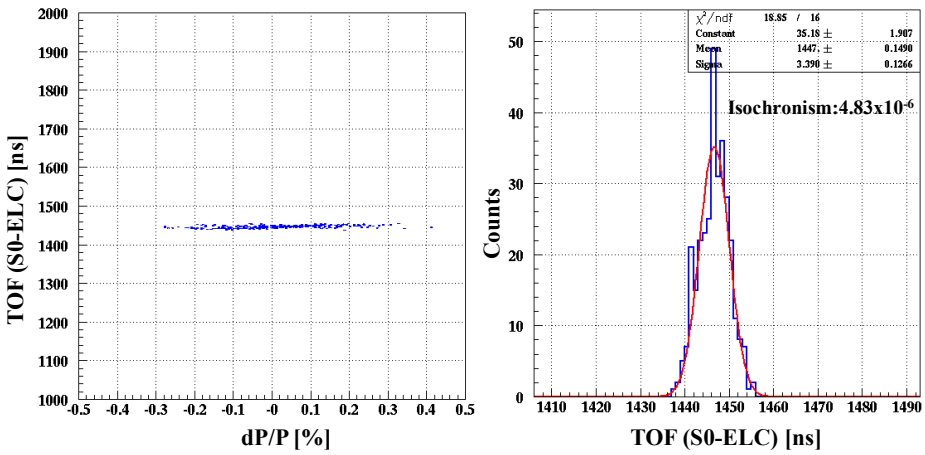

Fig. 3.4 The isochronous curve after isochronous tuning by the trim coils. The TOF spectrum of isochronous nucleus ^{78}Ge indictes the isochronism of Rare-RI Ring of the value of 4.83 x 10^{-6}.

isochronous nucleus is ^{78}Ge. As shown in Fig. 3.5, the momentum dispersion dependence of the in-ring TOF is flat only for the ion species of ^{78}Ge and for other nuclei, a slope-like dependence is observable. From the histogram, we can imagining that the TOF distribution of non-isochronous nuclei can be corrected by this strong momentum dependence.

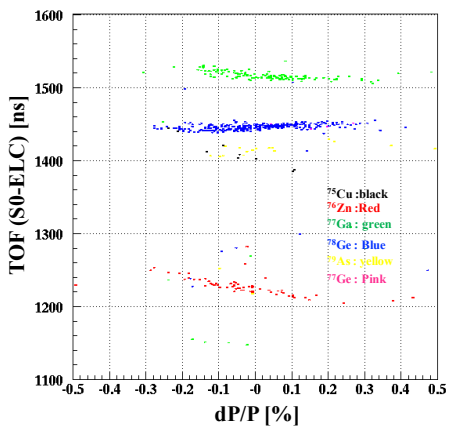

Fig. 3.5 2D extraction spectrum of the total TOF from S0 focus to ELC as a funtion of the relative momentum dispersion. Different extracted ions are identified firstly and marked with different colors.

3.1.4 Double kicker TOF

As the total TOF start from the focal plane S0 detected with foil-MCP detector and stop at the plastic scintillator at the extraction line. The TOF from the focal plane S0 to the kicker

center during injection before first turn of circulation and TOF from kicker center to the ELC plastic in extraction after last turn of revolution do not take place in isochronous condition in the Rare-RI Ring. To exclude the effect of this non-isochronous period of TOF, the double kicker experimental run is carried, in which the ions are injected with a phase of $3\pi/2$ and extracted with another phase $3\pi/2$ symmetrically without circulation. The double kicker spectra are shown in Fig. 3.6. The 2D histogram (left)corresponds to the double kicker TOF as a function of the relative momentum dispersion and the 1D TOF spectrum (right) in double kicker mode shows the different double-kicked ions in different colors. As the total beam time for the experiment is quite limited, the counts of the extracted ions is relatively low and for the reference nucleus of ^{78}Ge, there peaks appears and strongly affects the accuracy and precision of the double kicker TOF measurements.

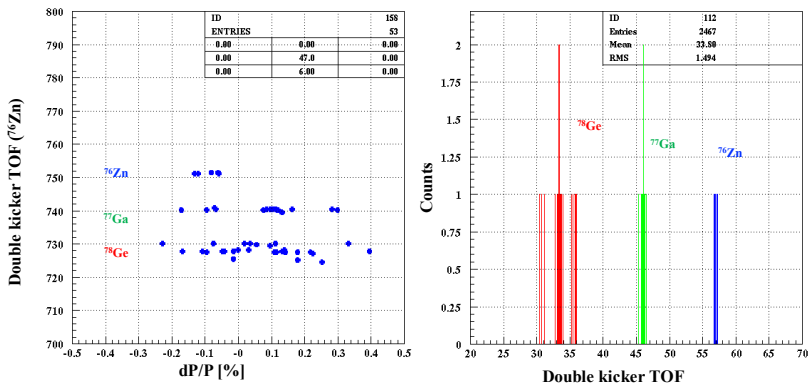

Fig. 3.6 2D histogram of double kicker TOF as a function of the relative momentum dispersion and the 1D TOF spectrum (right) in double kicker mode shows the different double-kicked ions in different colors.

3.1.5 d E-E for PID

At the end of the extraction line, an IC to measure the ΔE of extracted RIs and a NaI detector to derive the ΔE of extracted RIs are installed for alternative PID. The extracted ions of ^{78}Ge, ^{77}Ga and ^{76}Zn are identified in the 2D histogram of correlation of ΔE and E which is demonstrated in Fig. 3.7 with three type of colored points. Therefore, the powerful PID method utilizing the correlations of $B\rho$-ΔE-TOF-E are established at the Rare-RI-Ring to identify all RIs extracted and separate the charge state, charge change ions at the same time.

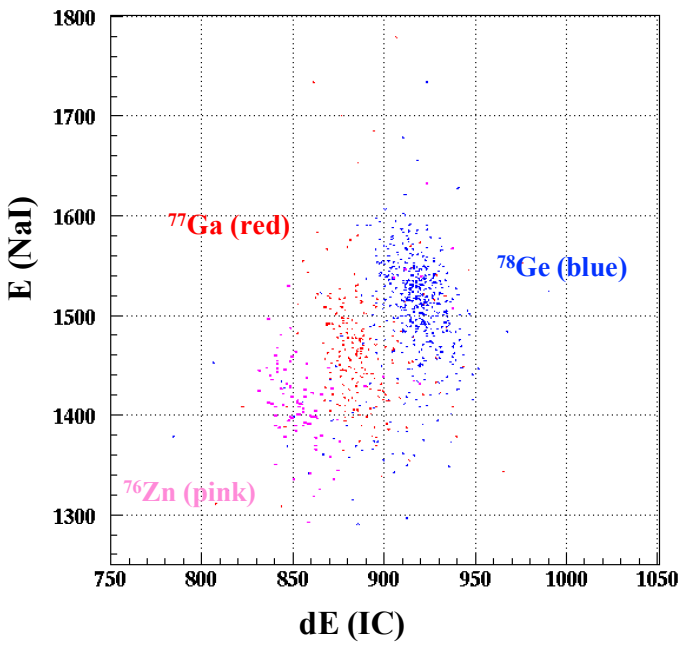

Fig. 3.7 2D histogram of correlation of ΔE and E for the extracted ions of ^{78}Ge, ^{77}Ga and ^{76}Zn marked with three type of colored points for PID.

3.1.6 Nuclear mass and m/q of bare ion

The reference nuclides for mass calibration usually need to have a well-determined mass from the newest Atomic Mass Evaluation and a lack of long-lived isomeric states (100 ns). The published atomic mass excesses in AME2016 of the reference nuclei have to be converted into nuclear masses. For each nucleus with atomic mass number A and atomic number Z, this process consisted of converting atomic mass excess $ME_{atom}(Z, A)$ to atomic mass $M_{atom}(Z, A)$ and then converting the atomic mass to nuclear mass $M_{nuc.}(Z, A)$ by subtracting the mass of the electrons masses m_e and adding back the energy given by their binding energies $B_e(Z)$. This process resulted in the following conversion:

$$ME_{atom}(Z, A) = M_{atom}(Z, A) - (Z+N)\cdot\mu \Longrightarrow M_{atom}(Z, A) = ME_{atom}(Z, A) + (Z+N)\cdot\mu, \tag{3.1}$$

$$M_{nuc.}(Z, A) = M_{atom}(Z, A) - Z \cdot m_e + B_e(Z), \tag{3.2}$$

where $m_e = 510.998928$ keV, with $\mu = 931494.061$ keV being the atomic mass unit. The total electron binding energy of each element is obtained by summing over the individual binding energies of each electron. The individual electron binding energies $B_e(Z)$ are deduced from:

$$B_e(Z) = 14.4381 \cdot Z^{2.39} + 1.55468 \cdot 10^{-6} \cdot Z^{5.35}\, eV. \tag{3.3}$$

Then, the m/q value of a bare ion can be calculated:

$$m/q = \left(A + [ME_{atom}(Z, A) - Z \cdot 510.998928 + B_e(Z)/1000]/931494.061\right)/Z \quad (3.4)$$

3.1.7 Velocity and momentum correction IMS mass measurements

After the extraction of the RIs with well-known mass, they are employed to confirm the feasibility of and principle of mass determination using velocity (v) or momentum ($B\rho$) correction employing R3 as an isochronous mass spectrometer (IMS). A β or $B\rho$-resolution of 10^{-4} or better is required to achieve a mass resolution of about 100 keV (A = 100) for nucleus with m/q close to m/q_0 with ideal isochronicity (10^{-6}) as reference. The extracted RIs circulated in the ring about 1800-1900 turns in a total period of about 701 μs are used for the IMS mass measurements study with Velocity and momentum correction. As discussed in

Table 3.1 Parameters of extracted ions.

RI	TOF S0-ELC (exp)	Double-kicker TOF	Double-kicker turns	In ring TOF	in ring virtual turns	IMS turns	Turn numbers	Revolution time
^{78}Ge	701446.9	728.09	1.951574536	700718.81	1878.20872	1880.160294	1878	373.1197071
^{77}Ga	701515.8	740.28	1.957673032	700775.52	1853.203297	1855.16097	1853	378.1843065
^{76}Zn	701228.06	751.26	1.958619013	700476.8	1826.221519	1828.180138	1826	383.6127054
^{79}As	701395.43	718.0234089	1.949240656	700693.7466	1902.195278	1904.144519	1902	368.3983946
^{75}Cu	701411.77	764.486326	1.963176801	700630.9437	1799.198191	1801.161368	1799	389.4557775

chapter 2, additional velocity (v) and magnetic-rigidity ($B\rho$) measurements for each injected ion on a event-by-event basis have been realized before injection operating Rare RI-Ring as an IMS. To insure the accuracy of the velocity (v) and magnetic-rigidity ($B\rho$) measurements, the in-ring TOF information for several injected non-isochronous ions together with the reference ion species in isochronous condition can be utilized to reconstructed the in-ring velocity (v) and magnetic-rigidity ($B\rho$) corresponding to the reference obit. Typically, the reconstructed in-ring velocity (v) and magnetic-rigidity ($B\rho$) can reach a accuracy of 10^{-5} or better due to the excellent isochronism of 4-5 x 10^{-6} and long circulation period of all the ions of about 700 μ with a TOF measurement uncertainty of 100 ps or less under the condition of individual injection with high resolution PID event-by-event.

Velocity correction IMS mass measurements

The m/q values of the extracted and identified nucleus of ^{78}Ge, ^{77}Ga, ^{76}Zn, ^{79}As, ^{75}Cu with well-known masses and no long-lived isomeric states are calculated based on the AME2016 Mass Excess data. The ^{78}Ge m/q as utilized as the reference m_0/q_0 and other calculated m/q values are used for accuracy checking and principle verification. The information of the measured velocity and in-ring TOF of all the extracted ions of ^{78}Ge, ^{77}Ga, ^{76}Zn, ^{79}As,

^{75}Cu, are employed to confirm the velocity correction IMS mass measurements function expressed as: $\frac{m_1}{q_1} = \frac{m_0}{q_0}\frac{T_1}{T_0}\sqrt{(1-\beta_1^2)/(1-(\frac{T_1}{T_0})^2{\beta_1}^2)}$, which has been discussed in Chapter 2 in detail. The K=$\sqrt{(1-\beta_1^2)/(1-(\frac{T_1}{T_0})^2{\beta_1}^2)}$ corresponds to the velocity correction factor.

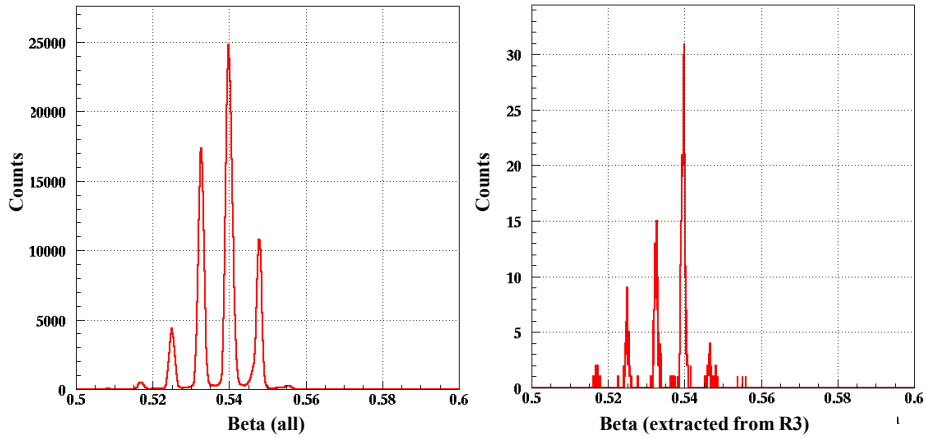

Fig. 3.8 The calculated velocity in form of histogram spectra from measurement of the beam-line TOF (F3 to S0) for all the ions arriving at S0 focus (left) and the extracted from R3 (right)

The calculated velocity (β) in form of histogram spectra by the beam-line TOF (F3 to S0) are shown in Fig. 3.8 for all the ions arriving at S0 focus (left) and the extracted from R3 (right), respectively. The details for calibration and calculation have been discussed in Chapter 2. The 2D histograms of β as a function of relative momentum dispersion dp/p are

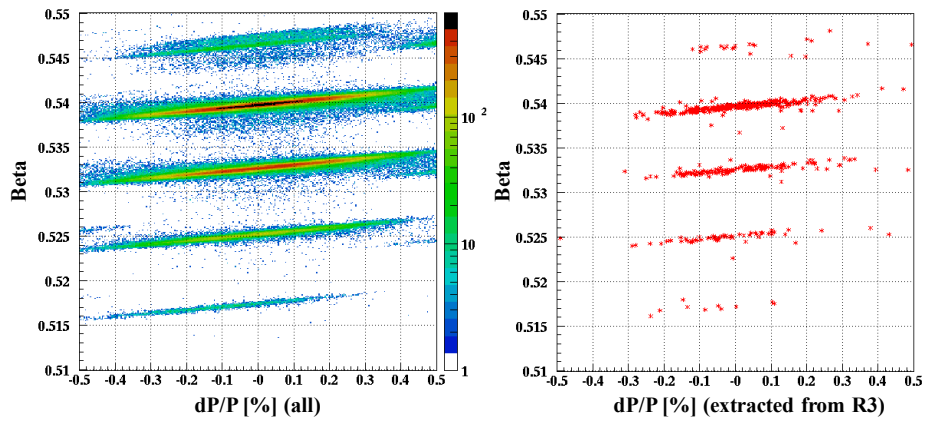

Fig. 3.9 The 2D histograms of β as a function of relative momentum dispersion dp/p for all ions (left) and extracted ions (right).

demonstrated in Fig. 3.9 for all ions (left) and extracted ions (right).

The measured total TOF from S0 focus to ELC extraction line can be divided into three parts: TOF1 of injection part between the S0 and the kicker, TOF2 of extraction part between the kicker and the exit area of R3, and TOF3 of the in-ring flight part. The revolution time is calculated from the in-ring flight part and the (TOF1 + TOF2) part should be subtracted from the total TOF, which can be measured by the double kicker experiment. At left side of Fig. 3.10, the 2D spectra of in-ring revolution time for the extracted ions of ^{77}Ga employing PID gate as a function of relative momentum dispersion is illustrated. After correcting the in-ring revolution time with the velocity correction factor. The 2D spectra of velocity-corrected in-ring revolution time of fully stripped ^{77}Ga as a function of relative momentum dispersion are displayed at right of Fig. 3.10. It is observable that the significant momentum dependence of the revolution time is corrected to have nearly no momentum dependence by employing the velocity correction method.

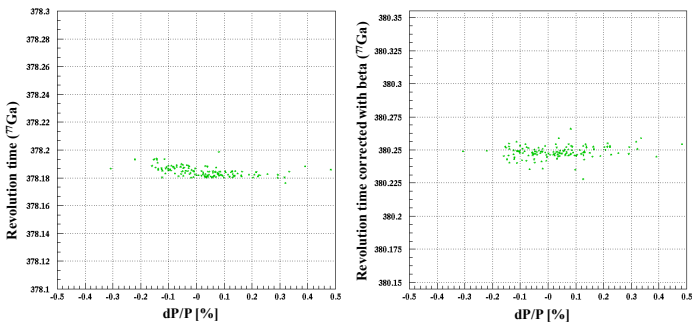

Fig. 3.10 (Left) spectrum of the measured revolution time of fully stripped ^{77}Ga as a function of the relative momentum dispersion. (Right) spectrum of the velocity-corrected revolution time as a function of the relative momentum dispersion.

By utilizing ^{78}Ge as reference ion, which is the isochronous nucleus in this experiment, and with the help of velocity correction IMS mass measurements function $\frac{m_1}{q_1} = \frac{m_0}{q_0}\frac{T_1}{T_0}\sqrt{(1-\beta_1^2)/(1-(\frac{T_1}{T_0})^2{\beta_1}^2)}$, we obtain the values of mass-over-charge ratio m/q of the fully stripped ions of ^{77}Ga, ^{76}Zn ^{79}As, ^{75}Cu and a self-calibration m/q value of the ^{78}Ge itself and the m/q value of 2.434542499 is from the newest atomic mass evolution (2016). Taking ^{77}Ga as an example, three histograms of the calculated m/q, mass excess, and relative $relative-mass-accuracy$ (RMA) defined as:

$$RMA = \frac{(m/q) - (m/q)_{(AME2016)}}{(m/q)} \tag{3.5}$$

where $m/q_{(AME2016)}$ is the deduced m/q of ^{77}Ga from AME2016, are shown in Fig. 3.11. The calculations are carried out based on event by event scheme. 2D histograms of relative

momentum dispersion dependence of the calculated m/q (left), relative $mass_accuracy$ (middle) and mass excess (middle) of the fully stripped ions of ^{77}Ga extracted are illustrated in Fig. 3.12. It is obviously that there is no distinct momentum dependence of the momentum dispersion of the calculated mass value.

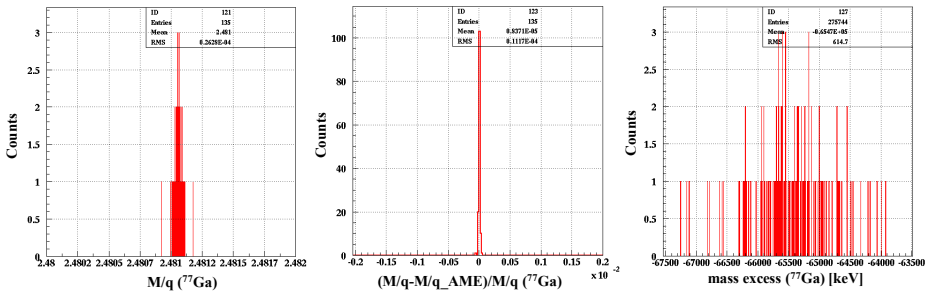

Fig. 3.11 Calculated m/q (left), relative $mass_accuracy$ (middle) and mass excess (middle) spectra of fully stripped ions of ^{77}Ga based on velocity correction IMS mass measurements function with a event-by-event scheme.

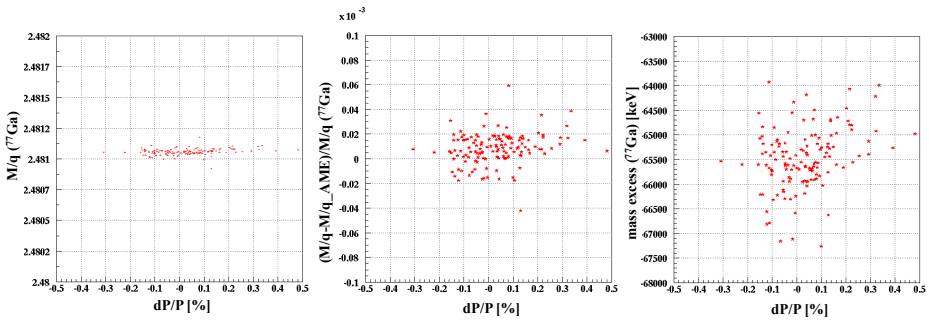

Fig. 3.12 2D histograms of relative momentum dispersion dependence of calculated m/q (left), RMA (middle) and mass excess (middle) of fully stripped ions of ^{77}Ga based on velocity correction IMS mass measurements function.

Momentum correction IMS mass measurements

In addition to velocity correction IMS mass measurements method,the extracted and identified ions of ^{78}Ge, ^{77}Ga, ^{76}Zn, ^{79}As, ^{75}Cu with their measured information are utilized to confirm the momentum correction IMS mass measurements function expressed as: $m_1/q_1 = (m_0/q_0)(T_1/T_0)\sqrt{(1-(T_0/T_1)^2)(((m_0/q_0)c)(B\rho))^2}$, see Chapter 2 for detail description. The P=$\sqrt{(1-(T_0/T_1)^2)(((m_0/q_0)c)(B\rho))^2}$ corresponds to the momentum correction factor.

At left side of Fig. 3.13, the 2D spectra of in-ring revolution time for the extracted ions of ^{76}Zn employing PID gate as a function of relative momentum dispersion is illustrated. The

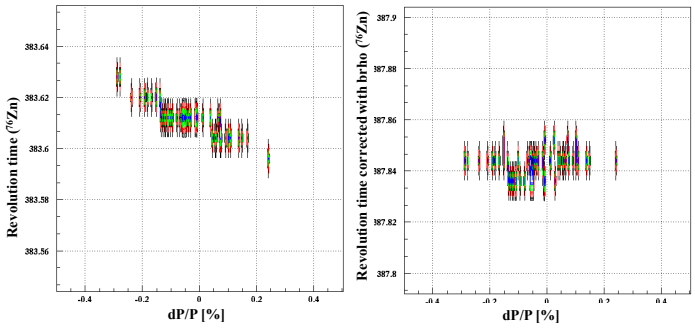

Fig. 3.13 (Left) 2D spectra of in-ring revolution time for the extracted ions of ^{76}Zn employing PID gate as a function of relative momentum dispersion. (Right) 2D spectra of momentum-corrected in-ring revolution time of fully stripped ^{76}Zn as a function of relative momentum dispersion.

2D spectra of momentum-corrected in-ring revolution time of fully stripped ^{76}Zn as a function of relative momentum dispersion are displayed at right of Fig. 3.13. After correction, the revolution time becomes momentum independent.

By utilizing ^{78}Ge as reference ion and with momentum correction IMS mass measurements function $m_1/q_1 = (m_0/q_0)(T_1/T_0)\sqrt{(1-(T_0/T_1)^2)(((m_0/q_0)c)(B\rho))^2}$, we obtain the values of mass-over-charge ratio m/q of the fully stripped ions of ^{77}Ga, ^{76}Zn ^{79}As, ^{75}Cu and a self-calibration m/q value of the ^{78}Ge itself and the m/q value of 2.434542499 is from the newest atomic mass evolution (2016). Taking ^{77}Ga as an example, there histograms of the calculated m/q, mass excess, and relative $relative-mass-accuracy$ (RMA) are shown in Fig. 3.14. The calculations are carried out based on event by event scheme.

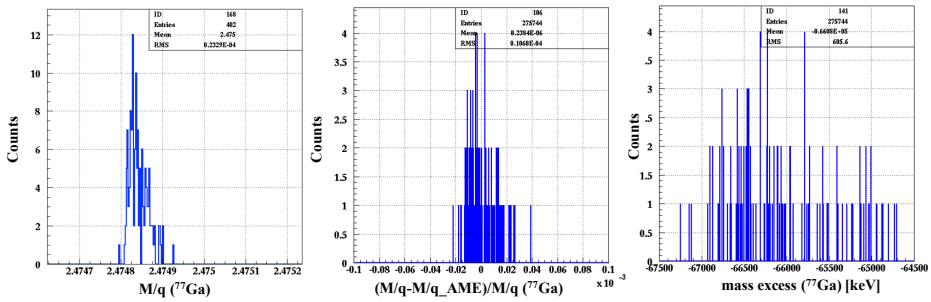

Fig. 3.14 Histograms of the calculated m/q, relative $relative-mass-accuracy$ (RMA) and mass excess of ^{77}Ga by Momentum correction function event by event.

Summary of IMS mass measurements

For comparison of the IMS mass measurements without correction to the velocity or momentum correction method in IMS mass measurements, two species of ions ^{77}Ga, ^{76}Zn, are

utilized to carry out the mass determination. 2D spectra of the relative $relative - mass - accuracy$ (RMA) as a function of the relative momentum dispersion are shown at left and middle of Fig. 3.15. A strong momentum dependence of the accuracy of the measurements of IMS method is shown for both nuclei, which in turn indicates the importance of the velocity or momentum correction in IMS mass measurements.

At right side of Fig. 3.15, a self-calibration spectrum of ^{78}Ge RMA are demonstrated. The accuracy is -4 x 10^{-7} with an uncertainty of σ as 6.9 x 10^{-6}, corresponding to precision of 6.9 x $10^{-6}/\sqrt{(297)}$ = 4 x 10^{-7} with the counts of 297. These results demonstrates the excellent accuracy of our IMS mass measurements system and shows a good prospects of higher accuracy with the m/q near that of the reference nucleus.

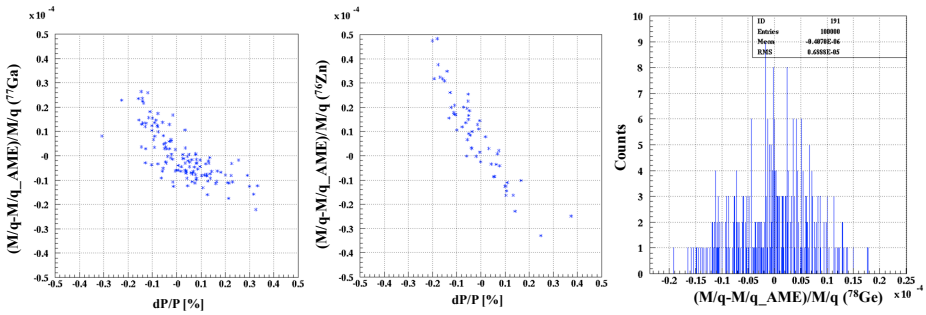

Fig. 3.15 2D spectra of the relative $relative - mass - accuracy$ (RMA) as a function of the relative momentum dispersion for ^{77}Ga (left) and ^{76}Zn (middle). 1D self-calibration spectrum (right) of ^{78}Ge RMA.

As in this experiment, there is a destructive detector with gas (PPAC) at F6 has resulted in energy loss of the passing ions. To solve this problem, there are many methods for extra corrections for the velocity and momentum due to the energy. There are various manually ways to carry out corrections, and one result with velocity and momentum correction are shown in Fig. 3.16.

As the masses of the injected ions are all well known with very good precision, the analysis of these masses deduction are to show the importance of the additional measurements of velocity or momentum in IMS mass measurements. The next chapter demonstrates the $B\rho$-TOF method for mass measurements in the same experiment and a new mass value of the isotope ^{74}Ni which is not included in the newest atomic mass evolution are obtained.

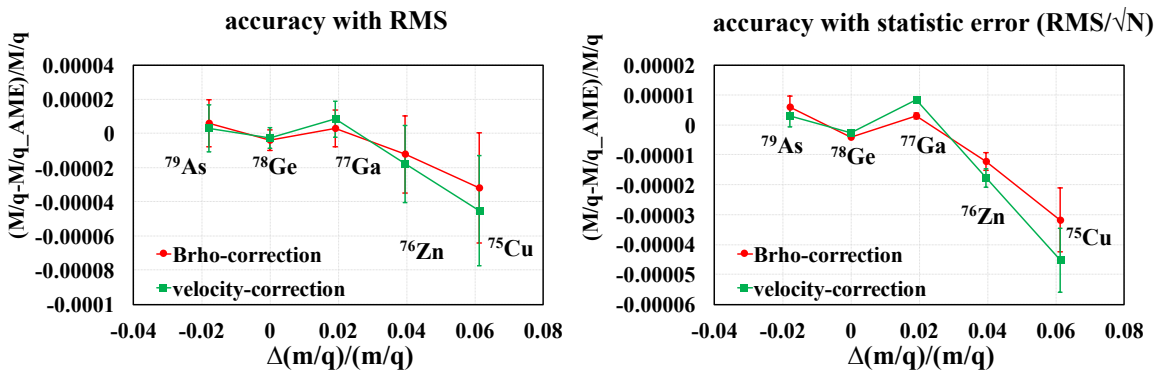

Fig. 3.16 Relative $relative - mass - accuracy$ (RMA) of ^{78}Ge, ^{77}Ga, ^{76}Zn, ^{79}As, ^{75}Cu with error bar of root mean square (RMS) at left, and root mean square (RMS) over square root of counts as statistic error, corrected with momentum correction function (in red) and velocity correction function (in green), respectively. X axis is the relative difference of m/q to reference nucleus ^{78}Ge value for both figures. The nuclei of a relative m/q difference range of 8% were injected into the Rare-RI Ring for mass determination, and the relative momentum dispersion is $\sim \pm 0.3\%$.

3.2 Analysis results of Bρ-TOF mass measurements

Fig. 2.4 shows the layout of the experimental setup for mass measurements by utilizing BigRIPS-HA beam-line as Bρ-TOF Mass Spectrometer, which is discussed in detail in Chapter 2.

The Bρ of each ions that arriving at S0 focus were determined by the dispersive position measurements at the F6 dispersive focus, which is in a proportional relationship. The TOF (F3 focus to S0 focus) were determined by the timing difference between the timing of S0 foil-MCP timing detector and the average timing of both ends of F3 plastic scintillator.

3.2.1 TOF determination with magnetic rigidity correction

Before fitting the mass-TOF surface to obtain a calibrated relationship, the final TOFs and their uncertainties of observed nuclei have to be determined. This consisted of identifying all events belonging to the corresponding nucleus and excluding the contaminates, correcting TOF according to their initial emittance dependence, magnetic rigidity dependence, and determining the mean value of the final TOF distribution and its uncertainty. The final mean value of magnetic-rigidity corrected TOF (F3 focus to S0 focus) distributions and their uncertainties are obtained via a Gaussian fit.

The relationship between the Bρ (F6 X-direction position) and TOF (F3-S0), which needs to be determined to momentum-corrected TOF, was determined individually for each nu-

cleus. The procedure for determining the slope of the TOF(F3-S0)-X_{F6} relationship consisted of fitting the relationship between F6X and TOF(F3-S0) for all events identified belonging to a given nuclide according its PID gate. Then projecting the Bρ-corrected relationship onto the TOF dimension, fitting the projected TOF distribution with a normal distribution to get the mean and standard deviation σ, making a cut in TOF to only include events within Nσ of the mean rigidity-corrected TOF, and repeating the procedure for the data after the Nσ cut was applied, where N should be checked to remove the contaminations from nuclei nearby. Note that the 'pivot point' of the magnetic rigidity correction was correction of the TOF(F3-S0) for all ions to the central orbit TOF, under the condition of X_{F6} = 0. The deviation of the TOF t of each ion from the central TOF t_0 for each isotope fitted with a quadratic function of the dispersive focus F6 position x:

$$t_0 = t - c_1 x - c_2 x^2, \tag{3.6}$$

where c_1, c_2 are fitting parameters from the slope of the 2D TOF(F3-S0)-X_{F6} spectrum and this formula is employed on an event-by-event basis to obtain the TOF distribution mean values t_0 for each ion species. The correction parameters are slightly different for different kind ions.

The linear relation between TOF(F3-S0) and X_{F6} is apparent as shown at the left of Fig. 3.17. Higher-order (3rd) X_{F6} dependence of TOF(F3-S0) has also been checked, but not strong change for the final mean and standard deviation σ of gated nuclei. To avoid the unclear higher order effects to increase the statistical uncertainty of the final masses by adding too many parameters, second order correction is utilized.

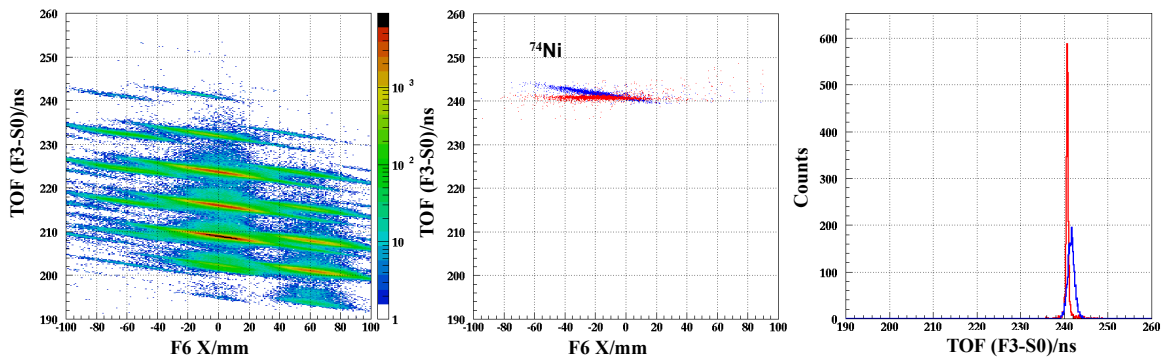

Fig. 3.17 (Left) shows the relation between TOF(F3-S0) and X_{F6} in 2D histogram. (Middle). Relation between TOF(F3-S0) and X_{F6} for gated ^{74}Ni. Blue is the relation before correction and red illustrates the one after correction. (Right). TOF spectrum of TOF(F3-S0) before (in blue) magnetic rigidity correction and the one (in red) after.

For ions of thirteen species with well-determined mass: ^{74}Ni, ^{79}As ^{79}Ge, ^{78}Ge, ^{77}Ge, ^{78}Ga, ^{77}Ga, ^{76}Ga, ^{77}Zn, ^{76}Zn, ^{75}Zn, ^{75}Cu, ^{74}Cu, within $27 < Z < 34$, accumulated counts more than 10000, except ^{74}Ni with a count of $\sim$ 3200, which is an mass unknown nucleus, are corrected with the TOF(F3-S0) and X_{F6} relationship in the two-dimensional histogram as shown in left of Fig. 3.17. The fitted slop information from TOF(F3-S0) and X_{F6} histogram of each nucleus are used for the TOF(F3-S0) correction. As shown in middle of Fig. 3.17, the blue scattering points corresponds to the original TOF(F3-S0) versus X_{F6} of the ions of ^{74}Ni, and the red indicated the magnetic rigidity corrected TOF(F3-S0) distributions as a function of the X_{F6}. The corrected TOF(F3-S0) in red shows a good momentum independent distribution. The projected original TOF(F3-S0) distribution and final rigidity-corrected TOF(F3-S0) distribution for ^{74}Ni are both very close to Gaussian function as shown in blue and red in right part of Fig. 3.17. The gaussian function fitted original TOF(F3-S0) distribution for ^{74}Ni is shown at left side of Fig. 3.18, and the standard deviation σ of the TOF(F3-S0) distribution is 573.4 ps. After magnetic rigidity correction, the fitted TOF(F3-S0) distribution of ^{74}Ni ions is shown at right of Fig. 3.18, and the standard deviation σ of the distribution is 208.3 ps.

As in this experiment, we have only one unknown mass to be determined, for which the local dependence have been well shown in Fig. 3.17, and the local relation of TOF(F3-S0) and X_{F6} is about -49.391 ps/mm for the slope.

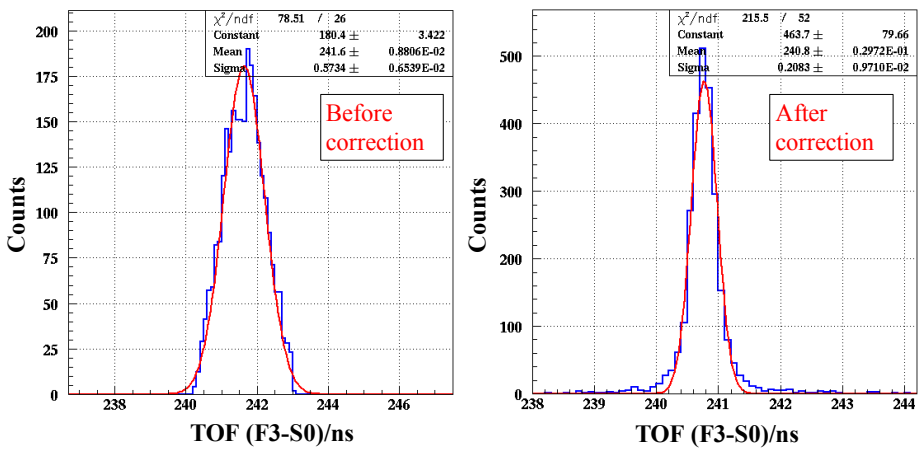

Fig. 3.18 Zoomed TOF spectrum of TOF(F3-S0) before (in blue) magnetic rigidity correction and the one (in red) after.

For the future $B\rho$ experiments, if low-statistics nuclides with unknown masses, which are particularly important since they are the most exotic and therefore the most interesting ones, are acquired by the beam-lines, a global rigidity correction for TOF (F3s0) should be done to reconstruct dependencies of TOF (F3s0) on X_{F6} for those low-statistics nuclides.

It will also help to reduce the systematic biases that affect the rigidity correction and ensure smooth behavior of the rigidity correction. A global rigidity correction method using $(d(TOF_{(F3-S0)})/d(F_{6X}))_{global} = f(A/Z, Z, A, X_{F6})$ can be used for reconstructing the local dependence of each nucleus including the ones with too low-statistics to show the trend, and the orders for the A, Z, A/Z should be adjusted to get the most reasonable fitting results. By this fitting the energy loss of ions in the the PPAC can be excluded with the relation $\Delta E \sim Z^2$.

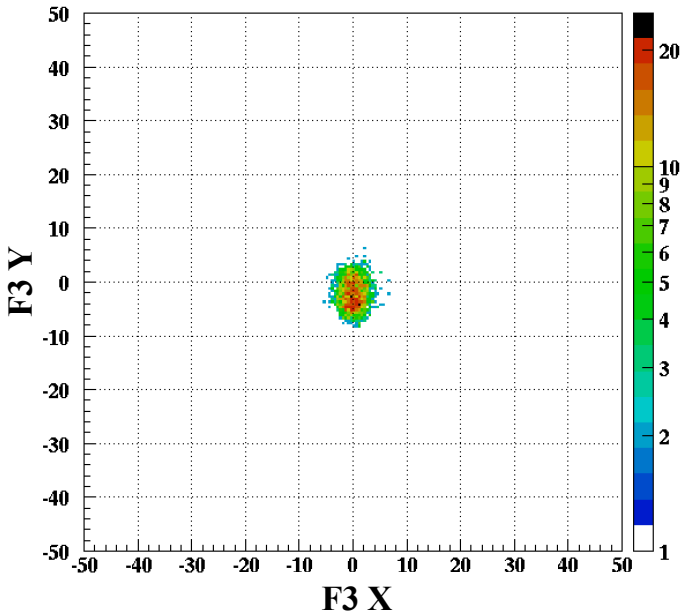

Fig. 3.19 F3 initial position distribution of the identified and gated ions of ^{74}Ni.

As can be seed from Fig. 3.19, the initial beam size of interesting nucleus ^{74}Ni is very large with a very large angular distribution as shown in last chapter and at y direction there is a small offset. To avoid the effect of initial position of the beams on the optical relationship of TOF(F3-S0) and X_{F6}, a TOF(F3-S0)-F3A and TOF(F3-S0)-F3X correction has been done to correct the mean values of central TOF(F3-S0) of each ion species. The typical influence of these TOF(F3-S0)-F3A and TOF(F3-S0)-F3X correlation is around 10-20 ps, which is relatively very small compare to the influence of the resolution of TOF(F3-S0). The contribution of this correction is relatively not as large as that of the correction by magnetic rigidity. Actually, in last Chapter, it has been discussed that, the magnetic rigidity is also influenced by the initial emittance of the beams. In consideration of these two effects, the correction based on TOF(F3-S0)-F3A and TOF(F3-S0)-F3X correlation are carried together with the dependencies of TOF (F3s0) on X_{F6} for all nuclides.

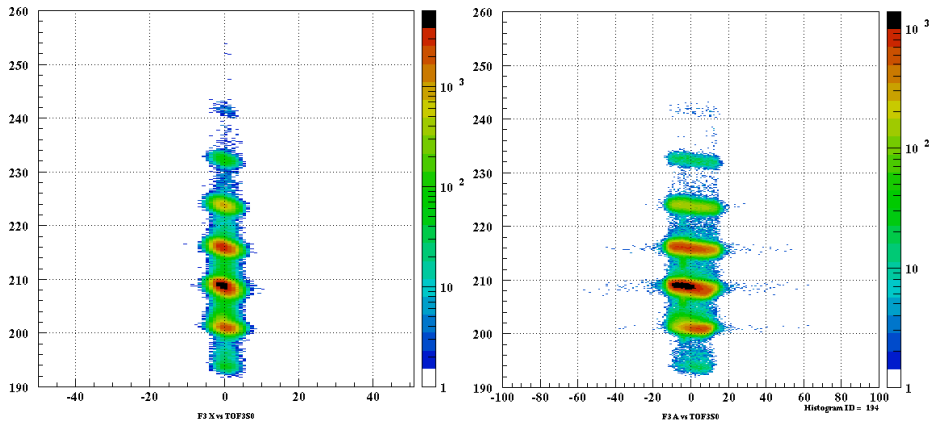

Fig. 3.20 2D spectra of TOF(F3-S0)-F3A and TOF (F3-S0)-F3X correlation to demonstrate the effect of initial beam emittance to the distribution of TOF (F3-S0).

The final statistical uncertainties for the mean TOF (F3-S0) values for all twelve nuclei are generally below 2 ps (typical TOF (F3-S0) standard deviation σ of the distribution is a bit more than 200 ps), as can seen in Tab., and the resolution of TOF (F3-S0) distributions for observed nucleus ^{74}Ni is 208.3 ps. The statistics for calibration and evaluated nuclides are also shown in Tab., where the minimum number of counts required to obtain a reasonable statistical TOF (F3-S0) uncertainty is ~10000. The TOF (F3-S0) resolution roughly agreed with the sum of expected contributions, where a $\sim$ 30 ps resolution can be attributed to the timing detection at F3 plastic scintillator. The main contribution to the TOF resolution likely can be attributed to the deviation are the timing MCP detector (previous test for timing resolution is about 130 ps or worse in σ). After optimizing the performance as demonstrated in chapter3, now the foil-MCP timing detector can reach $\sim$ 40 ps in σ. Note the remaining contribution to the TOF resolution, is poorer due to the spread introduced from the beam-line ion-optics, which results in deviation from linearity in the $TOF_{(F3-S0)}$-F6X relationship (from $TOF_{(F3-S0)}$-F3X and $TOF_{(F3-S0)}$-F3A about 10 ps to the resolution), and from the finite position resolution of the PPAC used for the ion-rigidity correction.

3.2.2 Mass fit procedure

The mass fit is the final step of the $B\rho$-TOF mass determination data analysis, where nuclides with well-known masses and well determined TOF (F3-S0) are used to obtain a calibrated relationship between TOF and mass. After the optimum fit function was chosen and getting the fitting parameters, the fitting parameters are then utilized to determine the unknown masses with the measured TOF (F3-S0) and other additional information.

Mass fit method 1

From last section, the centroid of the time-of-flight (TOF F3-S0) distribution are corrected with the information of the F3X, F3A and most importantly the F6X position information corresponding to the magnetic rigidity.

The typical and classic calibration function (polynomial) for mass-TOF relation is widely used written as[2]:

$$\left(\frac{m}{q}\right)_i (T, Z) = a_0 + a_1 \cdot T_i + a_2 \cdot T_i^2 + a_3 \cdot T_i^3 \tag{3.7}$$

where i indicates different nucleus, and T_x is the TOF from F3 focal plane to S0 focal plane. This function works well for m/q calibration of in-ring circulating ions depending on their revolution time of each ion species. As in this experiment, there is a PPAC gas detector in between the start and stop TOF. Extra information with the help of reference nuclei has to be added to calibrate the ion energy loss, which is in order of worse than 10^{-4}. The calibration function mass-TOF surface are then written to include the effect of the energy loss of each ions in the PPAC detector:

$$\left(\frac{m}{q}\right)_i (T, Z) = a_0 + a_1 \cdot T_i + a_2 \cdot T_i^2 + a_3 \cdot T_i^3 + b_1 \cdot Z_i + b_2 \cdot Z_i^2 + b_3 \cdot Z_i^3, \tag{3.8}$$

where i indicates different ion species, Z the proton number of each ion species and T_i the TOF from F3 focal plane to S0 focal plane.

The calibration function is employed to fit to the known masses through a χ^2 minimization procedure. The results of first attempts to calibrate the known masses are shown in Fig. 3.21, and left two panels shows the difference of fitted m/q to the AME2012 without/with the Z term for fitting, right two panels corresponding to different m/q values from different sources as a function of the TOF (F3S0). As can be easily checked from the fitting residuals, the fitting residuals from fitting with Z term is much smaller than the one without Z term fitting.

To reduce the multicollinearity of fitting parameters (large correlations in the errors of the fit parameters), an effective nuclear charge, $z = Z - \langle Z \rangle$, and effective TOF, T, $T = TOF - \langle TOF \rangle$, where the offsets $\langle Z \langle \, and \, \langle TOF \langle$ are the average nuclear charge Z and time-of-flight TOF (F3S0) of the 12 reference nuclei. The general form of the calibration

[2] A linear least square fit based on the finding a minimum chi-square for the polynomial function

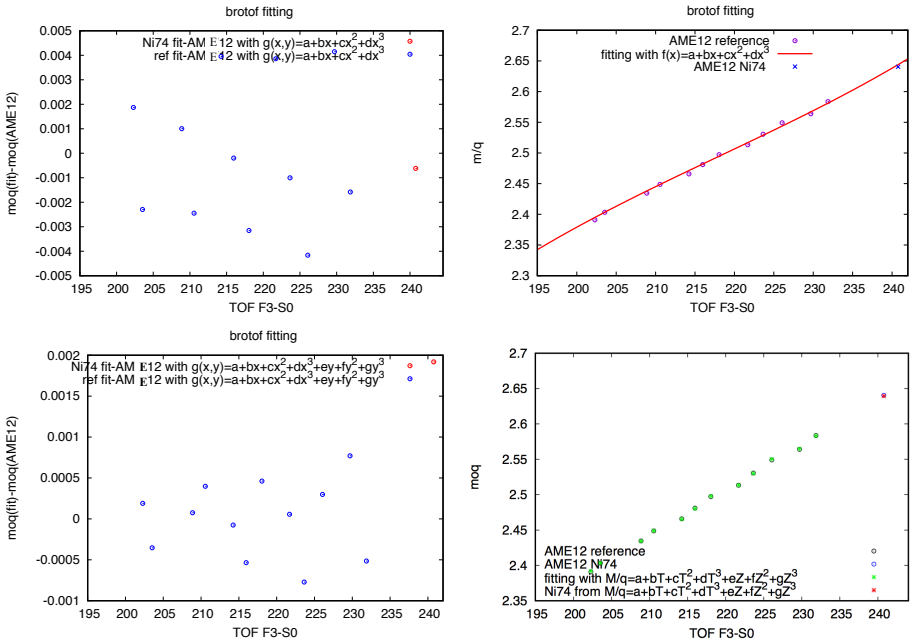

Fig. 3.21 Left two panels show the fitting residuals without/with the Z term for fitting, and right two panels corresponding to different m/q values from different sources as a function of the TOF (F3S0).

function can be written as:

$$\left(\frac{m}{q}\right)_i = g(T,z) = \sum_j \sum_k a_{jk} T_i^j z_j^k. \tag{3.9}$$

As all the reference ions nuclei are fully stripped and the events corresponding to charge states of the isotopes in the beam are excluded from the fit, thus the charge of the particles q is right their nuclear charge Z.

The parameters in Eq. 3.9 are determined by a reduced χ^2 minimization procedure using the isotopes with well-known m/q values calculated form the atomic mass evolution:

$$\chi^2 = \sum_i^m \frac{[(\frac{m}{q})_{AME} - g(T,z))]^2}{[\sigma_{AME}(\frac{m}{q})_i]^2 + [\sigma_{stat}(\frac{m}{q})_i]^2} \tag{3.10}$$

Each data point is weighted by combining its mass uncertainty from the literature σ_{AME} and the statistical uncertainty in the determination of its TOF, indicating as σ_{stat}. The TOF uncertainty (δTOF) is converted to mass units by multiplying it with the calibration function coefficient linear in TOF (a_{10} in Eq. 3.9, which is the dominant term). The σ_{stat} can be

expresses as:

$$\sigma_{stat}\left(\frac{m}{q}\right)_i = \frac{\sigma(T_i)}{\sqrt{N_i}} \sum_j^m \sum_{k=1}^{l-1} k a_{jk} T_i^{k-1} z_j^k. \tag{3.11}$$

in case of form Eq. 3.9. A none-linear least square function minimization, the m/q as a function of T and z, which the independent variables, is employed for the mass-fit. The initial uncertainty ascribed to the data points is the literature mass uncertainty added in quadrature to the statistical uncertainty, where the latter used standard propagation of uncertainty to translate uncertainty in TOF into uncertainty in mass over charge. The final statistical uncertainty assigned to each data point was determined in an iterative procedure where the data was fit to obtain a mass-TOF calibration function, statistical uncertainties are calculated for each of the data points corresponding to reference nuclei, and the process was repeated until convergence.

Upon completion of the first mass-fit, including literature and statistical uncertainties, the reduced χ^2 (χ^2 value per degree of freedom) of the fit is typically much larger than one for the Bρ-TOF method. This indicated that the uncertainty of the reference nuclide data-points was underestimated and that some additional unaccounted for uncertainty (effect created by many uncontrolled factors in the measurement, such as time-dependent magnetic fields of the dipole magnets along the beam line, time-dependent variations in the response of the timing electronics due to variations in temperature, or some other unidentified biases present in the data analysis) is present. To include this additional systematic uncertainty, the uncertainty of reference nuclide data-points is increased uniformly, i.e. each nucleus as calibrant has the same systematic uncertainty σ_{sys} added:

$$\chi^2 = \sum_i^m \frac{[(\frac{m}{q})_{AME} - g(T,z))]^2}{[\sigma_{AME}(\frac{m}{q})_i]^2 + [\sigma_{stat}(\frac{m}{q})_i]^2 + [\sigma_{sys}(\frac{m}{q})_i]^2} \tag{3.12}$$

This process is then repeated iteratively until statistical and systematic uncertainties converged and reduced χ^2 is close to one. The fitting function resulting from this procedure is the final mass-TOF calibration function which is then used to obtain masses for nuclide with unknown mass whose TOF has been measured (only ^{74}Ni). The number of terms in the mass-fit function should be checked from comparison, and goal of this approach is to find the minimum number of terms that reproduce the calibration mass-TOF surface without any or smallest systematic trends in the residuals. A similar technique is employed to assess their systematic uncertainty for the analysis of storage ring mass measurements operating in a isochronous mass spectrometry.

For the final determination of unknown masses, the statistical error σ_{stat}, the systematic error determined from the calibration σ_{sys} , and the error introduced by the uncertainty of the calibration function parameters σ_{fit} are take into account. σ_{fit} accounts for the propagation of the uncertainty of the calibration functions into the final results. It can be calculated from the error propagation equation for $g(T, z)$ from Eq. 3.9 by the covariance matrix, described as:

$$\sigma^2_{fit}\left(\frac{m}{q}\right)_i = \sum_j \sigma^2_{a_j} \sum_{j\neq i} \sigma^2_{a_j a_i} = \sum_j \sum_{i=0}^{m} \left\{ {\sigma_i}^2 \left[\frac{\partial g(T,z)}{\partial a_i}\right]^2 \right\} + \sum_{j=0\neq i} \sum_{i=0}^{m} \left\{ {\sigma_{ij}}^2 \left[\frac{\partial g(T,z)}{\partial a_j}\frac{\partial g(T,z)}{\partial a_i}\right] \right\} \tag{3.13}$$

The variances in each parameter σ_{a_j} of the calibration function is included in the first term of the upper equation. The cross terms $\sigma_{a_j a_i}$ in the second sum are covariances of fit parameters, described as the correlation in the errors of the fit parameters. In many cases The covariances can be a negative value occassionally and will help reduce the extrapolation error. The sums of the σ_{fit} are carried over each data point i and parameter j.

The form of reduced χ^2 then can be written as

$$\chi^2_{norm} = \frac{1}{n-p} \sum_{i=1}^{n} \frac{\left[\left(\frac{m}{q}\right)_{AME} - \left(\frac{m}{q}\right)_{fit,i}\right]^2}{\left[\sigma_{stat}\left(\frac{m}{q}\right)_i\right]^2 + \left[\sigma_{fit}\left(\frac{m}{q}\right)_i\right]^2 + \left[\sigma_{AME}\left(\frac{m}{q}\right)_i\right]^2 + \left[\sigma_{sys}\left(\frac{m}{q}\right)_i\right]^2}, \tag{3.14}$$

where n is number of calibrants as reference nuclides, n-p is the degree of freedom, and χ_{norm} follows the χ^2 distribution. χ_{norm} is between the values of $1 \pm \sqrt{1/(2n)}$.

The final uncertainty in the mass-to-charge results can be calculated by adding the different error terms in quadratic form:

$$\sigma\left(\frac{m}{q}\right)_i = \left[\sigma_{stat}\left(\frac{m}{q}\right)_i\right]^2 + \left[\sigma_{fit}\left(\frac{m}{q}\right)_i\right]^2 + \left[\sigma_{AME}\left(\frac{m}{q}\right)_i\right]^2 + \left[\sigma_{sys}\left(\frac{m}{q}\right)_i\right]^2 \tag{3.15}$$

To select the optimum calibration function, the fit was performed for all possible polynomials up to third order in T and z, including cross terms (Tz, Tz^2, zT^2). The goal of this test was to find a parameterization of the calibration function that includes as few parameters as possible, but with the smallest fitting residuals. With a small number of parameters, the fitting parameters are better constrained by the calibration points , thus the extrapolations of the calibration functions will be more robust (δfit is minimized). An example using $\left(\frac{m}{q}\right)_i(T, Z) = a_0 + a_1 \cdot T_i + a_2 \cdot T_i^2 + a_3 \cdot T_i^3$ as a calibration function is shown in Fig. moq-rma-brho-tof-tof-only-fit. Without including the Z terms for fitting, the resulting δsys is about 2 x 10^{-3}. The parameterization that offered the best results is: $\left(\frac{m}{q}\right)_i(T, Z) = a_0 + a_1 \cdot T_i + a_2 \cdot T_i^2 + a_3 \cdot T_i^3 + b_1 \cdot Z_i + b_2 \cdot Z_i^2 + b_3 \cdot Z_i^3$. This calibration func-

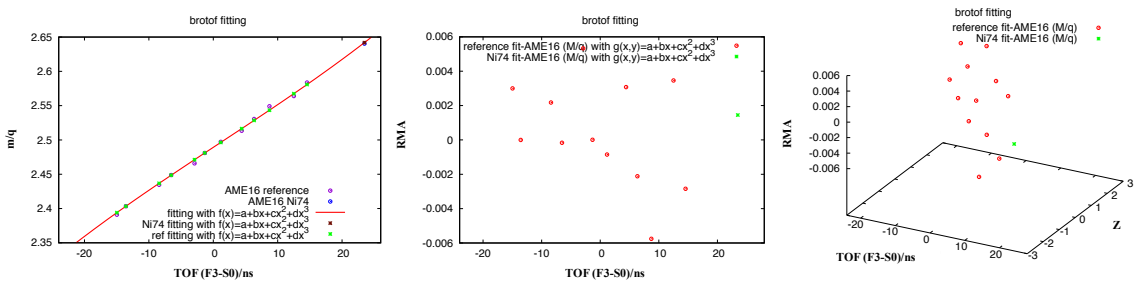

Fig. 3.22 (Left) m/q as a function of TOF (F3S0) by fitting with $\left(\frac{m}{q}\right)_i(T,Z) = a_0 + a_1 \cdot T_i + a_2 \cdot T_i^2 + a_3 \cdot T_i^3$ as the calibration function. (Middle) RMA from difference of fitting m/q and literature m/q as a function of TOF (F3S0) . (Right) RMA as a function of TOF (F3S0) and Z.

tion results in the smallest estimate for the δsys near 5 x 10^{-4} to make reduced χ^2 closest to 1. The inclusion of the T^3 term in the calibration function produces the most improvement in the quality of the fit with respect to the functions with only second order terms as shown in Fig. 3.23. Including too many additional terms will not improve the quality of the fit too much, while reducing its number of degrees of freedom. As in this experiment, due to the worse TOF (F3S0) resolution $\sim$ 200 ps, mainly coming from the detector resolution, together with the average TOF (F3S0) $\sim$ 500 ns, resulting the relative TOF resolution of 200 ps/ 540000 ps = 4 x 10^{-4}. Comparing to the momentum resolving power of high resolution beam-line of about 7600, the TOF resolving power of about 2500 has made the largest contribution to the final mass resolution of $B\rho$-TOF mass measurements as discussed in D.

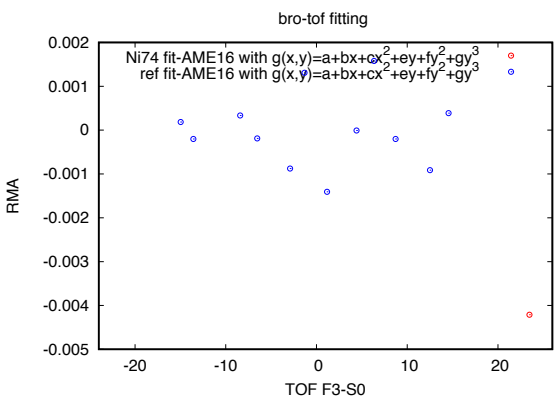

Fig. 3.23 Example of fitting with $\left(\frac{m}{q}\right)_i(T,Z) = a_0 + a_1 \cdot T_i + a_2 \cdot T_i^2 + a_3 \cdot T_i^3 + b_1 \cdot Z_i + b_2 \cdot Z_i^2 + b_3 \cdot Z_i^3$. The TOF (F3S0) dependence of RMA is demonstrated.

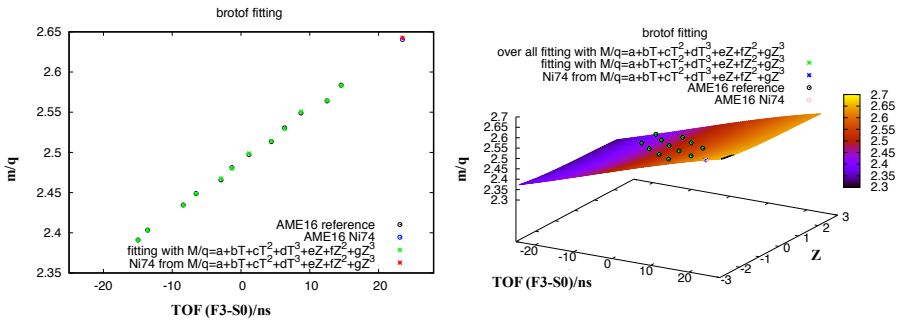

Fig. 3.24 (Left) m/q as a function of TOF (F3S0) by fitting with $\left(\frac{m}{q}\right)_i(T,Z) = a_0 + a_1 \cdot T_i + a_2 \cdot T_i^2 + a_3 \cdot T_i^3 + b_1 \cdot Z_i + b_2 \cdot Z_i^2 + b_3 \cdot Z_i^3$ as the calibration function. (Right) 3D m/q-TOF-Z correlation. The surface in color demonstrates the fitting function m/q(T,Z) surface. The blue points indicates the calculated m/q of reference ion species by the calibrated fitting function. The m/q value of unknown nuclide ^{74}Ni calculated with the calibrated fitting function are shown in red circle on the mass surface.The black circle corresponds to the m/q values form the AME2016.

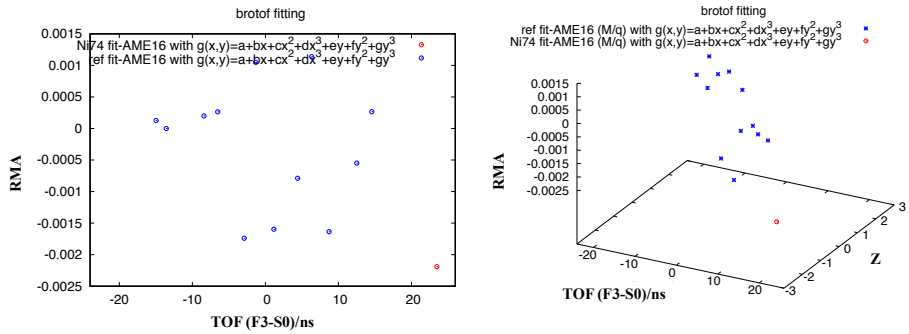

Fig. 3.25 RMA from difference of fitting with $\left(\frac{m}{q}\right)_i(T,Z) = a_0 + a_1 \cdot T_i + a_2 \cdot T_i^2 + a_3 \cdot T_i^3 + b_1 \cdot Z_i + b_2 \cdot Z_i^2 + b_3 \cdot Z_i^3$ and mass values of AME2016, in 2D and 3D forms, as a function of TOF (F3S0) and TOF (F3S0)-Z respectively.

Higher order optics correction

To correct the TOF dependence on the higher order optical distortion due to the Inclination of the focal plane in systems with curved axis, the optical Inclination of the focal plane at F6 was reconstructed. As shown in Fig. 3.27, the typical focal plane in use for optical matrix is dependent on the Gaussian plane (in red), which is used for first order optical matrix elements calculation. The position at F6 can be calculated as: $x_1 = (x|x)x_0 + (x|\delta)\delta + (x|a)a_0 + (x|a\delta)a_0\delta$, and as can be seen from the Fig. 3.26, the tilted angle λ can be deduced by: $tan\lambda = -\frac{(x|a\delta)}{(a|a)D_k}$, where $\delta = dP/P$ and D_k is the dispersion function.

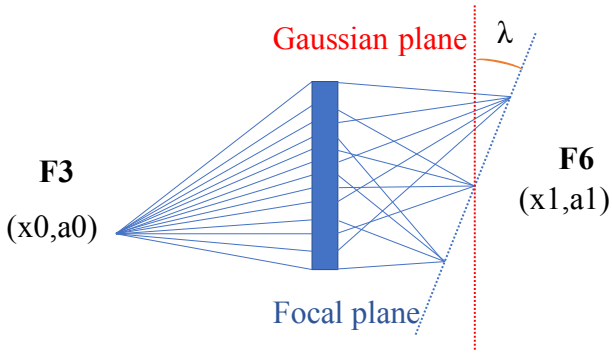

$$x1 = (x|a)x_0 + (x|a)a_0 + (x|\delta)\delta + (x|a\delta)a_0\delta$$

$$\tan\lambda = -\frac{(x|a\delta)}{(a\mid a)D_K}$$

Fig. 3.26 Inclination of the focal plane in systems with curved axis.

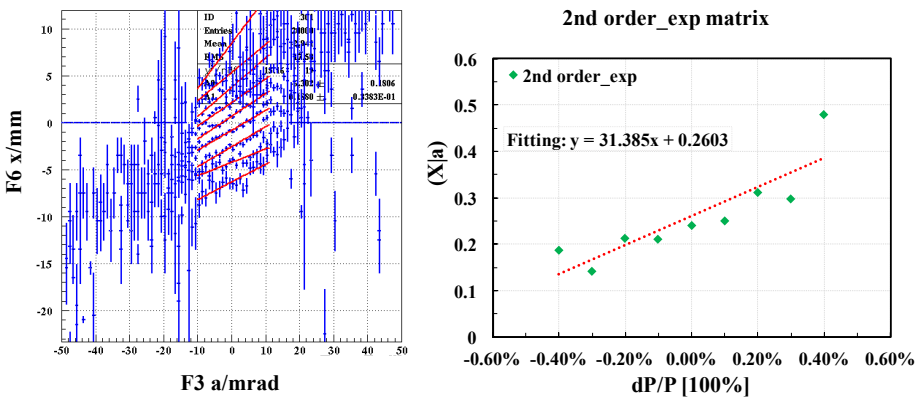

Fig. 3.27 Second order matrix element of $(x|a\delta)$ calculation. The red lines at left panel corresponds to the lines of fitting of F6 X versus F3 a with relative momentum dispersion gates at a range from - 0.4% to 0.4% with a step 0.1%, the gates is done by the TOF F3-S0. The right panel shows the correlation of $(x|a)$ as a function relative momentum dispersion with a fitting to deduce the matrix element of $(x|a\delta)$.

By correction of the inclination of the focal plane in systems with curved axis, the distribution of F6 X get optimized and demonstrates a better relation to the momentum dispersion. The uncertainty of ^{78}Ge TOF (F3-S0) distribution are globally changed from ~210 ps to ~200 ps. This method is useful for fine correction, but for the now ~200ps TOF resolution, to solve the final mass resolution worse problem, the better performance of the TOF detectors are most significant. With a better TOF resolution of about 40 ps for the tested detector, the correction by this method will be of great help to minimize the optical distortion effect on the final resolution of $B\rho$-TOF mass measurements.

Mass fit method 2

Based on the analysis and experience from the conventional method 'method 1' for $B\rho$-TOF mass determination. A new method based on event by event TOF utilization of each ion species are developed for this experiment. As demonstrated in last section, the TOF distribution of each ion species, after correction based on the momentum and optical modification, are fitted with a gaussian function to get the uncertainty of the centroid. which is the statistical uncertainty of the final mass deduction. In this section, every TOF of each ion species is utilized for parameterization with a calibration function described as:

$$\left(\frac{m}{q}\right) = g(T, F3x, F3a, F3y, F3b, F6X, F6y, z) = \sum_i^3 \sum_j^3 \sum_k^3 \sum_l^3 \sum_m^3 \sum_n^3 \sum_o^3 \sum_p^3 a_{jklmnop} T^p X_3^o A_3^n Y_3^m B_3^l X_6^k Y_6^j z^i. \tag{3.16}$$

where T and z are the effective TOF from F3 focal plane to S0 focal plane, and F3 X, F3 Y, F3 A, F3 Y, F6 X, F6 Y are the position and angle information measured by PPACs at the corresponding focal planes. One example of the calibrated function which is utilized in calculation of m/q of each ion on a event-by-event scheme are shown in Fig. 3.28.

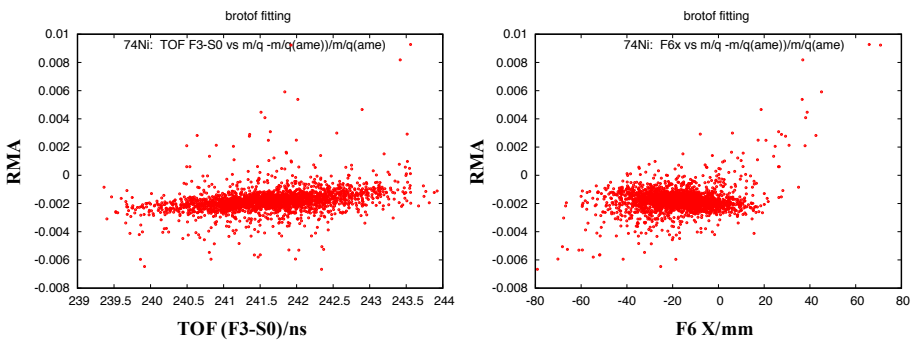

Fig. 3.28 The RMA (relative mass accuracy defined in last section) as a function of the original TOF (F3S0) (left) and F6 X (right). The fitting is based on event by event scheme with 8 independent variables and third order in the calibration function.

From the idea of event by event m/q fitting, the TOF (F3S0) and the measured F3x,F3a ,F3y,F3b,F6X,F6y information are also used for the correction of the TOF firstly and then the distribution of the TOF (F3S0) are used for the calibration of the mass, which has been discussed in detail during section of 'method 1' to use the corrected TOF for mass calibration. Several correction function of $TOF = g(F3x, F3a, F3y, F3b, F6X, F6y, z) == g(x1, x2, x3, x4, x5, x6, x7)$ is used to correct the TOF (F3S0) as shown in Fig. 3.29. The relative TOF (F3S0) difference in Fig. 3.30 indicates a good none-momentum dependence and no systematic trend of the TOF after correction y this method. The calibration of m/q by this method will be the future consideration.

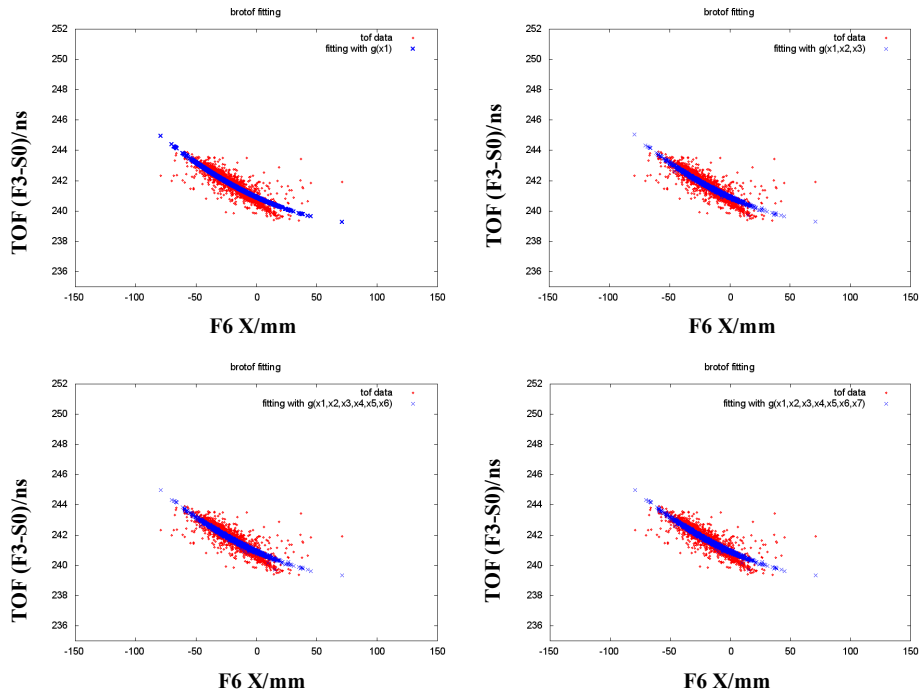

Fig. 3.29 4 correction function of $TOF = g(T, F3x, F3a, F3y, F3b, F6X, F6y, z) = g(x1, x2, x3, x4, x5, x6, x7)$ are used to correct the TOF (F3S0).

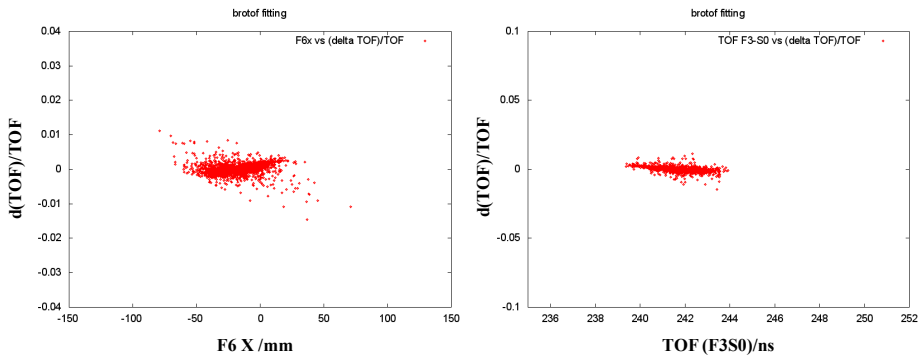

Fig. 3.30 Relative TOF (F3S0) difference (difference of calibrated TOF value and corrected value, over calibrated value) as a function of F6 X (at left) and TOF of F3 to S0 (at right).

With the help of Eq. 3.16 as a calibration function, m/q of the ions of ^{78}Ni are calculated event by event. The m/q and RMA of ions the calibrant of ^{78}Ge are displayed in histograms in Fig. 3.31, which demonstrates a relative accuracy of ∼ - 3.6 x 10^{-5} and a precision of ∼ 6 x 10^{-5} from the comparison of the calibrated m/q and the m/q from literature.

The final calculated m/q, relative difference of m/q to the literature, the mass excess of ^{74}Ni are shown in histograms in Fig. 3.32. The first mass value of an un-evaluated mass of

^{74}Ni are deduced at the Rare-RI ring in this work. The mass excess of -72190 keV (-48456 keV in AME2016) and mass uncertainty of 927.31 keV (401 keV in AME2016).

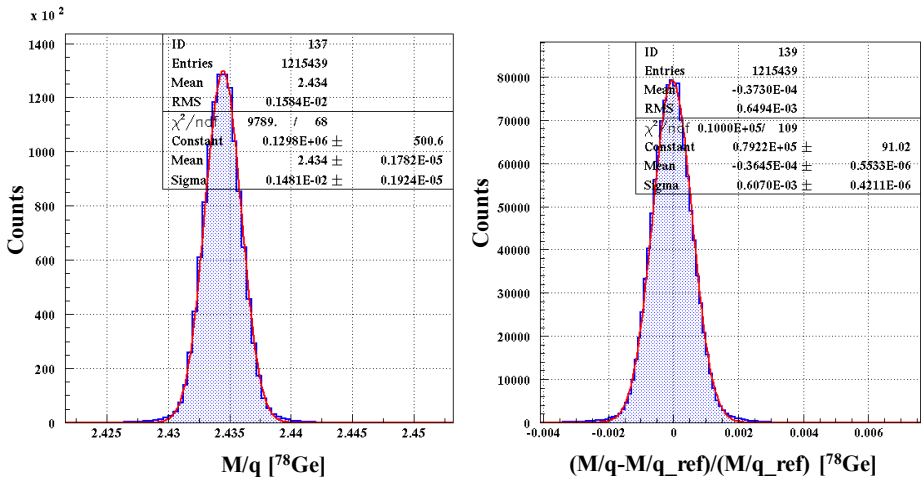

Fig. 3.31 The m/q and RMA of ions the calibrant ^{78}Ge are displayed at left and right panel, respectively , which demonstrates a relative accuracy of ∼ - 3.6 x 10^{-5} and a precision of ∼ 6 x 10^{-5} from the comparison of the calibrated m/q and the m/q from literature.

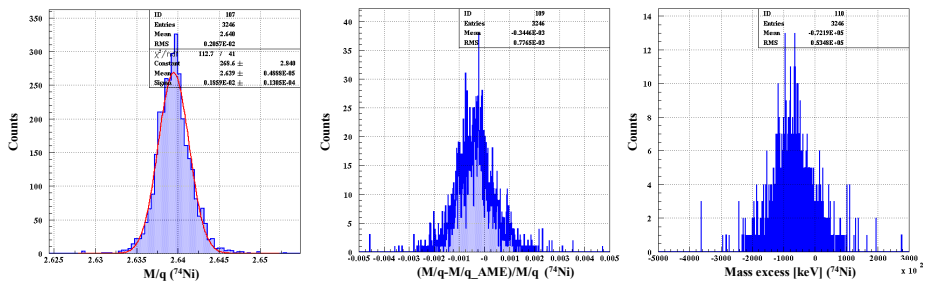

Fig. 3.32 Histograms of the final calculated m/q (left), relative difference of m/q to the literature (middle), the mass excess (right) of first deduced unknown-mass nuclide ^{74}Ni at the Rare-RI Ring. 3.32.

3.3 Conclusion

An experiment aimed to study the principle of mass measurements and performance of the Rare RI Ring performing as an Isochronous mass spectroscopy has been carried out at RIBF, and the fisrt fission fragments, created by ^{238}U projectiles in a beryllium target at the entrance of the BigRIPS focus F_0, were spatially separated by and injected into the R3. In the experiment, we succeeded in selection, injection, accumulation and extraction of 5 different nuclei

to R3 and the isochronism ~5x10^{-6} was achieved by checking the TOF spectrum of ^{78}Ge. The results of these pilot experiments on nuclides of well-known mass are in agreement with the mass values given in the literature of AME2016. A mass resolving power of about $\delta m/$ m = 62 000 (FWHM) has been achieved according to the isochronism of the reference nucleus ^{78}Ge. A two stage selection and particle identification method has been carried out with the $B\rho$-TOF-ΔE-E method based on individual injection technique, and with this new method, all the ions have be well separated and identified for mass deduction analysis.

From the analysis, it is confirmed that from one experiment run, two complementary mass measurements methods (IMS and $B\rho$-TOF) can be employed simultaneously to deduce masses and benefit each other, in which it is very suitable to save beam time and cover large area of nuclide of chart and large momentum area of secondary products from experiment of very exotic nuclei. It is also proved that to achieve high resolution, the revolution time measurement of the storied ions and the magnetic rigidity or the velocity for correction of the in ring TOF should be simultaneously measured, thus we can achieve high resolution with small systematic error to cover relative large range of $\delta m/m$ relative to reference ion in isochronous condition for the IMS method. Besides, new mass of ^{74}Ni (mass excess -72190 keV and mass uncertainty 927 keV) which is not included in the newest atomic mass evolution (2016) is deduced in this work by $B\rho$-TOF method. The mass of ^{74}Ni is very important for the research of nuclear shell effect and also show importance of the impact on the r-process modeling.

Chapter 4

The Rare-RI Ring and high resolution beam-line at RIBF

As discussed in the previous in-flight fission experiment part, there is large energy loss in the PPAC at F6 dispersive focus, which is for position measurement to deduce the momentum. Do to the large energy loss inside the gas detector, the influence of energy to the mass accuracy is enormous. At the same time, the timing resolution of the timing MCP detector of about 200 ps from the analysis, can not satisfy the requirements of high resolution mass measurements by the TOF methods (for both $B\rho - TOF$ and IMS). For these reasons, to develop a detector which should possess a higher timing resolution and has a capability to measure the position (to deduce velocity and magnetic-rigidity) at the same time with low energy loss and a large active area is significant for high resolution and accuracy mass measurements at the Rare-RI Ring and the beam-lines.

4.1 Introduction of MCP detectors for mass measurements

Foil-MCP detectors, by transporting induced secondary electrons(SEs) stripped from a thin foil towards an MCP detector with different arrangements of the electromagnetic field, to deduce the information of the heavy ions, is widely utilized in mass measurements experiments for TOF or position measurement.

Timing foil-MCP detectors have been longly used in mass measurements experiments of exotic nuclei in two heavy-ion storage ring facilities: the ESR/GSI [113] and CSRe/IMP [116], where precision mass measurements by revolution time measurement with these timing detectors have been successfully performed by IMS method. This type of detector is also developed at R3 with a resolution of ∼130 ps with efficiency of ∼56% (effective area of MCP

95 mm x 42 mm) in 2013 [180] and 40 ps timing resolution with efficiency of ∼98% (effective area of MCP 40 mm in diameter) recently, respectively. Meanwhile, position-sensitive foil-MCP detector using for magnetic-rigidity-time-of-flight ($B\rho$-TOF) mass measurements at NSCL/MSU [89] have also demonstrated its high performance and special characteristics for position measurements to deduce the momentum of exotic nuclei at dispersive focus plane. All the above described detectors were mostly optimized for timing measurements at the cost of only timing information (GSI/IMP) or good position resolution but with worse timing resolution (MSU), and relatively small detection active areas.

As discussed at section 1.4, TOF measurement with an additional $B\rho$ (equivalent to position at dispersive focus) measurement is needed for high precision mass measurements by TOF methods. In this work, to achieve high precision and accuracy mass measurements of exotic nuclei, a large-area foil-MCP detector coupled with a position-sensitive anode, which possesses high position resolution and good timing resolution at the same time by utilizing SEs from foil with the detection by MCP, was developed for the purpose to measure the TOF of interesting nuclei along with its position, at the Rare-RI Ring in RIBF, RIKEN Nishina Center, Japan.

Therefore, the TOF-$B\rho$, Obit-IMS method, In-ring TOF-$B\rho$-IMS, and TOF-$B\rho$ at beam-line & Obit-IMS by ring described in section 1.4 will be easily established with the development of this type of detectors. By developing this type of detectors, we can measure the masses with two complementary TOF methods in one experiment run, and separate the secondary ions from fission or projectile fragments with high resolution by TOF-$B\rho$-ΔE-E method.

Besides, a foil detector with a timing anode dedicated for TOF detection are optimized and characterized to achieve improvements of performance in both efficiency and and timing resolution. Both of these detectors have been tested offline with radioactive α source and online with heavy ion beams at Heavy Ion Medical Accelerator in Chiba (HIMAC).

The timing and position resolution reached are $40 - 50\,ps$ (in σ) and $1\,mm$ (in σ) with a heavy ion detection efficiency of $\sim$ 95 % for the detector with position-sensitive delay-line anode, and the timing resolution for the detector with timing anode is $\sim 40\,ps$ with an efficiency of $\sim$ 96 % for heavy ion.

With the good performance and excellent characters, this type of detector will be versatile instrument for nuclear physics and astrophysics study at RIBF. For the utilization in mass measurement area,

1. the mirror detector with two dimensional delay-line anode which possesses both good position and timing resolution can be used on the beam-line for two dimensional position measurement to reconstruct beam trajectory, beam-line momentum measure-

ments for velocity reconstruction, which can be used for $B\rho$ or velocity correction of revolution time to improve in-ring mass measurements resolution, meanwhile, it can be used for position monitoring and revolution time measurement turn by turn inside the storage ring (the Rare-RI Ring) to deduce mass directly.

2. the TOF detector with timing anode which can be used for revolution time measurement inside R3, start TOF of the total TOF for in-ring circulation, beam-line TOF measurement for beam-line mass determination and velocity reconstruction for in-ring mass correction. At the same time, offline test results with α source ^{241}Am are also described in this contribution.

In the next two chapters, the main contents are divided into the following sections: 1. Requirements of detectors for high precision and accuracy mass measurements; 2. Description of the electrostatic mirror detector; 2. Principles for position and timing determination; 3. Theory of ion induced secondary electrons; 4. Structure of the MCP detector. 5. Anodes for position-sensitive MCP 6. DAQ setup and electronics. 7. structure and HV apply; 8. Offline test; 9. Online measurements and analysis; 10. Applications of the TOF-Position measurements in R3; 11. Summary and prospects.

4.2 Requirements of detectors for high precision and accuracy mass measurements

For designing of position-sensitive and/or TOF detectors for mass measurements, several conditions are to be considered:

1. **Very good timing resolution is essential (less than** $100\,ps$**)**

   High resolution TOF is crucial for mass measurements via TOF methods, such as isochronous TOF in a storage ring or beam-line Bρ-TOF method. The TOF information can also be used for velocity measurement for mass correction. The high resolution TOF measurements will also benefit the high resolution particle identification.

2. **Very good position resolution is essential** ($\leq 1\,mm$)

   To deliver a precise position (X and Y) sensitive Beam Profile Monitor (BPM) for each passing ion is important to measure the momentum dispersion of RI. On the beam-line, combined with the high precision TOF measurement with this detector together with energy loss information in ΔE detectors like ion chamber. With the $TOF - B\rho - \Delta E$ method, the mass-to-charge ratio A/q and proton number Z can

be deduced, thus particle identification of the RIs can be obtain sufficiently with high performance of the detector. The high accuracy $B\rho$ information of each ion can be used for mass correction in IMS (in-ring or on beam-line) and directly utilized in Bρ-TOF mass measurements.

3. **Low energy loss and small angular scattering of the heavy ions**

   For high high precision and accuracy mass measurements, ideal case is non-destructive detector. The energy loss and angular scattering should be as small as possible which means thinner foil to be kept at a minimum is needed with an acceptable efficiency.

4. **Large active area to cover large beam size if located at dispersive focus plane or in ring**

   For a dispersion focus at F6 with dispersion of $\sim 76\,mm/\%$ and momentum acceptance of $\pm 0.5\%$, lateral beam size should be at least 76 mm large. In the case of in the Rare-RI Ring, with adispersion of $\sim 70\,mm/\%$, momentum acceptance of $\pm 0.5\%$, together consideration of the Betatron oscillation, the lateral beam size will be very large. For the ring, an effective are of $\sim 190\,mm \times 42\,mm$ MCP with delay-line anode will be installed, and for the beam-line, an diameter of 120 mm MCP detector will be utilized.

5. **Large detection efficiency**

   The efficiency should be as good as possible.

6. **No magnetic field to disturb the isochronous magnetic field when using in the ring**

   R3, which consists of only dipole magnets, can not use detectors with magnetic field now because of the accumulation of the bending power of magnet for multi-turn circulation of fully striped heavy ions, so we choose the mirror electric field type detector for in-ring TOF-position measurements.

The electrostatic mirror-type detector equipped with high performance MCP described by detecting SEs (induced by the particles) with an angle of 90° towards an MCP detector to reconstruct the timing or position information of heavy ions in this work satisfy all the mentioned conditions above and will be a versatile instrument for mass measurements and beam diagnostic of exotic nuclei at RIBF in RIKEN.

This mirror type detector are widely used for many purposes, and one of them is normally to construct TOF system incorporating with multichannel-plate (MCP), which is very suitable for mass identification studies [119–122], including fission fragments, decay of superheavy nuclides (the nihonium, $_{113}Nh$ was discovered with the help of this type of timing

detector). The advantage of these detectors for timing is that they can be very fast, compact and offer optimum timing resolution.

The detector consists of one micro-channel plate (MCP), a position sensitive anode and a mirror electrostatic field for bending the secondary electrons ejected from a thin conversion foil. Emphasis on our diagnostic and measurement detector is that it is based on the detection of SEs resulting from the interaction of the beam with a thin detection foil (carbon/mylar coated with aluminum).

4.3 The electrostatic detector

To measure the masses of the heavy ions with high energy, the ions should not be guided or bended into MCP channels directly, and not cause large energy loss or wide angular dispersion in material during their single or circulating pass, the way to use SEs induced by the heavy projectiles in a thin foil is a good choice, in which the SEs are easy to be measured by MCP and used to reproduce the information of the heavy ions. A wide variety of applications of this kind of detector based on the detection of secondary products (electrons) resulting from the interaction of the heavy ion beam with a thin detection conversion foil (Carbon foil et. al) are utilized for heavy ion measurements.

As the timing stamp determination and position measurement in mass measurement experiment is very important, several successful MCP detectors have been developed in GSI (Germany), MSU (USA), IMP (China) for mass measurements and beam parameter monitor for increasing mass precision. $B\rho$-TOF Mass Measurements of very exotic nuclides for astrophysical calculations at the NSCL using MCP detector for $B\rho$ measurements, Isochronous mass measurements in storage rings in GSI and IMP using MCP detectors for timing determination are very successful examples for MCP detector application and for our present requirement, the first prototype Beam-Profile-Monitor-Time-Of-Flight BPM-TOF MCP detectors of mirror type have been designed and tested for future mass measurements experiment at R3 and on SHARAQ-OEDO-Injection beam-line.

4.3.1 Description of the electrostatic mirror detector

Two photos of the deigned BPM-TOF electrostatic mirror detector and the delay-line anode are shown in Fig. 4.1. The operating principle of the detector with an electrostatic mirror is based on emission of SEs induced by the detected particles from the conversion foil of the detector. When ions penetrate the conversion foil, SEs are produced and then accelerated by the accelerating grid wires. After the acceleration, SEs will enter the detector interior and

pass a field-free region and then are bent by the electrostatic mirror harp wires. Finally, the SEs are freely drifting to another field-free region and reach the MCP front surface and are detected by the coupled anode. These processes are schematically shown in Fig. 4.2, thus the detector can be divided into mainly three functional parts:

1. **SE generation and acceleration:** Front wall with a conversion foil with a potential U_2, an accelerating plate with grids at the potential U_2,

2. **SE reflection:** An electrostatic mirror plate at U_3 with grids as back wall to reflect SEs,

3. **SE field-free region and SE detection:** Bottom plate (U_1) with a circular or rectangular hole and two side walls (U_1) to keep equal potential inside and serve for fixing, chevron type MCP (front surface at U_1) with metal/delay-line/resistive anode (U_4) to detect SEs.

Besides, an additional aluminium plate (at U_1) with grids, to balance the force of the foil and to prevent foil deformation or breakage due to the electrostatic force, is placed in front of the foil and have the same potential as the accelerating grid U_1. The detector construction materials were selected with respect to both the high voltage requirements (dielectric strength) and vacuum conditions (material degassing) inside the detector. The conductive plates is made of aluminium and the all the grids are consist of gold-plated tungsten (W+Au) (40 mm in diameter). When the MCP is coupled with a timing anode, it will be used for timing determination, while if an two dimension position-sensitive delay-line anode is mounted below the output plate of MCP detector, it can be used for timing and position measurements at the same time. Accelerating grid wires made of gold-plated tungsten (W+Au) possesses a distance of 6 mm - 20 mm (10 or 12 mm is distance used for 6000 V acceleration high voltage supply) from conversion foil with 1 mm pitch, and wires (W+Au) for the inner and outer mirror grids are arranged with 1 or 3 mm pitch. Typical thicknesses of carbon foil at 10-60 $\mu g/cm^2$ (40 $\mu g/cm^2$ for 40 mm MCP in diameter and 60 $\mu g/cm^2$ for in-ring larger MCP) or mylar foil coated with aluminium at 1-2 μm is employed as the conversion foil for SEs emission. The BPM-TOF detector being developed in the framework of this thesis is equipped with a position sensitive Dual Delay Line (DDL) anode. The Micro-channel plate (MCP) and anode will be introduced in section 4.5 and 4.6.

If two such BPM-TOF detectors are placed alongside the primary beam axis, the timing of arrival and trajectories, including angle and positions, of all passing ions are able to be reconstructed event-by-event. Besides, the timing information of two detectors together with the known distance and the precisely detected positions of the RI can be used to deduce the velocity.

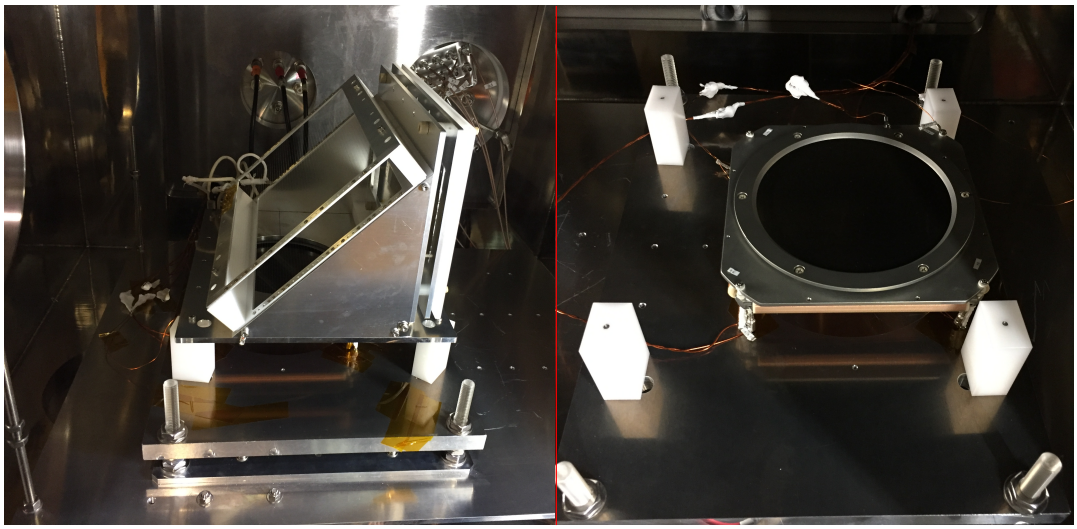

Fig. 4.1 Photographs of the electrostatic mirror detector (left) and MCPs in chevron stack with delay-line anode (right).

To achieve high time and spacial resolution for the electrostatic mirror detector with high efficiency, estimation of the SEs yield, careful calculations of the relationships between the motion of SEs inside the detector and potentials supplied for the plates of the detector are required.

4.3.2 Principles for timing and/or position sensitive MCP detector for heavy nuclei

Electrostatic Mirror position sensitive MCP detector

The electromagnetic force created by an electric field $\vec{E}$and a magnetic field $\vec{B}$ on a charged particle with charge q to bend and direct the SEs can be given as:

$$\vec{F} = m\frac{d^2\vec{r}}{dt^2} = q(\vec{E} + \frac{d\vec{r}}{dt}\vec{B}) \tag{4.1}$$

In order to perform the calculations of the electromagnetic motion of the SEs, the whole system, consisting of the conversion foil, accelerating grid, the mirror grids and the MCP detector is subdivided into three regions. The first one extends from the accelerating grid to the inner mirror front side, which is a field free part. The second one is between the inner and out mirror surfaces, where a homogeneous electric field is assumed. The third region is from the inner mirror front side to the MCP front which is assumed to be field free too. In the first order approximation, electrostatic field inside the triangular part shown in Fig. 4.2,

and the part in between the inner & out mirror of the detector as homogeneous. A simulated electrostatic field distribution of the detector is shown in FIg. 4.3. Three particles, starting from the different points and in the same direction but with different energies are traced inside the system as shown in Fig. 4.2.

The typical initial energy of "ture" SEs induced from foil the is several eV. The SEs are accelerated by an acceleration potential and then deflected towards the MCP by an electrostatic-mirror potential. Because the magnitudes of potentials at several keV are applied and the whole system can be described non-relativistically, we neglected the initial energy ($V_0\delta$) of SEs in following calculation. As is displayed in Fig. 4.2, the conversion foil is kept at the potential U_2 and the accelerating grid at the potential with $U_1 > U_2$. The resulting electric field strength between the potential girds of the detector accelerating plate (same as conversion foil U_2) and front wall of the triangular structure (accelerating grid U_1) which are located in the mutual distance x_{acc} is:

$$E_{acc} = \frac{U_1 - U_2}{x_{acc}} = \frac{U_{acc}}{x_{acc}} \tag{4.2}$$

Here, U_{acc} is the potential between the conversion foil and accelerating grid, and $U_{mir}$is the potential between the mirror grids.

$$\Delta V_f = U_1 - U_2 = U_{acc}, \quad \Delta V = U_1 - U_3 = U_{mir}, \quad \Delta V/\Delta V_f = \frac{U_{acc}}{U_{mir}}. \tag{4.3}$$

When a SE is knocked out which has initial velocity $v_0\delta$ from the conversion foil into the interior of the detector by the impact of an incoming ion, the electrostatic force $\vec{F}$ acts on this electron which is consequently accelerated by the acceleration force $\vec{a}_{acc}$ towards the accelerating grid:

$$\vec{F} = -e\vec{E}_{acc} = m_e\vec{a}_{acc} \quad \Rightarrow \quad \vec{a}_{acc} = -\frac{e}{m_e}\vec{E}_{acc}. \tag{4.4}$$

The time spent inside the interior of the conversion foil and accelerating equipotential grid is t_{acc}, during which electron gains the velocity $\vec{v}_{acc}$ in the direction opposite to the electric field. When the electron initial velocity $v_0\delta$ is neglected, $t_{acc}$and $\vec{v}_{acc}$:

$$t_{acc} = \sqrt{\frac{2x_{acc}}{|a_{acc}|}} = \sqrt{\frac{2x_{acc}m_e}{eE_{acc}}}, \tag{4.5}$$

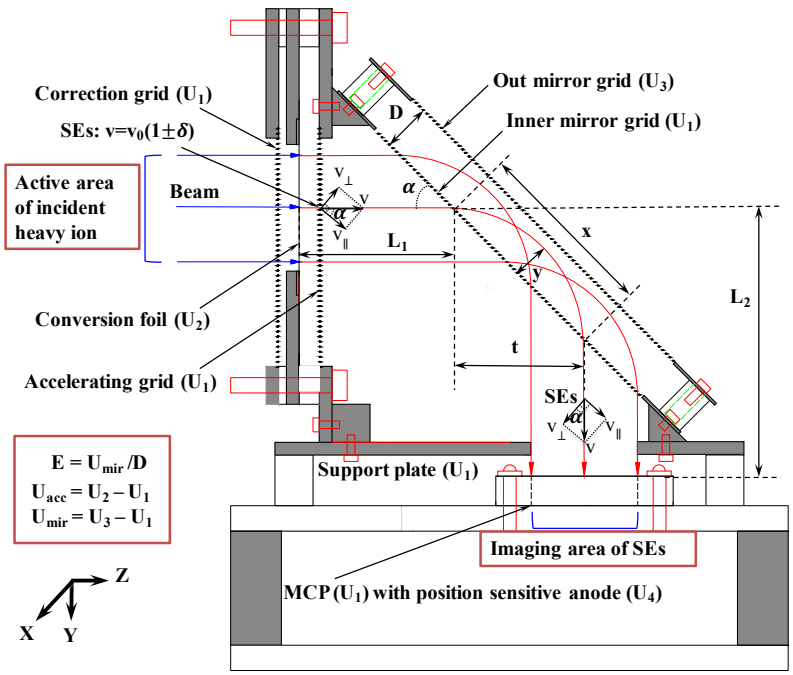

Fig. 4.2 Structure of the electrostatic mirror detector and description of the parameters of the detector.

$$v_{acc} = |a_{acc}|t_{acc} = \sqrt{\frac{2x_{acc}eE_{acc}}{m_e}}. \tag{4.6}$$

When entering the field free region, the accelerated electron has the total velocity $\vec{v} \approx v_{acc} = v_0\,(v_0\delta \ll v_0)$ and the total kinetic energy approximately $eU_{acc} = e\Delta V_f$. In order to describe the electron path through the electrostatic mirrors, the velocity $\vec{v}$ is divided into two components, one perpendicular to the mirror plane$\vec{v}_\perp$ and another parallel with the mirror plane $\vec{v}_\parallel$:

$$v_\parallel = v\sin\alpha \approx v_{acc}\sin\alpha = v_0\sin\alpha, \qquad v_\perp = v\cos\alpha \approx v_{acc}\cos\alpha = v_0\cos\alpha. \tag{4.7}$$

When the electron enters the inner part of the mirrors, the acceleration $\vec{a_{mir}}$ in the direction opposite to the mirror electric field $\vec{E}_{mir}$ $(U_1 > U_3)$ acts on the electron:

$$E_{mir} = \frac{U_1 - U_3}{x_{acc}} = \frac{U_{mir}}{x_{mir}} \quad \Rightarrow \quad \vec{a}_{mir} = -\frac{e}{m_e}\vec{E}_{mir} = -\frac{e}{m_e}\frac{\vec{U}_{mir}}{x_{mir}}. \tag{4.8}$$

At a certain time t_{mir} when the velocity component $v_{\|}$ is decelerated to zero and the electron reaches the maximal depth y inside the mirrors vertically from the entrance mirror grid plane:

$$v_{\perp} - |a_{mir}|t_{mir} = 0 = \frac{v_{\perp} m_e}{eE_{mir}} \tag{4.9}$$

$$y = v_{\perp} t_{mir} - \frac{1}{2}|a_{mir}|t_{mir}^2 \quad \Rightarrow \quad y = \cos\alpha^2 x_{mir}\frac{U_{acc}}{U_{mir}}. \tag{4.10}$$

After the $v_{\|}$ went zero, the electron is accelerated by acceleration $\vec{a}_{mirr}$ in the direction opposite to the electric field $\vec{E}_{mir}$ again. When escaping the mirror (with a distance of $D = x_{mir}$), the electron gains the velocity $v_{\perp}$ and continues freely drifting towards the MCP detector through the field free region. x, y are parallel and vertical path length of SEs in the mirror parts, and t is the shift of SEs along the Z direction inside the mirror:

$$x = 2v_{\|}t_{mir} = 2x_{mir}\sin(2\alpha)\frac{U_{acc}}{U_{mir}} = 2D\sin(2\alpha)\Delta V_f/\Delta V \tag{4.11}$$

$$t = x\sin\alpha = 2x_{mir}\sin\alpha\sin(2\alpha)\frac{U_{acc}}{U_{mir}} = 2x_{mir}\sin\alpha\sin(2\alpha)\Delta V_f/\Delta V \tag{4.12}$$

The most convenient way for the design is to set $\alpha = 45^{\circ}$. When substituted for α with 45°, the following relationships for x, y and t are obtained:

$$x = 2x_{mir}\frac{U_{acc}}{U_{mir}} = 2D\Delta V_f/\Delta V \tag{4.13}$$

$$y = \frac{x_{mir}}{2}\frac{U_{acc}}{U_{mir}} = \frac{D}{2}\Delta V_f/\Delta V \tag{4.14}$$

$$t = \sqrt{2}x_{mir}\frac{U_{acc}}{U_{mir}} = \sqrt{2}D\Delta V_f/\Delta V \tag{4.15}$$

Using foils instead of a grids would create a better homogeneous field (if the side effects are neglected), but due to the energy loss in the foils we can not uses too thick foils in storage ring. Hence a solution to use wires or meshes has to be chosen. An additional foil in front of the conversion foil is installed to compensate for the electrostatic forces in Fig. 4.2.

A disadvantage of this solution is the inhomogeneous field close to the wires (grids). As a result, the electrons will not have the same TOF from foil to MCP over the whole active area, assuming they are all emitted exactly perpendicular to the conversion foil. For an ideal homogeneous field without material where SE can scatter, the distances travelled are the same, whether the SEs are emitted in a corner or in the middle of the conversion foil. Since if the arrangement of the distance of the wires is small enough, the field disturbances

introduced by the wires could be small and nearly constant. The effect left influencing the

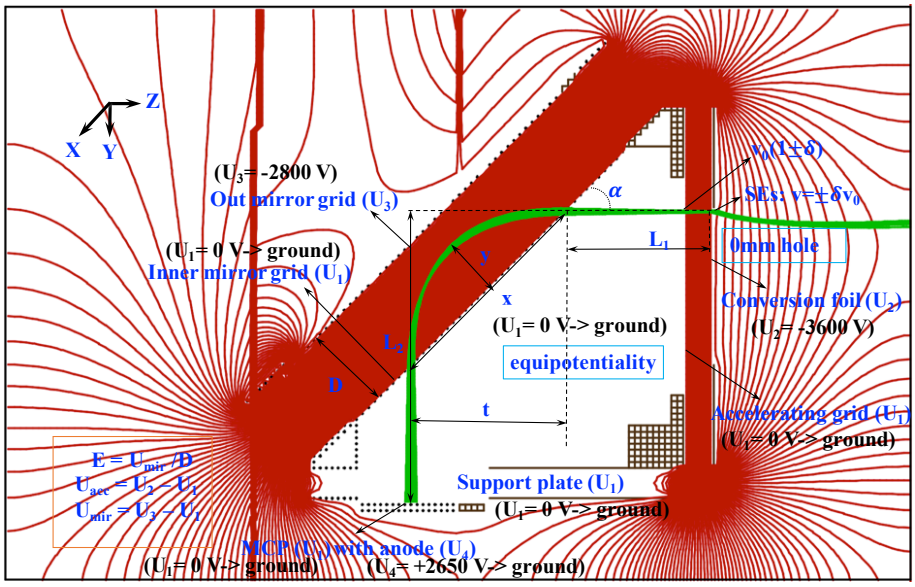

Fig. 4.3 Simulation of the electrostatic field for the mirror detector by SIMION [133] and schematic flight paths of SE emitting from one point of the foil at a certain energy and angular distribution. The high voltage supplies in the simulation are illustrated in the figure for each plate.

TOF of the SEs would be the initial energy and angular distribution of the SEs. This is an intrinsic problem and cannot be overcome, but can be minimized by choosing a high accelerating field gradient to direct and extract the SEs towards the mirror grids (it is shown in the Fig. 4.3 by simulation and in experiment, the dependence of the position and timing resolution on electric field are both tested as shown in later section). Independent of this problem, there is one superposing effect influencing the SEs trajectories and TOF either one considers an ideal, material free field or a wire induced field.

As indicated in the simulation shown in Fig. 4.3 , even if a set of SE is emitted at precisely the same spot on the conversion foil and neglecting their energy distribution, they would enter the electrostatic mirror at different spots and thus have a varying flight path with varying TOF.Early attempts to describe the flight path consider the field and the SEs initial energy to be homogeneous and the angular dispersion to be negligible, all in first order. Assuming this idealization and a deflection of the SE by 90 degree, the parabola inside the reflecting mirror can be described by means of the foil and mirror potential gradients, ΔU_{acc} and ΔU_{mir}.

To achieve high timing resolution, an isochronous condition [132] is chosen. The total time of flight consists of 3 parts: the foil to the inner mirror wires, bending path between the inner and outer mirror wires, free drift region from the inner mirror wires to the MCP. The

exact solution of the equations of motion for the three regions gives the following relation for the total TOF of the probed particles when the initial velocity of SEs is considered to be $v_0\delta$:

$$T = T_0 + \left(\mp \frac{L_1 + L_2 - D\sqrt{2}\Delta V_f/\Delta V}{v_0} \pm \frac{2m_e v_0 D \sin\alpha}{e\Delta V} \right)\delta$$
$$T_0 + \left(\mp \frac{L_1 + L_2 - x_{mir}\sqrt{2}\frac{U_{mirr}}{U_{acc}}}{v_0} \pm \frac{2m_e v_0 D \sin\theta}{eU_{acc}} \right)\delta, \tag{4.16}$$

Where L_1 and L_2, as shown in schematic view Fig. 4.2 and simulation Fig. 4.3, corresponds to length from the conversion foil to the incident point of SEs at the inner mirror plate along Z direction, the length between the incident point of SEs at the inner mirror plate with the MCP front surface along Y direction. To let the second term of the right part of the upper equation to be zero, we get the so-called isochronous condition:

$$D/(L_1 + L_2) = 0.236(\Delta V/\Delta V_f) = 0.236\frac{U_{mir}}{U_{acc}} \tag{4.17}$$

The relation above enables us to optimize the foil acceleration and mirror deflection potentials such that the SEs reach the MCP isochronously. From the Eq. (4.15) and the condition $D \geq y$, the electrostatic mirror will reflect the SEs to the MCP front only if the following condition is satisfied:

$$\frac{U_{mir}}{U_{acc}} = \Delta V/\Delta V_f \geq 0.5 \tag{4.18}$$

From experimental tests and simulation of this type of detector, both results show that at higher accelerating voltages the mirror become transparent for the SEs, which demonstrate a good agreement with the above equation.

To have a good understanding of the initial condition of the SEs induced from the foils, the theory of ion induced SEs is discussed in the following section in detail.

4.4 Conversion foils and grid

When it comes to the conversion foil, there are several considerations before we choose it, like the SEs yields/material, thickness, energy loss for heavy ions in the foil depending on the case of in-ring or on beam line. The energy loss in the conversion foil is proportional to the square of the projectile charge, which corresponds to secondary electrons yields, thus the amplitude information of the signal of MCP can be used as a tool to extract the Z numbers of the projectile stored in R3. As the thickness have large influence on the energy loss of

the circulating ions in storage rings which circulate about 2000 turns, it should be as thin as possible to keep every turn the same revolution time for each ion for precise mass measurements. Besides, when utilizing the detector on the beam-line, to reconstruct the velocity information with uncertainty of less than 10^{-4}, the foil should be thin enough. The thickness also is related to the transmission efficiency of the circulating ions. we must make a fully consideration of this two opposite effects on the thickness of the foil.

Two kind of conversion foils are chosen for the detector (carbon foil for in-ring multi-turn and Aluminium Coating Mylar for beam-line one-pass) as listed below:

Aluminium Coating Mylar It is a compound of 0.2794 mg/cm^2 (2.0 μm) thick Mylar with a 0.027 mg/cm^2 (0.1 μm) aluminium coating. It combines nearly the stability of the polycarbonate backing with less material obstructing the ion beam at a relatively and absolutely larger amount of SEs emitting metal coating. The Mylar was evaporated the aluminium coating and then was glued on a frame. The size of the aluminium coated Mylar can be large enough to cover the whole area of the commercial MCPs (120 mm in diameter or 190 $mm \times 42$ mm).

Self-sustaining carbon The advantage of self-sustaining carbon is that a very small thickness can be achieved and the whole material accounts for the production of SEs without the need of a backing material, thus energy loss and angular scattering of ion beam obstructed the material can be decreased to an minimum. The only drawback is that its stability decreasing dramatically with decreasing thickness and/or increasing size, making the chance of its breaking during evaporation or mounting tremendous, while being very sensitive to vibrations or electrostatic force as well. The largest size of pure, self sustaining carbon foil which can be made till now in RIKEN is $130mm \times 50mm$, their density is $\sim$ 40 $\mu g/cm^2$ (0.178μm). The thickness of ordered foil pieces is $40-60$ cm^2(0.178 $-$ 0.266 μm), the thickness of the one contemporarily used is 40 $\mu g/cm^2$(100 $mm \times 50$ mm) for the timing MCP (40 mm in diameter) detector with a timing anode and 60 $\mu g/cm^2$ (130 mm $\times$ 50 mm). The foils are composed of the natural isotopic carbon with minor impurities. This feature and related measurement of a SE yield and a SE energy spectrum was studied in [135] with carbon foils serving as the SE emitters. Normally, from tens to hundreds of SEs with kinetic energies of $\sim 2eV\ of\ \sim 85\%$ for "ture electrons" and kinetic energies from tens of eV to several units of keV for other components are ejected from the foil in both the forward and backward directions.

The carbon foil has thickness approximately 178-266 nm corresponding to the $40-60$ $\mu g/cm^2$, with energy loss about several hundred (440-660) keV for a secondary

beam ($170 MeV/\mu\ ^{100}Sn^{50+}$ as example) and relative energy loss of the order of $\sim 10^{-5}$. The carbon foil is fixed on a 1 mm thick aluminum frame with a central square hole by a so-called water floating method.

Wiring grid The mirror detector accommodate 3 electrostatic wires as shown in Fig. 4.1 and they are designed to create effective and sufficiently homogeneous equipotential electrostatic-field, and also as transparent as possible to minimally hinder the ions when passing through them. In addition to have a large open area ratio, the wiring grids should have a certain physical strength. Due to an electric field gradient of accelerating $\sim$ 0.4-0.8 kV/mm when adding 3-6 kV at a distance of 8 mm, the wiring needs to be mounted at a high physical tension, in order to avoid a possible curvature. Furthermore, with respect to the large area of the reflecting mirror, the grids should withstand this tension without losing their stiffness over time, thus time by time maintenance or change of the wires is needed to keep high performance of the detector. The density of gold (19.3 g/cm^3) and tungsten (19.25 g/cm^3) are very similar meaning plating tungsten will not significantly change the density versus unplated wire. The grid we use is a gold-plated tungsten wire with a diameter of $40\mu m$. This type of wire was selected due to an extreme strength of tungsten which results in possibility of utilizing the wire so thin. The gold cover layer ensures absence of burrs which can occur during the wire fabrication when the HV is applied to them. The distance between two neighbouring wires, regularly along all frames, is 1.0 mm or 3.0 mm. The geometrical transparency of the accelerating gird is 96% with $1mm$ pitch, and for the mirror grid as tilted 45° to the beam direction, transparency is 94.34% and 98.11% with 1 mm or 3 mm pitch, respectively.

4.5 Micro-channel plate (MCP)

4.5.1 Introduction of MCP

Micro-channel plate (MCP) of microscopic small bundled electron multiplier channels (several million) which are made of leaded-glass is a two-dimensional sensor that detects electrons, ions, vacuum UV rays, X-rays and gamma rays in a vacuum system, and amplifies the detected signals. Channel diameters for MCPs typically range from approximately $4 - 100\,\mu m$ and $0.20\,mm$ to $1.5\,mm$ in length fused together and sliced in the shape of a thin plate. The leaded-glass channels are often treated to enhance secondary electron emission and made to be semiconducting [141, 142]. MCPs also range in plate shape and size in various dimensions for circular plates and can also be fabricated into rectangular plates.

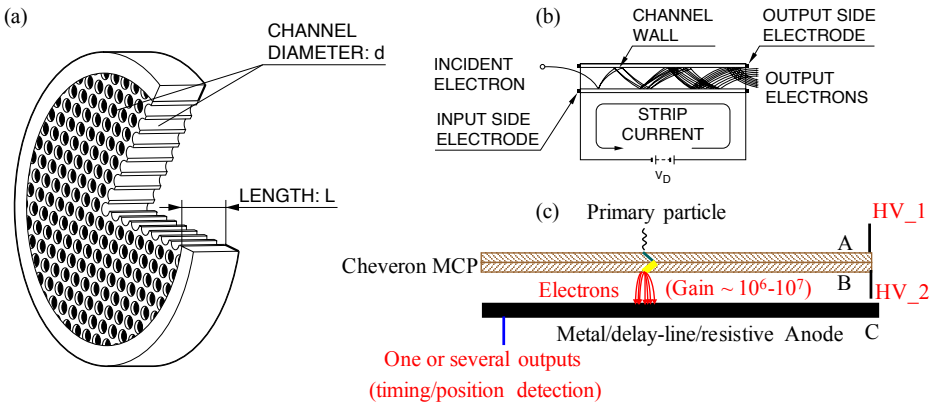

Fig. 4.4 (a). Schematic structure of MCP and indication of avalanche principle of the incident particles of single channel. (b) and chevron assembly (c). Principle of electrons multiplication in Chevron MCPs stack. Figure (a) and (b) are from [142].

Since MCPs are highly sensitive to electrons and capable of two-dimensional electron multiplication, they have mainly been used as electron multipliers in image intensifiers. As an extremely useful tool for scientific applications, MCPs are also widely used in many types of analytical equipment such as for “mass spectroscopy”, “surface analysis” and “semiconductor inspection”.

4.5.2 MCP Operating principle and structure

As shown in the Fig. 4.4, a potential gradient is established along the channel when the voltage V_D (about 1000 V) is applied between the MCP upper and lower surfaces, which are metallized electrodes. The inner surfaces of the micro-channels are semiconducting. A weak current through the channel surface produces a homogeneous electrical field inside the channel. Multiple secondary electrons are emitted when an electron enters a channel from the input side and strikes its inner wall (under vacuum). These secondary electrons are accelerated by the potential gradient to travel along their parabolic trajectories which are determined by their initial velocities. They then strike the opposite wall in the channel causing further secondary electrons to be emitted. The electrons in this way travel towards the rear of the channel while striking the inner wall of the channel repeatedly. Thus an electron avalanche will occur in the channel and finally emerge from the rear of the plate.

There are a variety of shapes and sizes of MCPs, which allowing users to choose an optimum type. The MCP is roughly categorized by shape into circular and rectangular types.

If two or more MCPs are placed in series, a single electron can generate a pulse of $10^7 - 10^9$ electrons at the output. The gains of multiple plates when stacked is not multiplicative due to space charge effects with coulomb repulsion of a large number of electrons in close proximity at the rear of the MCP.

MCP channels need to be tilted at a bias angle (typically $5^\circ - 15^\circ$), which is chosen by taking a full consideration of the following factors: radiation detection efficiency, preventing effectiveness of incident particles from passing through the channels, ion trap efficiency and the spatial resolution when two or more MCPs are stacked. The Open Area Ratio (OAR) is the ratio of the total open area to the entire effective area of an MCP. The OAR is typically about 60%, which is preferably as large as possible to allow primary electrons to enter each channel more effectively. The electrodes on the input and output surfaces of an MCP are processed to have a surface resistance of $100\,\Omega\, to\, 200\,\Omega$. The thickness of an MCP is nearly equal to length of the channels. The ratio of channel length (L) to channel diameter (d) is indicated by $\alpha = L/d$.

The Chevron configuration MCPs utilized in this work are made of two parallel plates. The upper and lower surfaces of these plates are metalized electrodes to which a voltage of typically $\sim 2000 - 2500\,V$ is applied. Good response time characteristics of rise time and fall time can be achieved by reducing the size of the MCP while keep the gain of an MCP determined by $\alpha\,(= L/d)$. Small channel diameter and thickness of the chevron MCP, which corresponds to the small electron transit distance are desired for excellent timing performance.

Since the individual channels confine the pulse, the spatial pattern of electron pulses at the rear of the plate preserves the image-pattern of particles incident on the front surface. The output signals can be typically collected in several ways, including metal or multi-metal anodes, resistive anodes (one- or two- dimensional), wedge and strip anodes, delay-line anodes, or on a phosphor screen deposited on a fiberoptic or other substrate. The spatial resolution of the MCP depends on the diameter and pitch of channels arrayed in two dimensions. When the output from the MCP is observed on a delay-line anode, the spatial resolution also depends on the MCP output electrode penetration depth into the channels, distance between the MCP and the delay-line, the accelerating voltage, and the propagation in the delay-lines. The tested performance of the MCPs are demonstrated in the section 4.8.

Specifications of the MCPs together with cautions of storage, handling and operation of MCPs (from PHOTONIS [143]) are listed in Appendix B.

4.6 Anodes for position sensitive MCP

MCPs without position measurements are widely utilized in a broad range of applications as for their excellent timing performance, a fast response time and a small time jitter, the extra use of position sensitivity adds importance to the detector's usefulness. Due to their timing characters, MCPs, with or without position sensitivity make an excellent choice in time-of-flight measurements. Simultaneous measurement of a particle's position together with its TOF allows us better determination of the track information of an ion. If the precise spatial resolution does not decrease the detectors timing resolution, the position character is particularly useful. Position sensitive MCPs has anode that collect the electrons leaving the MCPs. Individual channels of MCPs confine the pulse so that the spatial pattern of the pulse exiting the back of the MCP creates the same image as the incident particle on the front of the MCP. Determination of the position of the beam on an ion-by-ion basis, a position sensitive anode is indispensable. The function of the anode which mounted behind the MCPs is to code the incoming charges in a certain way, which makes it possible to estimate the position of the original ions.There are variations of techniques and various methods that have been utilized in creating position sensitive MCPs in previous work around the world. There is a comparison of different anodes as listed in Fig. 4.5, and a few of the most common methods which have been widely used are described as following.

4.6.1 Delay-Line Anodes (DL)

Delay-line anodes make use of the principle of an electronic RC circuitry which is able to slow down the propagation of pulses. The propagation time of electronic signals is reduced, so that it can be measured even at small distances. Thus the distance covered by a signal may be estimated from the traveling time of that signal. If a signal is injected at a certain position of a delay line, the difference in arrival times at both ends of this line can be used to estimate the exact position of the injection of this signal. The precision in the position determination depends only on the characteristic propagation time of the signal and on the precision of the time measurement, but not on the length of the line. A critical point is that both delay lines should have nearly the same characteristic propagation time. Fig. 4.6 shows the layout of several different types of delay-line anodes. The timing information of this type of detector can be acquired from the MCP front or back signal separately from the anode signal.

The most common and easy read-out delay-line anodes are helical (multi-planar pattern) [154–157] and serpentine (a planar zig-zag pattern) [158]. The Double Delay Line (DDL) and Cross Delay Line (XDL) are delay-line anode patterns where the charges col-

	Vernier Anode	Intensified CCD	Intensified APS	Delay line	Parallel strips – interpolated position	Discrete pixel array	Medipix2
Image Format	30×20 mm (flexible)	25 mm Ø	25 mm Ø	Up to 100×100 mm	Currently 45×45 mm (Cross-Strip)	32×32	256×256
Pixel Format (resolution elements)	3000×2000	2048×2048	>2k×2k	3000×3000	Currently 5k×5k (up to 10k×10k - Cross-Strip)	32×32	256×256
Number of channels	9	256×256 (CCD pixels)	256×256 (APS pixels)	4	128/axis (2D parallel strip) 2/mm/axis (Cross-strip)	1024	64k
Readout Resolution (FWHM)	10 µm	<10 µm	MCP limited	30 µm	MCP limited	0.5 mm	55 µm
Dynamic range							
Global	1×10^5	2×10^5	400 kHz >1MHz (goal)	> 1MHz	>10MHz (2D parallel strip)	MCP limited	266 µs / frame
Local	MCP limited	CCD frame rate	MCP limited	kHZ/pixel	MCP limited	>10 MHz/channel	200 kHz / pixel
Deadtime	10 µs	CCD frame rate	2 µs	400 ns (10 ns inter-event) (Hexanode 0 ns inter-event)	10 ns (2D parallel strip – NINO ASIC)	10 ns	500 ns
Time resolution	~ ns	CCD frame rate limited	2 µs	<100 ps	~10-20 ps (using NINO ASIC)	< 10 ps	266 µs
Digital resolution	12 bit	-	-	13 bit	12 bit (Cross-Strip)	n/a	13 bit counter
MCP gain	1.5×10^7	5×10^5	5×10^5	10^7	$\sim5\times10^5$ – 2D parallel strip 5×10^6 - Cross-strip	5×10^5	$\sim10^4$
Comments	High MCP gain 4 µm electronic noise limited. Flexible format	Can suffer from cyclic nonlinearity due to centroiding errors	Can suffer from cyclic nonlinearity due to centroiding errors	Low channel count but requires high gain, limited parallel capability	High channel count for realistic formats, multiple simultaneous event capability	Event rate MCP limited, crosstalk →double counting, overcome with intelligent readout	Single MCP, low unsaturated gain, thresholding inaccuracies

Fig. 4.5 Comparison of performance and characters for different kinds of readout for position encoding anodes, from [144].

lected on strips are tapped into the delay lines, which can be serpentine or helical. The DDL anode uses a charge division approach to measure the 2 dimensional position.

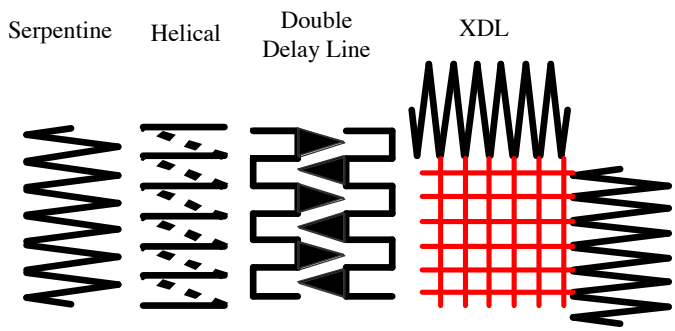

Fig. 4.6 List of several different types of delay-line anodes. Adopted from [154].

FIG. 4.7 shows the schematic view of the theory of operation for the serpentine delay line readout, showing two independent delay lines lying in different planes. Each delay line

is a serpentine, and the two single delay lines are placed orthogonal on each other. The read-out principle is similar as described before, and two or four channels are set as read out. In each plane, a portion of the electron cloud from the MCP produces two voltage pulses traveling toward the ends of that delay line. The time difference between the pulses codes the one dimension position. The perpendicular position is obtained from the time difference of clouds produced by MCP electrons collected on the other delay line.

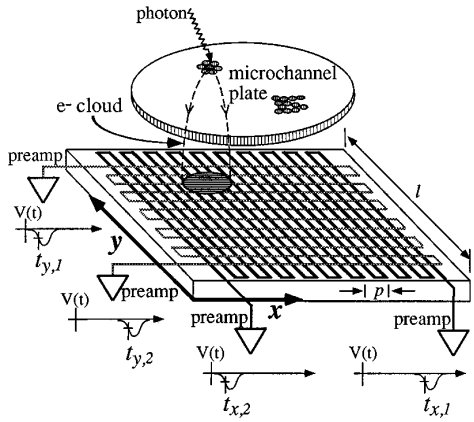

Fig. 4.7 Schematic of the theory of operation for the serpentine delay-line readout, showing two independent delay lines lying in different planes. Each delay line is a serpentine, and the two single delay lines are placed orthogonal on each other. Figure from [158].

For the helical delay line anode shown in FIG. 4.6, a wire is usually wound from one corner to the other one alongside a metal plate which is fixed in isolating braces at the corners, both for the X axis and the Y axis. The signal's propagation time through the wire can be used to determine the position of the induced signal by measuring the time difference between the arrival of the signal at the two ends of the delay line. Two orthogonal wire planes are needed to achieve position information for a two-dimensional detector.

Because of the effect of capacitive coupling of the parallel wires which might lead to an induction of false signals, an additional reference delay-line per axis, wound midway between the turns of the existing delay-line are utilized to avoid this effect. Fig. 4.8 schematically shows the dual delay-line anode (DDL). A certain gap between the MCP and the DL allows for the charge cloud to spread over several coils of each DL and thus interpolating between them. In this approach, a more precise centroid for each axis can be obtained [159, 160]. In comparison to the cross-strip method (CS) with discrete anode strips in which the strip pitch impacts the position resolution, this characteristic is an advantage. Typical propagation time for helical dual delay-line in a desired size is in a order of 100 ns, which would result in a roughly maximum possible rate of 10 MHz. In principle, the position resolution limit for an MCP is the channel center-to-center distance. The typical position resolution of this type

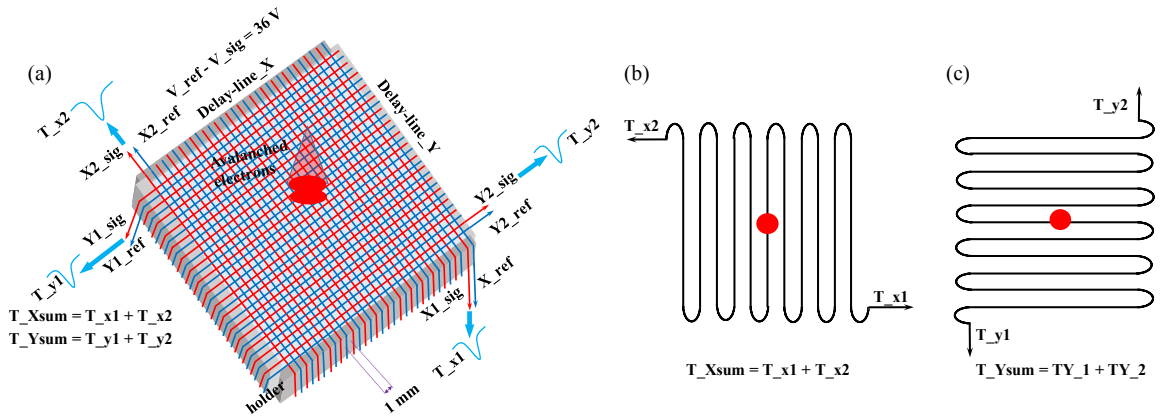

Fig. 4.8 Schematic view of the theory of operation for helical delay-line anode (a), and the total delay in the line for X (b) and Y (c) direction. Each delay line is helical and the two single delay lines are placed orthogonal on each other. The read-out principle to code the position is similar to serpentine delay-line readout. To determine the position in one dimension, the arrival of the Signal at the two ends of the delay line T_{x1} *and* T_{x2} are taken with Reference to the signal pulse on the MCP or other trigger signal. The position of the charge centroid is proportional to the time difference of $T_{x1} - T_{x2}$, while the sum of $T_{x1} + T_{x2}$ is a known constant for the total delay in the line. The position in the orthogonal direction can be determined in the same approach by $T_{y1} - T_{y2}$. The two timing sums, one for each dimension, gives a check to ensure a valid position signal.

of anode is about 100 μm and the timing resolution can reach less than 100 ps. This design has been developed further to hexagonal, helical dual delay lines being suitable for multi-hit read out [156].

Since the electronics to process the time information are faster than charge integrating electronics, a delay-line anode detector can handle higher rates and even multi-hits as compared to a charge integrating approach. Development of fast multi-hit time-to-digital converters (TDC) in particular has enabled helical delay-line MCPs to provide multi-hit information. The two blocks diagram of readout electronics both show their favor to use the MCP signal directly from the MCP surface. As dynamic equilibrium and saturation causes the pulse height distribution of the MCP , which plots the number of counts as a function of the output pulse height. We can use the signal amplitude to identify nuclei with different proton numbers, for which the square are proportional to the SEs yields induced from the foil. On the other hand, MCPs have a fast response time and a small time jitter which provide a sub-nanosecond or better timing signal. Advantages of the excellent timing characters of the MCP are taken for our design and the fast timing information can also act as a trigger or start of the TDC (or TAC), which was used for the offline test in this work.

4.6.2 Selection of anode

Beam-line/in-ring TOF and position measurements in RIBF require a large area position sensitive detector with good position resolution and fast timing signals. In most applications the delay-line anode is superior to the wedge and strip detector and other electronics consuming detectors. The biggest advantage is very fast, simple readout allowing a count rate of better than 1 MHz. Another advantage is that large area delay-line anodes can be made without any loss of position resolution whereas the wedge and strip detector results in proportional reduction of the resolution to the size of the anodes. Thus, chevron configuration MCPs with a delay-line anode are chosen for our BPM-TOF spectrometer. The typical MCPs we employ have an active diameter of 120 mm in round shape and 190 mm x 42 mm in rectangular shape as shown in Appendix B. The detail of the delay-line and its performance are discussed in section 4.8.

4.7 Simulation for the electrostaic detector

To optimize the design and performance of the electrostatic mirror detector, a simulation of the transport of SEs induced from the conversion foil is done by SIMION software package [133]. Results of simulation can be very different due to different initial SEs conditions and simulation method. The initial kinetic energy and SEs emittion angle distribution utilized in this work are shown in the Fig. 4.9. SEs energies were assigned to a range of 0-20 eV with a mean value ~2.0 eV which corresponds to the "ture" electrons emitted from the foil with a percentage of 85 %. The angles lie between -90 and +90 degrees (corresponds to -180 and 0 degrees in Fig. 4.9) relative to the foil surface and the ions mainly emitting from forward side of the foil are guided to the surface of MCP. Each parameter of the uniformly distributed ions was generated using a random generator in SIMION. These distributions are shown in Fig. 4.9. The structures of the mirror type detectors in SIMION are shown in Fig. 4.10 and two different shapes of MCPs are included as shown in the figure.

The real electric field usually contains disturbances compared to the perfect designed electric field. Because of that, the time resolution and spatial focusing can be different from that of the calculated ideal case. However, the analytical solution (simulation) can be useful to define the direction of the investigations

In order to determine the timing and position resolution, SEs are assigned to groups and start from the same point of the foil with the initial energy and angle distributions demonstrated in Fig. 4.9. Different High voltage (HV) supplies are added to the potential plates or grids and varied during the simulation for different settings as shown in Fig. 4.3, 4.2 and 4.11. The time-of-flight distribution, and 2-dimension position distributions of initial SEs for each

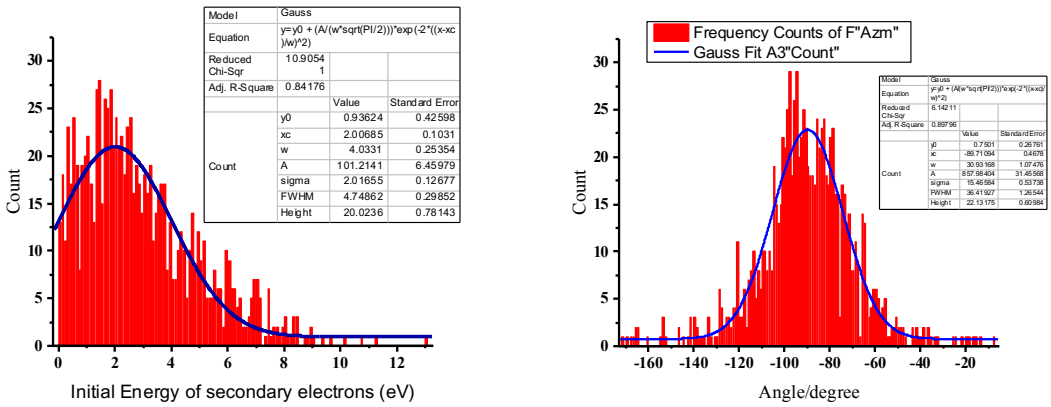

(a) Initial condition of the kinetic energy of the SEs

(b) Initial condition of the emitting angle distribution of the SEs.

Fig. 4.9 Initial condition of the SEs for simulation. In the simulations, 1000 ion trajectories were calculated and each ion has its own initial parameters. The values of the SE energy and emission angle were created using a random generator and a uniform distribution of ions.

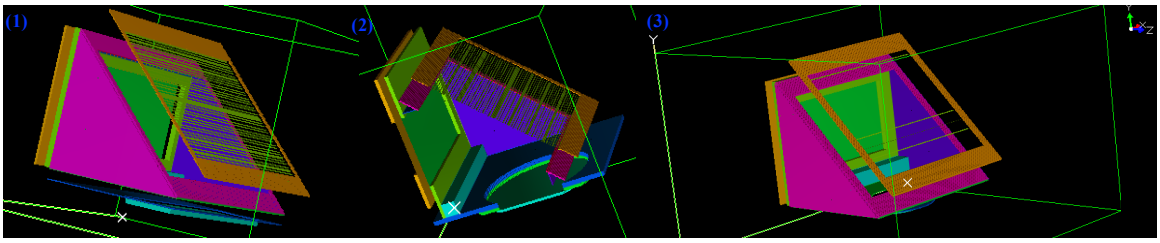

Fig. 4.10 Geometry setup of the mirror type detector in SIMION for secondary electron transportation to determine timing and position resolutions. In (1), (2) and (3), the utilized chevron MCPs are rectangular type with size of 42 mm x 190 mm, circle type of 120 mm in diameter, for position and timing determination and circle type of 40 mm in diameter dedicated for timing measurement respectively.

group from the foil reflected onto the MCP are fit by a Gaussian distribution. The peak width is characterized by the Full Width at Half of Maximum (FWHM) and it is defined as 2.355δ, where δ is the uncertainty parameter of Gaussian distribution.

During the simulation, the acceleration and/or reflection potentials are varied in different values and the MCP potential together with the inner triangular structure are kept at ground/same potential thus to define the field free drift region demonstrated in Fig. 4.3. In this way, SIMION is used to investigate the timing and position resolutions of SEs imaging by the detector depending on the HV settings. Figure 4.12 indicates that the timing and position resolution results from one set of simulation as indicated in Fig. 4.3.

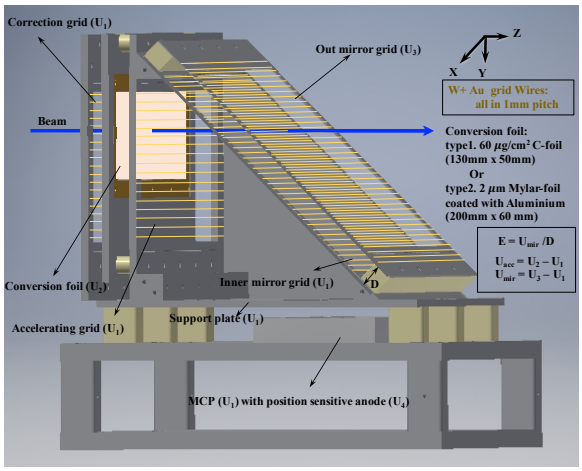

(a) 3D CAD picture of the position-sensitive and timing MCP detector

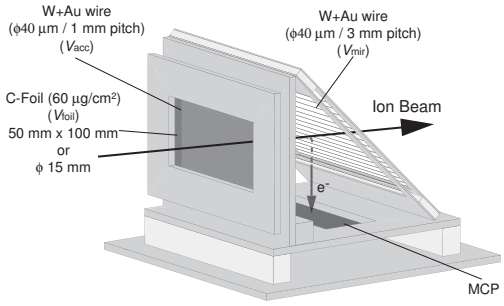

(b) 3D CAD picture of the timing MCP detector

Fig. 4.11 3D CAD pictures of the structures for the BPM-TOF detector with delay line anode and dedicated timing detector with timing anode.

According to the Eq. 4.17, it turns out to be possible to find out special conditions for the geometry and the voltages for the detector that will minimize the influence of the initial velocity spread of the SEs on the timing.

Table 4.1 and Table 4.2 show several isochronous conditions for two different sizes of detectors, for which the distance between the mirror grids is set at different values and the $\frac{U_{mir}}{U_{acc}}$ fulfills the condition $\frac{d}{(L1+L2)} = 0.236\frac{U_{mir}}{U_{acc}}$.

Table 4.1 Distance of the mirror grids for isochronous condition and compared to the original 8mm design (timing detector coupled to 40 mm diameter MCPs and metal anode with a size of 120 mm x 120 mm for the triangular structure). The detector structure is shown in Fig. 4.11 and Fig. 4.10.

d/(L1+L2)	$\frac{U_{mir}}{U_{acc}}$	condition
20/145	0.584	isochronous
24/145	0.701	isochronous
28/145	0.818	isochronous
32/145	0.934	isochronous
8/145		nonisochronous

The isochronous relation $D/(L_1 + L_2) = 0.236(\Delta V/\Delta V_f) = 0.236\frac{U_{mir}}{U_{acc}}$ is fulfilled in the simulations with 4 different D (X_{acc}) values as shown in Fig. 4.13a and listed in table 4.1. One isochronous structure ($D = 28$ mm) is compared with the existing mirror detector, for which D have a value of 8 mm. If $D = 8mm$ and we need to set $\frac{U_{mir}}{U_{acc}}$ to be 0.236, which

Table 4.2 Distance change of the mirror grids for isochronous condition for position-sensitive timing detector mounted with MCPs possessing a size 120 mm in diameter or 190 mm x 42 mm in rectangular shape. The mirror grid is 2 mm in thickness and made of aluminium. The size of the triangular structure is 140 mm x 140 mm. The structure is shown in Fig. 4.3, Fig. 4.1, Fig. 4.10 and Fig. 4.11.

(Ignore thickness of mirror plate)			(Consider thickness of mirror plate)		
d/(L1+L2)	$\frac{U_{mir}}{U_{acc}}$	condition	d/(L1+L2)	$\frac{U_{mir}}{U_{acc}}$	condition
20/152.5	0.556	isochronous	22/152.5	0.611	isochronous
24/152.5	0.667	isochronous	26/152.5	0.722	isochronous
28/152.5	0.778	isochronous	30/152.5	0.834	isochronous
32/152.5	0.889	isochronous	34/152.5	0.945	isochronous

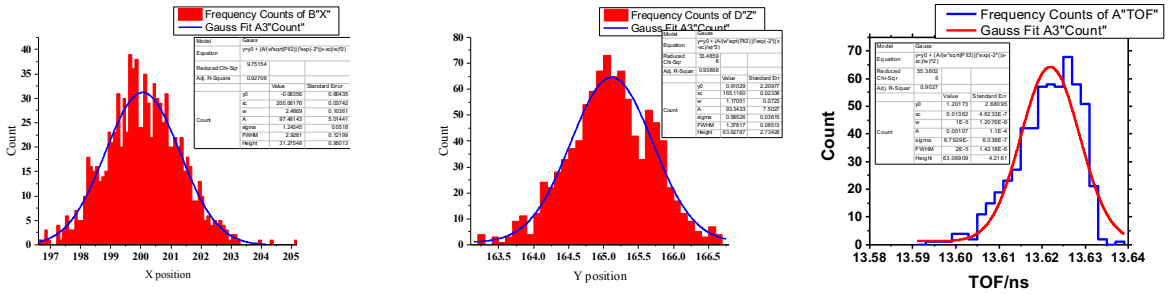

Fig. 4.12 X (left figure), Y (middle figure) direction position distribution and TOF (right figure) distribution of the SEs arriving at the MCP surface from point source at the foil plane. All the distributions are fitted with a gaussian function and the fitting parameters are demonstrated on the figures. The sigma value and the FWHM value are typically used to display the resolutions of the position and timing of the detector at different settings. HV settings are: foil, -3000 V; mir., -2334 V; MCP front, 0 V; triangular potential plates (Δ: accelerating grid, inner mirror grid, and support plate with two side walls), 0 V.

does not satisfy $\frac{U_{mir}}{U_{acc}} = \Delta V/\Delta V_f \geq 0.5$ (in this structure, the isochronous condition can not be achieved). Fig.4.14 shows the summary of the 28 mm and 8 mm structure 2-D position resolutions with different arrangements of the grid directions. Though it is reported that the SIMION have a resolution of 1mm for geometry structure settings, the results still shows the influence of grid direction difference on the position resolutions of the detector at a same setting of HV for the plates/grids. A typical figures of detection imaging and transporting trajectories (on X-Y and X-Z planes) of SEs from 5 positions on the conversion foil after acceleration, free-drift, deflection, and then free-drift to the MCP front surface are shown in Fig. 4.16. Another simulation is done by changing the mirror distance and varying the distance of accelerating grid and conversion foil in isochronous condition and the results of timing resolution is displayed in Fig. 4.13b. From the results in left figure of Fig. 4.13b, we

can easily judge that the influence of changing of the the mirror distance is relative small when keeping the ratio of the accelerating HV and deflection HV as a constant. From the right of Fig. 4.13b, we can clarify that the timing resolution of distance of the accelerating grid and conversion foil at 15 mm is worse than these of 5 mm and 10 mm, and 5 mm, 10 mm cases have a nearly same timing resolutions at same accelerating HV supply. As the increasing of the accelerating HV supply, the timing resolution for 5 mm, 10 mm and 15 mm cases get nearly saturated and very close to each other.

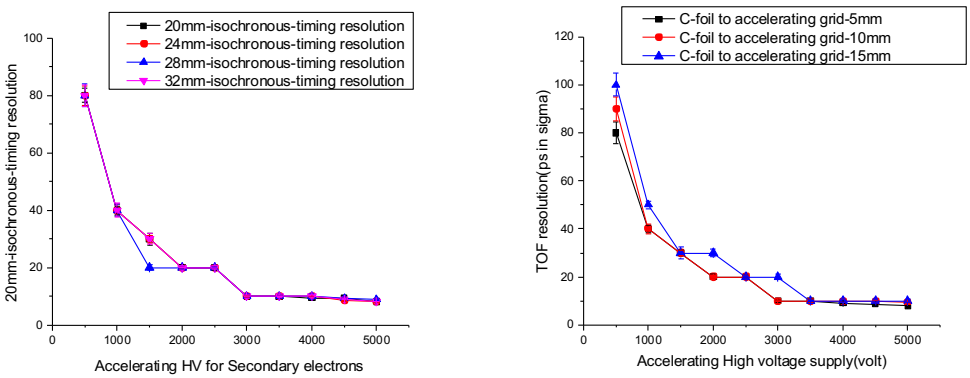

(a) Comparison of timing resolution by changing the distance of the mirror distance in sumulation

(b) Comparison of timing resolution by varying the distance of the accelerating grid to the foil in sumulation

Fig. 4.13 Comparison of timing resolution of different distances corresponding to X_{mir} and X_{acc}. The HV setting of different plates are all the same in the simulation and the accelerating HV values are all negative.

Typical trend of the position and timing resolutions as a function a the accelerating HV Comparison of timing and position resolutions of different dimensions (140 mm x 140 mm and 240 mm x 240 mm for the triangular structure) are simulated and the results are demonstrated in Fig. 4.15. It is obvious that the position resolutions and timing resolution is better for smaller size of detector, in which the total TOF and path length of SEs are smaller and result in a smaller influence from initial energy and angular distribution of SEs from the foil with the same settings for the HVs. The typical trends of timing and position resolutions for the mirror detector as shown Fig. 4.18 indicates that as the increasing of the accelerating HV, the timing and position resolution will get improved accordingly and finally get nearly saturated at a plateau. Imaging paths of SEs of a point source, and SEs sources with 0.5 mm and 1 mm holes in radius. Fig. 4.19 shows the simulation results of different sizes of SEs sources, which demonstrate a significantly influence of the mask hole sizes on the position distributions after transportation when using the mask for checking the position resolution of

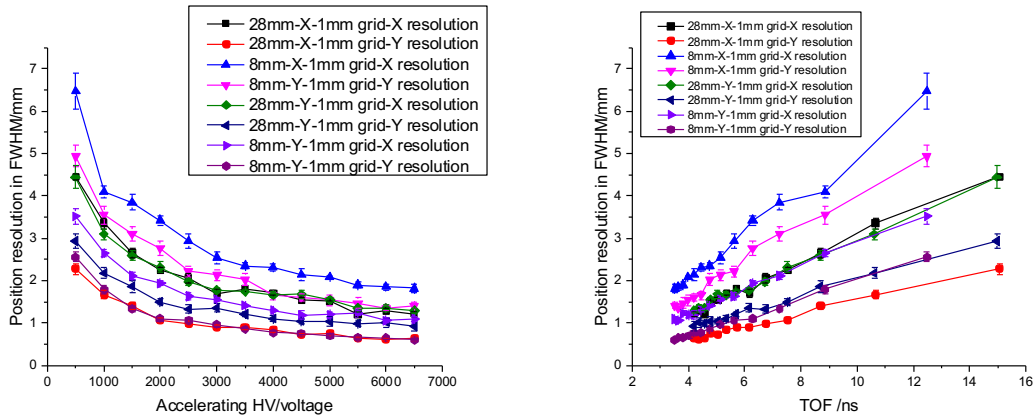

Fig. 4.14 Comparison of position resolution of different distance values of 8 mm (isochronous) and 28 mm (non-isochronous) for X_{mir}. The HV setting of different plates are all the same and the accelerating HV values are all negative in the simulation. "28mm-X-1mm grid-X resolution" in the legend means: 28 mm of D value, grid direction parallel to X with 1 mm pitch, the X resolution is demonstrated from the simulation. "8mm-Y-1mm grid-X resolution" in the legend means 8 mm of D value, grid direction parallel to Y with 1 mm pitch, the X resolution is displayed in the figure. Other legend items are listed in the same way.

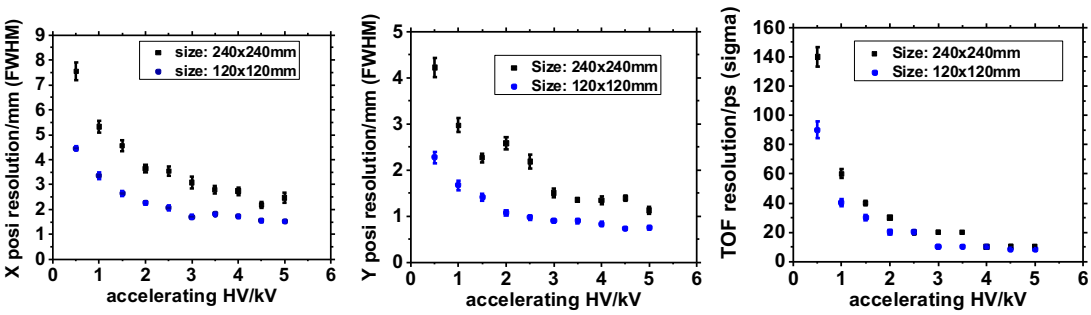

Fig. 4.15 Comparison of timing and position resolutions of different dimensions (140 mm x 140 mm and 240 mm x 240 mm for the triangular structure). The HV setting of different plates are all the same and the accelerating HV values are all negative in the simulation.

the detector. Typically, the holes size influence is less than 0.5 mm according to simulation by comparison of a 0.5 mm hole and 1 mm hole SEs source, but as we use single hit TDC and the broaden SEs beam sizes will contribute to worsen the quality of acquired timing information.

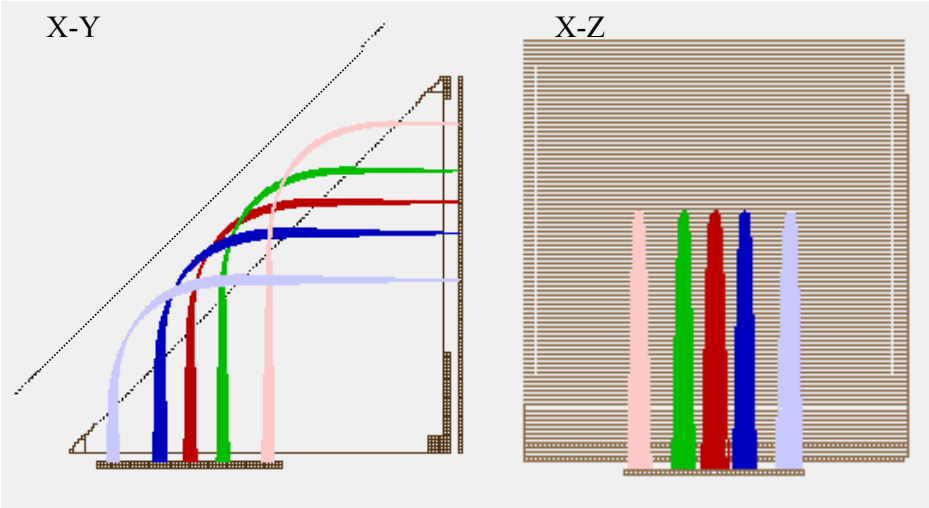

Fig. 4.16 5 points imaging of SEs from the foil onto the MCP surface in the X-Y and X-Z view in the simulation.

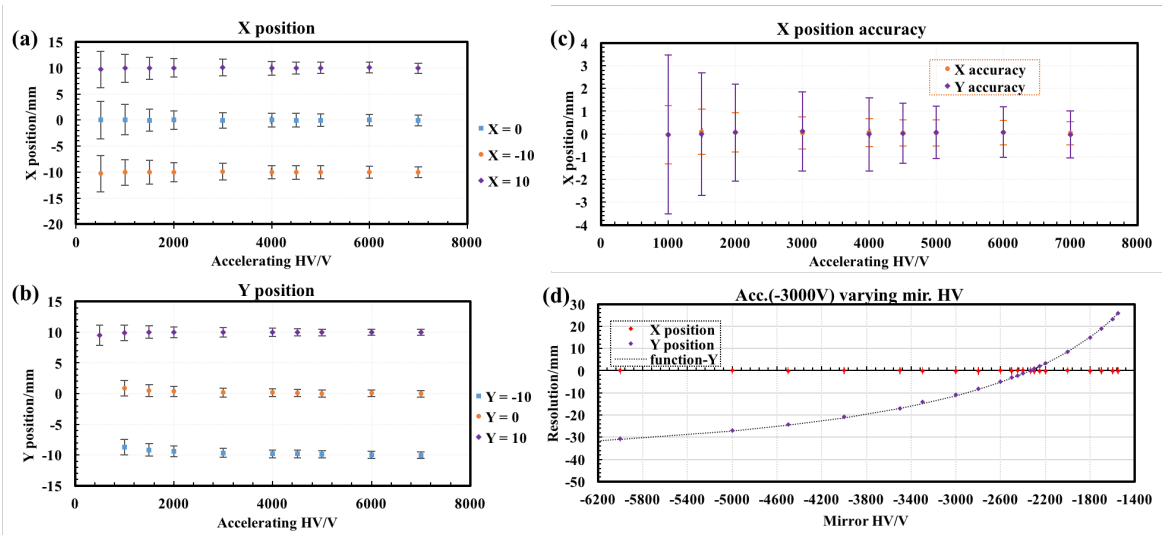

Fig. 4.17 (a) and (b) demonstrate the position with the error bars of the position resolution of 3 points (3 points in Fig. 4.16 near central area) on X and Y as a function of the accelerating HV. (c) shows the position accuracy (deviation between the imaging position on the foil and the imaging position on the MCP of one point source of SEs on the foil). In (a), (b) and (c), the ratio of the accelerating HV to the mirror HV value is kept as a constant (isochronous condition) and the accelerating HV, the mirror HV are varied together in the simulation. (d) indicates imaging position of the one point source of SEs at center of the foil onto the MCP as a function of the mirror detector (keeping the accelerating HV at -3000 volts and varying the mirror HV). The ”function-Y” is a function from Eq. 4.15, which demonstrate good consistences with the theoretical calculations.

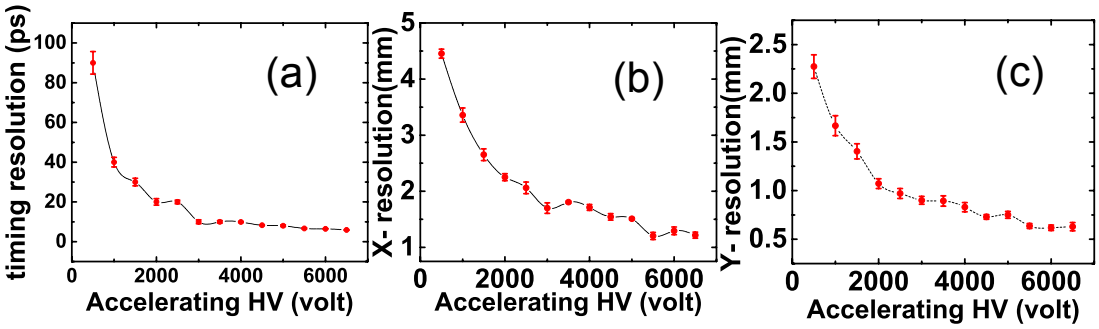

Fig. 4.18 Typical trend of the position and timing resolutions as a function a the accelerating HV. the ratio of the accelerating HV to the mirror HV value is kept as a constant (isochronous condition) in the simulation. are all negative in the simulation.

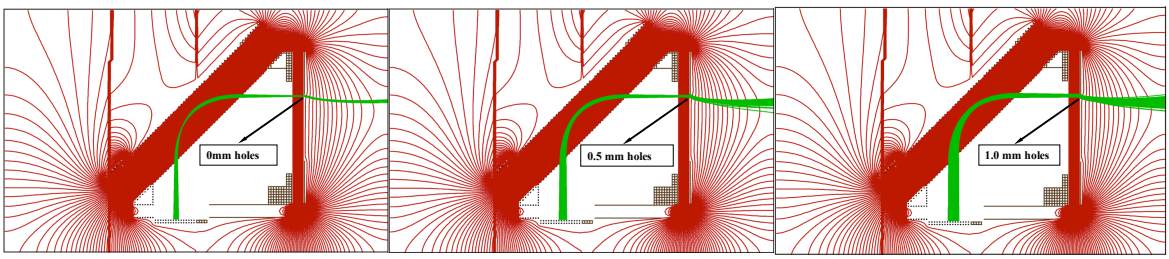

Fig. 4.19 Imaging paths of SEs of a point source, and SEs sources with 0.5 mm and 1 mm holes in radius. The HV settings are the same in the simulation. It is obvious that the SEs position distribution on MCP is significantly influenced by the source size. For reducing the influence of the hole sizes on the mask when using it for checking the position resolution of the detector, the hole size of the mask should be as small as possible.

4.8 The performance of delay-line anode MCP detector

The MCP detector system is based on the delay-line detector with MCPs of an active area of 120 mm in diameter (DLD120) system developed by RoentDek [140]. The diameter of each micro-channel is 25 mm, and the center-to-center distance between adjacent channels is 35 μm. The micro-channels are inclined at 19° relative to the normal direction of the MCP surface. The specification of the MCPs and basic performance, characteristics of the MCPs and the detector assembly are listed in Appendix B.The delay-line anode utilized in the work have two delay-line layers. Some anodes like the RoentDek Hexanode, have a third redundant delay-line layer that can give redundant detection opportunities either to improve the multi-hit performance, linearity or to allow the use of a MCP setup with central hole and minimized blind detection area.

4.8.1 The delay line anode

The Delay Line Anode (DLA) has been discussed in section 4.6.1. DDL as shown in Fig. 4.8 consists of a holder and two coils for X, Y directions. Each coil (dual delay-line) with two wires is convoluted in parallel with a pitch of $\sim$ 1 mm around the holder, and one of the wires acts as Reference and the other one as charge collection wire. The Holder has a metal core with four checkered ceramic insulators at the edges. Around these insulators the delay-lines are convoluted, the first one in one direction with a smaller circumferences (X), the second in direction perpendicular to the first one with a larger circumference (Y). Signal is on a more positive potential than Reference (+ 36 V). Thus the Signal wire is more attractive to the electrons coming from the MCP back plate and produces a larger signal then Reference wire. If a electron cloud propagates along a collecting wire, a current will only be induced in the neighboring Reference wire and thereby can be registered. The anode holder acts as a reflecting plate, so that nearly all electrons from the charge cloud can be collected by the Signal wires. The single pitch propagation time (for 1 mm) on the delay line is $\sim$ 1.24 ns for DLD120, thus the correspondence between 1 mm position distance and relative time delay in the 2-dimension image is twice of this value: about $\sim$ 2.48 ns. Reversely, relative time delay of 1 ns in the 2-dimension image corresponds to $\sim$ 0.4 mm position distance.[1] Each line has a length of approximately300 ns and a resistance of $\sim$ 24 Ω. The x-coordinate is encoded with the inner coil, and y-coordinate is determined by the outer coil.

[1]Note that these numbers are only accurate within 5% and are slightly different for each dimension. In order to calculate the position in mm from the digital X and Y values, the bin width of the TDC and the single pitch propagation time for the respective layer have to be taken into account.

4.8.2 Preparation, assembly and mounting of the Delay-line detector

Before using the DLD, we need to verify with an Ω meter that no dust particles have electrically shortened the anode wires and neither the two wires of one pair nor the wires of the different layers should be in contact (>10 $M\Omega$). From one end to the other the resistance is around 24 Ω for this DLD120. No electrical connection between the wires and the Holder plate which is the metal anode body should also be varied before operation with HV. When carrying out the assembly of MCP-stack, the second MCP will be placed with its mark also pointing upwards and should be rotated by about 180 azimuthal degrees with respect to the mark position on the MCP under it. In a side view cross section of the stack, the pores of the MCPs would resemble a (broad) "v" shape (chevron structure) to achieve a correct orientation of the channels the MCPs. Such an angle orientation is very important for proper stack performance and any relative azimuthal angle between 150° and 210° will serve the same as having exactly 180° between marks. The delivered MCPs usually are matched in resistance within 10% for direct stacking. After stacking all MCPs, the MCPs are well-aligned with each other and centered in the indention should be ensured.

For DLD120, two MCPs are fitted between a metal square-shaped rear support plate (holder) which mates to the delay-anode and a metal front ring. The rear holder and the metallic front ring have an indention for the MCP on one side [140]. The MCP stack is fixed by 6 special M3 screws made from PEEK (an insulating UHV-compatible polyimide material). The CAD drawings of metallic front ring and metallic holder for MCP from RoentDek are Fig. B.2b and Fig. B.2a in Appendix B.

For the connection cables for the MCPs and the delay-line anode to connect to a feedthrough flange FT12, they are delivered from the manufacturer when ordering the FT12TP (see Fig. 4.20a) together with feedthroughs of type FT12 (see Fig. 4.20b) from RoentDek. For the DLD120, connections of all 8 cables from the delay-line and the other 3 (or 4) in vacuum cables for MCP front, MCP back, anode holder plate and optional mesh from the vacuum side of the 12-pin feedthrough flange FT12 are indicated in Fig. 4.20b. The cable for the "MCP back" connection can be fixed by a M2 screw to the rear MCP plate. The cable for the "MCP front" connection is either clamped to the front ring with one of the M3 polyimide screws or alternatively via an M2 screw that can be fixed to the front ring. A calibration mask can be supplied for being placed on the MCP front side through M2 screws. A cable for the anode body "Holder" can be connected anywhere on one of the metal M2 rods in the anode, or any part electrically connected to that as shown in Fig. 4.21(2) and (4). The MCP rear support plate is insulated from the M2 rods that pass through the anode Holder by collared ceramic eyelets. FT12 is used for the delay-line connections and also accommodate the bias for the other detector parts: Holder, MCP front and MCP back (and an optional mesh).

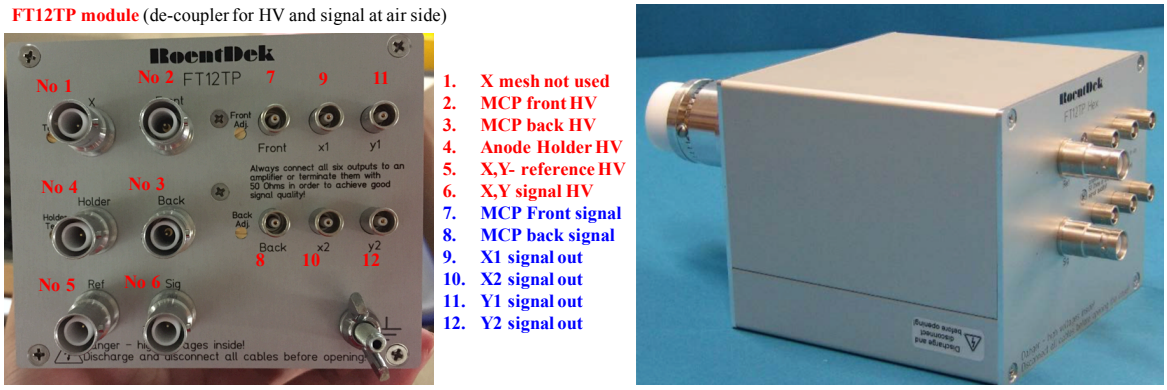

(a) Left: Front panel of FT12TP plug for DLD with rectangular case (the output not used must be closed with a 50 Ω terminator). Right: Side view of FT12TP module.

(b) Left figure shows air side connection of FT12 module and the text in middle gives FT12 pin description for connection to MCPs, holder and delay-line of DLD detector. Right is the photo of the copper cables for connection inside the vacuum.

Fig. 4.20 Function of the FT12 pins, FT12TP and connections of the MCPs, delay-lines, and the holder.

For the MCPs and Holder connection, 3 (single) cables are used, while for the anode, 4 cable pairs with proper impedance (ideally 100-150 Ω) are needed as shown in Fig. 4.21(1). A well-transmitting twisted pair cable line can be formed by twisting a cable pair at least 3 turns per 10 cm and two cables of a pair must have equal lengths within a few mm. For connecting these cables to the delay-line terminals special 2 mm connector pins are provided to connect to the FT12 at vacuum side. The three other single cables are needed for “MCP front”, “MCP back” and “Holder” (see the Fig. 4.21(1,2,4). A fourth single cable can be used for connecting a mesh (post-acceleration grid).

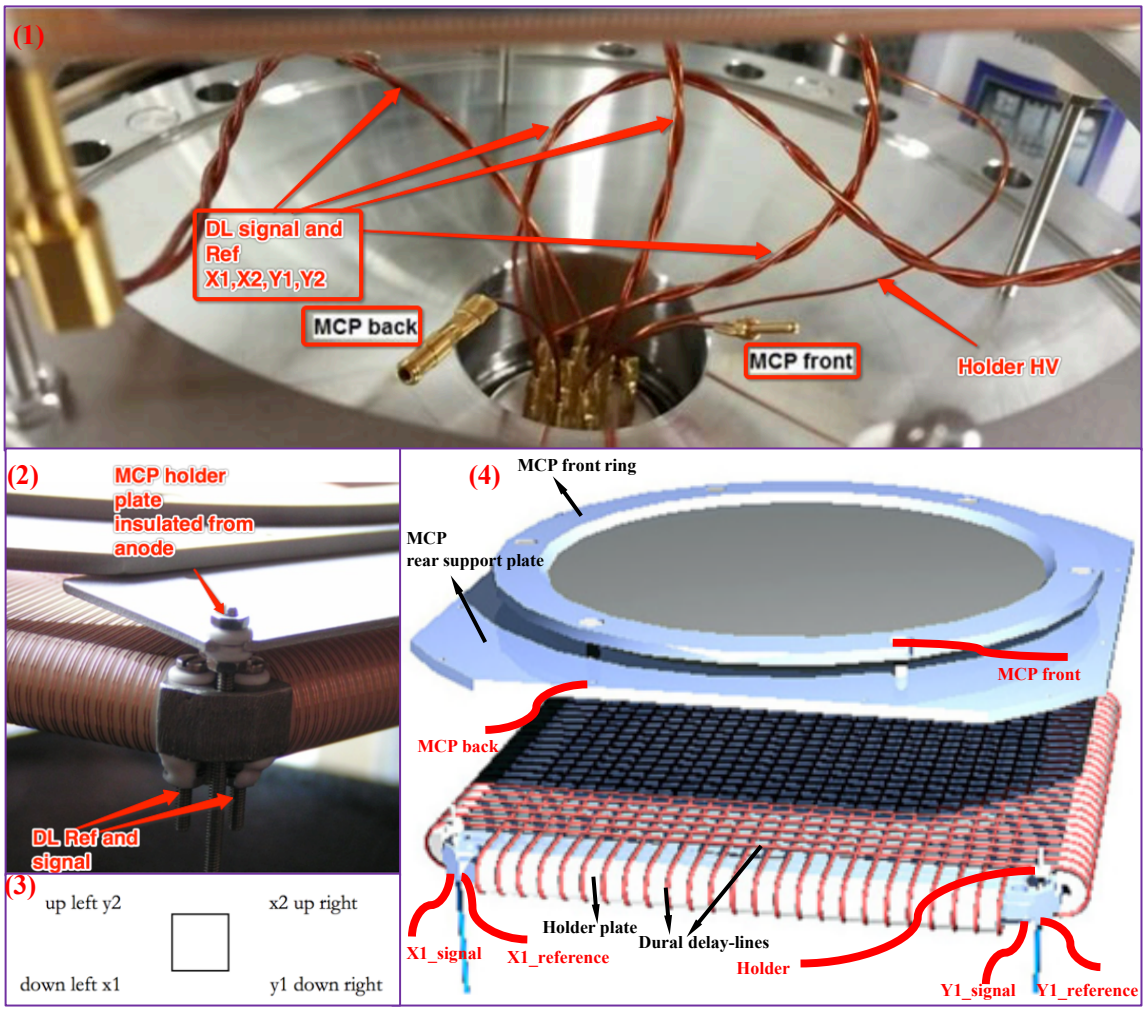

Fig. 4.21 (1): Typical picture of cable connection of FT12 pins to MCP and anode. (2): Zoom figure of the cable connection of the holder and one corner delay-lines. (3): Connection scheme in the corners recommended for the DLD detectors by the manufacturer. (4) Side view of the cable connection on the MCP front/back and delay-line Reference/Signal to the vacuum side of FT12 pins.

The so-called FT12TP provides the voltage supply and performs signal decoupling of the front, the back of MCP and the delay line signals as shown in Fig. 4.20a. A teflon insulated air-side connector plug at the bottom is used to connect it to the 12-pin feedthrough FT12. In the left panel of FT12TP one can see the six high voltage connectors for detector voltages ($U_{Reference}$, U_{Signal}, U_{Holder}, $U_{MCPfront}$, $U_{MCPback}$, U_X) via SHV input cables sockets. At the right the six Lemo connectors for the MCP bakc/front and the delay line signals can be found as well as 2 adjust potis for MCP font/back. The FT12TP plug provides adequate RC decoupling circuits and special transformer circuits as shown in Fig. 4.22 to turn the differential delay-line signals into single-line signals with 50 Ω line impedance output

connectors. All eight signals from Signal and Reference from each delay-line ends (X_1, X_2, Y_1 and Y_2) are firstly decoupled from the high voltage, by four 4 nF capacitors as shown in Fig. 4.22[2]. Afterwards, at each end of the delay lines the Signal from Reference is subtracted to one Lemo socket from the corresponding signal of the signal line for noise reduction. The connections on the FT12 have to be placed in a certain order to work correctly with the coupled FT12TP which is plugged onto the FT12. The orientation of each end of the delay-lines and MCP back/front and Holder are marked with different numbers shown in Fig. 4.20. The HVs for Signal and Reference are supplied via a $\sim$ 1 $M\Omega$ resistance (see Fig. 4.22), which eliminates the noise picked up from the HV cables and protects the delay-line from voltage swings. The signals from Signal and Reference are each decoupled by a 4 nF capacitor.

4.8.3 The high voltage supply for DLD and the foil detector

Before applying any voltage to the detector for the first time it should be verified that [140]:

- the detector is in appropriate vacuum conditions ($< 10^{-6}$ Torr) for at least 24 h, see also the Appendix A
- all connections inside the vacuum are complete and have been carefully verified, also for absence of shorts (delay line anode is very sensitive to dust and impurities, because it can easily cause a shortcut between Reference and Signal and spoil the position information and one should diagnose the shortcut between Signal and Reference before installation or check from the FT12 pins or FT12TP after installation)
- safe distances are kept or sound insulation is installed between all biased parts of the detector (including attached cables) and the chamber wall and or other metal parts on ground or other potentials (i.e. mounting gear)
- safe distances are kept between the MCP front contacts and exposed cable parts to any other part of the detector (double-check also exposed cable/connector parts on the vacuum feedthrough)
- all feedthroughs, decoupling circuits and high voltage cables are rated for the targeted maximum detector voltage
- potential EM noise sources are turned off

[2]RoentDek has not provided the circuits for the signal processing inside the FT12TP and Fig. 4.22 is drawn partly according to the manual from RoentDek. The resistance and capacity values in the circuits maybe not the exact value in FT12TP

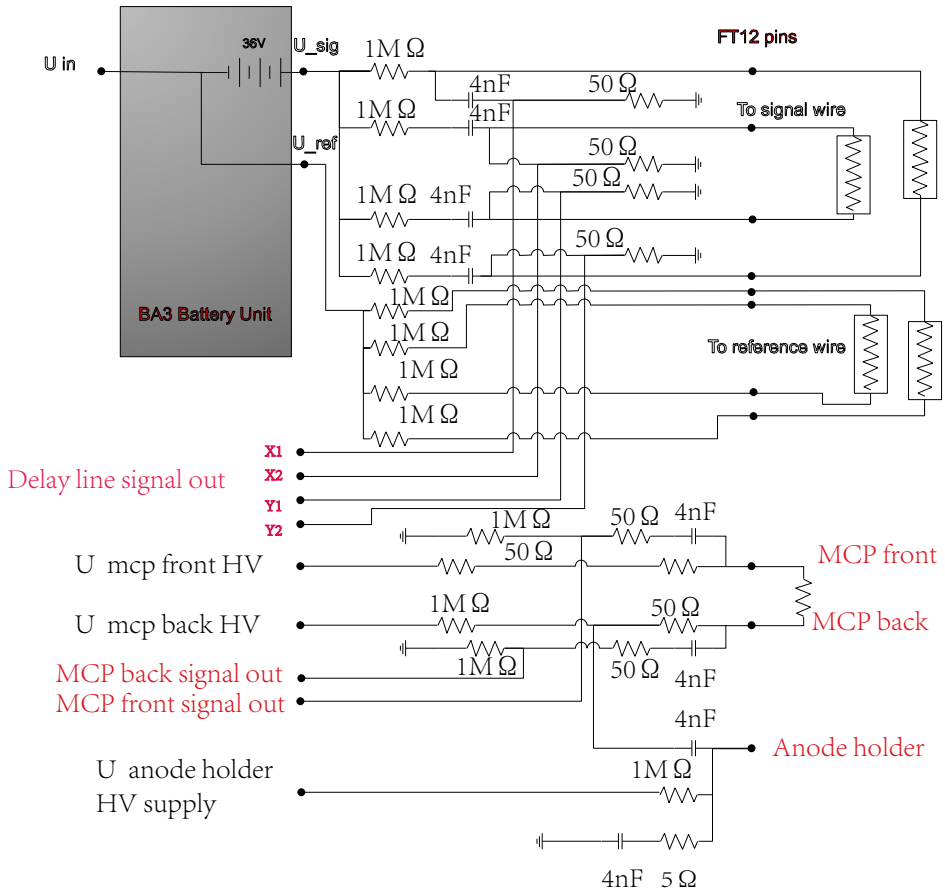

Fig. 4.22 Schematic view of the connecting of the MCP and delay-line readout to FTP12 decoupler and the inside circuit of FTP12 decoupler. Eight ends of the delay-line signals, references, holder HV together with the MCP front and back signal are connected to decoupler FTP12.

- UV sources, high power laser sources, charged particle sources (also ion gauges or ion pumps, discharge gaps) in the detector's vacuum recipient are turned off.

As shown in Fig. 4.22, the front side and back side of the MCP assembly, delay-line anode wires (Reference/Signal) and the holder ($U_{Reference}$, U_{Signal}, U_{Holder}, $U_{MCPfront}$, $U_{MCPback}$) are biased through the FT12TP decouple which connects the MCP front, back, anode wires, holder with copper cables inside the chamber. The bias voltages applied to the front and back side of the MCP, the holder electrode and the delay-line anode wires are listed in Table 4.3 and supplied by ISEG HV supply modules. A picture of the ISEG HV supply: NHQ236L/NHQ235M/NHQ224M/NHQ205M series are shown in Fig. 4.23. The accelerating grid HV, the outer mirror HV and the triangular structure (Δ) HV of the mirror detector

Fig. 4.23 The NHQ 235M/205M/224M/234L modules [165] power supply system from ISEG company used for the voltage supply of the foil-detector and DLD.

are also supplied by these modules separately. Typically two modes of detection, as shown in Table 4.3 and Fig. 4.25, are tested and utilized during the experiment. In the future we will use the ion detection mode which can supply relatively larger potential difference for the mirror detector. Between the front and back of the MCP, a bias voltage of 2400 V is applied,

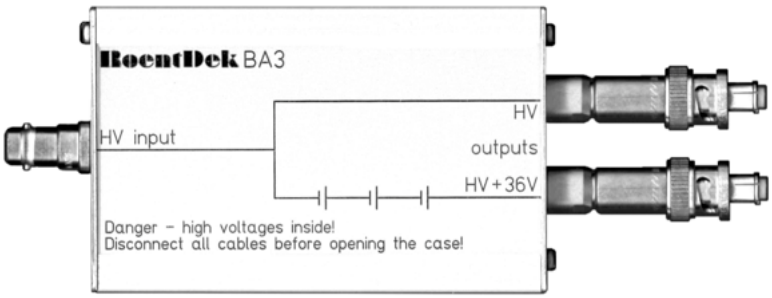

Fig. 4.24 Picture of battery pack BAT3 for the voltage offset between Reference and Signal.

Table 4.3 Typical detector voltage settings for test (chevron sets of 60:1 MCP)

	Ion or Photon Detection mode	Electron Detection mode
MCP front	−2400 V	0 V
MCP back	0V	+2400 V
Delay-line anode Holder	0V to 250V	+2400 V to +2650 V
Reference wires (respectively timing anode)	+250 V	+2650 V
Collecting (Signal) wires	+286 V	+2688 V

and the overall gain of the two MCPs is $\sim 10^7$. The avalanche of electrons leaving the MCPs induces a fast positive signal on the back/front side of the MCPs and is collected by the signal wires of the X and Y delay lines. The reference wires wound next to the signal wires are biased with slightly different voltages (+36V) by a battery box, called Roentdek BAT3 with one SHV-5 input and two SHV-5 outputs, and are used to suppress the electromagnetic noise picked up in the vacuum chamber [140].

The relation of the HV of the MCP stack to the current of the MCP measured from the HV supply module is demonstrated in Fig. 4.26. The effective dynamic resistance of the MCP stack after coupled with the FT12TP is $\sim 52.30\ M\Omega$ as indicated by the slope of the fitting line in both ion/electron mode of HV supply. The two linear curves illustrate the effective dynamic resistance remains constant for wide range of operating voltages for the MCP stack system.

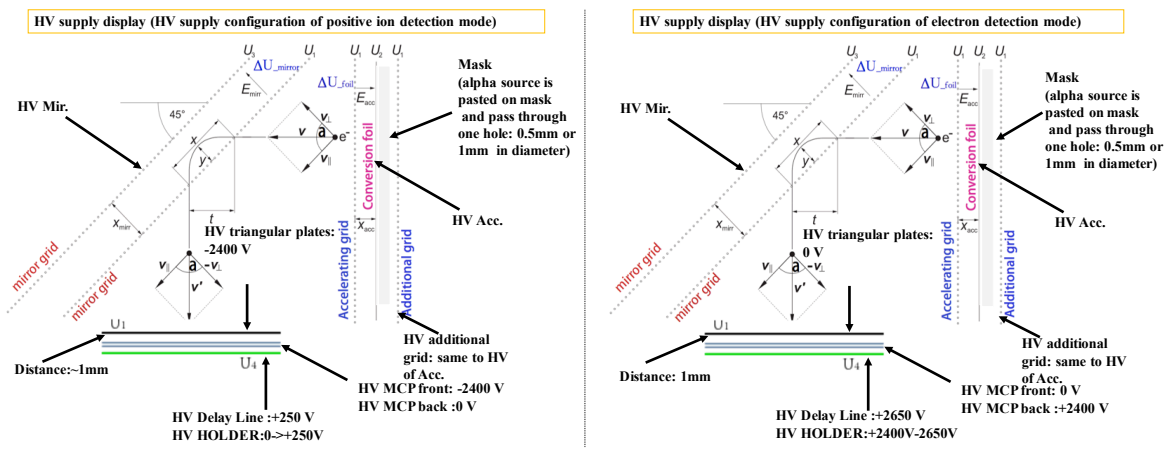

Fig. 4.25 DLD and detector potential plates HV supply for (a) ion detection mode and (b) electron detection mode. The two modes HV supply values are listed in Table 4.3.

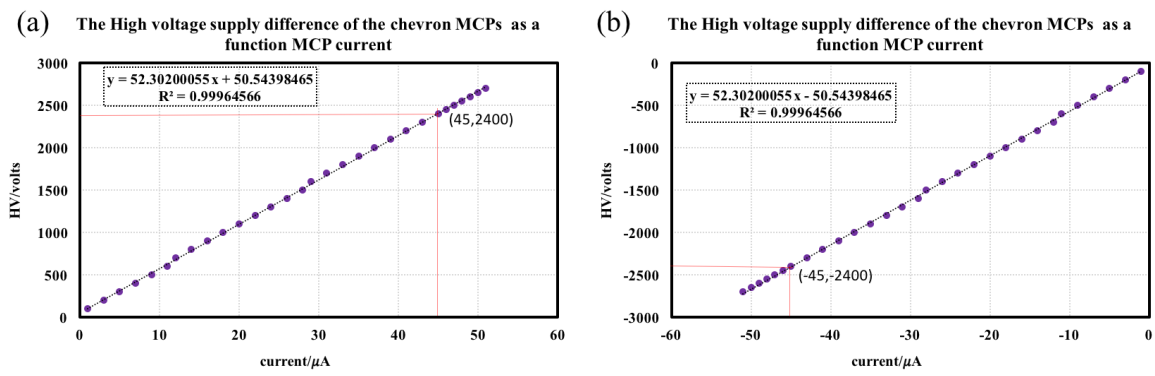

Fig. 4.26 MCP HV as a function of the current for (a) ion detection mode and (b) electron detection mode. The two modes HV supply values are listed in Table 4.3.

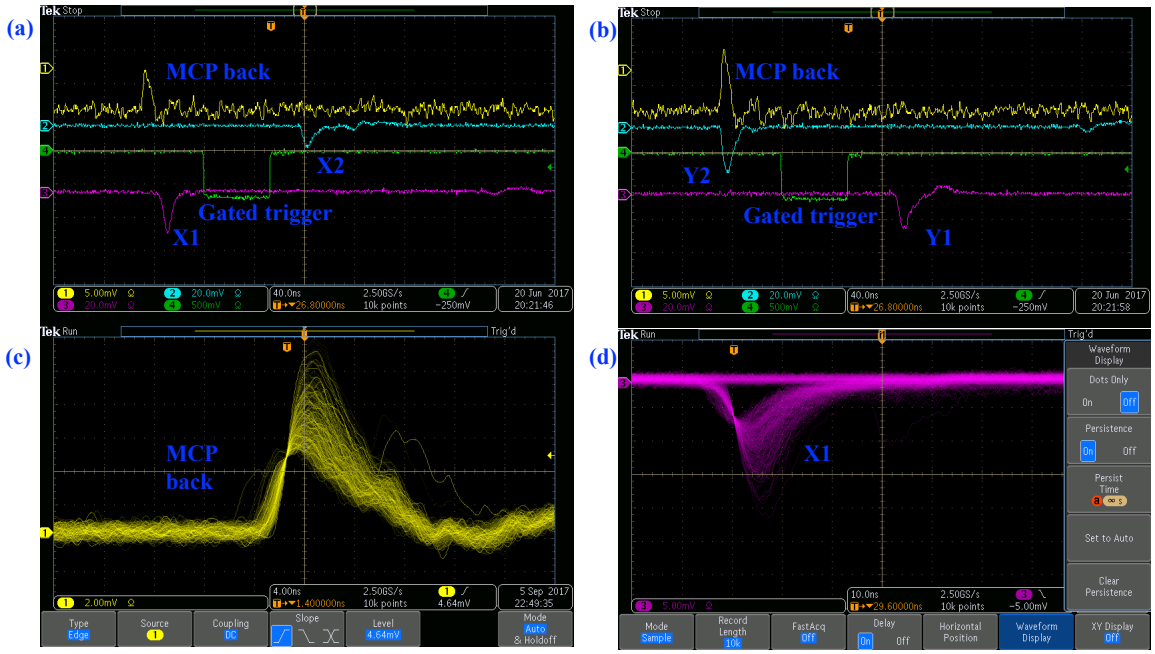

Fig. 4.27 Exemplary screen shot of raw signal pictures taken with oscilloscope. As the MCP signal is set as trigger in the front end electronics, it comes earlier than the DDL signals.

4.8.4 The delay-line and MCP signal, the signal processing

After installation of the DLD120 in vaccum chamber and connection verified, five raw signals are read out from the FT12TP Lemo sockets: one from the MCP back or front side, two from the ends of the X delay line, and two from the ends of the Y delay line. The gain of all channels after these amplifiers is $\sim 25 - 100$. Fig. 4.27(a) shows raw signal pictures of five read-outs taken with oscilloscope. The yellow trace is the MCP back signal (normally have nearly same shape and amplitude as the MCP front signal), the green one is the trigger pulse of the MCP signal, the red, blue traces are the X1, X2 delay-line signals taken with the oscilloscope. In Fig. 4.27(b), the red, blue traces are corresponding to Y1, Y2 delay-line signals and the other two traces are the same as in Fig. 4.27(a). In Fig. 4.27(a) and Fig. 4.27(b), the MCP and the X1 signals are zoomed out in display mode. The rising time is defined as the time during which a signal needs to get from 10% to 90% of is maximal value. The typical rising times for MCP signal and the delay-line signals are $\sim$ 5 ns and $\sim$ 10 ns, and amplitude about 5-10 mV and 5-20 mV respectively (source is the vacuum gauge).

The MCP back or front-side signal is inverted and then amplified twice by an photomultiplier amplifier (PM-AMP, Kaizu KN2104 [166], with an amplification factor of 10 without 50 Ω termination). The four delay-line signals are also amplified twice by the same PM-AMPs. Afterwards the signals are all lead to a Constant Fraction Discriminator (CFD, ORTEC 935 [167]). A CFD works in a principle: When a signal above the threshold arrives, it creates two signals: a delayed signal, an inverted and attenuated signal. In a second step it adds both signals and gives a trigger at the time of the zero crossing. The zero crossing appears always at the same time independently of its amplitude, when the delay T_{delay} and the fraction f are chosen via the equation:

$$T_{delay} = T_{rising}(1 - f), \tag{4.19}$$

where T_{rising} is the rising time of the signal, T_{delay} denotes the delay time of the delayed signal and f corresponds to the attenuation factor.

In the FT12TP, the MCP signal and each end of the delay line the signal from the Reference line are subtracted from the Signal line after they were decoupled from the high voltage by the use of 4 nF capacitors. Afterwards they can be picked up at the outputs labeled MCP front/back, X_1, X_2, Y_1 and Y_2.

For offline test, the MCP trigger serves as a common start signal for an 8 channel TDC as described in Fig. 5.4b. The stop signal from the same CFD with MCP signal as input serves as stop signal for channel 4 of the TDC. The delay between the Stop signal and the TDC can be adjusted by a delay box. The four delay line triggers serve as stop signals for the first four

channels TDC (channel 0–3) one for each channel, to record the position information. The delay between the LD and the TDC can be adjusted with a delay box. Meanwhile the charge information of the 5 outputs can be collected by QDC as shown in Fig. 5.4b. For the detail description of the signal processing circuits, see the Fig. 5.24.

With the BPM-TOF/TOF MCP detector constructed, measurements were performed to characterize the performances, including detection efficiency, position resolution and timing resolution measurements. The detection efficiency, position resolution were checked offline by α source ^{241}Am and also online, and the position resolution, intrinsic timing resolution was tested online together with another two timing detectors.

Chapter 5

Foil-MCP Detector Experimental Test

The timing and/or position resolution are most crucial characteristics to be tested for the detector systems. Another important characteristic of the detector system is the efficiency to detect the heavy ion through detection of the secondary electrons (SEs) ejected from the conversion foil. The number of secondary electrons produced in the $40 - 60\mu g/cm^2$ carbon foil is directly proportional to the energy lost (dE/dx) by the primary ion based on the square of its nuclear charge. Thus, heavier elements have a higher energy transfer value and produce a relative higher secondary electron yield. SEs are emitted from both sides of the carbon foil, so the electron detector may be placed either upstream or downstream of the foil. SEs emitted in the "backward" direction (upstream, or opposite the heavy ion direction) have a lower kinetic energy as well as a decreased yield. As during the offline test, it is easier to align the mask in the forward direction and convenient to collimate the α sources, so through all the online and offline test, the forward SEs were employed. The advantage of using the backward SEs is the SEs induced backward normally possess a lower initial energy distribution compared to the forward SEs and lower δ electron yield.

5.1 Calibration of the MCP with helical delay-lines

The MCP detector system is based on the DLD120 system developed by RoentDek with two MCPs (active area of 120 mm in diameter) mounted in a chevron configuration [140]. The diameter of each micro-channel is 25 mm, and the distance between adjacent channels is 35 μm. The micro-channels are inclined at 8° relative to the normal direction of the MCP surface to avoid ion feedback. As discussed in previous section 4.5, distorted signals may happen if the channels are arranged in parallel. Because electrons leaving the channel after the amplification process can create positively charged ions which travel back in the MCP channels when they collide with the channels wall. A similar phenomena appears when the

MCPs are oriented correctly but operated in bad vacuum (worse than 10^{-3} Pa) and rest gas atoms are present in the micro-channels.

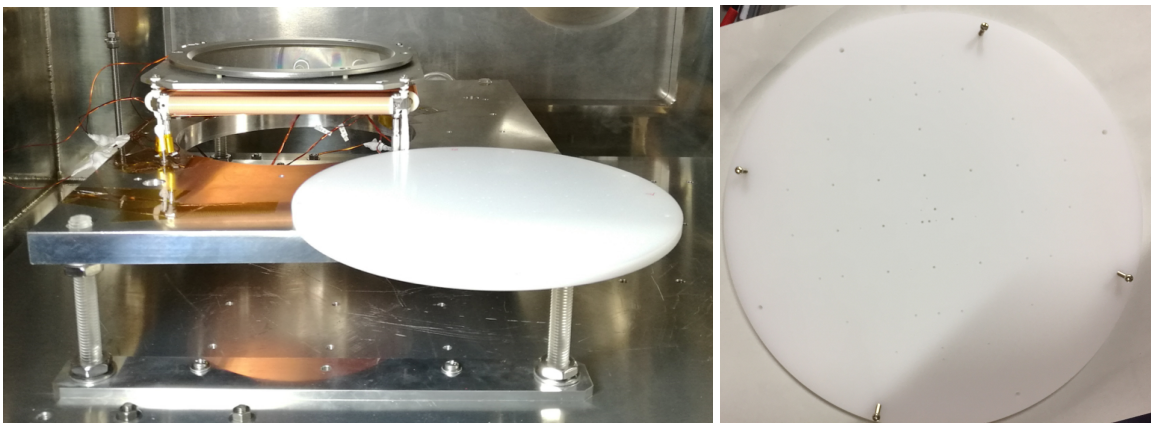

(a) (b)

Fig. 5.1 (a). The mask (white circle made of POM) for calibration and DLD120 system in the test vacuum chamber. (b). Front view photo of the mask. The mask is mounted on the MCP front plate with M2 screws at the edge of the mask. CAD drawing of MCP mask is shown in Fig. 5.2.

As shown in Fig. 5.2 the outer diameter of the mask is 180 mm and at center area range of the mask with a active area of 120 mm which is same as the MCP active area, there are many 0.5 mm or 1 mm holes, at which defines the detection area for ions and α particles. As the vacuum condition is little worse than required operation condition, the dark rate of the MCP is about 400 counts per second. With the electron detection mode, we usually turn the CFD threshold relatively higher when the vacuum condition is rather worse. The front side and back side of the MCP assembly, delay-line anode wires and the holder are biased through the FT12 decouple which connects the MCP front, back, anode wires, holder with copper cables inside the chamber. The bias voltages applied to the front and back side of the MCP, the holder electrode and the delay-line anode wires are listed in Table 4.3. Between the front and back of the MCP, a bias voltage of 2400 V is applied, and the overall gain of the two MCPs is $\sim 10^7$. The avalanche of electrons leaving the MCPs induces a fast positive signal on the back/front side of the MCPs and is collected by the signal wires of the X and Y delay lines. The reference wires wound next to the signal wires are biased with slightly different voltages (+36V) by a BA3 module and are used to suppress the electromagnetic noise picked up in the vacuum chamber. Five signals are read out: one from the MCP back or front side, two from the ends of the X delay line, and two from the ends of the Y delay line. The MCP back-side signal is inverted and then amplified twice by an photomultiplier amplifier (PM-AMP). The four anode signals are amplified twice by the same PM-AMPs The gain of all

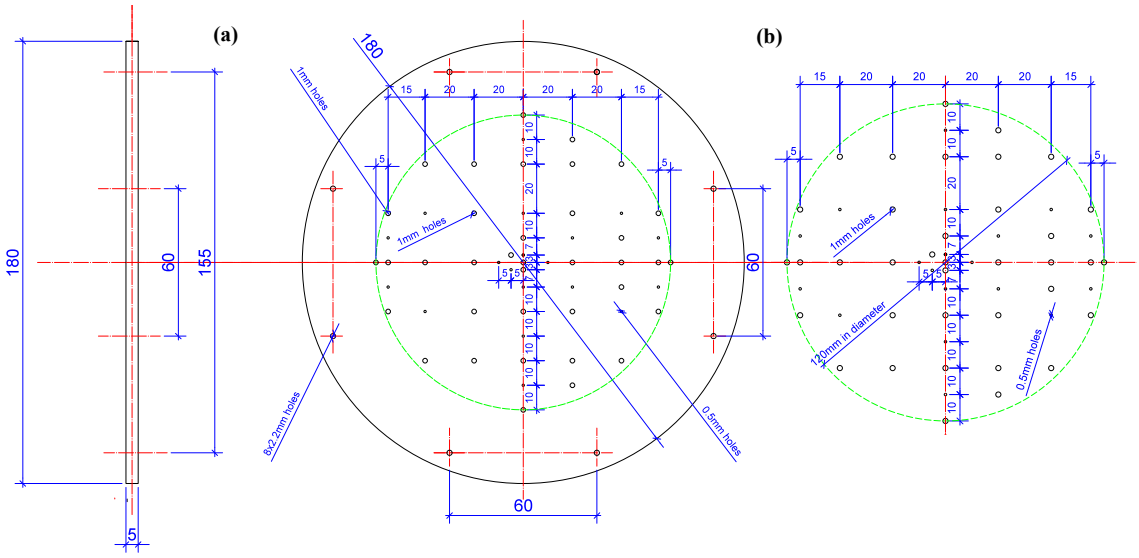

Fig. 5.2 (a). The front and side view of mask. (b) The cut-off green circle demonstrates the effective area with ions though.

channels after these amplifiers is $\sim 25-100$. The position where the incoming particle hits the MCP detector is determined by the time difference between the two signals from each end of the same delay-line anode. Two sets of delay-lines are wound at 1 mm pitch, and their directions are orthogonal with respect to each other. The single pitch propagation time (for 1 mm) on the delay line is $\sim$ 1.24 ns for DLD120, thus the correspondence between 1 mm position distance and relative time delay in the 2-dimension image is twice of this value: $\sim$ 2.48 ns. The MCP position readout (X,Y) can be expressed as:

$$X = a_x(T_{X1} - T_{X2}) + b_x,\ Y = a_y(T_{Y1} - T_{Y2}) + b_y, \tag{5.1}$$

where $T_{X1}, T_{X2}, T_{Y1}, T_{Y1}$ are the timings of the four delay-line anode signals in ns. The ns-to-mm conversion factor a_x, a_y can be calibrated with mask, and timing offsets b_x, b_y, which are introduced in the pulse propagation and amplification, can also be deduced at the same time. Although this basic correction scheme by Eq. 5.1 can not restore rotations and non-linear distortions of the MCP image, it makes the calibration algorithm easier to implement. A typical setup for the calibration is shown in Fig.. 5.2.

The chamber pressure is maintained $\sim 1 \times 10^{-3}$ Pa via two pumps (turbo-molecular pump mounted on the interconnecting tube and connected to a rotary pump) mounted on the bottom of the chamber. When carrying out the calibration for the DLD120 system, the source of ions used is usually the vacuum gauge with low energy ions produced or the ^{241}Am α sources put above the mask on the chamber with a distance of $\sim$ 380 mm when supplying

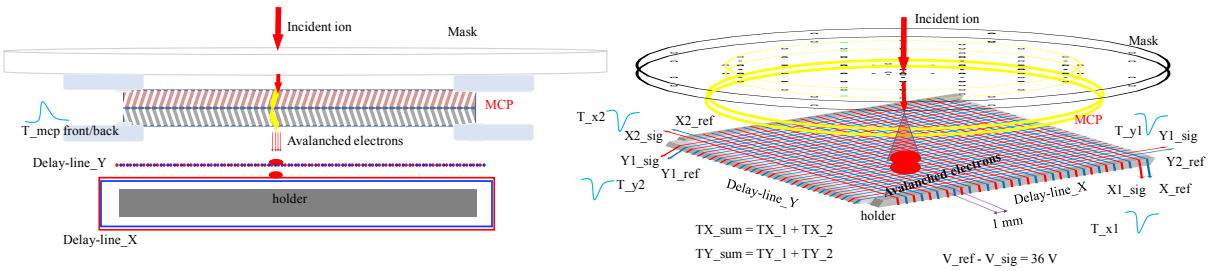

Fig. 5.3 Calibration setup for the helical delay line anode by using an α source ^{241}Am and schematic view of the connecting of the MCP and delay-line readout . Eight ends of the delay-line signals and references together with the MCP front or back signal are connected to decoupler FTP12 form RoentDek.

the HV for DLD system in the so-called ion mode. For the electron detection mode as the gauge ions can scarcely arrive at the MCP front surface with a 0 volt potential, the source applied is the ^{241}Am α sources. CAMAC DAQ system is applied for the offline/online test and block diagram of readout electronics for the DLD120 calibration by using MCP signal as trigger is shown in Fig. 5.4. Firstly the TDC is calibrated with Time Calibrator ORTEC 462 as shown in Fig. 5.5. The raw signal histograms of the T_{X1}, T_{X2}, T_{Y1}, T_{Y2} are shown in Fig. 5.6a and the calibrated signals are indicated in Fig. 5.6b.

As there are usually offset of delay-line signals due to the transmission and delay of the circuits and cables for the connection of the delay-line from the decoupler FT12TP. To remove the circuits and cable transmission difference for the delay-line signals after the FT12TP on the chamber flange, the outline calibration is carried out, during which a pulser is used to divided into 5 channels to represent the outputs from the FT12TP Lemo sockets (X1, X2, Y1, Y2, MCP back/front). The outline offsets for both X- and Y-direction are illustrated in Fig. 5.7a by a gauss fitting. The effects of cable length difference on the dTx = T_{X1} - T_{X2} and dTy = T_{Y1} - T_{Y2} time difference is removed as shown in Fig. 5.7b.

When conducting experiment with position measurement or calibration of the DLD, the sum condition on the timing of the signals is imposed for event selection in order to rule out false triggers by electronic noise and pile-up events.

As the total length of the delay-lines are fixed, the sum of the propagation times from the charge impact position to the two ends of the delay-lines are fixed, independent of position at which the event happens. Thus, the timing sums:

$$T_{X\,sum} = T_{X1} + T_{X2}, T_{Y\,sum} = T_{Y1} + T_{Y2} \tag{5.2}$$

are both expected to be constants, where T_{X1}, T_{X2}, T_{Y1}, T_{Y2} are the timing of both end signal of 2-dimensional delay-lines relative to the MCP back-side signal, which is used as trigger.

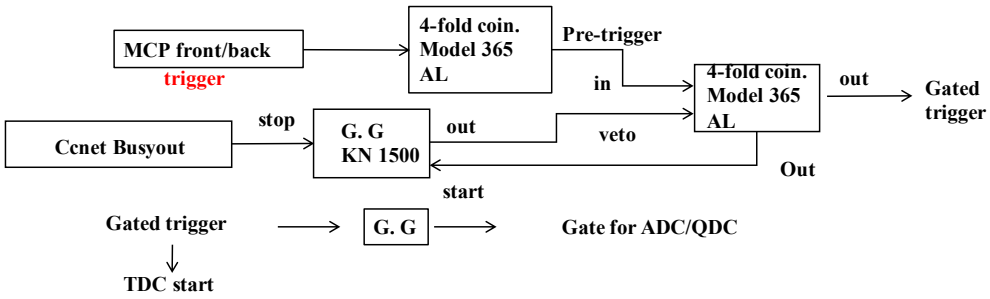

(a) Block diagram of readout electronics for trigger circuit (MCP signal as trigger)

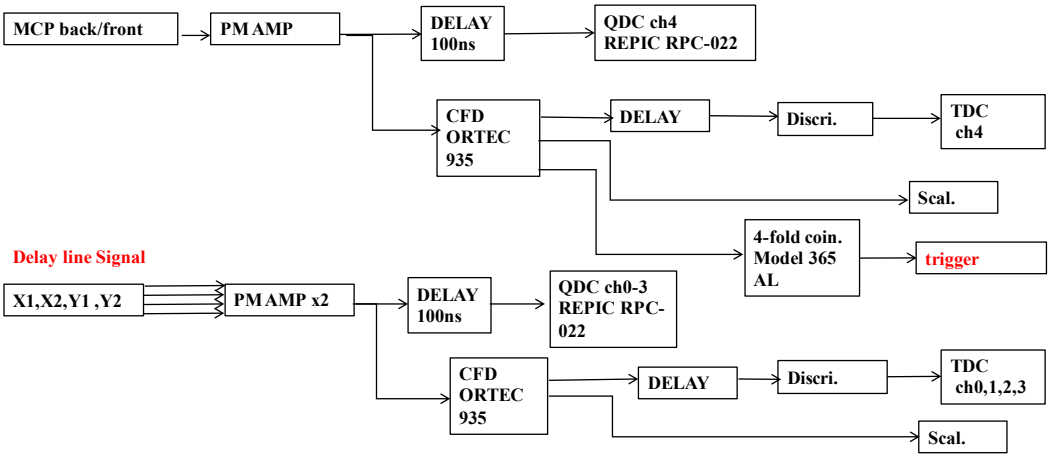

(b) Block diagram of readout electronics for the MCP and delay-line signals

Fig. 5.4 Block diagram of readout electronics for the delay-line MCP detector using MCP signal as trigger. The delay-line amps, which amplify the pulses leaving the delay lines, are photomultiplier amplifier (PM-AMP). The four channel constant fraction discriminator CFD , which provides amplitude-independent precise timing of the amplified pulses, is a ORTEC 935 [167]. The time-to-digital converters TDC that convert stop pulses from the CFDs are 8 channel Kaizu 3780 [166] with a range of 200 ns and $\sim$ 50 ps resolution. The 12-bit ADC is multiplexed to convert the x- and y-coordinate 4 channels amplified amplitude signals to digital signals, along with the MCP event amplitude signal. The trigger from the MCP CFD output triggers a pulse generator which in turn triggers the ADC and TDC to begin the conversions and stretcher.

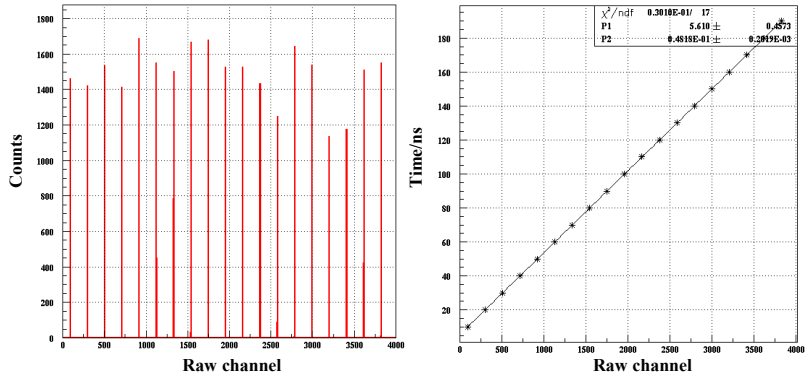

Fig. 5.5 The left shows the output of 1 channel from TDC and right indicates the relation of the channel to the time distances of each peaks. The TDC channels are calibrated by Time Calibrator ORTEC 462 [167] with a range of 320 ns and period of 10 ns. The slope on the right figure is fit by a linear function which shows the calibrated value for the channel to time parameter with a typical value of ∼0.050 ns/channel

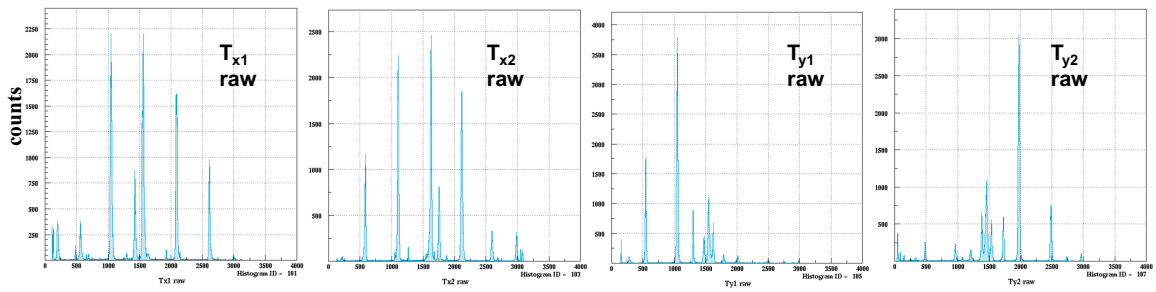

(a) Histograms of T_{X1}, T_{X2}, T_{Y1}, T_{Y2} raw signals. Y axis is the counts of the signals and X axis corresponds to raw signals from the TDC channels.

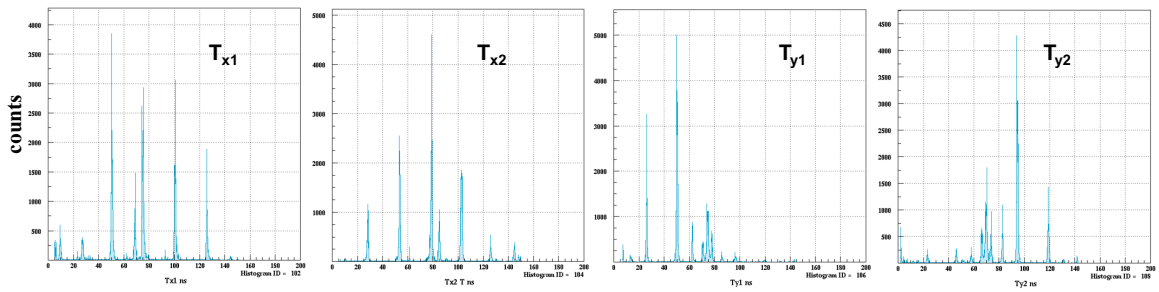

(b) Histograms of calibrated T_{X1}, T_{X2}, T_{Y1}, T_{Y2}. Y axis is the counts of the signals and X axis corresponds to calibrated Timing stamps from the TDC channels.

Fig. 5.6 Histograms of raw and calibrated T_{X1}, T_{X2}, T_{Y1}, T_{Y2} signals.

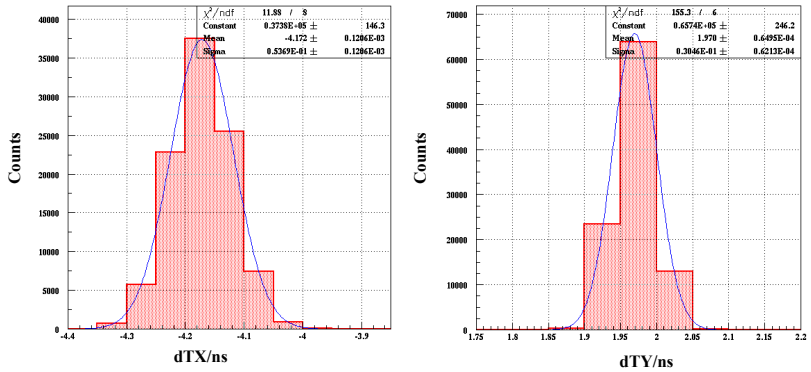

(a) dtx and dty of the 2-dimention delay-line output ($dTx = T_{x1} - t_{x2}$ and $dTy = T_{y1} - t_{y2}$)

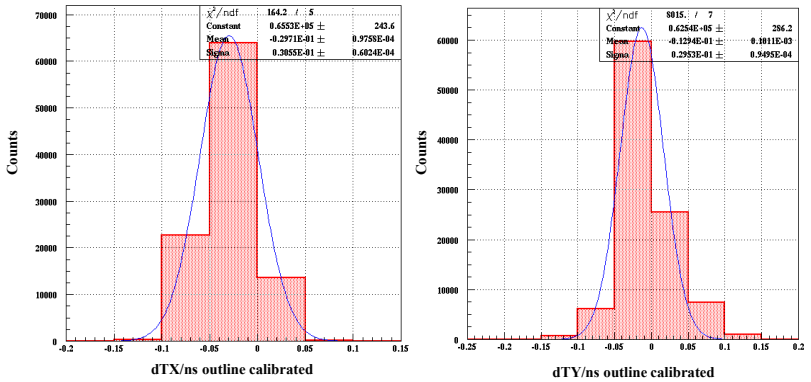

(b) Outline calibrated dTx and dTy and the offset of about -4.172 and 1.970 for x and y direction are removed after calibraton

Fig. 5.7 The outline calibration is carried out to remove the difference of the circuits and cable transmission for the delay-line signals after the decoupler FT12TP.

The spectra of $T_{X\,sum}$ and $T_{Y\,sum}$ for the calibration run are shown in Fig. 5.8. The sharp peaks with a $\sigma \sim 600\,ns$ in these spectra agree with the expectation described above. Events with $T_{X\,sum}$ and $T_{Y\,sum}$ away from the main sum peaks have false triggers in some channels, and thus are ruled out by applying a cut acceptance window around the peaks. Events cut out by imposing this condition are ˋ5% of the whole data set, and this condition is applied for all spectra in the rest of this thesis. In the calibration processes, a 3-σ gate is used for both X- and Y-direction sum of Timing to ensure no ghost events from noises or multi-hit events. But for experiments, the sum gates should be considered not to cut real events. Another way to judge the ghost events and quality of the sum gate is by drawing the 2D spectrum of T_{X1} versus T_{X2} and T_{Y1} versus T_{Y2} with (upper 2 figures)/without (lower 2 figures) sum of delay-lines timing gates as shown in Fig. 5.9. It is easy to judge the ghost events out of the linear line from the upper two figures and after the sum gate, the ghost events are removed as shown in the lower two figures of T_{X1} versus T_{X2} and T_{Y1} versus T_{Y2}.

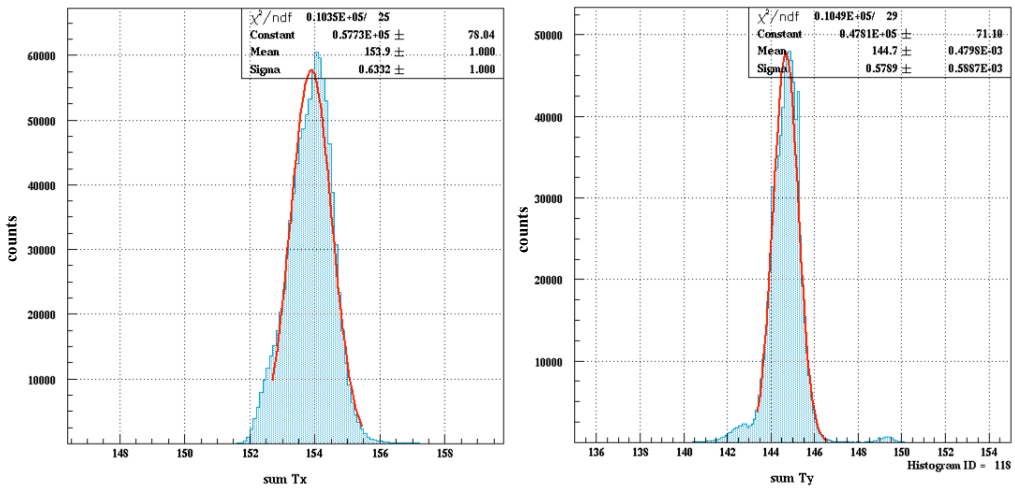

Fig. 5.8 Histograms of sum of x- and y-direction delay-line signals.

The physical positions (X_p,Y_p) of the hole points along the dealy-lines on the mask are determined from the designed values as shown in Fig. 5.2. A first order calibration function similar to Eq. 5.1 is constructed to correct the measured timing difference of each center positions (dT_X,dT_Y) on the holes to their physical positions. The parameters a_x, b_x, a_y, b_y from fitting are then applied to Eq. 5.1 to calculate the calibration points with measured timing difference from the both end of each dealy-lines.

A 2D spectrum of the ion-hitting positions (the image of holes on mask) is shown in Fig. 5.11 and the original delay-line timing information is displayed in Fig. 5.10. All holes at the active area of the mask are visible in both 2D figures.

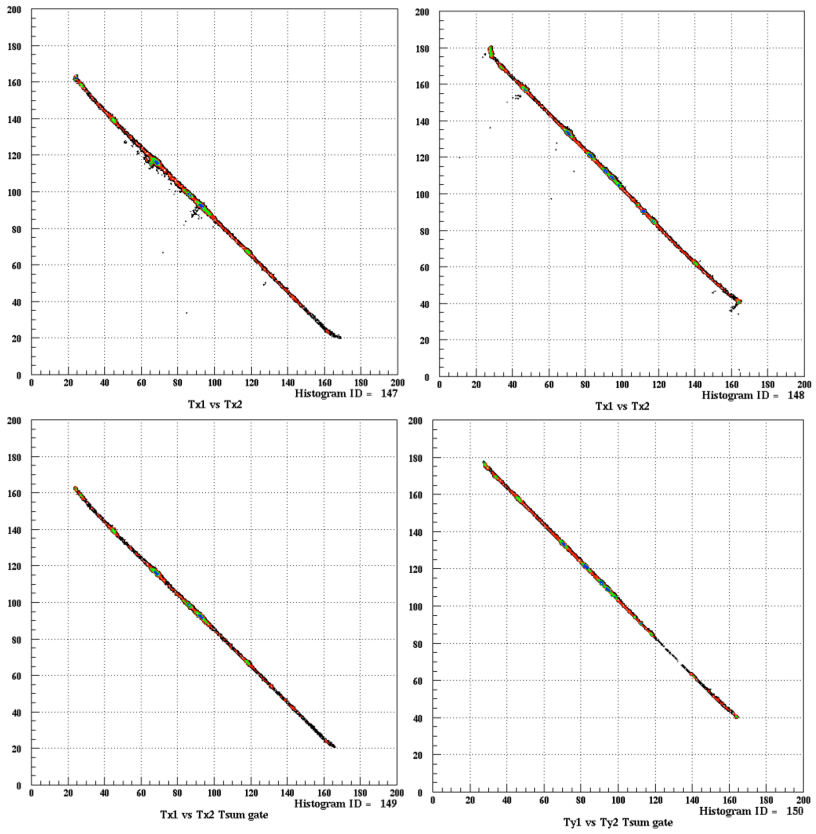

Fig. 5.9 2D spectrum of T_{X1} versus T_{X2} and T_{Y1} versus T_{Y2} with (upper 2 figures)/without (lower 2 figures) sum of delay-lines timing gates.

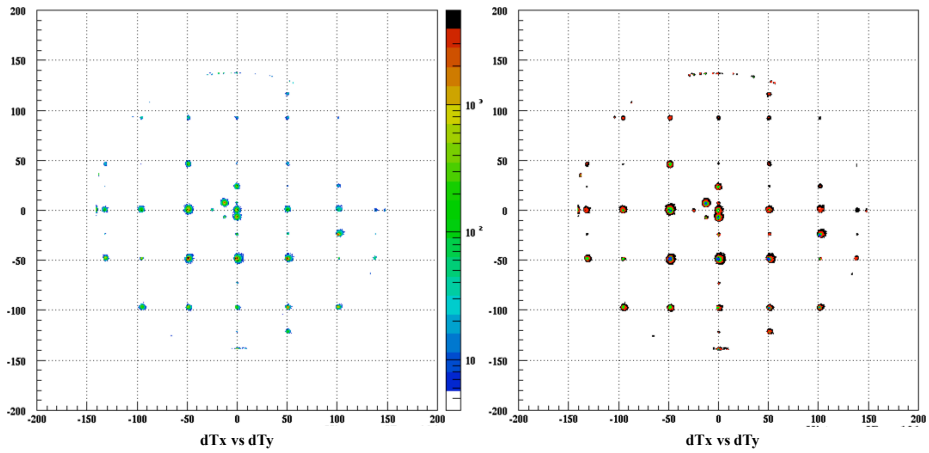

Fig. 5.10 Two-dimensional histogram of dT_X versus dT_Y of delay-line timing information when using gauge as source and mask on the MCP front plate. (Left) Two-dimensional histogram with color palette drawn and (Right) two-dimensional histogram contour display.[1]

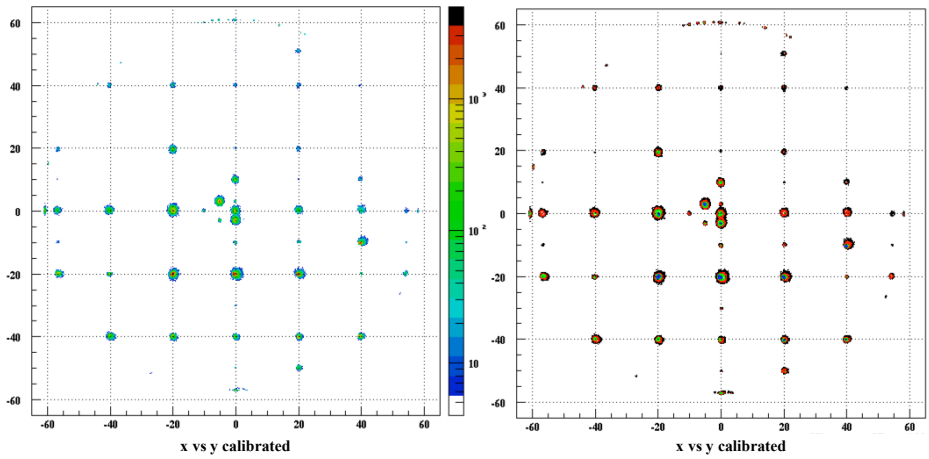

Fig. 5.11 Two-dimensional histogram of calibrated position imaging detected by the DLD120 system with color palette drawn (left) and contour display (right). The source is the gauge. The calibration parameters used is in second order with cross terms.

To investigate the linearity of the calibration parameters and position dependence on both X- and Y-direction in first order calibration case, a 5x5 division of the mask holes in vertical lines for both X- and Y-direction for individual calibration is carried out as shown in Fig. 5.12a. The calibrated parameters for each lines are listed in Tab. 5.1. The parameters a_x, a_y corresponds to the ns-to-mm for the dealy-lines which is constants as the velocity of transmission of signals in the wires is a constant. b_x, b_y represent the offsets of the X and Y position of the mask center to the DLD120 system detection center point. Normally, as the transmission distances from the dealy-lines detection center point are different, offsets of X and Y for the calibration after outline calibration are needed. As shown in Tab. 5.1 and Fig. 5.12, for both X- and Y- direction the linearity of the calibration function is very good near the ($-45\,mm \leq X \leq 45\,mm$, $-45\,mm \leq Y \leq 45\,mm$) area of the DLD120. The fluctuation of the a_x, a_y and the b_x, b_y are $\sim$ 0.001 mm/ns and $\sim$ 0.1 mm respectively, which are all inside the 1 σ error of the uncertainty of fitting. To estimate the distortions of the MCP image, we calculate the first order fitting deviations between the coordinates of the calibration points on the MCP image and their physical positions as shown in Fig. 5.12b. The mean absolute deviation is 0.44 mm and 0.42 mm for X- and Y- direction, and the maximum deviation is 0.85 mm and 0.92 mm for X- and Y- direction without large overall rotation of the mask when observing the whole MCP image. As displayed in 5.12b, the deviation has a position dependence and higher order correction is needed to correct this phenomenon.
To achieve a much more precise and accurate calibration for the DLD120 system, for each hole, we use two-dimension two- or three-variable polynomials with/without cross terms to transform the high-accuracy timing difference of each positions (dT_X, dT_Y) of the calibration

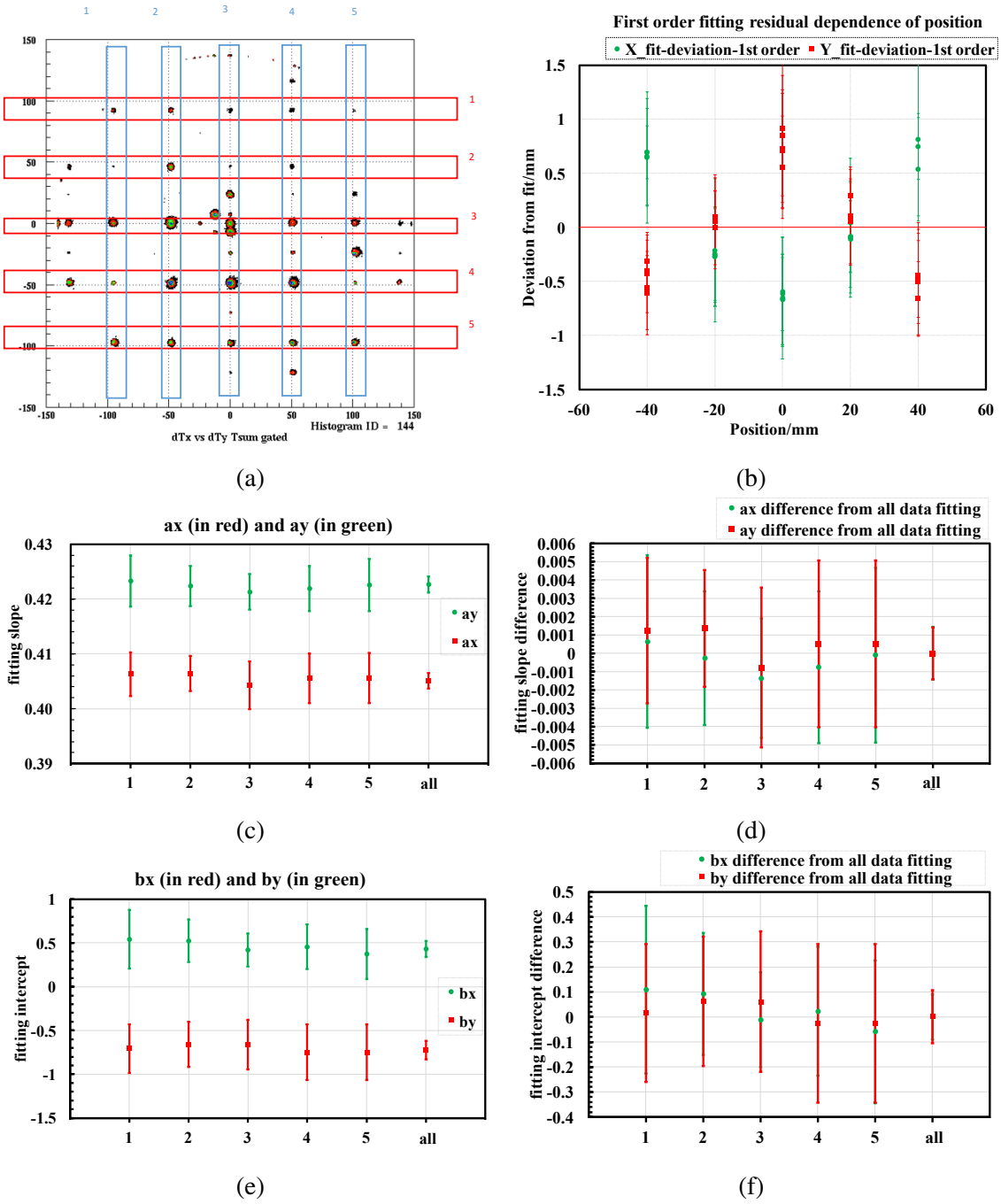

Fig. 5.12 (a) 5x5 lines separation of the mask holes for calibration. (b) First order fitting residual dependence of position. (c) a_x and a_y values from X- and Y-direction holes in five lines data fitting and all X-direction hole data fitting. (d) a_x and a_y values difference of X- and Y-direction five lines data fitting from all X-direction hole data fitting. Error bars are fitting error of the parameters. (e) b_x and b_y values from X-direction holes in five lines data fitting and all X- and Y-direction holes data fitting. (d) b_x and b_y values difference of X- and Y-direction five lines data fitting from all X- and Y-direction holes data fitting. Error bars are fitting error of the parameters. The a_x and a_y corresponds to the ns-to-mm parameter in X- and Y-direction for the delay-lines and a_x and a_y indicates the offset of mask center position to the MCP center position.

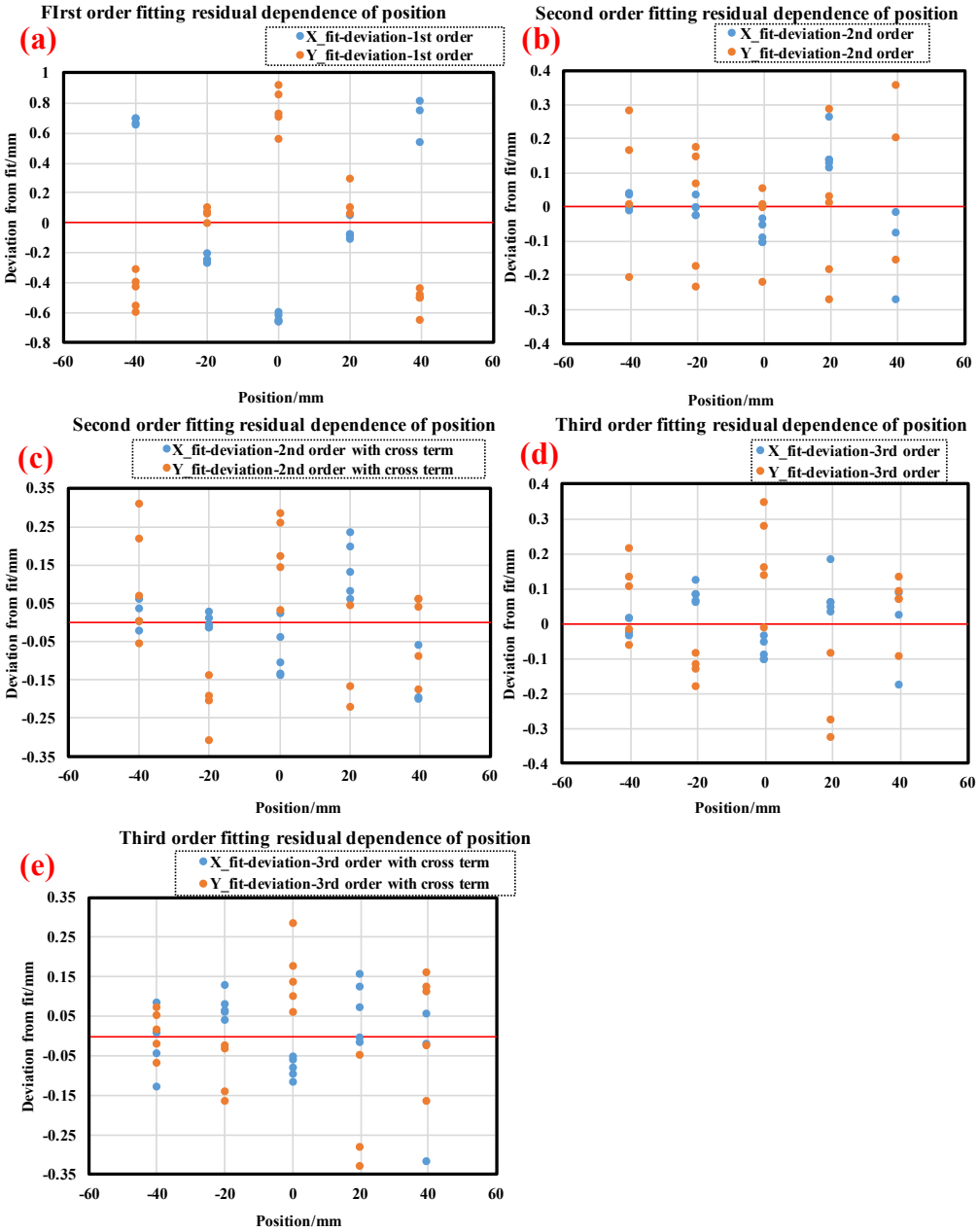

Fig. 5.13 Fitting residual dependence of position comparison of different calibration method. (a) First order calibration. (b) Secondary order calibration with cross terms in fitting. (c) Secondary order calibration without cross terms in fitting. (d) Third order calibration with cross terms in fitting. (e) Third order calibration without cross terms in fitting.

Table 5.1 Calibration parameters of 5 lines in X- and Y-direction of the delay-lines.

Fitting with x = $b_x + a_x \cdot$ dTx						
	X-line 1	X-line 2	X-line 3	X-line 4	X-line 5	overall point fitting (X)
Intercept b_x	-0.707702	-0.661598	-0.662116	-0.748605	-0.748605	-0.7231
Standard Error of b_x	0.2764	0.2586	0.2814	0.3168	0.3168	0.1061
Difference of b_x between every line and overall fitting	0.015474	0.061578	0.06106	-0.025429	-0.025522	0
Slope a_x	0.406305	0.40642	0.404292	0.405589	0.405589	0.40507
Standard Error of a_x	0.00397	0.003185	0.004358	0.004543	0.004543	0.00142
Difference of a_x between every line and overall fitting	0.001235	0.00135	-0.000778	0.000519	0.000522	0
Fitting with y = $b_y + a_y \cdot$ dTy						
	Y-line 1	Y-line 2	Y-line 3	Y-line 4	Y-line 5	overall point fitting (Y)
Intercept b_y	0.541947	0.525339	0.421485	0.455565	0.455565	0.43266
Standard Error of b_y	0.3352	0.244	0.1898	0.2568	0.2568	0.09071
Difference of b_y between every line and overall fitting	0.109286	0.092678	-0.011176	0.022904	-0.058754	
Slope a_y	0.423284	0.422366	0.421286	0.421889	0.421889	0.42263
Standard Error of a_y	0.004715	0.003265	0.003159	0.00414	0.00414	0.00143
Difference of a_y between every line and overall fitting	0.000645	-0.000273	-0.001353	-0.00075	-0.000106	0

points to their physical positions (X_p, Y_p) as closely as possible.The correction functions:

$$\begin{aligned} X_c &= p_0 + p_1 dT_X + p_2 dT_y + p_3 dT_X^2 + p_4 dT_X dT_Y \\ &+ p_5 dT_Y^2 + p_6 dT_X^3 + p_7 dT_Y^3 + p_8 dT_X^2 dT_Y + p_9 dT_X dT_Y^2 \end{aligned} \tag{5.3}$$

$$\begin{aligned} Y_c &= q_0 + q_1 dT_X + q_2 dT_y + q_3 dT_X^2 + q_4 dT_X dT_Y \\ &+ q_5 dT_Y^2 + q_6 dT_X^3 + q_7 dT_Y^3 + q_8 dT_X^2 dT_Y + q_9 dT_X dT_Y^2 \end{aligned} \tag{5.4}$$

where, $dT_X = T_{X1} - T_{X2}$ and $dT_Y = T_{Y1} - T_{Y2}$ timing difference of the both end delay-line signals of X and Y layer. In Eq. 5.3 and 5.4, (X_c, Y_c) is the corrected position of a calibration point with non-corrected timing difference (dT_X, dT_Y), and p_i and q_i (i= 0 - 10) are parameters determined by a fit using all the calibration points on an effective region $(-45\,mm \leq X \leq 45\,mm, -45\,mm \leq Y \leq 45\,mm)$ of the mask and setting (X_c, Y_c) to their physical positions. The regions near the outer edge of the MCP which have not good linearity are ruled out from the analysis. Then the position of all points on the active area of MCP is corrected using Eq. 5.3 and Eq. 5.4 with the parameter values listed in Tab. 5.2 associated with its corresponding physical position shown in Fig. 5.13. During the fitting,

cross terms is added or removed to give a insight into the effect of rotation from the mask by the fitting parameter values of the cross terms. A calibration parameters of 2D higher order (second/third) calibration methods with/without cross terms are listed in Tab. 5.2. From the magnitude of the values of the cross terms in the fitting functions, the values are relatively very small compared to the measurement dimensional parameter values. Thus the global rotation effect of the mask is very small so that it can be in ignored when using the same designed mask for calibration.

Table 5.2 list of calibration function and calibration parameters from ROOT linear fit. 2D higher order (second/third) calibration methods with/without cross terms are used.

calibration function	$X_c = p_0 + p_1 dT_X + p_2 dT_y + p_3 dT_X^2 + p_4 dT_X dT_Y + p_5 dT_Y^2$									
parameters p_i	p_0	p_1	p_2	p_3	p_4	p_5				
p_i	-0.1151391162	0.4061948945	0.0004874715	-0.0001355116	0.0000058578	0.0000028460				
p_i uncertainty	±0.1763247174	±0.0016732818	± 0.0016143547	± 0.0000266781	± 0.0000269608	± 0.0000260559				
calibration function	$Y_c = q_0 + q_1 dT_X + q_2 dT_y + q_3 dT_X^2 + q_4 dT_X dT_Y + q_5 dT_Y^2$									
parameters q_i	q_0	q_1	q_2	q_3	q_4	q_5				
q_i	-0.0053131984	-0.0002941808	0.4225033270	-0.0000097979	0.0000079603	0.0001235010				
q_i uncertainty	± 0.1763247174	± 0.0016732818	± 0.0016143547	± 0.0000266781	± 0.0000269608	± 0.0000260559				
calibration function	$X_c = p_0 + p_1 dT_X + p_3 dT_X^2$									
parameters p_i	p_0	p_1		p_3						
p_i	-0.1017072619	0.4063703461		−0.0001339538						
p_i uncertainty	±0.1379950025	± 0.0015989821		± 0.0000250306						
calibration function	$Y_c = q_0 + q_2 dT_y + q_5 dT_Y^2$									
parameters q_i	q_0		q_2			q_5				
q_i	-0.0392954449		0.4223870682			0.0001246970				
q_i uncertainty	± 0.1306475318		± 0.0015093588			± 0.0000255478				
calibration function	$X_c = p_0 + p_1 dT_X + p_3 dT_X^2 + p_6 dT_X^3$									
parameters p_i	p_0	p_1		p_3			p_6			
p_i	−0.1024330503	0.4039146329		−0.0001322314			0.0000003141			
$p_i uncertainty$	± 0.1380001074	±0.0043227573		±0.0000251886			±0.0000005138			
calibration function	$Y_c = q_0 + q_2 dT_Y + q_5 dT_Y^2 + q_7 dT_Y^3$									
parameters q_i	q_0		q_2			q_5		q_7		
parameters q_i	± -0.0462369473		± 0.4195638819			± 0.0001267703		± 0.0000003949		
calibration function	$X_c = p_0 + p_1 dT_X + p_2 dT_y + p_3 dT_X^2 + p_4 dT_X dT_Y + p_5 dT_Y^2 + p_6 dT_X^3 + p_7 dT_Y^3 + p_8 dT_X^2 dT_Y + p_9 dT_X dT_Y^2$									
parameters p_i	p_0	p_1	p_2	p_3	p_4	p_5	p_6	p_7	p_8	p_9
p_i	-0.1053315502	0.4037850141	0.0002858233	-0.0001360747	0.0000012873	0.0000072506	0.0000002515	-0.0000000615	0.0000001453	0.0000000659
p_i uncertainty	±0.1956941692	±0.0049738661	±0.0046070153	±0.0000306395	±0.0000290927	±0.0000328462	±0.0000005707	±0.0000005566	±0.0000005464	±0.0000004428
calibration function	$Y_c = q_0 + q_1 dT_X + q_2 dT_y + q_3 dT_X^2 + q_4 dT_X dT_Y + q_5 dT_Y^2 + q_6 dT_X^3 + q_7 dT_Y^3 + q_8 dT_X^2 dT_Y + q_9 dT_X dT_Y^2$									
parameters q_i	q_0	q_1	q_2	q_3	q_4	q_5	q_6	q_7	q_8	q_9
q_i	0.0269251083	-0.0000647272	0.4186714019	-0.0000203339	0.0001265038	0.0000080830	-0.0000000952	0.0000004853	0.0000000711	0.0000001324
q_i uncertainty	± 0.1956941692	± 0.0049738661	± 0.0046070153	± 0.0000306395	± 0.0000290927	± 0.0000328462	± 0.0000005707	± 0.0000005566	± 0.0000005464	± 0.0000004428

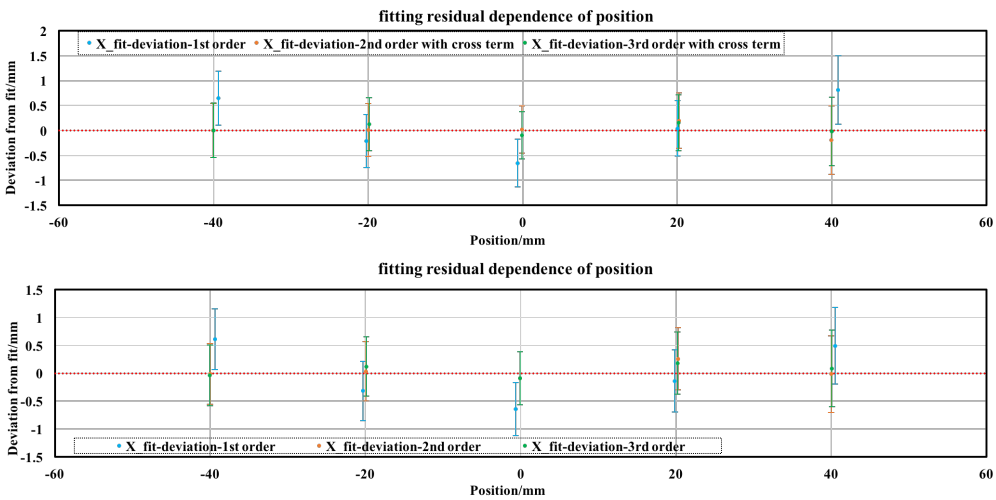

Fig. 5.14 Fitting residual dependence of position comparison of different calibration method to first order for one line of holes in X direction. (Upper) comparison of first order calibration, secondary order calibration with cross terms in fitting, and third order calibration with cross terms in fitting. (Lower) comparison of first order calibration, secondary order calibration without cross terms in fitting, and third order calibration with cross terms in fitting.

To test the performance of this position calibration method, we utilize the calibration parameters from one calibration run to correct another data set which is taken under the same conditions but statistically independent from the calibration run. A correction vector $\vec{V}_{ij}$ of each spot, which shifts the measured values to the expected mean values, is employed:

$$\vec{V}_{ij} = (X_{expected,ij} - X_{measured,ij})\vec{e}_x + (Y_{expected,ij} - Y_{measured,ij})\vec{e}_y, \tag{5.5}$$

where $X_{measured,ij}$, $Y_{measured,ij}$ are the expected X value and Y value, $X_{measured,ij}$, $Y_{measured,ij}$ the measured X value and Y value, and $\vec{e}_x$ and $\vec{e}_y$ the unit vectors in X- and Y-direction. The resulting correction matrix $\vec{V}_{ij}$ shifts each measured mean value to its expected position on the mask. A 2D vector field figure as shown in Fig. 5.15 displays the correction vector $\vec{V}_{ij}$ of each spot shifts on the mask with the angle and magnitude (line length) shown. For better visibility the magnitudes of the vector, the values are enlarged by a factor of 5. The edge of the active area of the MCP is marked by the dashed blue circle. As can be seen in the Fig. 5.15, the deviation amplitudes of the secondary order fitting are much smaller at each point than the first order fitting, which verifies that higher order correction is necessary and shows a better accuracy. Besides, a curl in the direction of the vectors is not observed in the first order fitting vector field map, the negligence of a rotation in the XY-plane seems to be reasonable. From Fig. 5.15a, the first order correction map, larger deviations comes up near the edge of the delay-lines. This data set was taken under the same conditions but statisti-

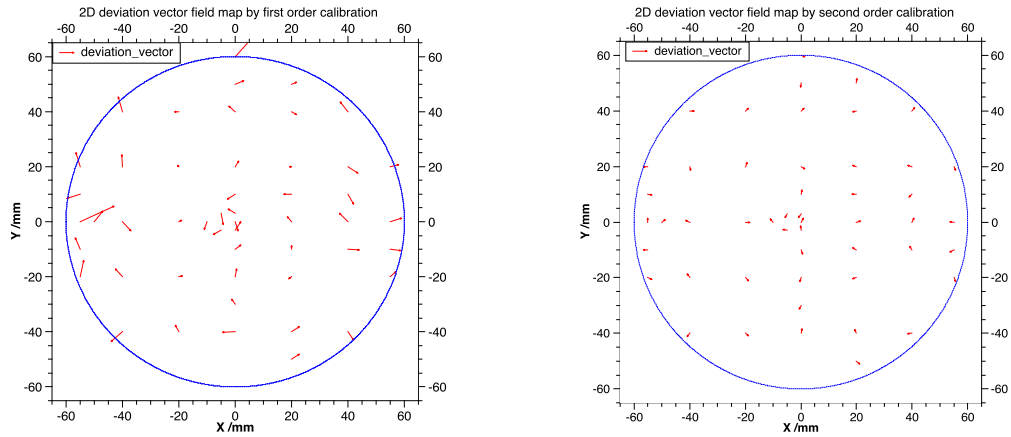

(a) (b)

Fig. 5.15 Vector field map of the correction vector $\vec{V}_{ij}$ created from the difference of the expected and the calibrated/measured mean values for each hole center spot. (a) shows a first order correction map and (b) illustrates a second order correction map. The lengths (magnitude) of the vectors are enlarged by a factor of 5 for better visibility. The edge of the active area of the DLD120 is marked by the dashed blue circle.

cally independent from the calibration run. Therefore, it is appropriate to use this data set to extract the MCP position resolution and the accuracy of this calibration scheme. The deviations of x and y coordinates from their physical values were calculated. The distributions of the deviations with the uncertainties of the measurements in the X and Y directions are shown in Fig. 5.14. The average absolute deviation (accuracy) of second order or third order correction with/without cross terms amounts to $\leq 82\ \mu m$ and $\leq 147\ \mu m$ for x and y coordinates, much smaller than the correction by first other of ~0.4 mm. The root-mean-square (RMS, resolution: σ_x, σ_y) of the higher other deviation distributions are all ≤ 0.068 mm and 0.142 mm for x and y coordinates, and in this test the maximum deviation is < 0.4 mm as shown in Fig. 5.14. For the radial position resolution, we transform X- and Y-resolution as follows:

$$R_{xy} = \sqrt{{\sigma_x}^2 + {\sigma_y}^2}. \tag{5.6}$$

Therefore, the radial position resolution: $R_{xy} = \sqrt{0.68^2 + 0.142^2} = 0.157\,mm$.

We also investigated the stability of the calibration by different HV supply and different environmental conditions (vacuum), and no significant drift was observed within the relative difference of the most important time-to-ns parameter p_1, q_2 in Eq. 5.3 and Eq. 5.4 or a_x, a_y in Eq. 5.1 in the order of $< 1.2\%$, which means in every 1.0 mm, shift of the position is less than 12 μm. This means good local quality of the dealy-lines and the parameters of ns-to-mm can be treated as constant.

In summary, when carrying out calibration, for every calibration run, we need to make sure that the events number for calibration should be large enough. In the calibration run in this context, at least 1 million events is ensured. From the first order and higher order calibration method comparison, the higher order is needed and secondary order is enough to pin down the position dependence of the deviation of fitting. As the rotation effect for the now designed mask is very small and secondary order calibration without cross terms is reasonable and good enough for the required precision and accuracy for our detector system (1 mm resolution in σ). Secondary order calibration with cross terms is desired to achieve relative higher accuracy and precision with rotation effect correction included. In different experiments, when using the delay-line anode, conventionally, only the offset values need to be reset and the other calibration parameters can be kept same, thus making the utilization of the MCP detectors easier. But anyway, we have to check the calibration parameters time by time to ensure the stability of the performance of the delay-lines. This will be discussed in the online test experiments in next section.

Discussion of performance of DLD120 system

The sum of the two corresponding delay-line timing $T_{X\,sum} = T_{X1} + T_{X2}, T_{Y\,sum} = T_{Y1} + T_{Y2}$ in some experimental runs demonstrates two peaks which should in principle be constant and show a well defined peak. One reason for occurrence of the double peaks maybe from the walk of the electronics, especially when a lot of modules and many cables are used as the requirement of use of connection panels for long transmission of signals. Importantly, the CFD should be well tuned to eliminate the walk effect when using a leading edge discrimination. Another reason that can be seen from the 2D spectrum as shown in Fig. 5.16 is that the deformation of the T_{sum} signals at the edge of the delay-lines. A relative smaller deformation of T_{sum} at the centeral area of the delay-lines are also observable. To have a better investigation of the original T_{sum} information of the dealy-lines, a gate on one hole of the imaging of the mask are applied to remove the position dependence of the T_{sum}. The gated $T_{X\,sum}$ and $T_{Y\,sum}$ spectra are shown in Fig. 5.17.

To make a rough estimate of the intrinsic position resolution, the sum of the arrival times can be utilized for simple case. In principle, a sharp peak is expected at a defined position which is broadened by the signal processing. For the standard deviation of this $T_{X\,sum}$ and $T_{Y\,sum}$ peak, we find the following relation:

$$\sigma(T_{X\,sum}) = \sqrt{\sigma(T_{X1})^2 + \sigma(T_{X2})^2} = \sigma(dT_X), \tag{5.7}$$

$$\sigma(T_{Y\,sum}) = \sqrt{\sigma(T_{Y1})^2 + \sigma(T_{Y2})^2} = \sigma(dT_Y). \tag{5.8}$$

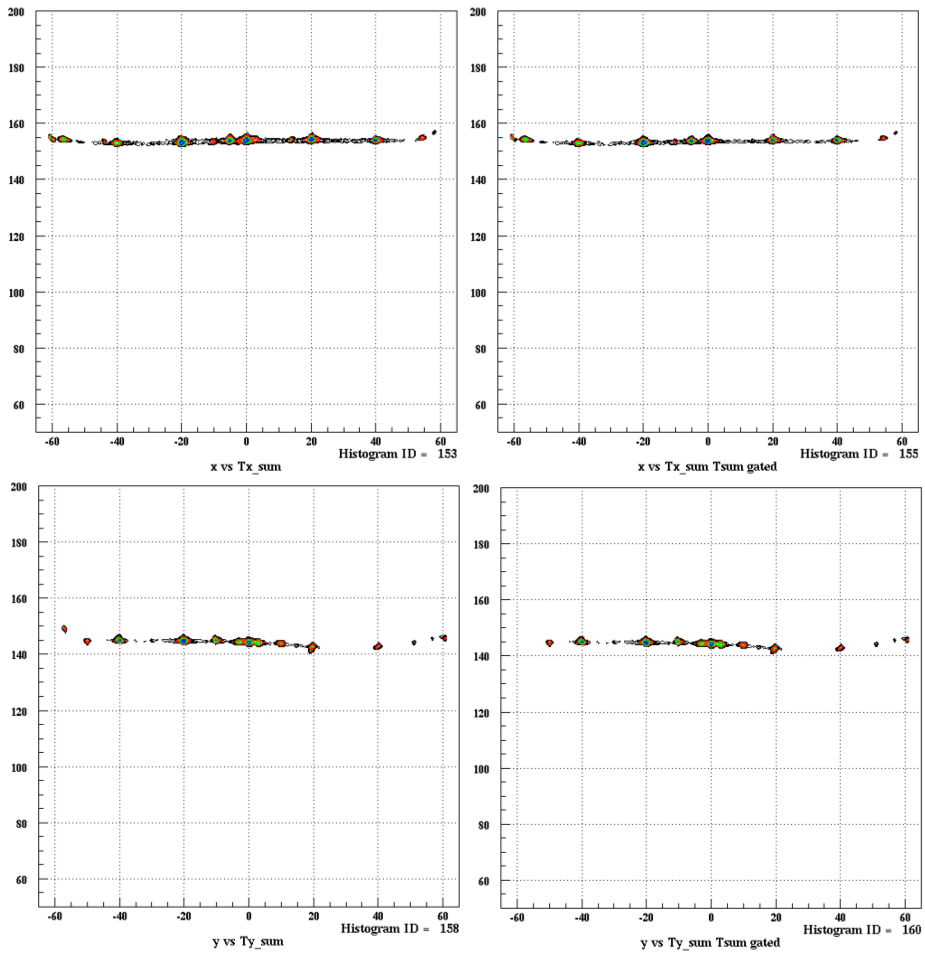

Fig. 5.16 (Upper) figures show the $T_{X\,sum}$ and gated $T_{X\,sum}$ as a function of the X position. (Lower) figures demonstrate the $T_{Y\,sum}$ and gated $T_{Y\,sum}$ as a function of the Y position. The gate is done by a 3σ gate of the sum information of the delay-lines. It illustrates that a large dependence of the position of the sum timing information for the edge area of the delay-lines and small ununiform of the sum of both ends of timing information appears for the centeral area of the delay-lines.

The standard deviation of the sums of two corresponding delay-line signals should be equal to that of the differences ($dT_X = T_{X1} - T_{X2}, dT_Y = T_{Y1} - T_{Y2}$). As the position is encoded by the difference of the timing difference of the delay-lines (dT_X and dT_Y), it will give an estimation on the position resolution. $T_{X\,sum}$ and $T_{Y\,sum}$ have standard deviations of about $\sigma(T_{X\,sum})$, $\sigma(T_{Y\,sum}) \sim 0.3\,ns$ (Fig. 5.17). Utilizing the conversion factor ($\sim 0.4\,mm/ns$) we find: $\sigma(T_{X\,sum}) \simeq 0.3\,ns \times 0.4\,mm/ns = 0.12\,mm, \sigma(T_{Y\,sum}) \simeq 0.3\,ns \times 0.4\,mm/ns = 0.12\,mm$, which is consistent with the given resolution of $\sim 0.1\,mm$ from the manufacturer [140]. The overall linearity can be estimated from the sum of timing information of the delay-lines of overall range of the delay-lines without position gate. The $T_{X\,sum}$ and $T_{Y\,sum}$ peak in Fig. 5.8 with a gaussian fit with a resulting $\sigma \sim 600$ ps indicates a linearity of about 0.4 mm/ns x 0. 6 ms = 0.24 mm. As the delay-lines signal actually form a covered area and the typical on-line sum information has a σ of ≤ 1 ns which corresponding to 0.4 mm of linearity for the delay-lines. The charge information of the delay-line signals are acquired

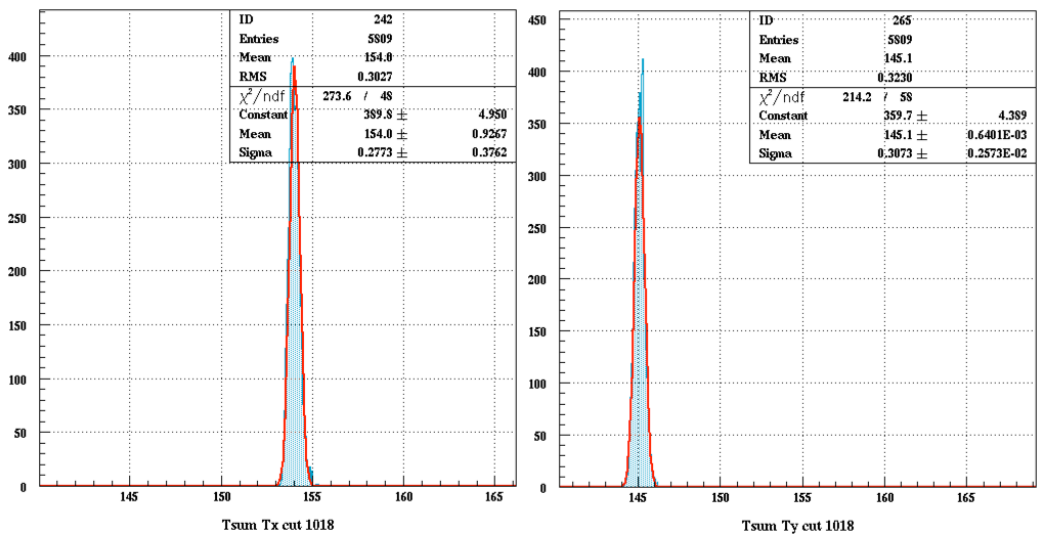

Fig. 5.17 Histogram spectra of the sum of timing at both ends of the delay-lines of X- and Y-coordinates $T_{X\,sum}$ and $T_{Y\,sum}$ with a position gate on one of the imaging holes of the mask.

and the 2D histograms of the charge information are shown in Fig. 5.18, Fig. 5.19. As can be seen from Fig. 5.18, Fig. 5.19, the raw charge amplitude (judgement of sensitivity when the MCP radiated by a source of uniform intensity and distribution) have a position dependence. This is consistent with the results shown in Fig. 5.21a, which is from a background run without mask mounted on the MCP front plate and only with the gauge on as a source to illuminate MCP. This phenomenon can be also observed in Fig. 5.6, as the sizes of the holes on the mask have only two values, 0.5 mm and 1 mm in diameter, but the counts during a

same time of data acquisition are varied from hole to hole with far more than two different vaules. Typically, as shown in the Fig. 5.18, Fig. 5.19, the timing and position information (timing difference) has no dependence of the charge accumulated by the delay-lines as the CFD can remove the slew effect and provides amplitude-independent precise timing of the amplified pulses.. In Fig. 5.20, it illustrates that the charge of electron clouds from the MCP rear side shared by both ends of the delay-line have a relative steady ratio corresponding to the linearity of the QX1 versus QX2 and QY1 versus QY2 2D histogram spectra. A histogram describing the timing of the MCP and charge information of the MCP is shown in Fig. 5.21b.

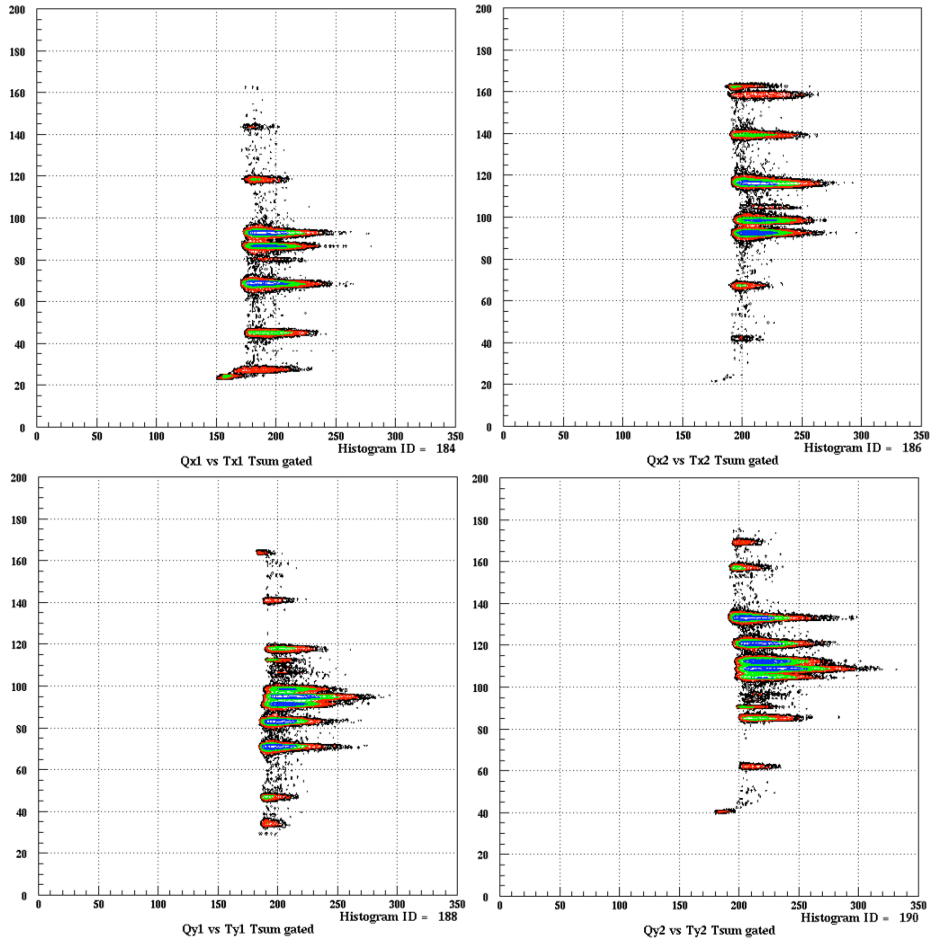

Fig. 5.18 Histogram spectra of Charge (raw) versus Timing (ns) for X1, X2, Y1, Y2. The signals are with the sum of timing at both ends of the delay-lines of X- and Y-coordinates gated.

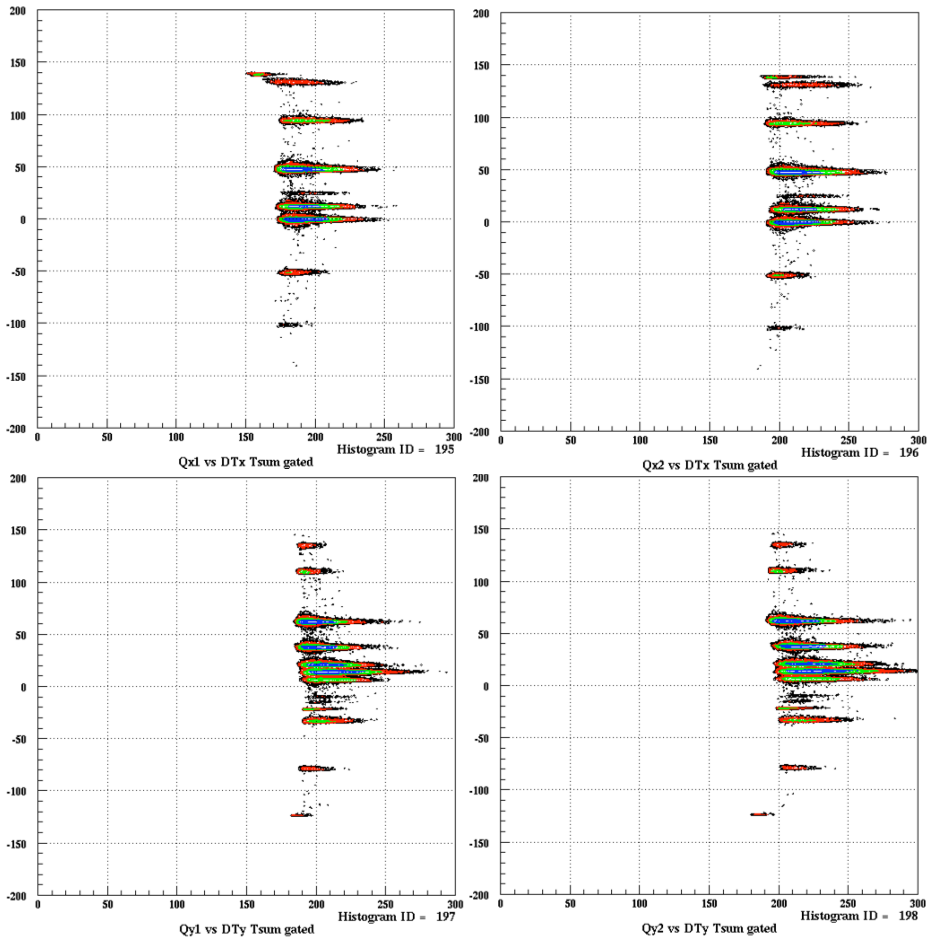

Fig. 5.19 Histogram spectra of Charge (raw) versus delay-line Timing (ns) difference (Q_{X1} versus dT_X, Q_{X2} versus T_X, Q_{Y1} versus dT_Y), Q_{Y2} versus dT_y. The signals are with the sum of timing gated.

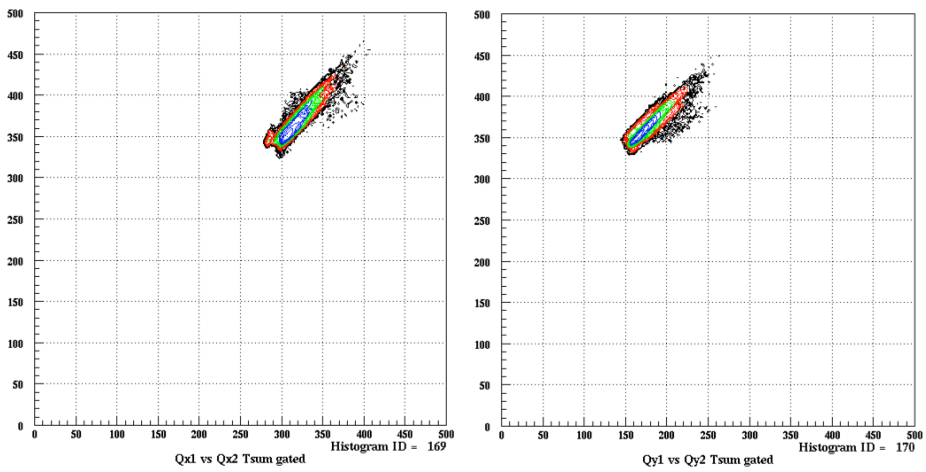

Fig. 5.20 Histogram spectra of Q_{X1} versus Q_{X2} and Q_{Y1} versus Q_{Y2} with the sum of timing gated.

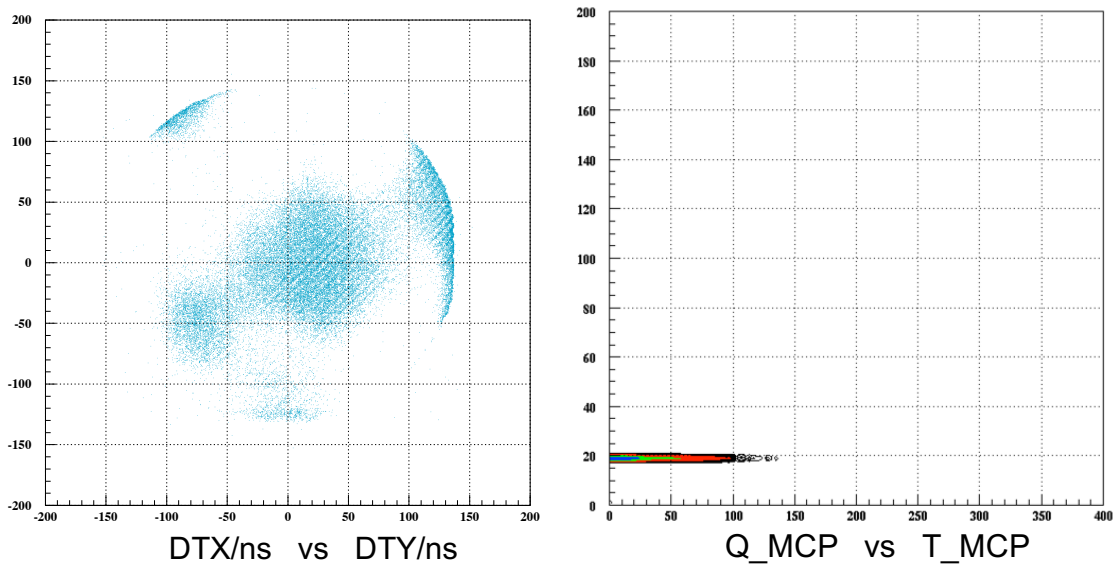

(a) (b)

Fig. 5.21 (a) dT_x versus dT_y in a background run without mask and only gauge on as source and (b) Q_{MCP} versus T_{MCP} 2D histogram spectrum in a calibration run with mask on and gauge as source

5.2 Offline test of the electrostatic detector with DLD120

5.2.1 Experimental setup and basis of analysis

The principle of the position detection and timing measurements of the electrostatic mirror detector has been described in Chapter 2, which is based on the detection of SEs emitting from a negatively biased thin-foil, when passing through by ions. The accelerating potential is defined as the potential difference between the accelerating grids and the conversin foil. After acceleration, the electrons are deflected by the electrostatic outer mirror directly on the MCP surface, and the deflection potential is defined as the potential difference of the outer and inner mirror.

The the most first designed detector system (Fig.5.22) was for the rectangular MCPs with resistive anode and the specification of the rectangular MCP detector is shown Appendix. B. As the performance of the designed anode from Photonics was bad and not solved by the company even with output signal performance, we change the anode of the MCP to delay-lines. For very early tests of the delay-line detector system (dimensions shown in Appendix. C) with circle-type MCPs (120mm in diameter), the trigger signal from the MCP back/front was chosen for easy case as shown in the Right of Fig. 5.23. The testbed and the electronics (shown in Fig. 5.4) were same as for the calibration of the DLD120 system. As the detector

Fig. 5.22 A photo of detector with rectangular Chevron MCPs (190 mm x 42 mm, two segments of 95.00 mm x 42.00 mm)

structure was put inside together with the DLD120 system, the vacuum condition, worse than calibration condition, for a long time was kept around the level of 3×10^{-3} Pa ($3\times10^{-5}mbar$), which was one order worse than the requirement of the operation vacuum of the MCP from the manual of the value of $2\times10^{-6}mbar$. Big efforts to solve the background of the test were done (including well tuning of CFD, noise deduction from the electronics and pumps, sum information utilization in the analysis). A turbo-molecular pump was mounted on the interconnecting tube through the right part of the bottom plate of the chamber and connected to a rotary pump. To further remove the background and make the test more efficiently, we finally use a plastic scintillator as a trigger (the coincidence signal of the both left and right from alpha source) of the DAQ system, the circuits of which is shown in Fig. 5.24.

The basic mechanical setup used to test for the BPM-TOF detector is depicted in the schematic drawing of Fig.setup-offline-test.pdf. To calibrate the detector and check the position resolution of detector with collimated holes and position reference, two masks system are used. The CAD drawing of the masks are shown in Fig. 5.25.

The connection system of the old mask system is shown in Fig.setup-offline-test.pdf. At central area of the old mask, symmetrically arranged 0.5 mm holes with 10mm distance are dug, and 0.5 mm holes with a horizontal (x-direction) distance of 30mm in pitch are at side area. The vertical (Y-direction) distances for all holes are all 10 mm. In Fig.setup-offline-test.pdf, the old mask are installed on the detector system just in front of the accelerating potential plate. The 10-6.5mm no threaded holes on the mask are used for the connection with the accelerating plate.

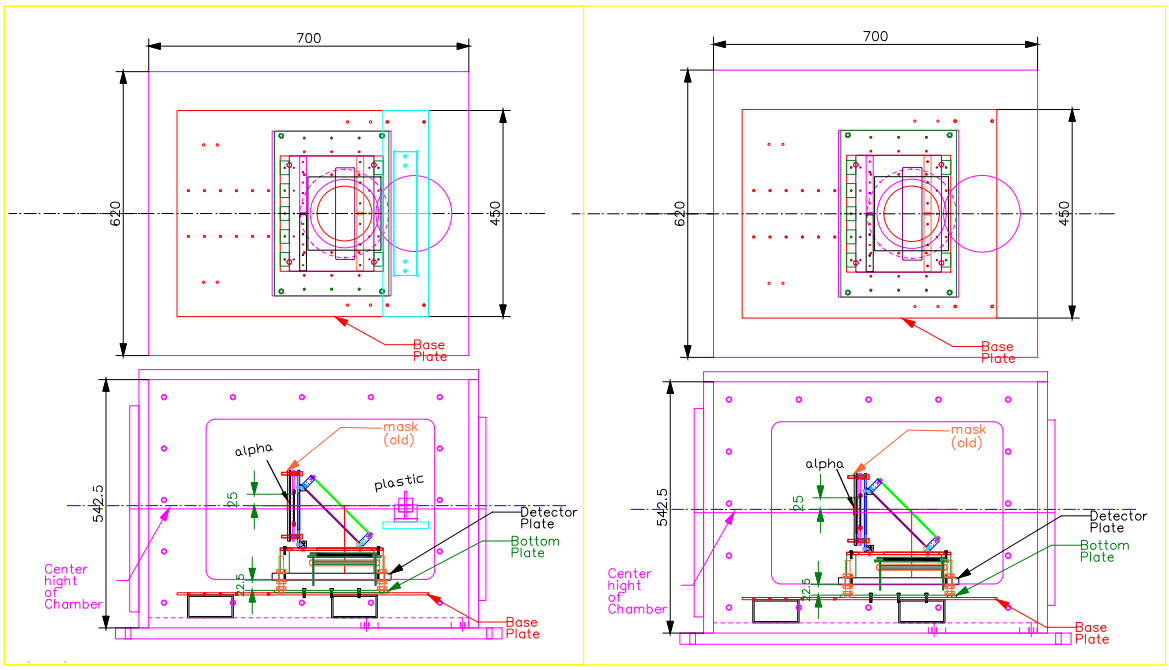

Fig. 5.23 Schematic (side/top) view setups for offline test. The Left figure demonstrates the test using alpha and plastic scintillator as trigger. The Right illustrates the test without scintillator as trigger. Three sealed alpha sources (^{241}Am with intensity of 4M Bq) are used optionally.

As the old mask can not adjust distance (at least 12 mm, and 0.5 mm in diameter collimated hole will disperse to be 3.5 mm in diameter circle source on the foil) much nearer to the foil, the new mask was designed with a holder system (holding the alpha source and the mask on the detector system) to adjust the distance of the mask to the foil. The assembly diagram of the new mask system is shown in Appendix. C. This consideration is discussed in Section. 4.7 and a Fig. 4.19 well illustrates the influence of the hole sizes on the mask when using it for checking the position resolution. and the influence of the source size for checking the resolution of the imaging was discussed.There are 5 number of 0.5 mm holes near the center of the new mask and other holes are 1 mm in diameter. The 4-M3 threaded holes on the mask are used for the connection with the support plate as shown in Appendix. C. In one test run for calibration we set the 3 alpha sources (^{241}Am) with same intensity of 4 M Bq at the hole places of (-30 mm, 0 mm), (0 mm, 0 mm), and (30 mm, 0 mm) on the mask with hole size of 1 mm, 0.5 m and 1 mm in diameter respectively. In another test run we set two alphas at the hole places of (0 mm, 15 mm), (0 mm, -15 mm) and the hole sizes are both 1mm in diameter. The two data run are accumulated in one analysis. For these two runs, the DLD120 system is operated in ion mode with the holder HV of +2650, and detector triangular potential plates (Δ) at a high voltage of 0 V, accelerating plate (Acc.) HV

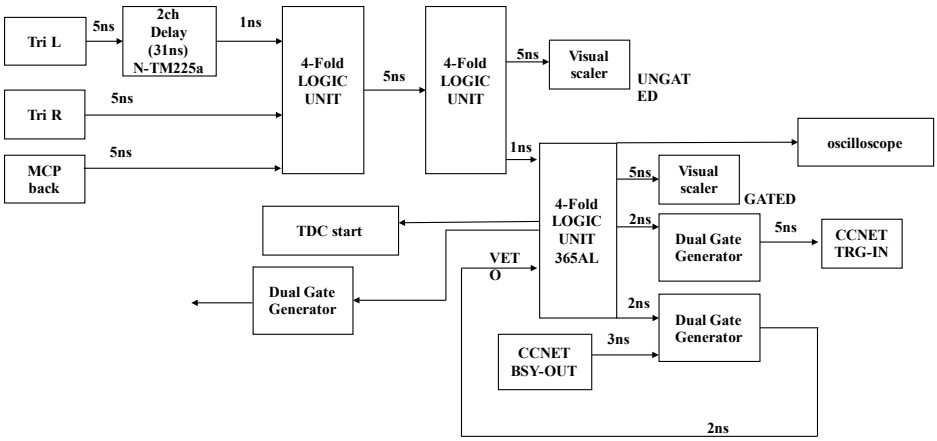

(a) Block diagram of readout electronics for trigger circuit (Plastic signals as trigger)

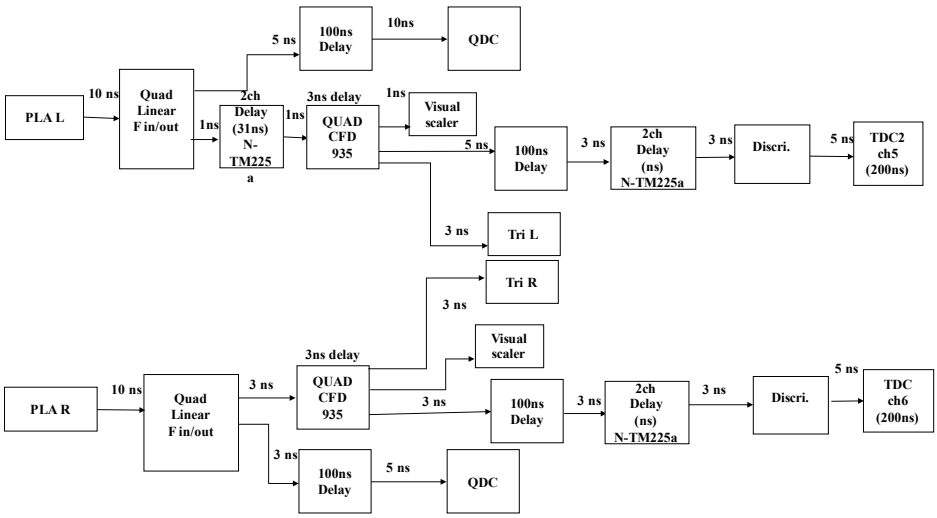

(b) Block diagram of readout electronics for plastic left and right signals

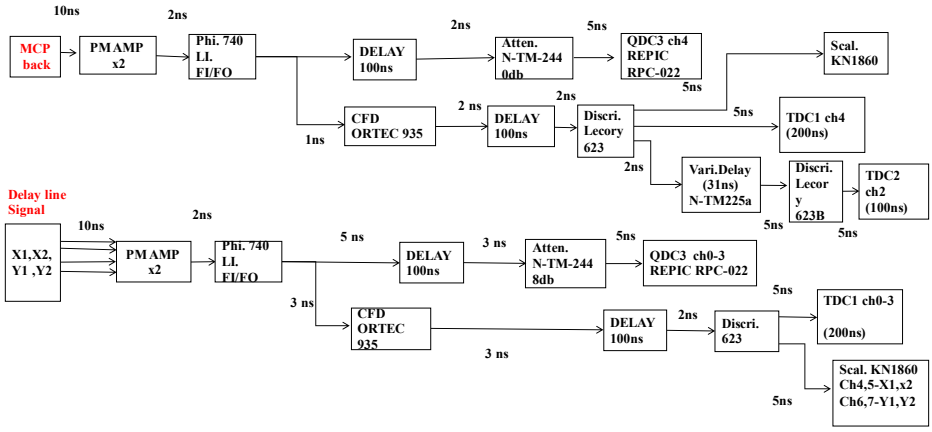

(c) Block diagram of readout electronics for the MCP and delay-line signals

Fig. 5.24 Block diagram of readout electronics for the delay-line MCP detector using coincidence signal of plastic left and right signals as trigger. The circuits are close to the circuit by using MCP signal as trigger.

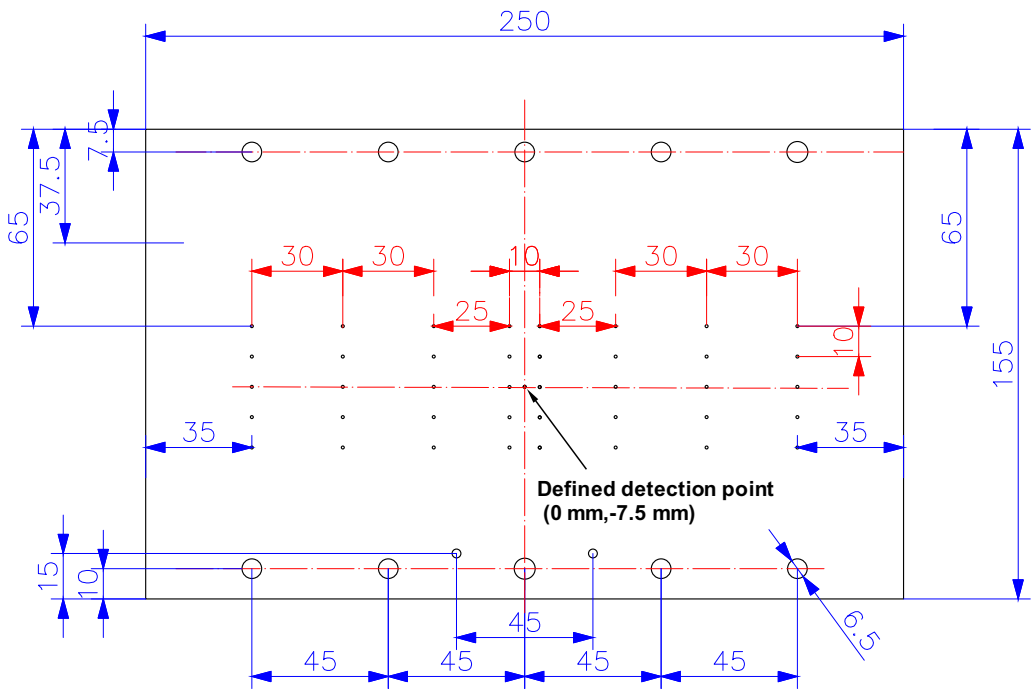

(a) Old mask.

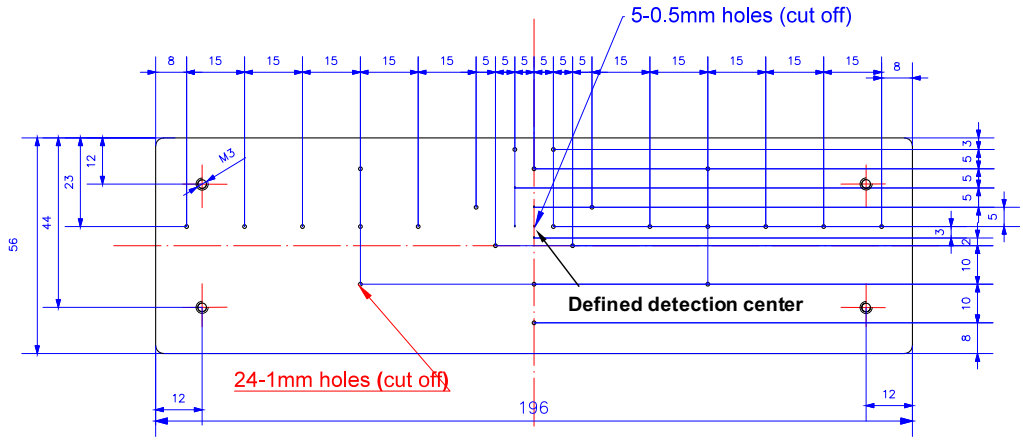

(b) New mask.

Fig. 5.25 Schematic drawing of a multi-hole masks used for tests. The dotted circles in center of the masks are collimated holes for tests. As the old mask can not adjust distance (at least 11 mm) much nearer to the foil, the new mask was designed with a holder system to adjust the distance of the mask to the foil. The assembly diagram of the new mask system is shown in Appendix. C. The distance of foil and the new mask can be adjusted as closer as possible, and the typical distance for the mylar foil to the mask about 1 mm, while for the carbon foil about 2-4 mm to avoid touch as the friability at the extremely thin thickness and easy shape deformation. The thicknesses of the masks are both 4 mm.

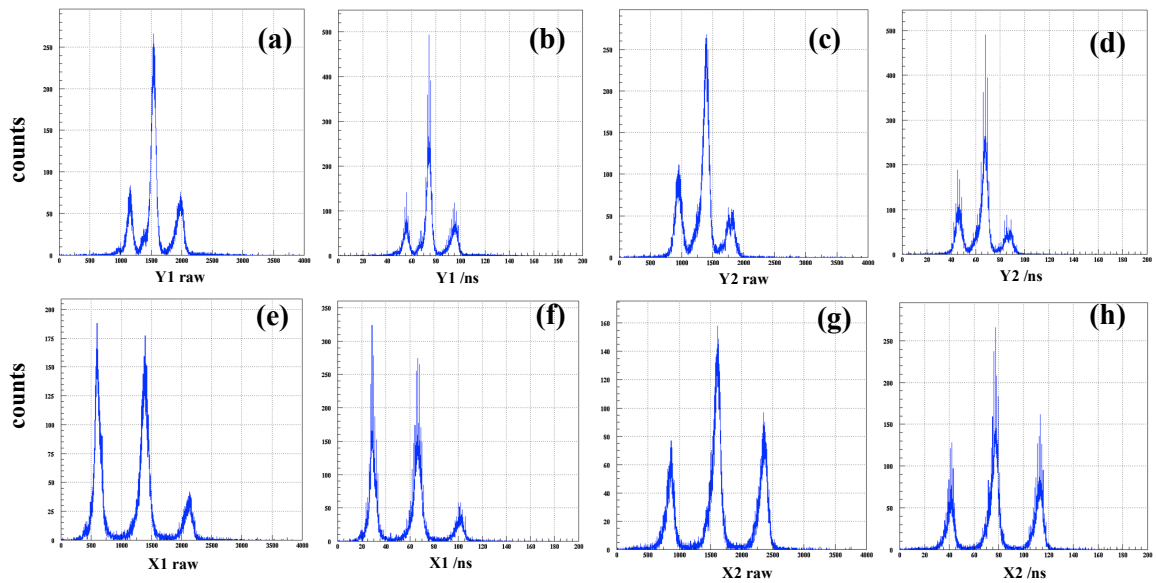

Fig. 5.26 The raw timing signals and calibrated timing signals from both ends of the delay-lines in BPM-TOF system. The source are five holes with collimated alpha.

of -6000 V, outer mirror grid (Mir.) HV of -4668 V. Different to the signals from calibration run, the signals for the electrostatic detector test are from accelerated SEs (typical 500-6000 keV) by the accelerating grids from the conversion foil bending onto the MCP by the mirror grids other than the α/ion from gauge interacting with MCP. The raw timing signals and calibrated timing signals from both ends of the delay-lines are shown in Fig. 5.26[2]. The timing difference $dT_X = T_{X1} - T_{X2}, dT_Y = T_{Y1} - T_{Y2}$ (upper 2 histograms Fig. 5.27) are converted to position information (lower 2 histograms of Fig. 5.27) by the calibrated parameters from Eq. 5.3 and Eq. 5.4 in second order. The 2D histograms of the timing difference and converted 2D position imaging is shown in Fig. 5.28. As there are some alignment offsets of the detection center of the detector and the measurement center of DLD120, the center hole imaging from the mask is off center of the DLD120 system. During every measurements, the sum information of Timing from both ends of the delay-lines should be take into consideration to remove ghost events. Alternative ways to show the timing information qualities which are also discussed in previous Section. 5.1 and the similar figures ($TY1$ vs $TY2$, $TX1$ vs $TX2$, Y vs TY_{sum}, X vs TX_{sum}) are shown in Fig. 5.29. During the analysis, gates are utilized to remove the far away peaks from the main TY_{sum}, TX_{sum} peak. After the sum information analysis, the geometrical offsets from many sources, such as detector system alignments offsets (~1-2 mm shifts), walk of MCP (~ 1 mm), DLD120 XY tilted

[2]In this context, the author have a preference of axises on each figures as 'A vs B' corresponding to 'X axis versus Y axis'

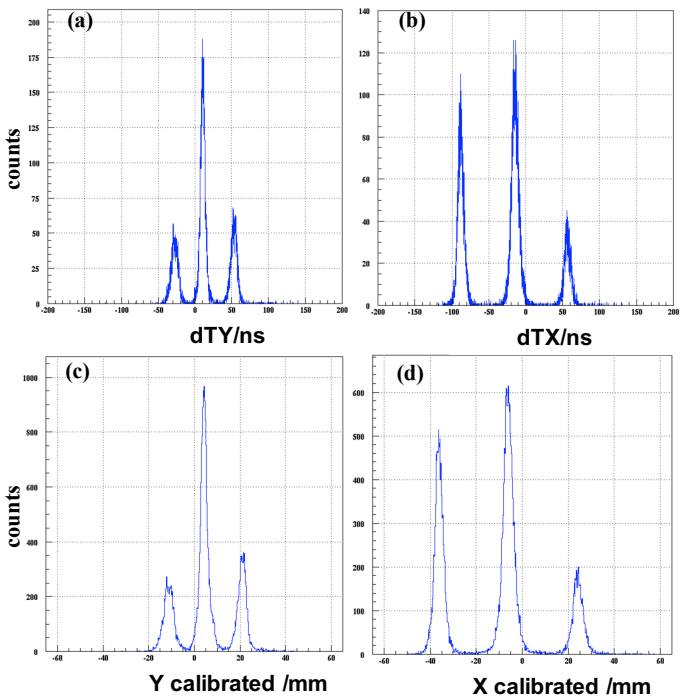

Fig. 5.27 Timing difference of Y- and X-coordinates (a, b) and calibrated position of Y and X (c, d).

($\sim$ 1-2 mm), difference of geometrical design requirements from manufacturer ($\leq$ 0.5 mm), are inserted into the analysis code to compensate the overall offset and shift the imaging of the mask center position measured on DLD120 to the center. The offsets are from the gaussian fitting (upper 2 histograms Fig. 5.30) from the original imaging histograms of X and Y on the DLD120, and after inserting of the offset in the code, the imaging histograms are shown in the lower histograms of Fig. 5.30. The final calibrated 2D alpha-source imaging histogram of the 5 collimated holes is shown in Fig. 5.31a with projection histograms on the X and Y-coordinates. The imaging of separated runs of 3 and 2 holes are illustrated in Fig. 5.31b. The figures to show the charge dependence of timing and timing difference (or position) are displayed in Fig. 5.32. The relationship of the collected charge clouds at both end of delay-lines is demonstrated in Fig. 5.33. The Fig. 5.32 and Fig. 5.33 are important tools for ruling out false events in the heavy ion beam experiments and as the yields of SEs have a dependence of the Z (proton number) of incident ions, the charge information can be directly used for particle identification. As shown in Fig. 5.30, gaussian fittings are carried out for the projection histograms of a hole's imaging on the X and Y-coordinates, and the sigma of the fitting is used to indicate the resolution of the electrostatic detector (E-detector) system. As described from simulation previously, the hole size of the source has influence

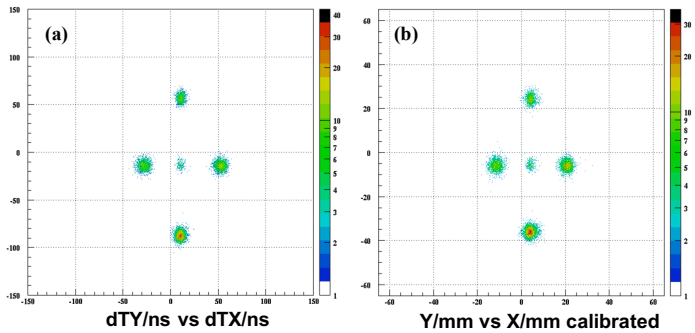

Fig. 5.28 2D histograms of timing difference and calibrated position Y versus X.

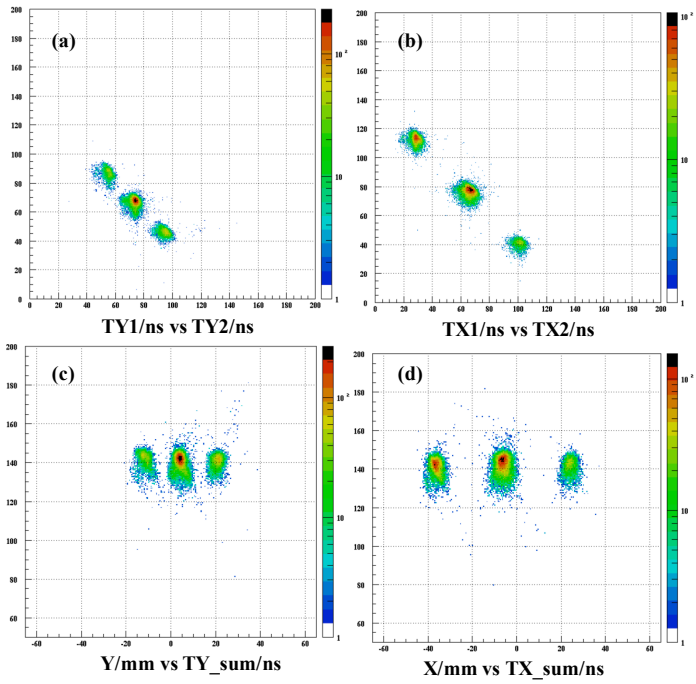

Fig. 5.29 TX1 vs TX2, TY1 vs TY2 and sum of timing as a function of timing difference on Y- and X-coordinates.

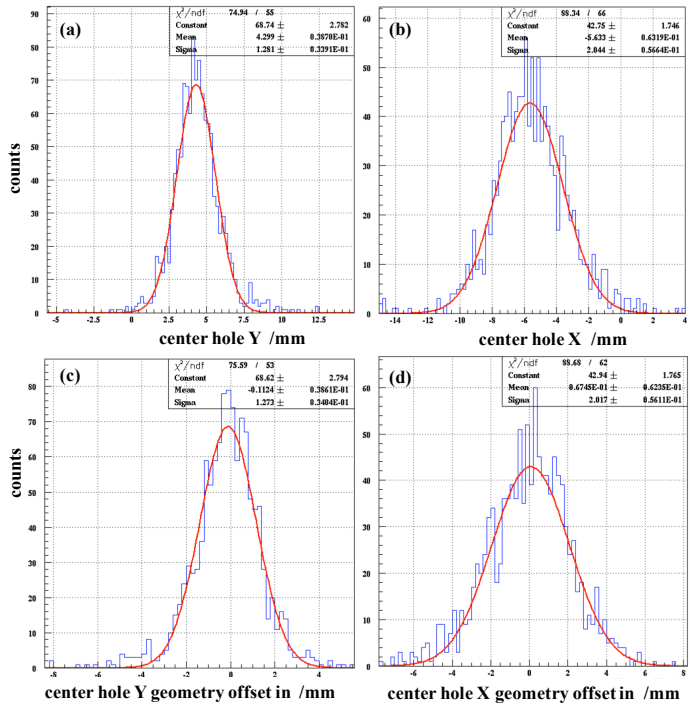

Fig. 5.30 Center point geometry offset measurements (fitting center value of 4.299 and -5.633) and view of calibrated final enter position.

on the resolution check of the E-detector, thus to get better description of the intrinsic resolution of the detector, small collimated hole as possible is desired. The detection ratio of the measured signal number (4 timing signals in coincide) on both ends of the delay-lines to the triggered events number by the plastic scintillator represents the efficiency and detection probability of one ion of the detector.

5.2.2 Offline test results with alpha source

Position resolution and accuracy check

Test with Mylar foil coated with aluminium To utilize the Electrostatic detector (E-detector) at the beam-line for position and timing measurements, a large size mylar foil (1-2 μm in thickness) coated with aluminium will be used as the conversion foil for SEs emission. In the offline test, as its robust properties and flatness of the surface, it is a good choice for test of position performance in low vacuum condition with 3 sealed high intensity α source ^{241}Am ($\sim$ 4 x 10^6 counts/s). The first designed mirror detector with the mirror grid pitch of 3 mm have been tested with the “electron mode” and the distance of the accelerating grid to

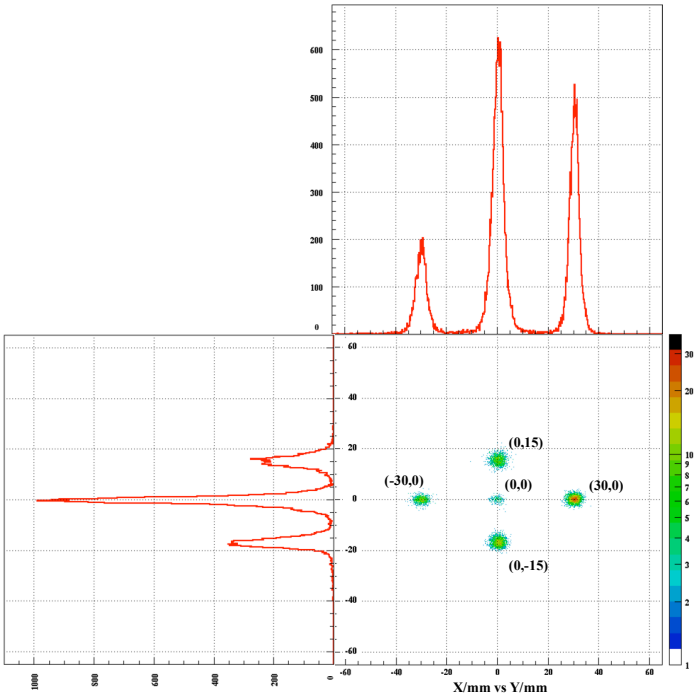

(a)

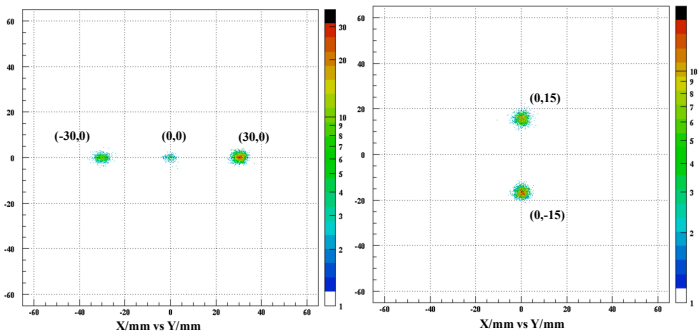

(b)

Fig. 5.31 (a) The final calibrated 2D alpha-source imaging histogram of the 5 collimated holes with projection histograms on the X and Y-coordinates. (b) The 2D imaging histogram of separated runs of 3 and 2 holes.

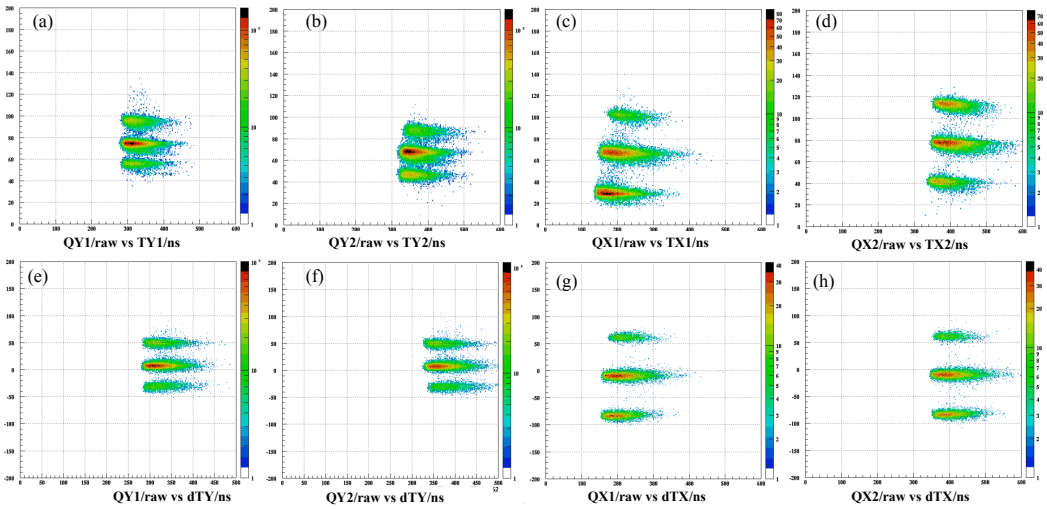

Fig. 5.32 Charge dependence of timing and timing difference for SEs emitting from collimated 5 holes though α.

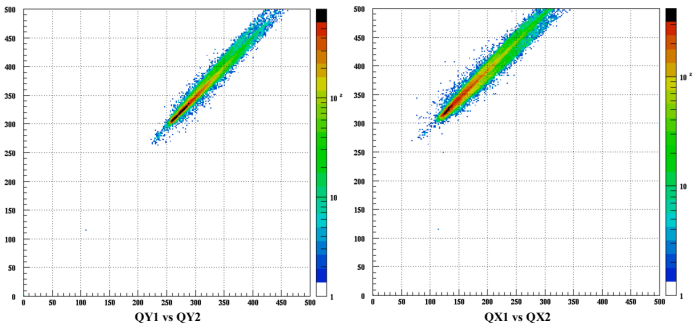

Fig. 5.33 Charge relationship of collected electrons from SEs induced by collimated α on X and Y-direction of delay-lines.

the foil of a distance of 8 mm is kept. The testbed is shown in the left side of Fig. 5.23 and alpha sources are paster on the old mask in front of the accelerating grid.

1. Test of **effect of accelerating HV varying to the resolution for 3 mm pitch mirror grid** is shown in Fig. 5.34. As can be easily seen from the trends of the resolution, the increasing of accelerating HV will results in better position resolutions for both X- and Y-direction.

2. **Accuracy check of for 3 mm pitch mirror grid by varying outer mirror HV with accelerating grid HV of -6000 V** is shown in Fig. 5.35. The deviations of the measurements from the real distance difference of the two holes are all in the range of the error bars (uncertainty of the measurement).

3. **Position resolution comparison of 1 mm and 3.5 mm distance of the MCP front plate to the bottom plate of Electrostatic detector** (3 mm grid pitch of mirror) is shown in Fig. 5.36. E-detector runs in in "ion mode" with 3 mm pitch mirror grid. The resolutions for same HV setting for the two cases do not change much due to the distance change of the MCP front plate to the bottom plate of Electrostatic detector, and the trents of outer mirror HV dependence of resolution for the two cases are the same.

4. **Position resolution of X and Y direction by keeping the ratio of accelerating potential and the deflection potential at 0.778** (3 mm grid pitch of mirror) is shown in Fig. 5.37. It obvious that as the increasing of the HV of accelerating potential and the deflection potential, the resolutions of X and Y get improved.

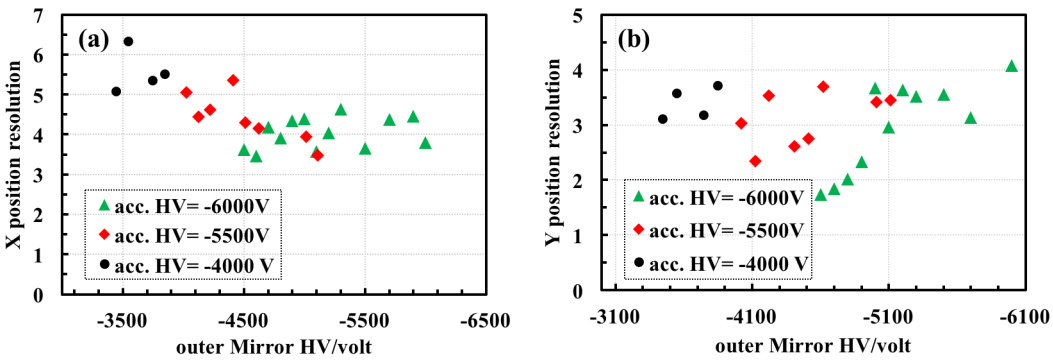

Fig. 5.34 Comparison of position resolution of X- and Y- coordinate of E-detector at 3 different accelerating HV by varying outer mirror HV for 3 mm pitch mirror grid. The HV is set at "ion mode".

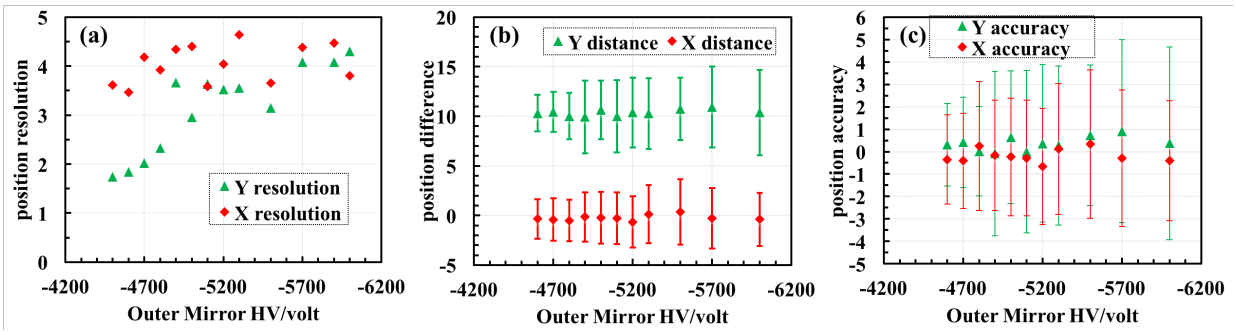

Fig. 5.35 (a) shows the two dimensional resolution of E-detector with 3 mm pitch mirror grid as a function of the outer mirror HV. (b). Position difference of two holes with X and Y displacement of 0 mm and 10 mm, respectively. (c). Accuracy as a function of the outer mirror grid. The indicator of accuracy is the deviation of measurement of the distance of the two holes from the real distance on the mask. The E-detector and DLD120 system runs in "ion mode" with accelerating HV = -6000 V.

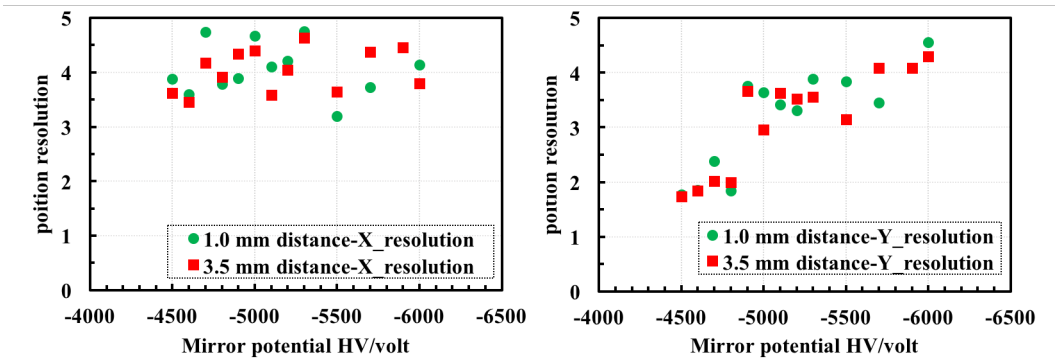

Fig. 5.36 Position resolution comparison of 1 mm and 3.5 mm distance of the MCP front plate to the bottom plate of Electrostatic detector.

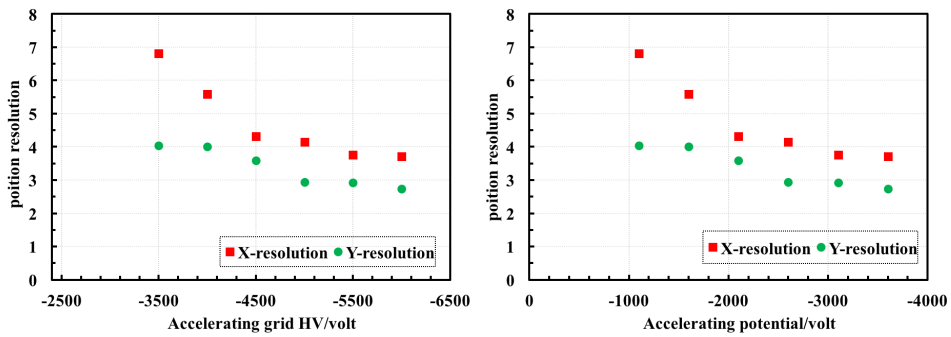

Fig. 5.37 Position resolution of X and Y direction. The ratio of accelerating potential and the deflection potential are kept at 0.778 (3 mm pitch mirror grid). The left and right figure difference is the X axis of left is accelerating HV and right accelerating potential (HV difference of accelerating grid to foil HV).

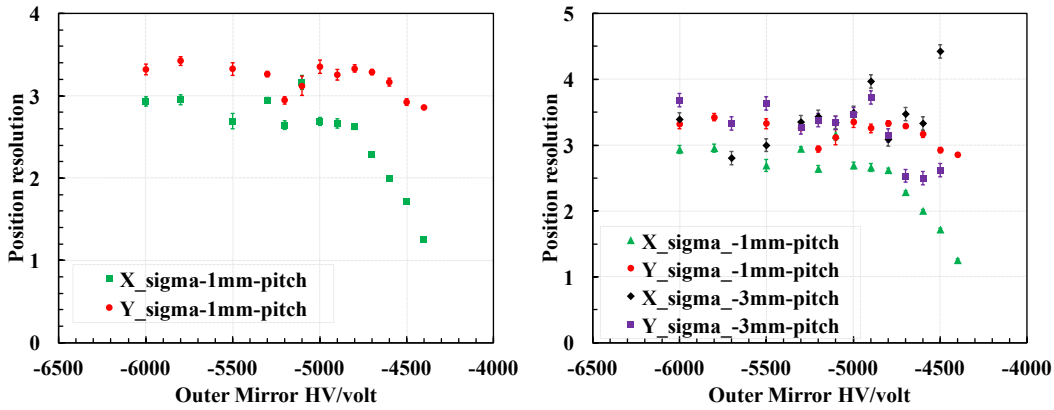

Fig. 5.38 Position resolution of 1 mm pitch grid as a function of the outer mirror HV are displayed on left side. The comparison of position resolution of 1 mm to 3 mm grid pitch of mirror as a function of the outer mirror HV. Both test are in the condition of varying HV of outer mirror and keeping accelerating grid HV at -6000 V in "ion mode" (MCP front HV of -2400 V).

5. **The comparison of position resolution of 1 mm to 3 mm grid pitch of mirror as a function of the outer mirror HV** is shown in Fig. 5.38. Both test are in the condition of varying HV of outer mirror and keeping accelerating grid HV at -6000 V in "ion mode" (MCP front HV of -2400 V). A relatively better position resolutions of both X and Y coordinates are displayed for the 1 mm grid pitch of mirror compared to the test results of 3 mm grid pitch case.

6. **Imaging position and difference of measurement check of one collimated hole with new mask in "electron mode" with the ratio of accelerating potential and the deflection potential kept at 0.778** is shown in Fig. 5.39. A good accuracy of ~ 0.5 mm for absolute value of accelerating HV larger than 1000 V are shown.

7. **Systematic study of position resolution as a function of outer mirror HV by keeping the the ratio of accelerating potential and the deflection potential at 0.778 and accelerating potential at -6000 V by vary the deflection potential (1 mm grid pitch of mirror).** are shown in Fig. 5.40. The DLD120 system and E-detector operated at "electron mode" with MCP front HV of 0 V.

8. **Systematic study of deviation of measured imaging position from theoretic calculated position and deviation of measured imaging position difference dependence of outer mirror HV by keeping the accelerating potential at -6000 V (1 mm grid pitch of mirror)**, while varying the accelerating potential, are shown in Fig. 5.41. The

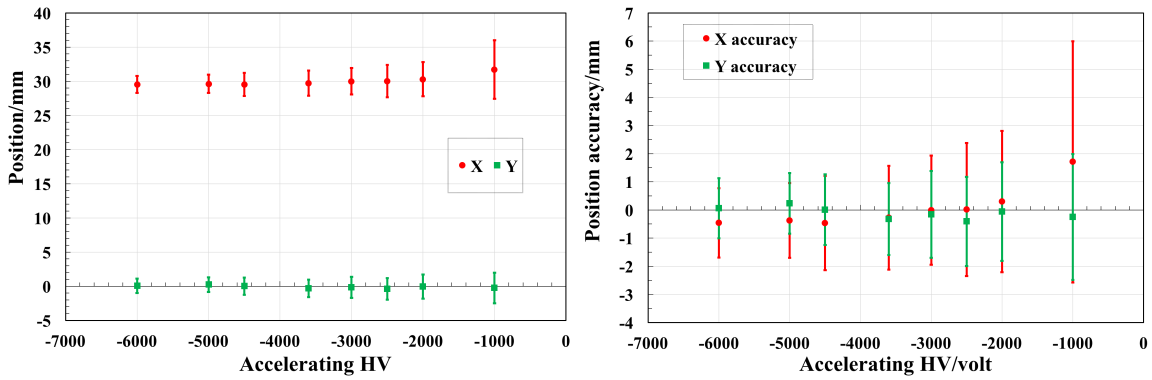

Fig. 5.39 Position as a function of Accelerating grid HV (left) of a imaging of a hole on the mask (30 mm, 0 mm). Dependence of difference of the measurement and the position on the mask on the Accelerating grid HV (right). The E-detector and DLD120 are set at "electron mode" with the ratio of accelerating potential and the deflection potential kept at 0.778.

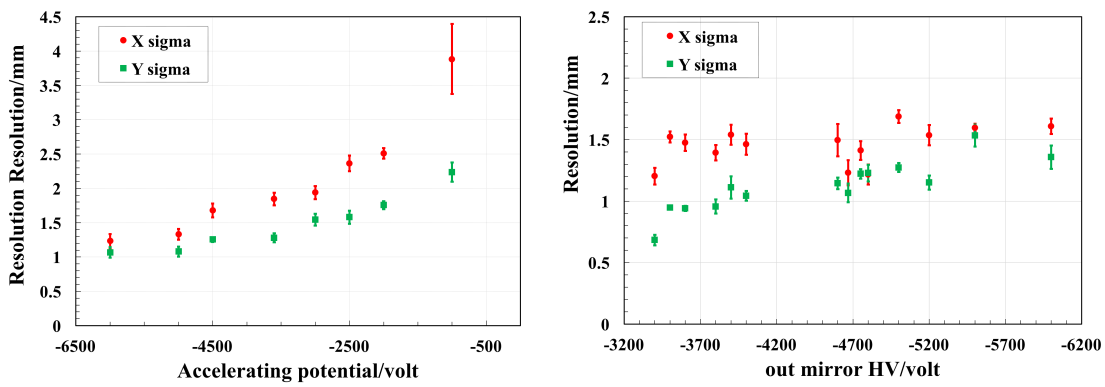

Fig. 5.40 (Left). Position resolution dependence of accelerating potential with the ratio of accelerating potential and the deflection potential kept at 0.778. (Right). Position resolution dependence of outer mirror HV by keeping the accelerating potential at -6000 V. The DLD120 system and E-detector operated at "electron mode" with MCP front HV of 0 V.

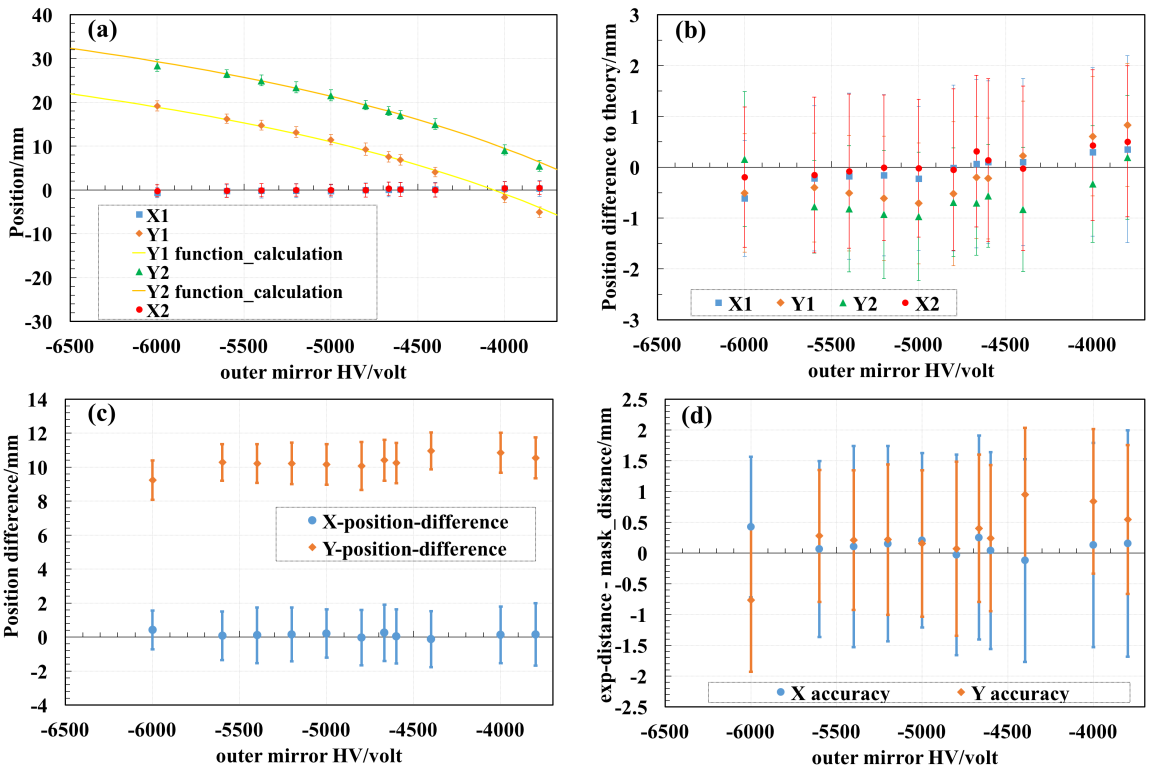

Fig. 5.41 (a). Measured position (X1, Y1, X2, Y2) of imaging on MCP of two holes (0 mm, 10 mm), (0 mm, 20 mm) as a function of the outer mirror HV. (b). Position deviation of the measured position to the position on the mask of the two holes resolution as a function of the outer mirror HV. (c).Measured position difference of the imaging of the two collimated holes on the mask at X- and Y- coordinates. (d). Deviation of the measured position difference of the two holes' imaging from the real distance on the mask of the two holes as a function of the outer mirror HV. The E-detector and DLD120 are set at "electron mode" with the accelerating potential kept at -6000 V.

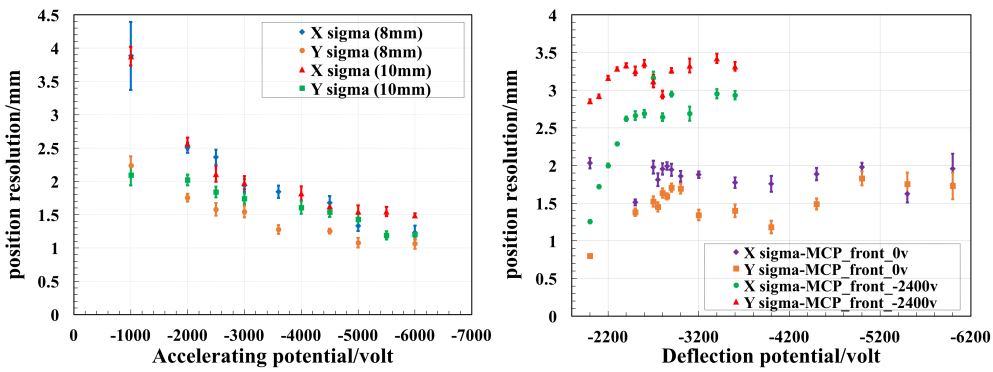

Fig. 5.42 (Left). Comparison of position resolution of 8 mm and 10 mm distance of the accelerating grid to the conversion foil conditions of the E-detector, dependence of accelerating potential, with the ratio of accelerating potential and the deflection potential kept at 0.778. (Right). Comparison of position resolution of ion mode (MCP front -2400 V, and accelerating grid HV of -6000 V) and electron mode (MCP front 0 V, and accelerating grid HV of -3600 V) dependence of outer mirror HV by keeping the accelerating potential.

differences/deviations are all in the uncertainty (resolution) of the position determination, which demonstrates a good validation of the principle of position measurements for the detector system.

9. **Test of the effect of distance of the accelerating grid to the conversion foil on position resolution of E-detector (two cases of 8 mm and 10 mm) and "ion mode", "electron mode" resolution comparison with the same accelerating potential settings via varying the deflection potential (1 mm grid pitch of mirror)** is shown in Fig. 5.42.

Test with c-foil **Test of the position resolution of carbon foil as conversion foil dependence of functional potentials of the E-MCP (1 mm grid pitch of mirror)** is shown in Fig. 5.43. The E-detector and DLD120 are set at "electron mode". The trends of 2D position resolution dependence for the two systematic studies have same trend for the carbon foil and mylar foil coated with aluminium as shown in Fig. 5.43 and Fig. 5.40.

Effective area check

Check of detector effective area by α source with collimated mask (left picture of Fig. 5.44) in front of the accelerating plate. The imaging of collimated holes shows the active area of the detector measuring ~**110 mm x 50 mm**. The active mylar foil size is the 200 mm x 50 mm.

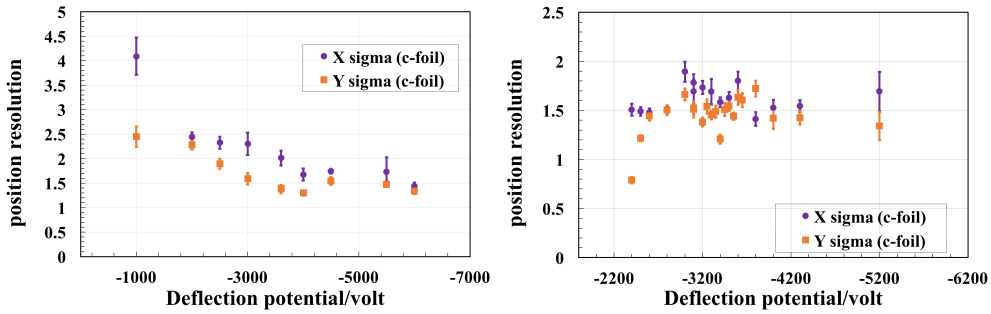

Fig. 5.43 (Left). Position resolution dependence of accelerating potential with the ratio of accelerating potential and the deflection potential kept at 0.778 with carbon foil as conversion foil. (Right). Position resolution dependence of outer mirror HV by keeping the accelerating potential at -6000 V with carbon foil as conversion foil.

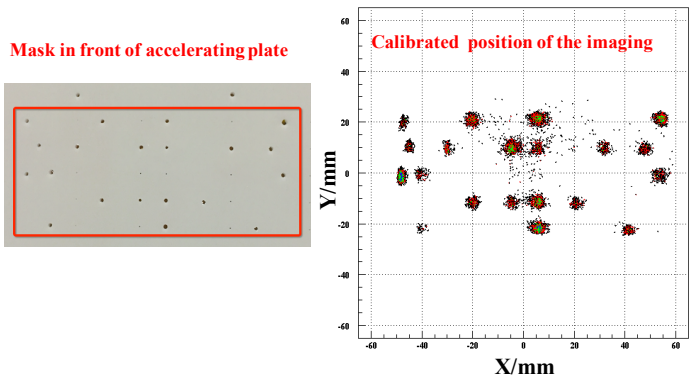

Fig. 5.44 (Left). Mask put in front of the accelerating plate, and the red square shows the effective holes that have imaging out on the MCP. (Right). shows the imaging of collimated holes corresponding to the active area of the detector measuring ∼110 mm x 50 mm.

Efficiency check

Efficiency check of BPM-TOF E-detector with **Mylar foil coated with aluminium** as conversion foil through by α from ^{241}Am are displayed in Fig. 5.45. The influence of the accelerating potential by keeping the ratio of accelerating potential and the deflection potential at 0.778, holder HV, deflection potential with two different set of accelerating grid HV on the efficiency are demonstrated in Fig. 5.45(a), (b), (c), (d) respectively. Efficiency check

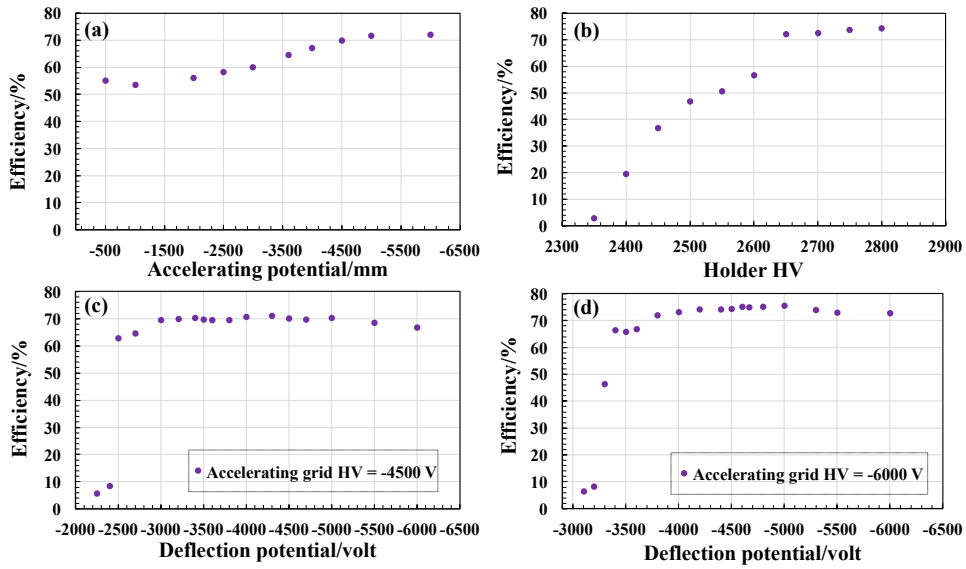

Fig. 5.45 (a). Efficiency of BPM-TOF E-detector with **carbon foil** as conversion foil testing with α from ^{241}Am, as a function of accelerating potential by keeping the ratio of accelerating potential and the deflection potential at ~ 0.778. (b). Efficiency as a function of the Holder HV (the Delay-line HV @ +2650 V). (c) and (d) are efficiency dependence of deflection potential with two different set of accelerating grid HV, -4500 V and -6000 V, respectively.

of BPM-TOF E-detector with **carbon foil** as conversion foil testing with α from ^{241}Am are shown in Fig. 5.46. The influence of the accelerating potential by keeping the ratio of accelerating potential and the deflection potential at 0.778 on the efficiency is displayed.

Position resolution from offline test comparing to simulation

The position resolution of the offline test by using collimated (holes size smaller than 0.5 mm in diameter) α from ^{241}Am for the BPM-TOF E-detector in "electron mode" keeping the ratio of accelerating potential and the deflection potential at ~ 0.778, are compared to simulation results by SIMION with the same setting of the HV supplies of the detector, as shown in Fig. 5.47 as a function of the accelerating potential. An example of the process

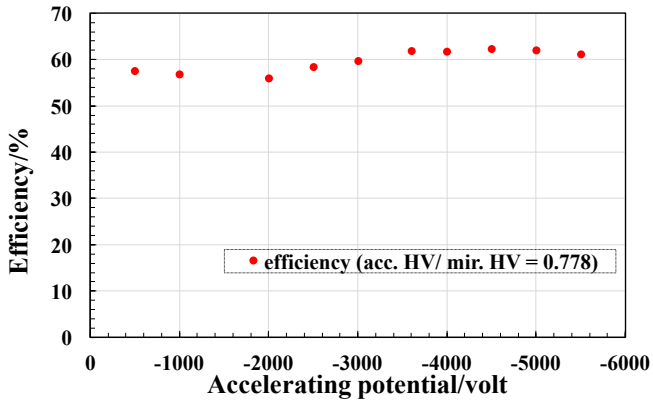

Fig. 5.46 Efficiency of BPM-TOF E-detector with carbon foil as conversion foil testing with α from ^{241}Am, as a function of accelerating potential by keeping the ratio of accelerating potential and the deflection potential at ~ 0.778.

to get the X- and Y-direction resolution of the accelerating potential of -6000 V setting is shown in Fig. 5.48.

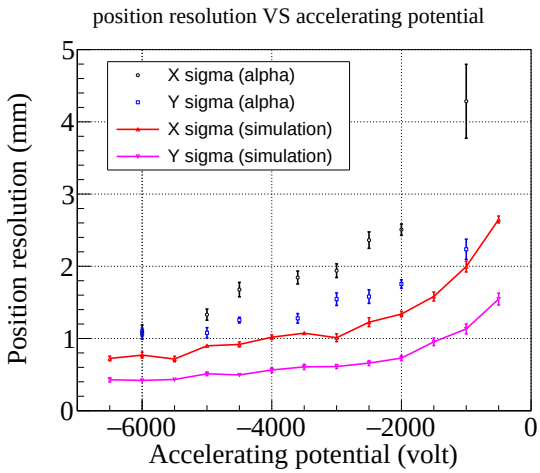

Fig. 5.47 Position resolution comparison of offline results (mylar foil in "electron mode") to simulation results as a function of the accelerating potential by keeping the ratio of accelerating potential and the deflection potential at ~ 0.778.

Trajectory confirmation by experimental data fitting with the function of motion

The trajectory of the SEs inside the electrostatic detector has been calculated theoretically and been verified in simulation and by offline test with α from ^{241}Am. The equation are demonstrated in Chapter. 4 and Eq. 4.15 demonstrates the position of Y direction of the imaging as functions of the accelerating potential and deflection potential. The X, Y direction

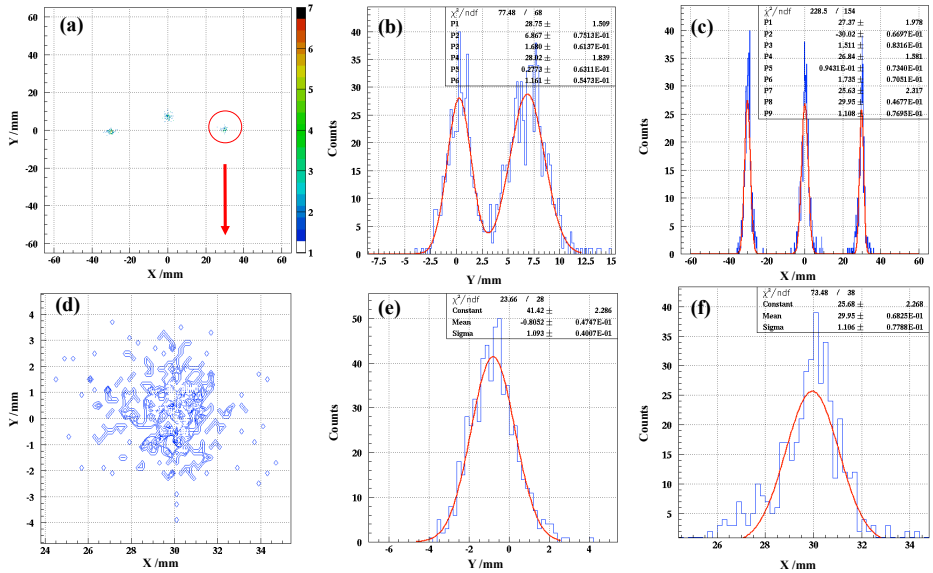

Fig. 5.48 An example of process of position resolution check. (a) is a imaging of collimated alpha source using the new mask, with taped holes less than 0.5 mm in diameter. (b) and (c) are two hole and two holes X or Y-coordinate projections, which demonstrate a good resolving of the holes. (d) is cut view of the right hole in a 2D histogram. (e) and (f) are projections of the cut hole imaging, and the best resolution (gaussian fitting value of sigma) 1D histogram with fitting are chosen to show the resolutions (X of 1.108 mm, Y of 1.098 mm). The holes' place on the mask are (-30 mm, 0 mm), (0 mm, 8 mm), (30 mm, 0 mm),respectively. The HV setting of DLD120 and E-detector are in "electron mode", with MCP front HV 0 V, MCP back +2400 V, Holder HV +2650 V, delay-line 'signal' HV +2650 V, delay-line 'reference' HV +2650 V, Outer Mirror HV -4668 V, accelerating plate (Foil) HV -6000 V.

position of the imaging of settings by varying outer mirror HV and keeping the accelerating potential at -6000 V with Mylar foil as conversion foil in “electron mode” are drawn at left side of Fig. 5.49 and the Y direction motion of the imaging is fit with Eq. 4.15 with two parameters P0 (the distance between mirror grids of 28mm in design) and P1 (shift of the SEs in the mirror along beam direction). Trajectory and mirror distance can be well reproduced as shown in left side of Fig. 5.49 with the P0 value of 28.66 mm and P1 value of 52.31 mm, which are very close to the designed value of 28 mm and 52.672 mm (47.672 mm designed value and + 5 mm shift in code), respectively. The right figure of Fig. 5.49 shows the imaging position of X- and Y-coordinates of the collimated hole (30 mm, 0 mm) on DLD120. As the ratio of potential of the deflection to accelerating is kept constant and the X and Y direction of the imaging will be the same for all the setting by varying the deflection and accelerating potential at the same time.

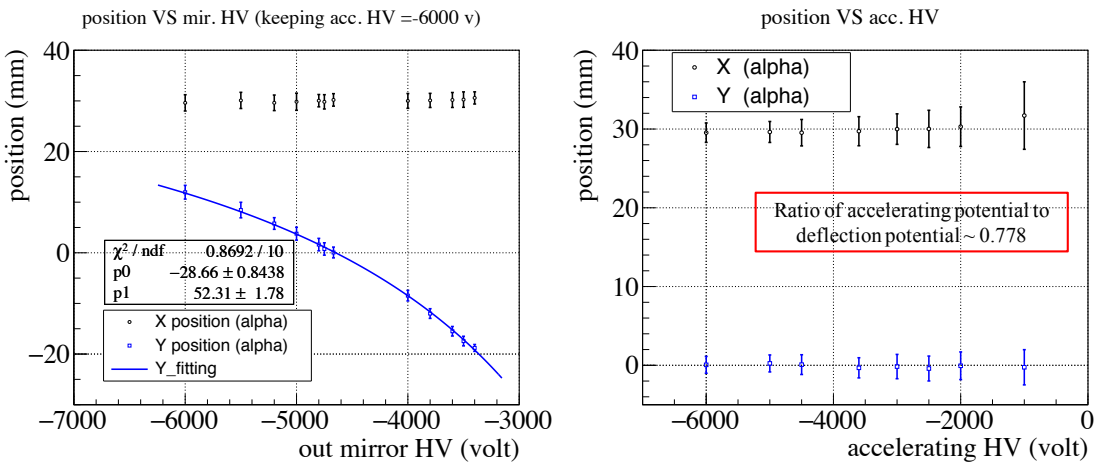

Fig. 5.49 (Left). shows the X , Y position of the SEs deflected onto MCP by the electrostatic detector deduced from collimated α at (30 mm, 0 mm) on mask, as a function of outer mirror potential while keeping the accelerating grid HV of -6000 V. (Right). display the X , Y position of the SEs’ imaging as a function of accelerating potential by keeping the ratio of potential of the deflection to accelerating as a constant.

5.3 Online test of the electrostatic detector

5.3.1 Position-sensitive timing detector online test

An experiment was carried out at the secondary beam line, SB2 course [171] in Heavy Ion Medical Accelerator in Chiba (HIMAC) [170] at National Institute of Radiological Science

(NIRS), Japan. A primary beam of ^{84}Kr at 200 MeV/μ was used to test the performance of the BPM-TOF E-detector. A schematic view of the experimental setup is shown in Fig. 5.50.

The detector arrangement in this experiment is shown in Fig. 5.51. The setup consists of two delay-line PPAC (parallel plate avalanche chamber) [172], one electrostatic micro-channel plate (MCP) detector, two plastic scintillators. The position of each ion are determined and tracked by two PPACs (PPAC1 and PPAC2) with a size of 100 mm × 100 mm placed in between the two plastic scintillators. The BPM-TOF E-detector with DLD120 was placed between PPAC1 and PPAC2, and the position on the foil of each ion when passing through is reconstructed by the two PPACs. Gates by the reconstructed position are employed to check the resolution and accuracy of the position-sensitive detector. The electronics for the CAMAC DAQ for the BPM-TOF E-detector is similar to that of offline test as Fig. 5.24c. Coincidence signal of pla1 left and right signals is utilized as trigger. Signals from both ends of the plastic scintillation detectors were split into two channels to provide both energy and timing information. One was delivered to a Charge-to-Digital Converter (QDC) for energy loss measurement. The other was fed to a CFD and CFD threshold was set as low as possible and just above the noise level of Photomultipliers (PMTs). In consideration of the long transmission distance between the experimental setup and the DAQ system, a discriminator was employed in the console room after the long cable transmission for each timing signal to reshape the timing signals.

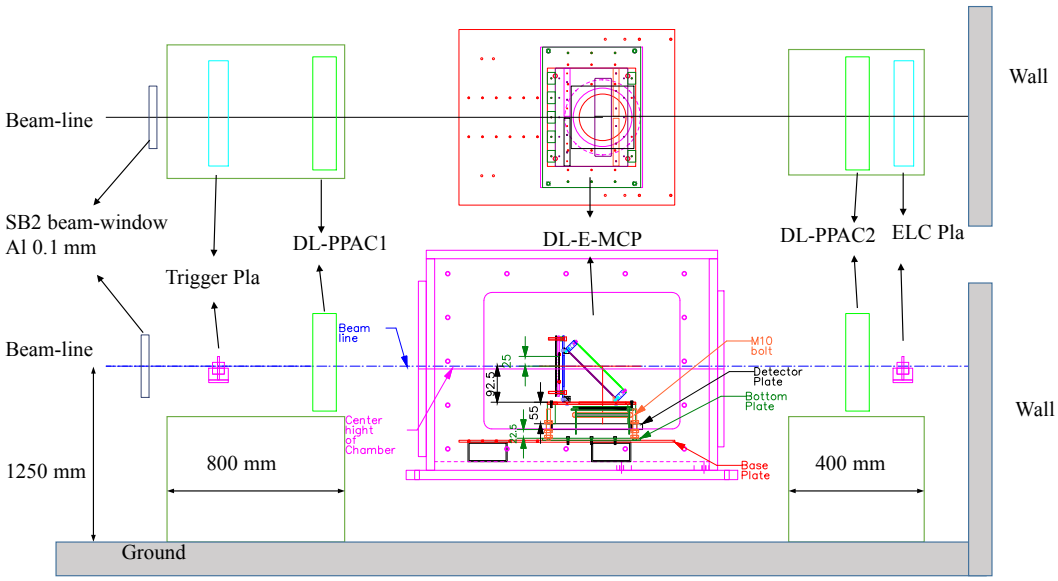

Fig. 5.50 Experimental setup at HIMAC for the performance test of the delay-line E-MCP detector system.

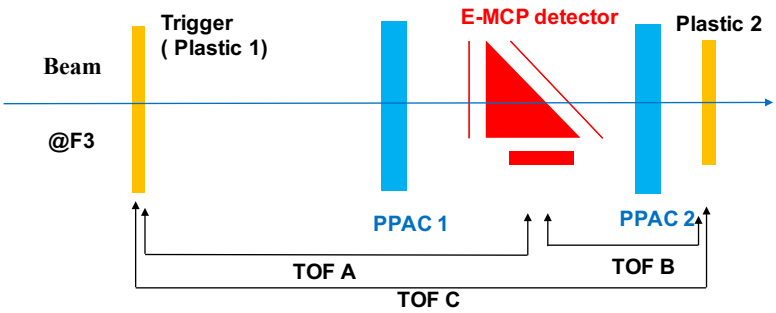

Fig. 5.51 Schematic view of detector arrangement of the experiment.

The timing of each plastic scintillator is calculated by taking the average time from both PMTs at the left and right sides of a plastic scintillator. For instance, the timing T_{pla1} of plastic scintillator (pla1) is determined from the right and left sides of the PMT, respectively:

$$T_{pla1} = (T_{left} + T_{right})/2 \tag{5.9}$$

Such an average of the both ends of the timing information of the plastic scintillator can minimize the hit position uncertainty, thus to reduce the dependence of timing resolution on the position. The delay-line PPAC detector shown in Fig. 5.52, consists of three plates.

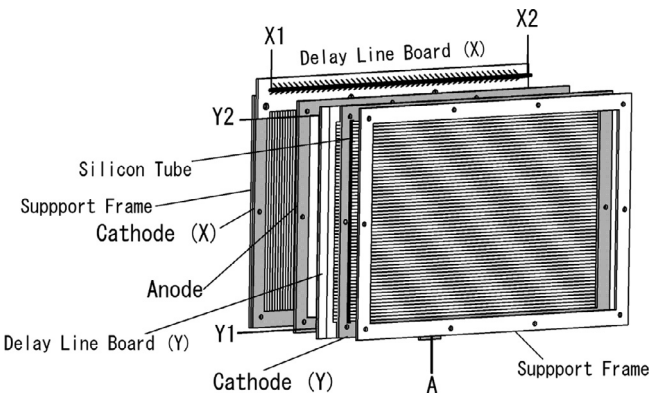

Fig. 5.52 Schematic view of the electrode setup in a PPAC detector. Figure adapted from [172].

The anode plate shown in Fig. 5.52 is located between two cathodes, which are connected to delay-lines. The detector gas of C_3F_8 is used with an operating anode bias of less than 2000 V (typically around $\sim$ 800 V). The principle of the position measurements of the delay-line PPAC detector is similar to the delay-line MCP detector. After feeding the X_1, X_2, Y_1, Y_2 and anode signal to the commercial integrated pre-amplifier, the signals are transmitted to

the fast timing amplifiers, then to the CFD and finally acquired by the TDC. Numerically, positions (X and Y) in the PPAC are given by the following equations:

$$X = K_x(T_{x1} - T_{x2})/2 + O_x, Y = K_y(T_{y1} - T_{y2})/2 + O_y, \tag{5.10}$$

where K_x and K_y are the slope factors for the X- and Y-direction delay-lines, respectively (typically 1.25 mm/ns), O_x, O_x are arbitrary offsets and T_{x1} and T_{x1} (T_{y1} and T_{y1}) correspond to the delay-timing (in ns) at both end of the delay-lines. During the 2 nights beam time (10x2

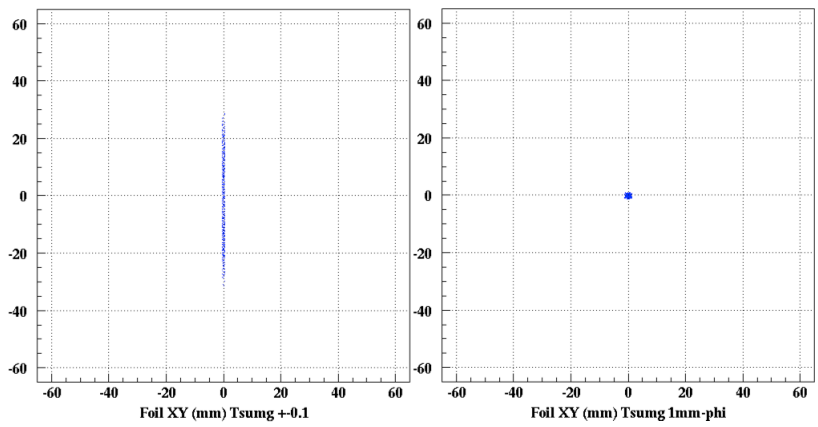

Fig. 5.53 Example spectra of the slit gate (left) of (-0.1 mm, 0.1 mm) and 1 mm circle (in diameter) gate (right) on the foil reconstructed by PPACs.

hour) including beam tuning, the distance of the accelerating grid to the foil was 8 mm and the distance of mirror HV and outer HV mirror was set at 28 mm. Mylar foil of 2 mm in thickness coated with aluminium was employed as conversion foil during the experiment. The grids were all in 1 mm pitch.

To **check the position resolution** of the E-detector, a typical gate on the reconstructed beam position on foil by the PPACs is utilized. This idea is borrowed from offline test with mask in front of the foil and the gated beam on the foil is equivalent to the collimated beams/ion sources. An example of the slit gate of (-0.1 mm, 0.1 mm) and 1 mm circle gate on the foil reconstructed by PPACs are shown in Fig. 5.53.

Normally, for one time-of-flight spectrum, the distribution contains the information of two timing detectors, which is characterized by the σ or full-width-at-half-maximum (FWHM) of the distribution. To **determine the intrinsic timing resolution** of the E-detector, another timing detector have to be applied. Assuming that the timing distribution of each timing detector follows a Gaussian distribution, the timing resolution of an individual detector can be determined by using three sets of time-of-flight between there timing detectors: $TOF(A)$, $TOF(B)$, and $TOF(C)$. The 3 sets of TOFs ($TOF(A)$, $TOF(B)$, and $TOF(C)$) are demon-

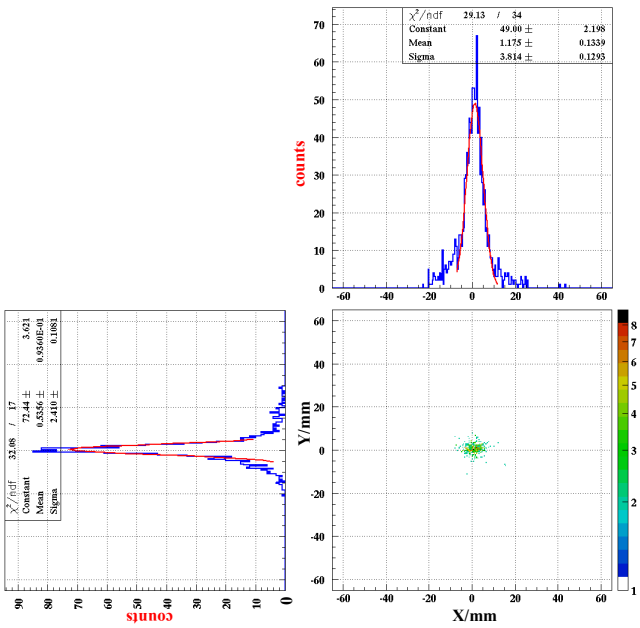

Fig. 5.54 Example of position resolution check by 1 mm cirlce gate of reconstructed beam position on the foil. The 2D histogram shows the imaging on the calibrated DLD120 system of 1 mm circle gate on the foil. The 1D histogram are the position projection on X- and Y-coordinate separately.

strated in Fig. 5.51. The resolutions of three TOFs describes as:

$$(\sigma_{TOF(A)})^2 = (\sigma_{pla1})^2 + (\sigma_{MCP})^2, \tag{5.11}$$

$$(\sigma_{TOF(B)})^2 = (\sigma_{MCP})^2 + (\sigma_{pla2})^2, \tag{5.12}$$

$$(\sigma_{TOF(C)})^2 = (\sigma_{pla2})^2 + (\sigma_{pla1})^2, \tag{5.13}$$

where σ_{pla1}, σ_{MCP}, and σ_{pla2} are intrinsic timing resolution of plastic scintillator 1, the E-MCP detector, and plastic scintillator 2, respectively. The $\sigma(TOF(A))$ (or $\sigma(A)$), $\sigma(TOF(B))$ (or $\sigma(B)$), $\sigma(TOF(C))$ (or $\sigma(C)$) are the fitting 'sigma' parameters of the 3 TOF sets. From these relationships, we can deduce the intrinsic timing resolution of E-MCP detector by solving the above equations:

$$\sigma_{MCP} = \sqrt{(\sigma^2(TOF(A)) + \sigma^2(TOF(B)) - \sigma^2(TOF(C)))/2}, \tag{5.14}$$

where the σ_{MCP} indicates the intrinsic timing resolution of the E-detector.

$$\delta(\sigma_{mcp}) = \sqrt{(\delta^2(\sigma(A))\sigma^2(A) + \delta^2(\sigma(B))(\sigma^2(B) + \delta^2(\sigma(C))(\sigma^2(C))/(4\sigma^2_{MCP})}, \tag{5.15}$$

here, the ($\delta(\sigma(A))$), ($\delta(\sigma(B))$), ($\delta(\sigma(C))$ are the uncertainties of the fitting "sigma" parameters, $\sigma(TOF(A))$ (or $\sigma(A)$), $\sigma(TOF(B))$ (or $\sigma(B)$), $\sigma(TOF(C))$ (or $\sigma(C)$), and the $\delta(\sigma_{mcp})$ indicates the uncertainty of the deduced precision value of σ_{MCP}. One example of the spectra of three TOF sets for the intrinsic timing resolution deduction of the timing detectors are demonstrated in Fig. 5.55. The "sigma" parameter and the fitting uncertainty of it corresponding to the σ and $\delta(\sigma)$ values in Eq. 5.14 and Eq. 5.15.

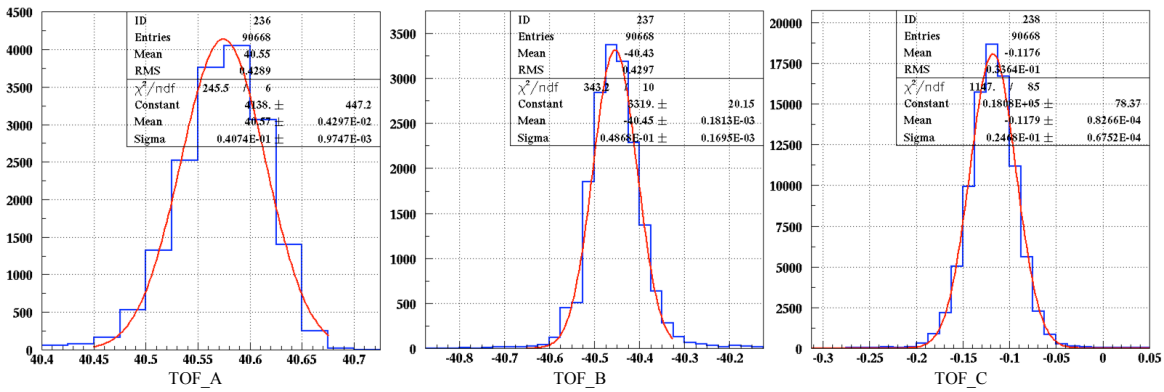

Fig. 5.55 Spectra of three TOF sets for the intrinsic timing resolution deduction of the timing detectors. The mean parameter means the mean value of the gaussian fitting of the TOF spectrum.

During the experiment, to search for the isochronous condition, satisfying imaging of the center of the foil when ion passes through to the center of DLD120 system, the **trajectory reconstruction method** was utilized for each setting of the accelerating grid HV (-6000 V, -5400 V, -4400 V, -3400 V, -2900 V). The efficiency with timing of sum gates of the PPACs is defined in this work is:

$$efficiency = \frac{((events\ measured\ by\ E\_detector) \otimes (events\ measured\ by\ PPACs\ with\ Timing\ sum\ gates\ of\ PPACs))}{events\ measured\ by\ PPACs\ with\ Timing\ sum\ gates\ of\ PPACs} \tag{5.16}$$

As the efficiency with timing of sum gates of the PPACs include the influence of the noise from the not satisfied vacuum condition and to check the efficiency after ruling out the noise by the timing sum gates of DL120 system, we define a parameter $efficiency_{ideal}$:

$$efficiency_{(ideal)} = \frac{((events\ measured\ by\ E\_detector) \otimes (events\ measured\ by\ PPACs\ with\ Timing\ sum\ gates\ of\ PPACs) \otimes (events\ with\ delay\_line\ T\ sum\ gates))}{(events\ measured\ by\ PPACs\ with\ Timing\ sum\ gates\ of\ PPACs) \otimes (events\ with\ delay\_line\ T\ sum\ gates))} \tag{5.17}$$

to check the ideal efficiency of the E-MCP detector after ruling out the unwanted double peak or long tail of the timing sum of DLD120 delay-line signals. The resulting timing resolution and efficiency of the E-detector from online test for the five "center to center" settings in "Ion mode" are shown in Fig. 5.56. The best achieved timing resolution is ~40-50 ps with a steady efficiency of ~ 95% without using the sum gates of the delay-line timing information. When

gated with the sum gates of from the delay-line timing information to rule out the noise like "δ-electrons", multi-hit events, events from reflected ions by the wires, the efficiency will be close to 100 %. As shown in Fig. 5.57, near the edge of the detector, the efficiency get dropped routinely. The kinks in the timing resolution trends as a function of the outer mirror HV shows the appearance of the isochronous condition, which is typically mounting to 10-20 ps influence on the total timing distribution. In Fig. 5.58, the TOF of SEs inside the

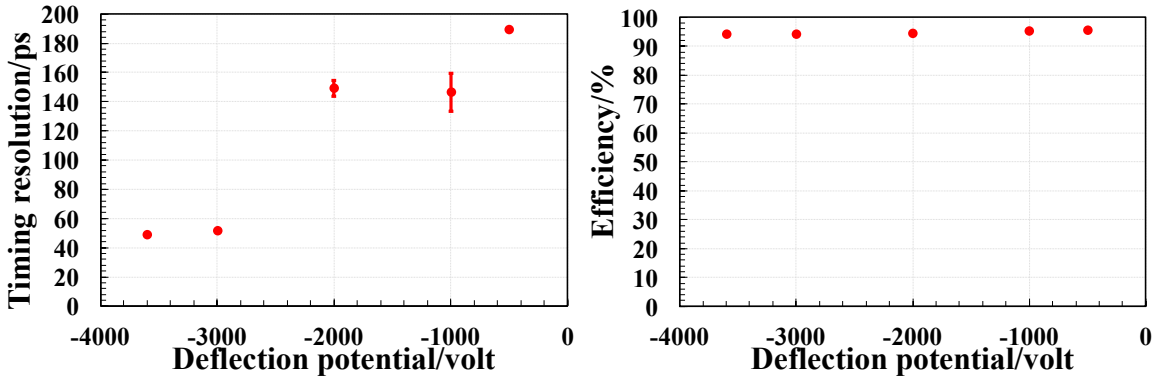

Fig. 5.56 Resolution and efficiency as a function of the deflection potential (diference of outer mirror HV and inner mirror HV). The 5 points in the figure corresponding to the five center to center settings.

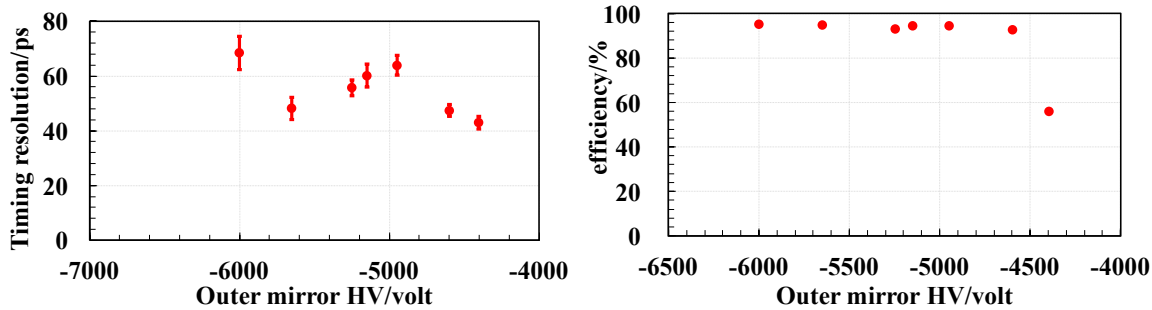

Fig. 5.57 Resolution and efficiency as a function of the outer mirror grid HV for the setting of -6000 V for the accelerating plate HV and varying the the outer mirror grid HV in "Ion mode".

E-detector is relative Time-of-flight of SEs, induced by ions when passing through, from the foil to the MCP front inside E-detector including the process of acceleration, free drift, bending and free drift to the MCP front. During these processes, the accelerating potential and deflection potential play a very important role in the TOF of the SEs inside the detector. If keeping the ratio of accelerating potential and deflection potential, as the increase of the the accelerating potential, the TOF inside the detector will get decreased, thus will result

in a short TOF. The results in Fig. 5.58 is consistent with the simulation results and as the decrease of the TOF of SEs inside the detector. The influence of the initial angle and energy distribution of the induced SEs will be reduced and short TOF will results in a better timing and position resolution as shown in online test Fig. 5.57, Fig. 5.57 and offline test Fig. 5.47. The timing and position resolution values of settings of (-6000 V,-5248 V), (-5400 V, -4775 V) are overlapped in Fig. 5.58 and this phenomenon show a saturation effect of the TOF of SEs inside the detector. The saturation effect have a final determination of the timing resolution of the detector, as shown in simulation results of about 10 ps. To test the position

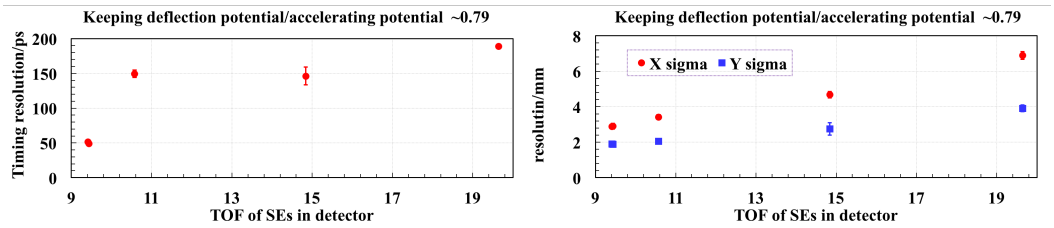

Fig. 5.58 Timing and position resolution as a function of the TOF of SEs inside E-detector, keeping the ratio of deflection potential to accelerating potential near 0.79 which corresponds to the searched center to center settings.

dependence of the detection sensitivity and position resolution of the E-detector system, **there defocus beams** were tuned to cover a wide range of the effective area of the E-detector. As shown in Fig. 5.59, the 3 defocus beams data are accumulated in one 2D histogram and the beam position at PPAC1, PPAC2, foil of E-detector reconstructed by the 2 PPACs are displayed together with the detected 2D imaging of the beam position by the DLD120 system after calibration. In these 3 runs, the E-detector system were set at "Ion mode" (MCP front with HV of -2400 V) with the accelerating grid HV of -6000 V and outer mirror grid HV of -5248 V. To show the imaging possibility and performance of the position-sensitive E-detector, gated points with 1 mm circle gate of the defocus beams tracked by the PPACs are utilized. One example of are 6 gated points at (30,0), (-30,0), (30,15) (30,-15), (-30,15), (-30,-15) and (0,0) by PPACs are illustrated in Fig. 5.60(a). As shown in Fig. 5.60(b), imaging on the DLD120 of E-detector of the 6 gated points on foil are displayed, which indicates a **clear imaging performance** of the E-detector system.

In order to check the **global accuracy** of the E-detector, the 2D position values of imaging points of the there defocus beam on the foil measured by calibrated E-detector system are used to subtract the tracked 2D position values by the PPACs. The global difference of the imaging of the there defocus beams are shown in Fig. 5.61. The mean value of the X- and Y-coordinate difference of the two measuring method are ~10 μm with uncertainty of 2.635 mm and ~ 8 μm with uncertainty of 2.463 mm respectively. The uncertainties include the

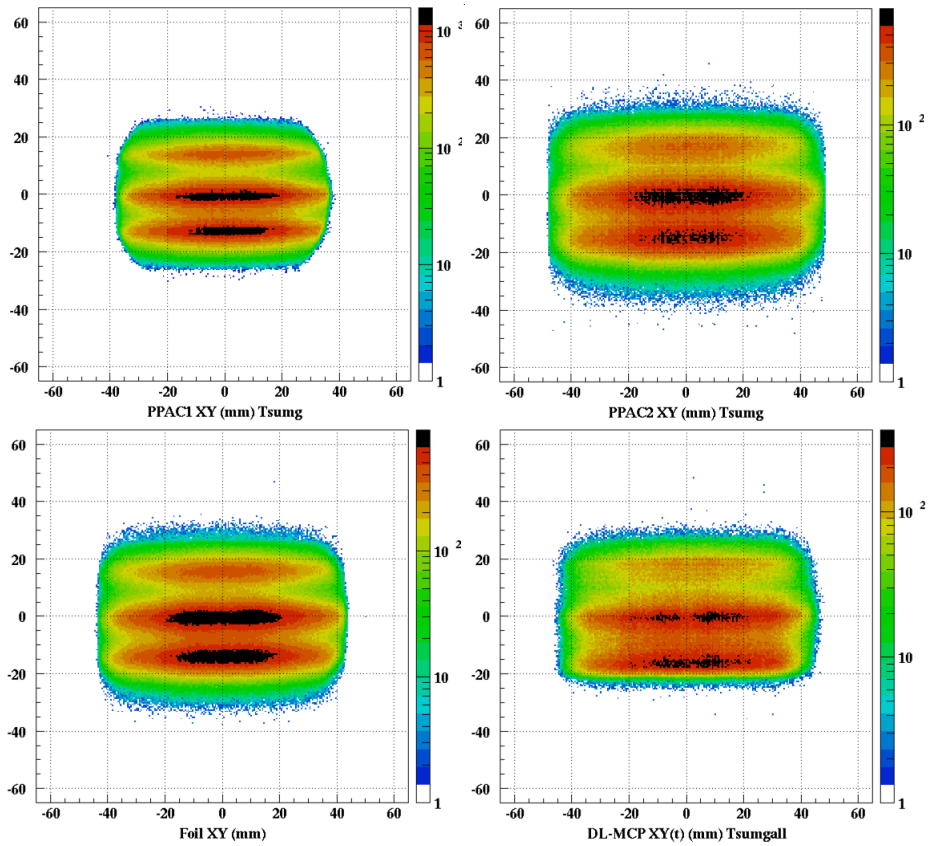

Fig. 5.59 Detected beam position on PPAC1 (left-up), PPAC2 (right-up), reconstructed beam position (left-down) by PPACs at the foil, and measured position imaging (right-down) at the foil by E-detector.

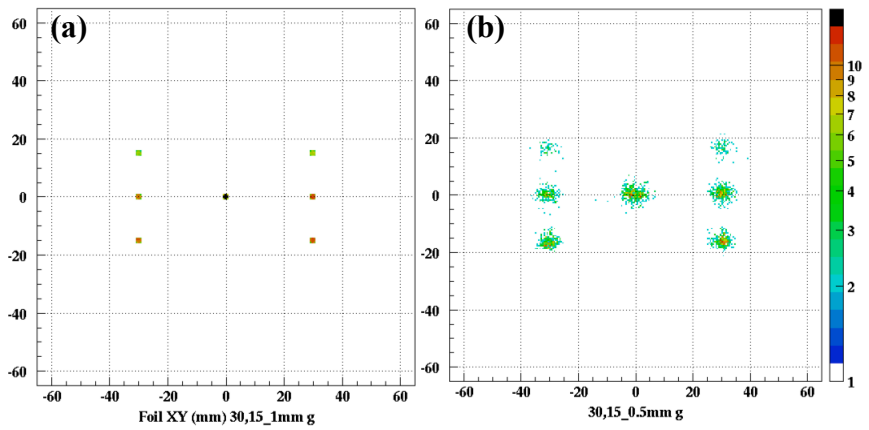

Fig. 5.60 Imaging on DLD120 of gated points at (30,0), (-30,0), (30,15) (30,-15), (-30,15), (-30,-15) and (0,0) by PPACs on foil. The DLD120 and E-detector system have both been calibrated to satisfy the center to center condition for imaging of ions on the foil to the DLD120 imaging.

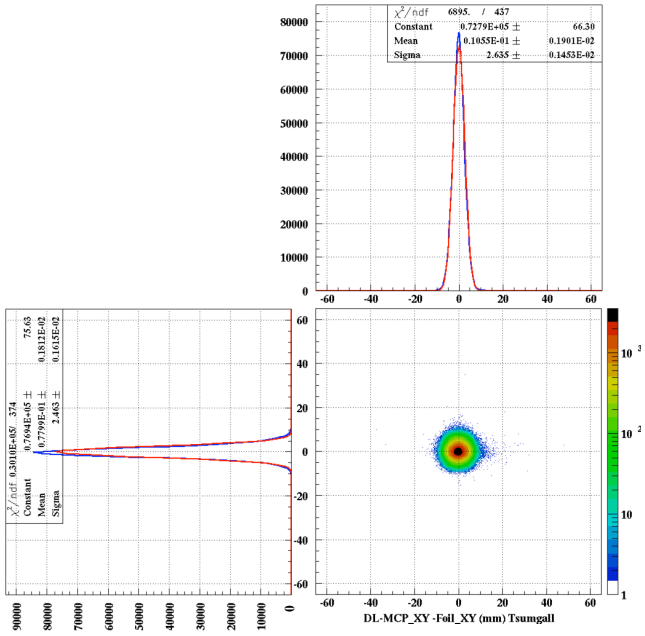

Fig. 5.61 The 2D spectrum and 1D projections of position difference distribution of the measured position of the beam on the conversion foil by calibrated E-detector system from the reconstructed position by the 2 PPACs.

intrinsic resolutions of the two detecting systems, which demonstrate a good consistence with the gated 1 mm point resolution check by PPACs.

The **local accuracy** check of the E-detector was done by gated circles on the foil with certain distances as shown in Fig. 5.62. X-projection of the 2D imaging histogram of the three gated holes was fitted with 3 gaussian fuction for the 3 peaks. Difference of the mean values of the peaks from fitting to the real values on the foil of -40 mm, 0 mm, 40 mm are -0.07 mm with uncertainty of 1.911 mm, -0.2543 mm with uncertainty of 2.942, -0.11 mm with uncertainty of 2.477 mm, respectively.

The resulting position resolution of **"Ion mode"** settings together with one hour run of **"electron mode"** settings (with the ratio of accelerating potential and the deflection potential kept at ~ 0.79) are shown in Fig. 5.63. As the limited beam time schedule of the last few setting, the electronics were not well set and the threshold of the delay-line timing signals and MCP timing signals which are typically a little different for the two settings of HV mode, especially for the case of vacuum at a very worse condition ($\sim\ 3-5\,x10^{-3}\,Pa$). The vacuum condition is one order worse than the requirement of the operation of the MCPs, which results a lot of feedback noises in the MCP. Another reason for not enough counts to check the timing resolution is that the TDC is not tuned after change of the HV settings, and most of MCP timing signals are out of range. The roughly timing resolution was demonstrated in Fig. 5.57.

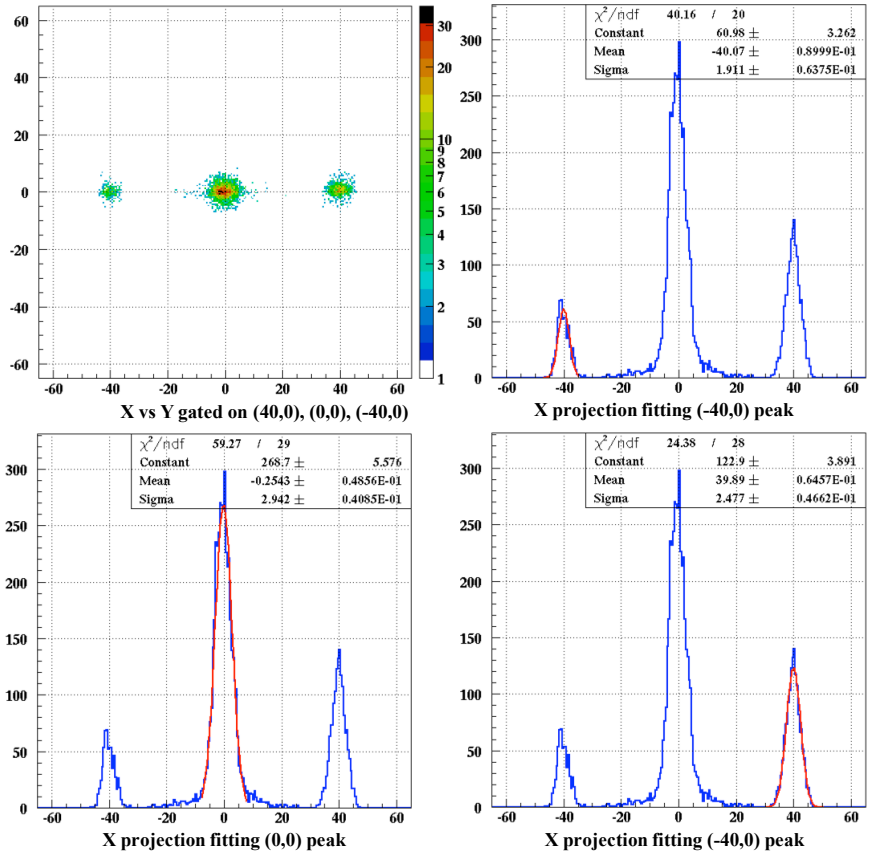

Fig. 5.62 Imaging of three gated 1 mm circles (distance of 40 mm) on reconstructed imaging of the foil by PPACs and gaussian fitting of 3 position peaks on X-projection spectra to demonstrate the local accuracy of the X direction position determination. The accelerating potential for the settings is -3600 V.

The position resolution values in Fig. 5.63 are cheched with a 1mm circle gate of the tracked beam on the foil by PPPACs, while in offline test, the mask hole of 0.5 mm was taped by Kapton and pricked with a pin at the hole center to be less than 0.5 mm in diameter were used to check the position resolution shown in Fig. 5.47 to remove the influence of the hole size as discussed in simulation section. The results in Fig. 5.47 which is much more close to the intrinsic position resolution of the E-detector is smaller than the ones checked online shown in Fig. 5.63.

In the online experiment, the position on the the foil when heavy ions passing though are measured by the E-MCP detector and also reconstructed by the PPACs. Uncertainty of position measurement difference of the PPACs and the E-MCP detector as a function of accelerating potential is shown in Fig. 5.64(a). As the uncertainty of the position difference contains the intrinsic resolution of the E-MCP detector and the PPACs tracking system. To demonstrate the intrinsic resolution of the E-MCP detector, position resolutions of 1 mm

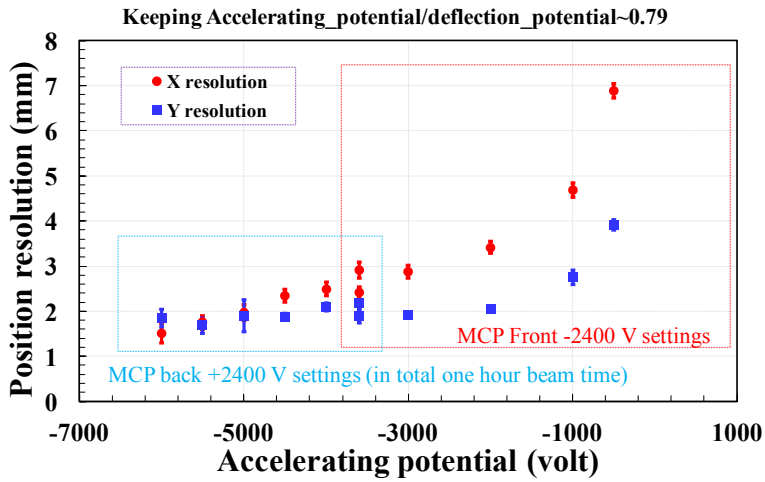

Fig. 5.63 Summarized position resolution as a function of the accelerating potential. The five points for the five main settings in "ion mode" with MCP front HV of -2400 V are drawn at right part, and rough resolution points of one hour run with E-detector in "electron mode" are displayed at left side.

for 2 dimensions of the PPACs tracking system are assumed to be subtracted from the uncertainty of the position difference. The derived intrinsic resolution of the E-MCP detector system, after subtraction of resolution of PPACs tracking system, as a function of the accelerating potential is shown in Fig. 5.64(b). The trend of position resolution as a function of the accelerating potential is consistent with those of offline test. and simulation shown in Fig. 5.63.

The previous efficiency is check by focus beams and efficiency correspond to the overall events measured by the E-detector over the gated trigger events with PPACs 2-dimensional sum of timing gates. The PPACs sum gate is indispensable for the efficiency check to insure that the events detected by the E-detector are not fake events.

Here, the **2D local detection efficiency** of the E-detector is checked with a 2D histogram with the X- and Y-coordinate bin size of 0.5 mm as shown in Fig. 5.65 and Fig. 5.66, and the efficiency is the value of the events measured by the E-detector over the gated trigger events with a PPACs sum gate or PPACs sum gate together with DLD120 system sum gates. A steady detection efficiency of $\sim$ 95 % for the E-detector are demonstrated and $\sim$ 100 % of detection efficiency is achieved when removing the events from the noise like δ-electrons, multi-hit events, feedback electrons when vacuum condition is bad.

The **1D local detection efficiency** of the E-detector can also be checked by a 1D histogram with the X- and Y-coordinate bin size of 0.5 mm as shown in Fig. 5.67, Fig. 5.68, and the efficiency is the events in each bin (covering X direction of 0.5 mm range with all Y direction events accumulated or covering Y direction of 0.5 mm range with all X direction

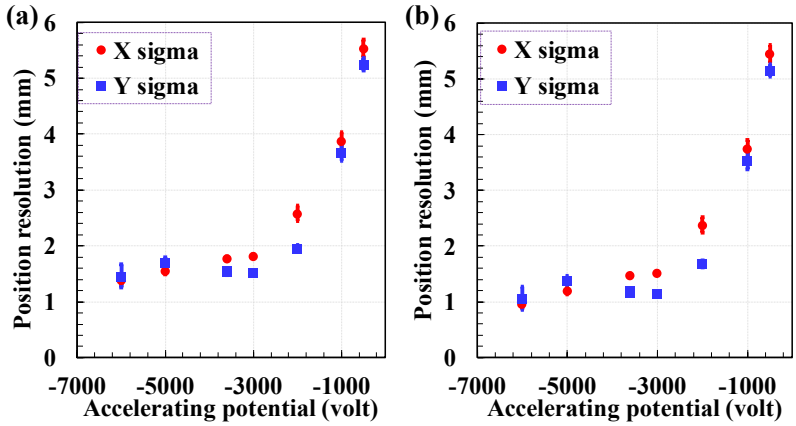

Fig. 5.64 (Colour online) (a) Uncertainty of position measurement difference of the PPACs and the E-MCP detector as a function of accelerating potential. (b) Uncertainty of position measurement difference subtracted with the resolution of the PPACs system (assuming a resolution of 1 mm for 2 dimensions) as a function of accelerating potential.

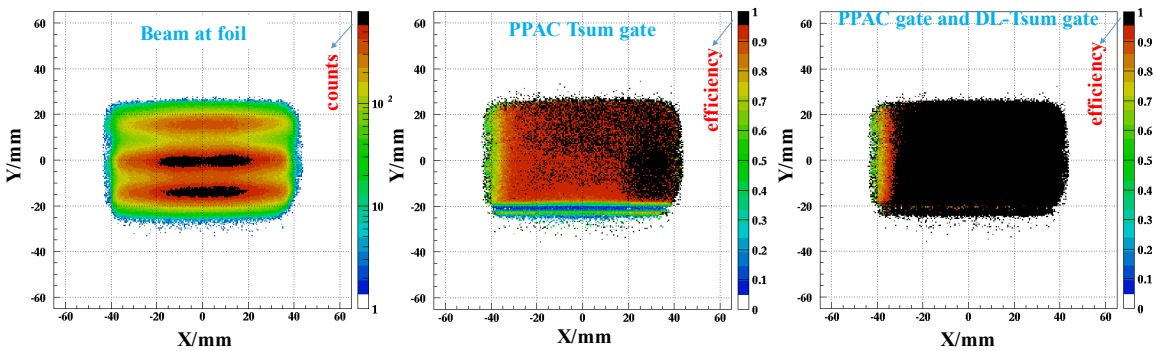

Fig. 5.65 2D local detection efficiency check with 3 defocus beams together. (Left) shows the beam position on the foil measured by the PPACs. (Middle) demonstrates the 2D local detection efficiency of the E-detector with the PPACs sum gates. (Right) illustrates the 2D local detection efficiency of the E-detector with the PPACs sum gate together with DLD120 system sum gates.

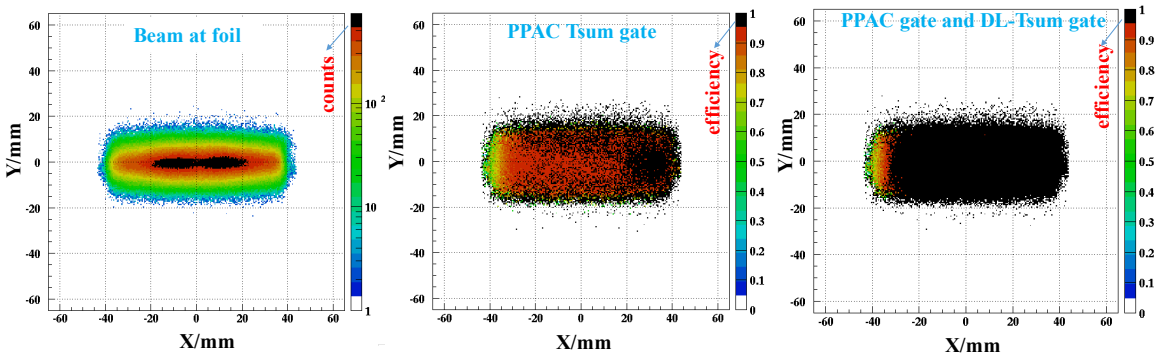

Fig. 5.66 2D local detection efficiency check with central defocus beam. (Left) shows the beam position on the foil measured by the PPACs. (Middle) demonstrates the 2D local detection efficiency of the E-detector with the PPACs sum gates. (Right) illustrates the 2D local detection efficiency of the E-detector with the PPACs sum gate together with DLD120 system sum gates.

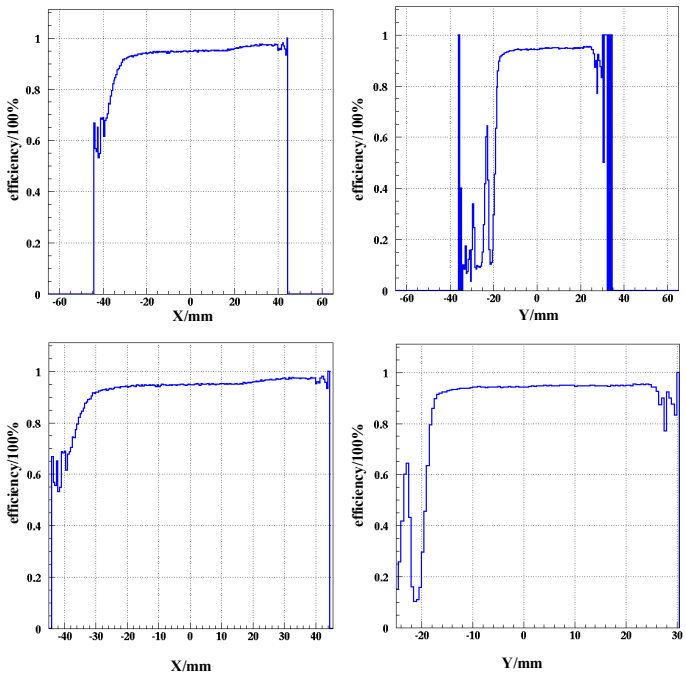

Fig. 5.67 (Left-up) and (Right-up) display the X- and Y-direction 1D local detection efficiency of the E-detector with the PPACs sum gates. (Left-up) and (Right-down) are zoomed figures to the edge of the MCP or edge of the coming beam.

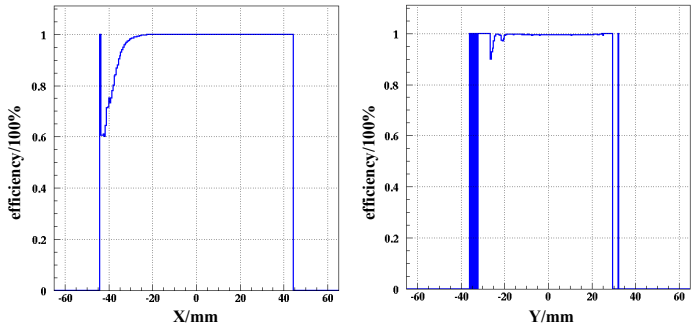

Fig. 5.68 (Left) display the X-direction 1D local detection efficiency of the E-detector with the PPACs sum gates. (Right) shows the Y-direction 1D local detection efficiency. the PPACs sum gates together with DLD120 system sum gates are used in the efficiency check.

events accumulated) over the gated trigger event with a PPACs sum gate or PPACs sum gate together with DLD120 system sum gates. For easily demonstrating the detection efficiency

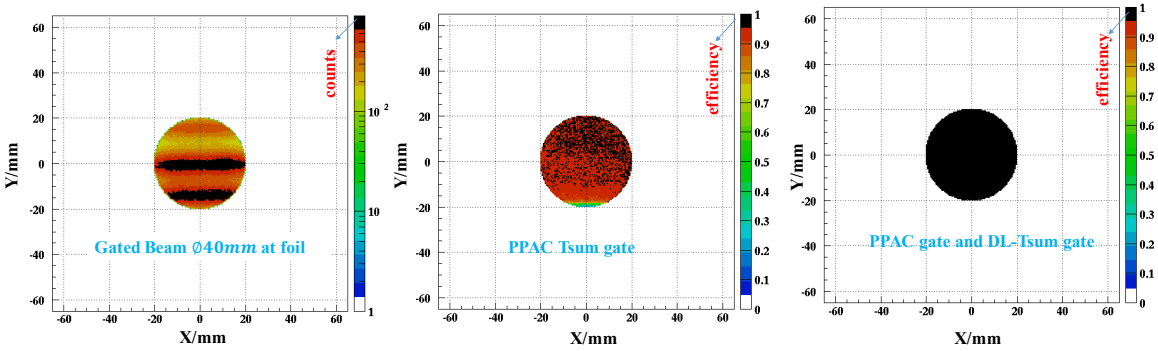

Fig. 5.69 2D local detection efficiency check with 40 mm circle gate on the defocus beams.. (Left) shows the beam position on the foil with 40 mm circle gate. (Middle) demonstrates the 2D local detection efficiency of the E-detector with the PPACs sum gates. (Right) illustrates the 2D local detection efficiency of the E-detector with the PPACs sum gate together with DLD120 system sum gates.

of the E-detector, a circle gate of 40 mm in diameter is employed on the tracked foil position as shown in left side of Fig. 5.69. The edge of the MCP (down side and off center 20mm area) and the less sensitive area of the MCP at the left side is nearly excluded in the Fig. 5.69, The efficiency of about 95 % with the PPACs sum gates and nearly 100 % with the PPACs sum and DLD120 system sum gates. This is also illustrated in the 1D efficiency histograms shown in Fig. 5.70. The inhomogeneity of the sensitivity of the MCP is demonstrated by the efficiency check of the E-detector. To improve the edge area, especially the left side of the MCP, the high voltage supply for the MCP can be increased to enhance the multiplicity

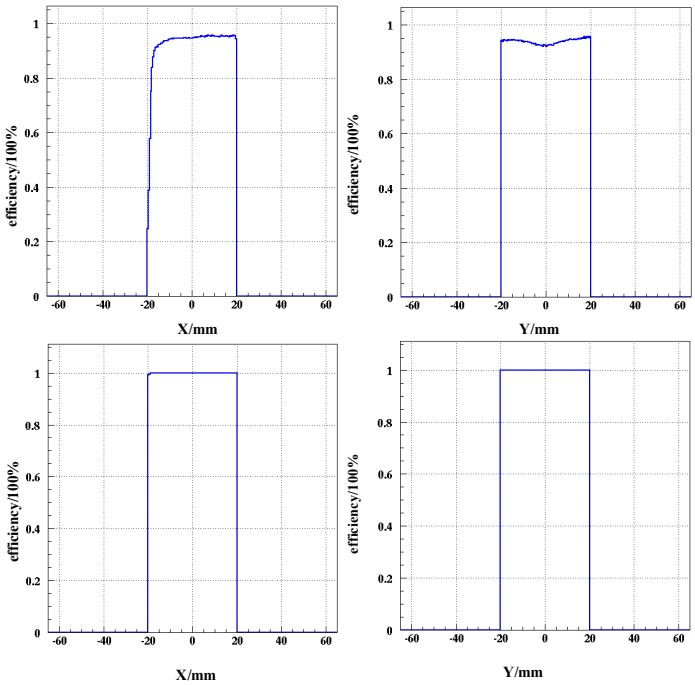

Fig. 5.70 (Left-up) and (Right-up) display the X- and Y-direction 1D local detection efficiency of the E-detector with the PPACs sum gates. (Left-up) and (Right-down) are with coincidence gate of the PPACs sum of timing and DLD120 system sum.

of the amplification factor of the MCP (the actual HV for chevron MCPs are less than the applied value of -2400 V). When checking the timing resolution of the E-detector, we need

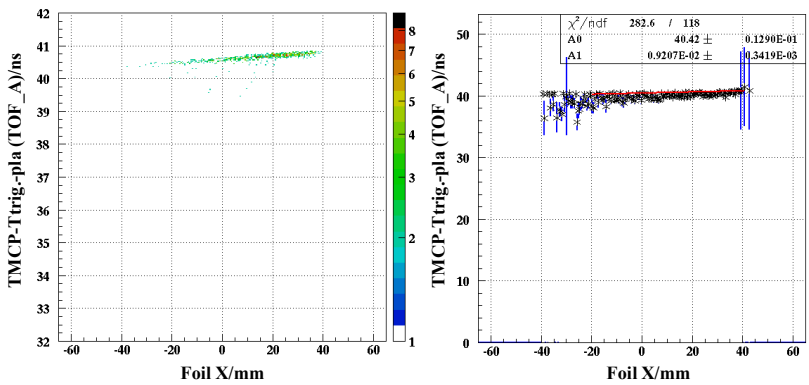

Fig. 5.71 (Left). 2D histogram of TOF of E-detector to trigger plastic (TOFA) as a function of the beam X position on foil. (Right). Projected 2D histogram into a profile histogram along X-direction with a first order polynomial fitting.

to take consideration of the **position dependence of the timing resolution** by the 3 sets of TOF method. This effects is shown in Fig. 5.71 and Fig. 5.71. The timing dependence of X-

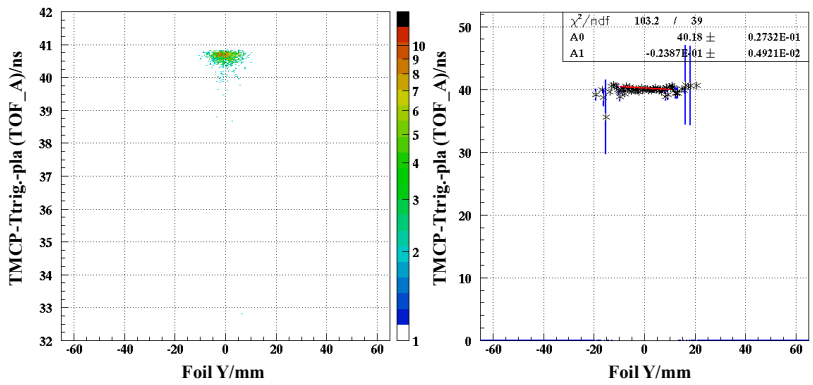

Fig. 5.72 (Left). 2D histogram of TOF of E-detector to trigger plastic (TOFA) as a function of the beam Y position on foil. (Right). Projected 2D histogram into a profile histogram along Y-direction with a 1 order polynomial fitting.

direction is about 9.2 ps/mm and Y-direction of about 23.9 ps/mm. This effect is quite large compared to the intrinsic resolution of the E-detector by checking the timing of MCP signal directly. There is two ways to solve this influence on the timing resolution determination. One way is to gate on the foil position of the E-detector with a central circle of 0.5-1 mm (assumed resolution of the PPAC tracking system).

It is strong advantage of timing detectors with position sensitivity, and in principle, timing resolutions can be improved with software corrections from position. To **verify the higher order calibration method for the DLD120 system**, two calibration functions parameters, withdrawn in two different experiments (time of 201709 and 201804 in HIMAC) with the same setting of the DLD120 system, are used in the position correction code. The difference of the calibrated positions checked via event-by-event method with the two sets of parameters are shown in Fig. 5.73. The projections of the 2D difference histogram on X- and Y-coordinate are fitted with gaussian functions, and the mean value of -5.52 μm with uncertainty of 0.275 mm for X-direction, while 2.87 μm with uncertainty of 0.166 mm are obtained. Actually, this is checked with a focus beam of 2D position range of (-10 mm, 10 mm; -10 mm, 10 mm) and if checked with larger beam position range, the edge deformation effect will appear. Higher order is needed for DLD120 system calibration, and second order is suitable for larger range of position correction compared to third order correction. While in relative smaller range of measurement (-40 mm, 40 mm; -40 mm, 40 mm), a third order correction function is preferable.

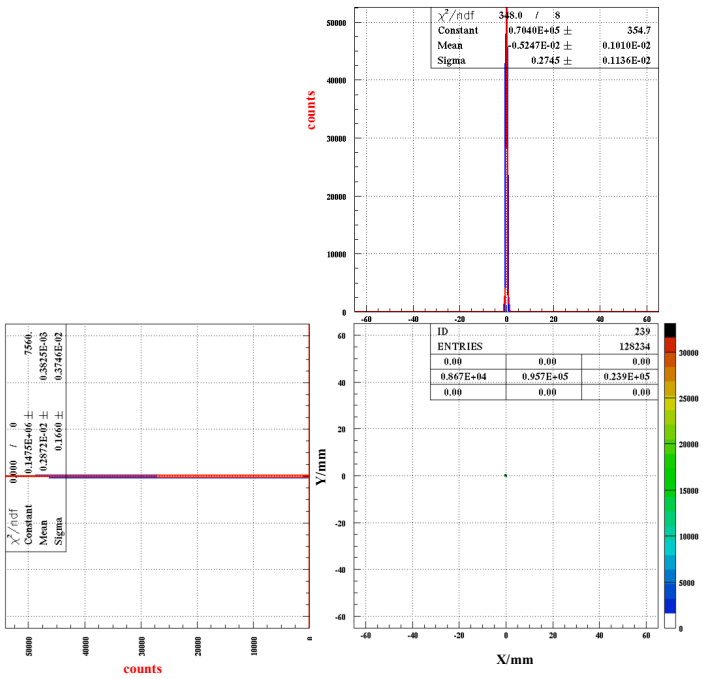

Fig. 5.73 The position difference 2Dand 1D projection histograms of the calibrated positions checked via event-by-event method with the two sets of parameters for a focus beam with 2D position range of about (-10 mm, 10 mm; -10 mm, 10 mm).

5.3.2 Timing electrostatic detector online test

High resolution time of flight (TOF) measurements is crucial for mass measurements via TOF methods, such as in-ring isochronous TOF or beam-line Bϱ-TOF. As shown from the simulation, the more compact structure of the E-timing detector, the better timing resolution will be in same settings for the detector. To improve the performance, an isochronous condition for SEs is adopted and resolution dependence of high voltage supplies of the potential plates has been investigated. To characterize and optimize the timing resolution of a relative smaller mirror-type MCP detector (triangular function plate size of 120 mm x 120 mm) with timing metal anode, an experiment aimed at studying the performance of the detector was conducted at HIMAC. The obtained time resolution was $\sigma \sim 130$ ps and a efficiency was about $\sim 72\%$ in previous HIMAC test [181].

To investigate the properties of the detector, a primary beam of $^{84}Kr^{36+}$ at the energy of 200 MeV/nucleon is used. The experimental detector setup is shown in Fig. 5.76.(a). The setup consisted of two PPACs (parallel plate avalanche chamber) for beam tracking, one electrostatic micro-channel plate (MCP) detector, 2 plastic scintillators for intrinsic timing resolution deduction of the Mirror detector. The structure of the timing E-detector mounted with a MCP a diameter of 40 mm, equipped with the metal anode, is shown in Fig. 5.74.

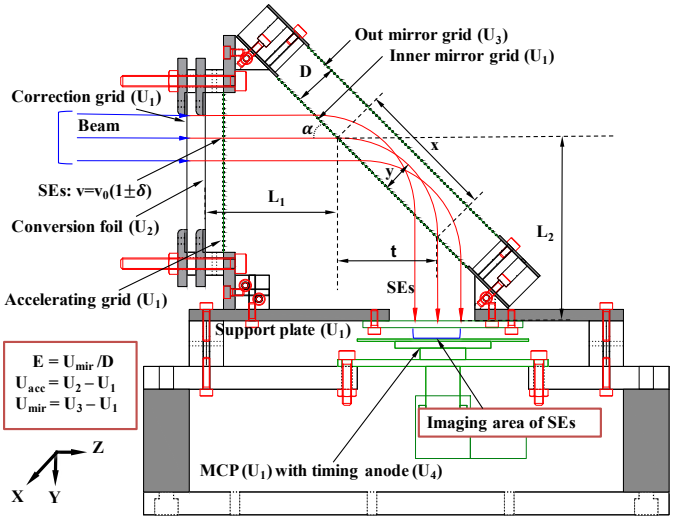

Fig. 5.74 Structure of the electrostatic mirror detector and description of the parameters of the detector.

The parameters and description are nearly same as that of the position-sensitive detector as shown in Chapter. 4 Fig. 4.2. Here, the description is jumped and please refer to Chapter. 4 explanations in the text corresponding to Fig. 4.2. The conversion foil is made of mylar (2 μm) coated with aluminium. Accelerating grid consisting of gold-plated tungsten (W+Au) wires (40 μm in diameter) possesses a distance of 8 mm from conversion foil with 1 mm pitch, and wires (W+Au) for the inner and out mirror grids are arranged with 3 mm pitch.

During the experiment, the high voltage (HV) potential of the MCP, accelerating grid and inner mirror was set at - 2500 V and the accelerating HV of the foil and out mirror grid were varied. The timing resolution results of the mirror-type MCP detector with isochronous and non-isochronous condition from the experiment are shown in Fig. 5.76(c) and (d) as blue points. For isochronous condition the out mirror and inner mirror distance is 20mm, while 8mm for the non-isochronous condition. As the increasing of the accelerating HV, the timing resolution get better for both configurations. The tendencies are also reproduced with the simulation results performed by SIMION , which are displayed as red points in Fig. 5.76(c) and (d).

As it can be seen from simulation results of Fig. 5.76(c) and (d), a timing resolution of less than 20 ps could be achieved. However, the experimental results could not be achieved and seems to saturated around 40 ps for both conditions. One possibility could be systematic error from the data acquisition electronics. Figure 5.76(b) shows detection efficiency of the detector as a function of the mirror potential. The efficiency get decreased when setting the HV of the mirror too high or too low because the SEs arrive at the edge of the MCP. The

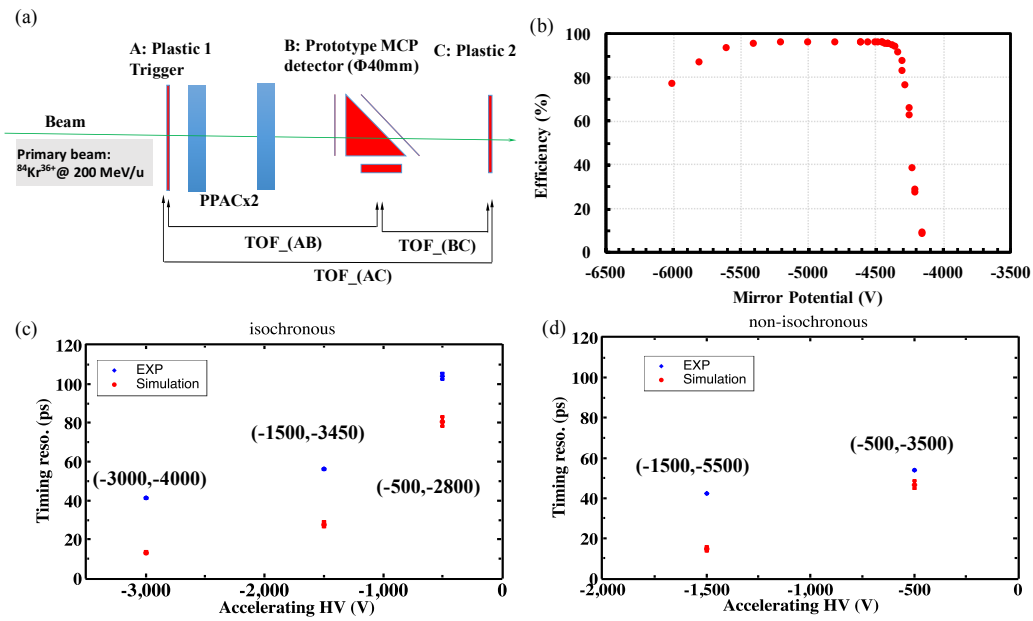

Fig. 5.75 (a) Schematic view of the setup for HIMAC experiment. (b) The detection efficiency as a function of mirror HV (by keeping accelerating HV = -3000 V). (c) and (d) depict the timing resolution as function of the accelerating HV potential (the HV difference between the accelerating grid and conversion foil) for isochronous and non-isochronous condition. The red points are simulation results and the blue points display the experimental results. Values in brackets correspond to (accelerating HV, out mirror HV).

detection efficiency has a steady value of $\sim$ 96% when the SEs reach the central parts of the MCP.

During this timing experiment, the 5 digital CFD output pulses (2 of each plastic, and 1 for MCP) from 3 timing detectors are divided to two. One is sent to a time-to-amplitude converter (TAC), which outputs a pulse whose amplitude is a linear function of the time between some input "start" signal and the input "stop" signal from the CFD. The TAC output signal with the precise time between 'start' and "stop" encoded in its amplitude is then sent to ADC. another divided pulser is send to normal TDC for sampling. The typical CFD (ORTEC 935) keeps walk to less than 50 ps and jitter to less than 25 ps. The resolution is about 25 ps for normal TDCs (REPIC RPC-170 [168], Kaizu 3780 [166]) with a range of 100 ns, while it is about 12.5 ps for the combination of TAC (ORTEC 567) and ADC (HOSHIN C008) [169].

5.4 Summary and Outlook

Electrostatic mirror-type detector for 2-dimensional-position and TOF measurements utilizing MCP and a thin conversion foil as a SEs emitter has been developed at the Rare-RI Ring. The mirror MCP detector with timing anode have been optimized and tested at HIMAC with heavy ion beam. The best achieved timing resolution for both isochronous and non-isochronous condition reached about $\sim$ 40 ps in σ with an efficiency of $\sim$ 96%. Meanwhile, a two dimensional position-sensitive mirror MCP detector with delay-lines anode has been developed and tested by using α source ^{241}Am and at HIMAC employing heavy ion beam as well. The effective area of detector is about 110 mm x 45 mm from the test. The best obtained timing resolution is about 40-50 ps and position resolution sim 1 mm for 2-dimensional positions, with a detection efficiency of $\sim$ 95%.

This mirror-type detector has demonstrated its excellent performance and potential applications for mass measurements and is ready to be used for mass measurements and beam monitoring of exotic nuclei at the Rare-RI Ring and will becomes a versatile apparatus for timing and 2-dimensional position measurements at beam-lines in RIBF as well.

Application of the MCP detectors for mass measurements and beam monitoring The designed foil MCP detectors coupled with a position-sensitive delay-line anode or timing anode in this work have excellent performances of timing resolution $\sim$ 40-50 ps with/without position-sensitivity of $1mm$ resolution and properties of: (a) low energy loss and small angular scattering of the heavy ions by using thin conversion foil; (b) Large active area to cover large beam size at dispersive focus plane or in ring; (c) Large detection efficiency ($\sim$ 95-96%); (d) No magnetic field to disturb the isochronous magnetic field when using in the ring.

For a foil detector with good timing resolution can be utilized for revolution time measurement inside Rare-RI Ring, start TOF detection of the total TOF for in-ring circulation, beam-line TOF measurement for beam-line mass determination, particle identification by $B\rho$-TOF-ΔE and velocity reconstruction for in-ring mass correction. High resolution timing measurement in ring is not only significant for high resolving identification of nuclei but can be also used for mass measurements directly.

As discussed previously, the simultaneous measurement of a particle's position together with its TOF allows for determination of the track information of an ion and its timing stamp at arrival, this is most suitable for TOF measurement with an additional $B\rho$ (equivalent to position at dispersive focus) measurement for high precision mass measurements by TOF methods.

The position-sensitive timing foil detector can be used on the beam-line for two dimensional position measurement to reconstruct beam trajectory for fast beam tuning, beam-line momentum measurements for velocity reconstruction, meanwhile, it can be used in-ring for position monitoring (beam profile measurements) to increase the injection efficiency, tune scan, close orbit correction, momentum dispersion and revolution time measurement turn by turn inside the Rare RI Ring. With performances of good position-sensitivity and high resolution timing, and characteristic of low-energy loss for the foil detector, the in-ring TOF mass measurement with $B\rho$ (momentum) or velocity measurements can be realized by one compact detection system with lower energy loss compared to the dual timing detectors (double TOF). This method will be developed in the new storage ring system Spectrometer Ring (SRing), in the developing next generation facility HIAF. This compact detector can be also directly used for $B\rho$-TOF measurements at a dispersive focus plane for $B\rho$ (momentum) measurements with a intermediary TOF measurements for charge state distinguishing or as the stop TOF together with position (momentum dispersion) measurements for $B\rho$-TOF path length correction.

One example of application of the position-sensitive detector is to measure the dispersion function of the isochronous R3 lattice. The deviation of the beam, which has a relative momentum shift:

$$\delta = \Delta P/P_0 = (P - P_0)/P_0, \tag{5.18}$$

from the reference orbit x_0 with momentum P_0, is defined as:

$$x(s) = x_\beta(s) + x_\delta(s). \tag{5.19}$$

The transverse motion of a particle is the sum of betatron motion (homogeneous part):

$$x_\beta = \sqrt{(\varepsilon_x \beta_x)(s)} cos(\varphi_x + \varphi_0) \tag{5.20}$$

and a displacement because of the momentum dispersion (inhomogeneous part):

$$x_\delta = D(s)\delta, \tag{5.21}$$

where $D(s)$ is the "dispersion function", φ_0 is the phase advance, φ is the phase function, β is Courant-Snyder parameter, ε is the emittance, and s the position along the reference beam trajectory. As betatron motion is homogeneous part in the, the averaged position of the beam can be described as:

$$x = x_0 + x_\delta(s) = x_0 + D(s)\delta = x_0 + D(s)\Delta P/P_0. \tag{5.22}$$

With the measured position x of ions turn-by-turn inside the storage ring, the in-ring dispersion function $D(s)$ can be calibrated by circulating particles with known relative momentum dispersion.

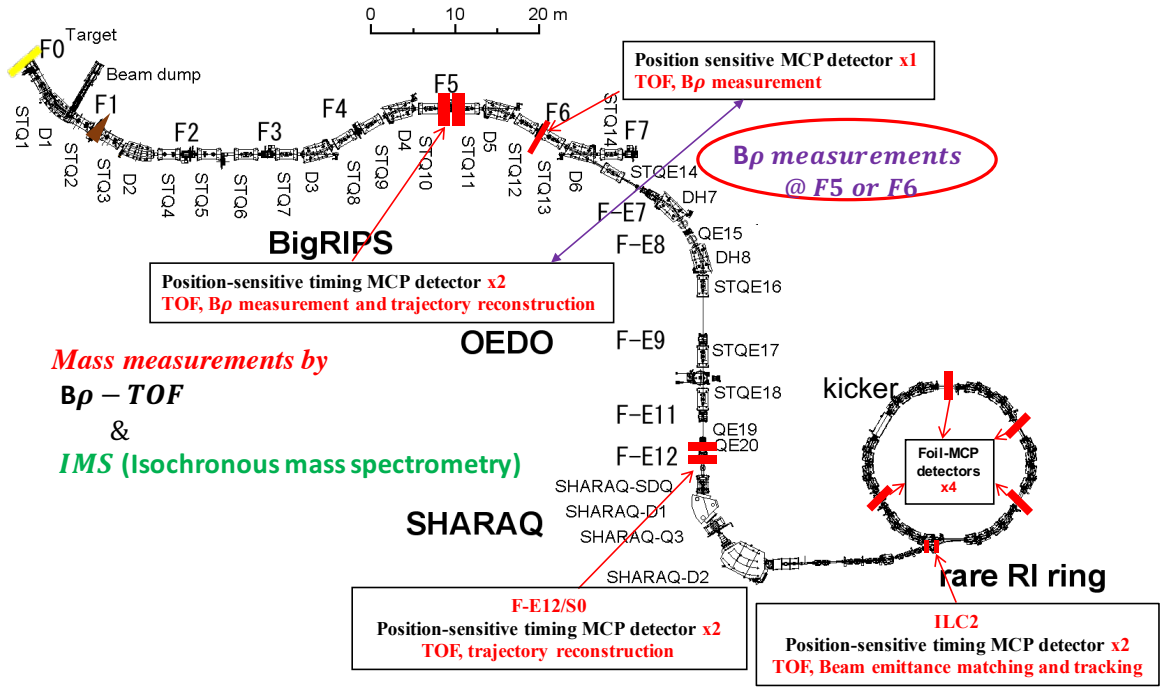

Fig. 5.76 The prospects of foil-MCP detectors completion status at the Rare-RI Ring.

Chapter 6

Summary and prospects

6.1 Summary

An experiment aimed to study the principle of mass measurements and performance of the Rare RI Ring performing as an Isochronous mass spectroscopy has been carried out at RIBF, and the fisrt fission fragments, created by ^{238}U projectiles in a beryllium target at the entrance of the BigRIPS focus F_0, were spatially separated by and injected into the R3. In the experiment, we succeeded in selection, injection, accumulation and extraction of 5 different nuclei to R3 and the isochronism ~5x10^{-6} was achieved by checking the TOF spectrum of ^{78}Ge. The results of these pilot experiments on nuclides of well-known mass are in agreement with the mass values given in the literature of AME2016. A mass resolving power of about $\delta m/$ m = 62 000 (FWHM) has been achieved according to the isochronism of the reference nucleus ^{78}Ge. From the analysis, nuclei of a wide range momentum distribution of $\pm$0.3% and difference of mass-over-charge ration $\sim$ 8% are within one $B\rho$ setting to be deduced with the masses by the orbit-IMS method. A newest machine study with the isochronism of ~4x10^{-6} and efficiency of 1.9% achieved shows a resolving power of about $\delta m/$ m = 78 000 (FWHM). From the analysis, it is confirmed that from one experiment run, two complementary mass measurements methods (IMS and $B\rho$-TOF) can be employed simultaneously to deduce masses and benefit each other, in which it is very suitable to save beam time and cover large area of nuclide of chart and large momentum area of secondary products from experiment of very exotic nuclei. It is also proved that to achieve high resolution, the revolution time measurement of the storied ions and the magnetic rigidity or the velocity for correction of the in ring TOF should be simultaneously measured, thus we can achieve high resolution with small systematic error to cover relative large range of $\delta m/m$ relative to reference ion in isochronous condition for the IMS method. Besides, a new mass of ^{74}Ni (mass excess -72190 keV and mass uncertainty 927 keV) which is not included in the newest atomic mass

evolution (AME2016) is deduced in this work by $B\rho$-TOF method. The mass of ^{74}Ni is very important for the research of nuclear shell effect and also show importance of the impact on the r-process modeling.

A large area position sensitive mirror-type foil MCP (Micro-channel plate) timing detector, which possesses specifications of low energy loss and energy straggling by detection of secondary electrons (SEs) induced from conversion foil, a large effective area (110 mm × 50 mm) to cover the large beam size, good timing and position resolution at the same time is being developed at the Rare RI Ring (R3). This type of detector is a versatile instrument which can be used on the beam-line for two dimensional position measurement to reconstruct beam trajectory, beam-line momentum measurements for velocity reconstruction, meanwhile, it can be used for position monitoring and revolution time measurement turn by turn inside the storage ring, R3. For high resolution mass measurements, high resolution momentum measurement with low energy loss and energy straggling is indispensable for reconstruction of the velocity for in-ring mass deduction or momentum measurement with good accuracy and high precision for Bρ-TOF mass measurements. High resolution TOF in ring is not only significant for identification of nuclei but also can be also used for mass measurements directly. To characterize and optimize the timing and position resolution of the detector, an isochronous condition is chosen and resolution dependence of high voltage supplies has been studied experimentally and by simulation. Experiments aimed at studying the performance of the detector was conducted at HIMAC (Heavy Ion Medical Accelerator in Chiba) with heavy ion beam and with alpha source of ^{241}Am. The performance of the detector have been optimized and the best achieved timing resolution and position is ≤ 50 ps and 1 mm in σ respectively, for which the detection efficiency is ~95 %. The performance of another same type of mirror detector coupled with timing anode which is dedicated for TOF measurement has been studied by heavy ions at HIMAC . The best achieved timing resolution is $\sim$ 40 ps (in σ) and detection efficiency is $\sim$ 96 % for heavy ion beams. This timing detector will be used for revolution time measurement inside R3, start TOF detector of the total TOF for in-ring circulation, beam-line TOF measurement for beam-line mass determination and velocity reconstruction for in-ring mass correction.

In summary, in this work, the basic features of isochronous mass spectroscopy (IMS) for the present facilities at RIBF in RIKEN and also for the future experiments have been experimentally and theoretically investigated. The prospects and limitations of IMS have been studied with calculations and experiments. The basic features and performance of isochronous storage ring mass spectroscopy (IMS) and $B\rho$-Time-of-flight mass spectroscopy for the present BigRIPS-SHARAQ-R3 conjugation system at RIKEN has also been experimentally and theoretically investigated. The fast low-energy-loss position-sensitive tim-

ing detector developed within this work in use for in-ring and on beam-line are discussed and summarized, and is ready to be utilized to realize a higher performance mass measurements simultaneously employing the Rare-RI Ring in conjunction with the high resolution beam-lines BigRIPS-OEDO-SHARAQ by the two complementary TOF Methods: Magnetic-rigidity-time-of-flight (Bρ-TOF) and Isochronous Storage Ring Mass Spectrometer (IMS).

6.2 Outlook

Storage ring spectrometers are powerful devices for high-accuracy mass measurements of very short-lived isotopes. New developments and efforts (the in-ring double-TOF method at CSRe/IMP, CR ring/ESR and the additional beam-line $B\rho$/velocity measurement coupled with individual injection at the Rare-RI Ring/RIKEN) in additional measurements of momentum/velocity techniques have extended the applicability and ability of storage ring mass spectrometry. With the newly developed Obit-IMS methods coupled with the $B\rho$-TOF method to measure the masses of exotic nuclei simultaneously in one experimental run at the RIBF, which now possesses the highest intensity of primary beams, being verified, a foreseeing productive and fruitful results will come out soon. The up-coming experiments at the Rare-RI Ring will provide a large number of new accurate masses values, which will contribute to a better understanding of nuclear structure, nuclear astrophysical processes, and even fundamental interactions.

In future experiments at the Rare-RI Ring, our goals are to increase the resolution and accuracy of the orbit-IMS method with the newly developed high timing and position resolution MCP detector. A modified electronics system with multi-hit function should be used for these MCP detectors to increase the capability of resolving multi-hit events and solve problem of the broaden timing sum of both end of one direction delay-line.

This result confirms in the frame work of this doctoral thesis that for IMS one need to measure the revolution time and the magnetic rigidity or the velocity independently for correction to achieve a higher mass accuracy and precision with a relative wide momentum acceptance for exotic nuclei with relative large difference of mass-over-charge to the reference nucleus. For the future IMS experiments in the new generation storage rings in HIAF in China or FAIR in Germany, this requirement can be fulfilled with the new dual foil-MCP ToF detector system developed in GSI and IMP separately. For a better choice, a foil-MCP detector possessing both high timing and position resolution, with sufficient circulation of the RIs should be developed for the storage rings in order to realize the the orbit-IMS method with one compact detector to let smaller energy loss for each revolution. The next gener-

ation facilities with storage rings for mass measurements are schematically shown in the below section.

6.2.1 Other next generation facilities with storage rings for mass measurements

The future next generation, Facility for Antiproton and Ion Research (FAIR) [188], is schematically illustrated in Fig. 6.1. It is proposed to extend the existing GSI facility by adding the heavy-ion synchrotrons SIS-100 and SIS-300, a two-stage large-acceptance superconducting fragment separator Super-FRS and a dedicated complex of storage rings (the Collector Ring (CR), the Recuperated Experimental Storage Ring (RESR), the New Experimental Storage Ring (NESR), and the High-Energy Storage Ring (HESR)). The key facility for mass measurements will be the CR, which is particularly designed for conducting IMS measurements. The ion- optical matching of the Super-FRS and the CR will provide a close to unity transmission of the secondary beams. The CR will be equipped with two time-of-flight (ToF) detectors installed in one of the straight sections as shown in Fig. 6.3, which will enable in-ring velocity measurement of each particle and is indispensable for correction of the non-isochronicity. Employing the novel resonant Schottky detectors will enable simultaneous broad-band mapping of nuclear masses and lifetimes by the SMS technique [48, 95, 188].

A High-Intensity Accelerator Facility (HIAF) [189], is planned at Huizhou, China. The facility is updated form the HIRFL facility and design of the facility is being optimizing. Figure. 6.2 illustrates a proposed concept design. Two types of ion sources will be adopted. One is Electron Cyclotron Resonance (ECR) ion source and the other is Laser Ion Source (LIS). The ions will be accelerated by a high current Superconducting linac(iLinac), and then accelerated by a heavy Fast cycle ring (FRing), which will have the maximum magnetic rigidity $B\rho = 25$ Tm. Further acceleration of the beam will be in the Booster ring (BRing) with the maximum magnetic rigidity $B\rho = 43$ Tm. The primary beam is then delivered to entrance of the High-resolution Fragment separator (HFRS) and bombard with a solid target to produce exotic secondary beams. The secondary beams is then separated and identified to inject into the following Spectrometer ring (SRing) as shown in Fig. 6.4 and Fig. 6.3, which has been designed for mass and half-life measurements. The experiments with stored exotic nuclei will be performed in the experimental SRing, which is connected to MRing (shape“8” ring) for Ion-ion merging.

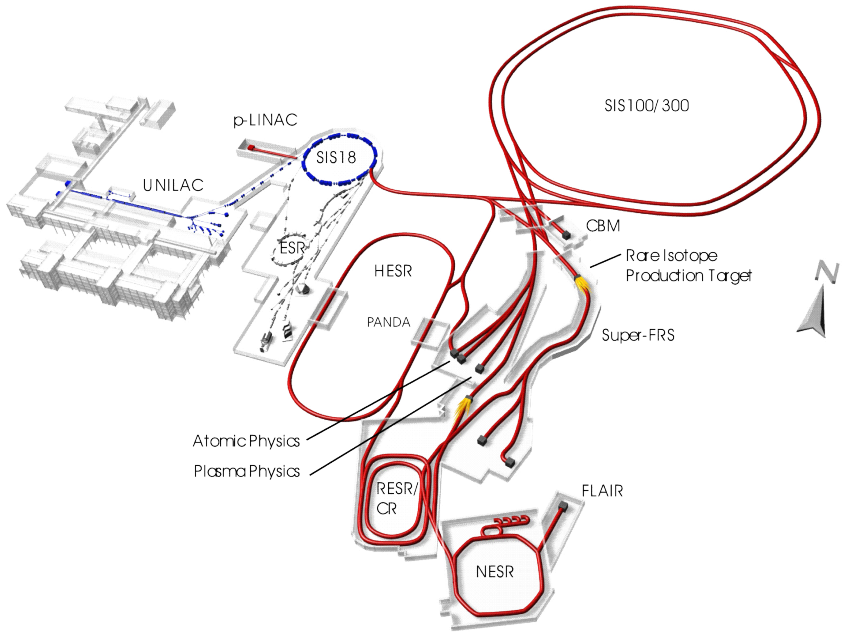

Fig. 6.1 Schematic layout of next generation facility FAIR [189] at GSI in Darmstadt, Germany. FAIR is proposed to extend the existing GSI facility.

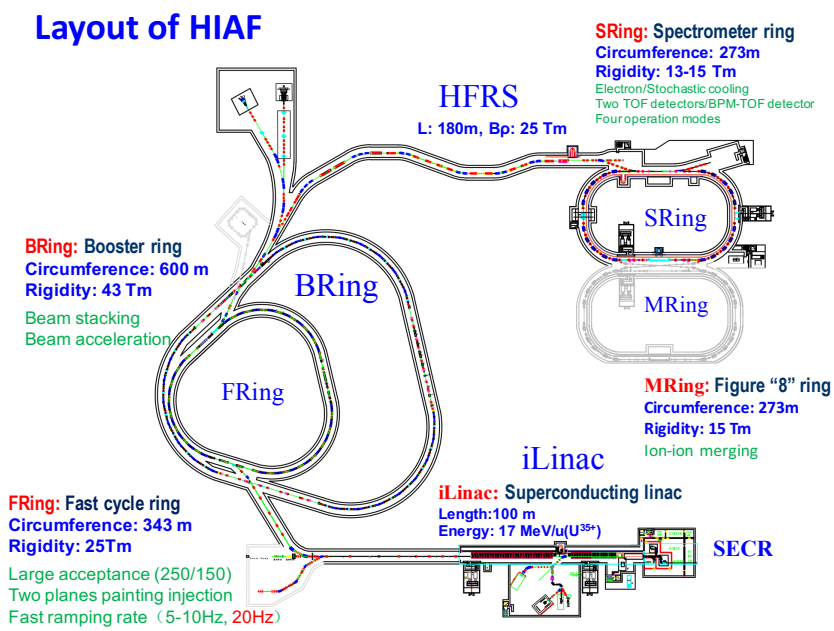

Fig. 6.2 Schematic layout of next generation facility HIAF, in China, which a newly proposed facility.

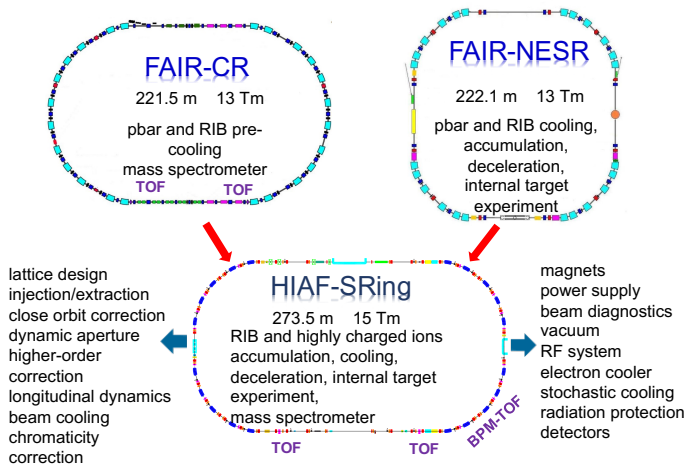

Fig. 6.3 Schematic view of storage rings of next generation facility for mass measurements. Compared the Collector Ring (CR) and New Experimental Storage Ring (NESR), it seems that SRing could integrate the tasks of CR and NESR which are very advanced and powerful storage rings for multi-functional experiments, into the one compact ring. The design of SRing will be a big challenge for beam dynamic simulation and hardware design. Courtesy of Mr. WU Bo in IMP.

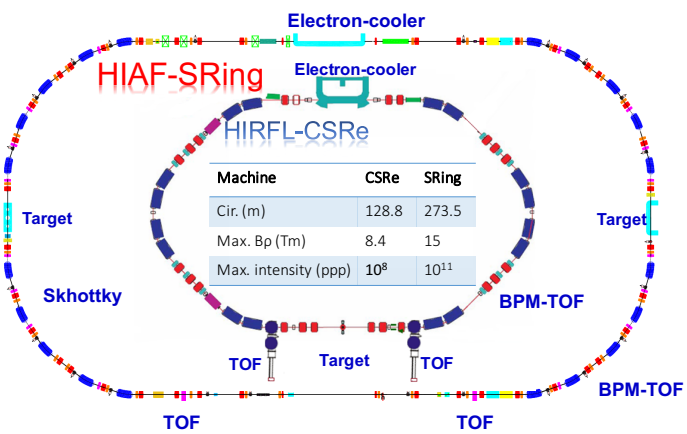

Machine	CSRe	SRing
Cir. (m)	128.8	273.5
Max. Bρ (Tm)	8.4	15
Max. intensity (ppp)	10^8	10^{11}

Fig. 6.4 Schematic view of storage rings for mass measurements in China and planed/developed detector systems in the rings. Compared with the existing facility HIRFL-CSRe, SRing seems to be an enhanced CSRe. With a dual-TOF and/or BMP-TOF system, higher precision and accuracy mass measurements will be performed in the future advanced SRing, which can be operated in orbit-IMS condition and hopefully will be performed in normal ion-optical mode with large momentum acceptance to realize the concept of long-$B\rho$-TOF method for mass measurements in storage rings.

References

[1] G. Audi. *The history of nuclidic masses and of their evaluation*. International Journal of Mass Spectrometry, 2006, **251**:85-94.

[2] Y. Litvinov, K. Blaum. *100 years of Mass Spectrometry*. International Journal of Mass Spectrometry, 2013, **349–350**:1-276.

[3] G. Audi, F. G. Kondev, M. Wang, W. J. Huang, S. Naimi *The Nubase2016 evaluation of nuclear properties*. Chinese Physics C, 2017, 41(3):030001.

[4] G. Audi, F.G. Kondev, M. Wang, B. Pfeiffer, X. Sun, J.Blachot, M. MacCormick. *The Nubase2012 evaluation of nuclear properties*. Chinese Physics C, 2012, 36(12):1157-1286.

[5] D. Lunney, J. M. Pearson, C. Thibault. *Recent trends in the determination of nuclear masses*. Review of Modern Physics, 2003, **75**:1021-1082.

[6] J. J. Thomson. Philosophical Magazine 1907, **44**:29.

[7] J. J. Thomson. Philosophical Magazine 1907, **13**:561.

[8] J. J. Thomson. Proceedings of the Royal Society A 1913, **89**:1.

[9] F. W. Aston *A positive ray spectrograph* Philosophical Magazine 1919, **38**:709.

[10] F. W. Aston Philosophical Magazine 1920, **39**:449.

[11] F. W. Aston. *Isotopes and Atomic Weights*. Nature, 1920, **105**:617.

[12] F. W. Aston Proceedings of the Royal Society, 1927, 115A:487

[13] F.W. Aston. *Mass Spectra and Isotopes, 2nd ed.* Edward Arnold Co., 1942.

[14] G.Münzenberg. *Development of mass spectrometers from Thomson and Aston to present*. International Journal of Mass Spectrometry, 2013, 349-350:9-18.

[15] A. J. Dempster. *A new Method of Positive Ray Analysis*. Physical Review, 1938, **53**:869.

[16] A. J. Dempster. Phys. Rev, 1918, **11**:316.

[17] A. J. Dempster. Proceedings of the American Philosophical Society, 1934, **89**:755.

[18] J. Mattauch, R. Herzog. Zeitschrift fur Physik, 1934, **89**:786.

[19] H. Ewald, H. Hintenberger. Methoden und Anwendungen der Massenspek-troskopie, Verlag Chemie GmbH, Weinheim, 1953.

[20] S. Fukumoto, T. Matsuo, H. Matsuda. Journal of the Physical Society of Japan, 1968, **25**:946-950.

[21] Yasushige Yano. *The RIKEN RI Beam Factory Project: A status report*. Nuclear Instruments and Methods in Physics Research B, 2007, **261**:1009-1013.

[22] A. P. Zuker. *Isobaric Multiplet Yrast Energies and Isospin Nonconserving Forces*. Phys. Rev. Lett., 2002, **89**:142502.

[23] Klaus Blaum. *High-accuracy mass spectrometry with stored ions*. Physics Reports, 2006, **251**:85-94.

[24] J. Jänecke et al. At. Data Nucl. Data Tab., 1988, **39**:265.

[25] T. Tachibana et al. At. Data Nucl. Data Tab., 1988, **39**:251.

[26] P. Möller et al. At. Data Nucl. Data Tab., 1995, **59**:185.

[27] J. Y. Zhang et al. Phys. Lett. B, 1989, **227**:1.

[28] P. Van Isacker et al. Phys. Lett. Lett., 1995, **74**:4607.

[29] R. B. Cakirli et al. Phys. Lett. Lett., 2005, **94**:092501.

[30] C. F. von Weizsačker et al. Z. Phys., 1935, **96**:431.

[31] H. A. Bethe et al. Rev. Mod. Phys., 1936, **8**:82.

[32] G. Audi et al. Nucl. Phys. A, 2003, **792**:337.

[33] K. Heyde. *The Nuclear Shell-model*. Springer, Berlin, Heidelberg, New York, 1994.

[34] W. Benenson et al. Rev. Mod. Phys., 1979, **51**:527.

[35] E. P. Wigner et al. Proceedings of the Robert A. Welch Foundation Conference on Chemical Research, Houston,, 1957, **1**.

[36] S. Weinberg et al. Phys. Rev., 1959, **116**:465.

[37] J. Britz et al. At. Data Nucl. Data Tab., 1998, **69**:125.

[38] M. MacCormick, G. Audi Nuclear Physics A, 2014, **925**:61–95

[39] H. Schatz et al. Phys. Rep., 1998, **294**:167.

[40] W. E. Ormand et al. Phys. Rev. C., 1997, **55**:2407.

[41] W. Satuła, J. Dobaczewski, W. Nazarewicz. Phys. Rev. Lett., 1998, **81**:3599.

[42] J. Dobaczewski et al Phys. Rev. C., 2001, **63**:24308.

[43] B. Franzke. Mass Spectrom Rev., 2008, **27**:428–69.

[44] H. Geissel, et al. Phys. Rev. Lett., 1992, **68**:3412–5.

[45] T. Radon, et al. Phys. Rev. Lett., 1997, **78**:4701–4.

[46] B. Sun, et al. Nucl. Phys. A, 2008, **812**:1-2.

[47] Eric Haseltine. *The 11 Greatest Unanswered Questions of Physics*. Discover, February 01,2002.

[48] Yuri A. Litvinov and Fritz Bosch. *Beta decay of highly charged ions*. Rep. Prog. Phys., 2011, **74:441**:C016301.

[49] P. Möller. Atom. Data Nucl. Data Tables,, 2012, **108**:052501.

[50] P. Möller. Atom. Data Nucl. Data Tables,, 2012, **108**:052501.

[51] S. Goriely et al. Phys. Rev. C,, 2010, **82**:035804.

[52] S. Goriely et al. Phys. Rev. C,, 2013, **88**:024308.

[53] Ning Wang et al. *Mirror nuclei constraint in mass formula*. Phys. Rev. C,, 2010, **82**:044304.

[54] Ning Wang et al. *Surface diffuseness correction in global mass formula*. Phys. Rev. B,, 2014, **734**:215-219.

[55] F. Bosch et al. Prog. Part. Nucl. Phys., 2013, **73**:84–140.

[56] A. Ozawa et al. *The rare-RI ring*. Prog. Theor. Exp. Phy., 2012, **2012**:03C009.

[57] H. Schatz. *The importance of nuclear masses in the astrophysical rp-process*. International Journal of Mass Spectrometry, 2006, **251**:293-299.

[58] F. Käppeler. Rev. Mod. Phys., 2011, 83:157–94.

[59] F.K. Thielemann et al. Prog. Part. Nucl. Phys., 2011, **106**:112501.

[60] M. Arnould et al. Phys. Rep., 2007, **450**:97–213.

[61] N. R. Tanvir et al. Nature, 2013, **500**:547–9.

[62] K. L. Kratz et al. Nature, 2013, **531**:610.

[63] K. L. Kratz et al. Astrophys. J., 1993, **403**:216–38.

[64] M. Eichler et al. J. Phys. Conf. Ser., 2016, **665**:012054.

[65] D. Atanasov et al. Phys. Rev. Lett., 2015, **115**:232501.

[66] P. T. Hosmer et al. Phys. Rev. Lett., 2005, **94**:112501.

[67] R. Caballero-Folch et al. Phys. Rev. Lett., 2016, **117**:012501.

[68] G. Lorusso et al. Phys. Rev. Lett., 2013, **114**:192501.

[69] D. Atanasov et al. Phys. Rev. Lett., 2013, **114**:192501.

[70] H. Schatz, et al. International Journal of Mass Spectrometry, 2013, **349–350**:145–150.

[71] H. Schatz, et al. Phys. Rev. Lett., 2001, **86**:3471.

[72] B. A. Brown, et al. Phys. Rev. C, 1994, **50**:R2270.

[73] J. Pruet, et al. Astrophys. J., 2006, **644**:1028.

[74] N. Weinberg, et al. Astrophys. J., 2006, **639**:1018.

[75] C. Frohlich, et al. Phys. Rev. Lett., 2006, **96**:142502.

[76] F. Herfurth, et al. Eur. Phys. J., 2006, **47**:75.

[77] E. Haettner, et al. Phys. Rev. Lett., 2011, **106**:122501.

[78] N. Weinberg, et al. Astrophys. J., 2006, **639**:1018.

[79] C. Frohlich, et al. Phys. Rev. Lett., 2006, **96**:142502.

[80] Y. M. Xing, et al. Phys. Lett. B, 2018, **781**:358-363.

[81] X.L. Tu, H.S. Xu, M. Wang, et al. *Direct Mass Measurements of Short-Lived A=2Z-1 Nuclides ^{63}Ge, ^{65}As, ^{67}Se, and ^{71}Kr and Their Impact on Nucleosynthesis in the rp-Process*. Phys. Rev. Lett., 2011, **106**:112501.

[82] Edmund G. Myers. *The most precise atomic mass measurements in Penning traps*. International Journal of Mass Spectrometry, 2013, **349-350**:107 C122.

[83] H. J. Kluge. International Journal of Mass Spectrometry, 2013, **349–350(0)**:26 – 37.

[84] R. N. Wolf. *ISOLTRAP's multi-reflection time-of-flight mass separator/spectrometer*. International Journal of Mass Spectrometry, 2013, **349–350(0)**:123 - 133.

[85] L. Bianchi, B. Fernandez, J. Gastebois, et al. *SPEG: An energy loss spectrometer for GANIL*. Nuclear Instruments and Methods in Physics Research Section A, 1989, **276(3)**:509 - 520.

[86] J. Wouters, D. Vieira, H. Wollnik, et al. *Optical design of the tofi (time-of-flight isochronous) spectrometer for mass measurements of exotic nuclei*. Nuclear Instruments and Methods in Physics Research Section A, 1985, **240(1)**:77 - 90.

[87] Z. Meisel and S. George. *Time-of-flight mass spectrometry of very exotic systems*. International Journal of Mass Spectrometry, 2013, **349–350**:145 - 150.

[88] A. Estrade, M. Matos, H. Schatz et al. *Time-of-Flight Mass Measurements for Nuclear Processes in Neutron Star Crusts*. Phys. Rev. Lett., 2011, **107**: 172503.

[89] S. Michimasa, et al. *Magic Nature of Neutrons in 54Ca: First Mass Measurements of 55–57Ca*. Nuclear Instruments and Methods in Physics Research Section A, 2012, **696(0)**:171 - 179.

[90] Z. Meisel and S. George. *Time-of-flight mass spectrometry of very exotic systems*. Phys. Rev. Lett., 2018, **121**:022506.

[91] G. Auger et al. Nuclear Instruments and Methods in Physics Research Section A, 1994, **350**:235 - 243.

[92] G. Auger et al. *Mass Measurements of* $^{100}S_n$. Phys. Rev. Lett., 1996, **77(12)**:2400-2403.

[93] B. Franzke et al. Nuclear Instruments and Methods in Physics Research B, 1987, **24/25**:18–25.

[94] H. Geissel et al. Nuclear Instruments and Methods in Physics Research B, 1992, **70**:286–97.

[95] Yuri.A. Litvinov,G. AUDI et al. *Technical Proposal for the ILIMA Project*. 2005.

[96] Y. H. Zhang et al. Physica Scripta, 2016, **91(7)**:073002.

[97] Fritz Bosch and Yuri A. Litvinov. *Mass and lifetime measurements at the experimental storage ring of GSI*. International Journal of Mass Spectrometry, 2013, **349-350**:151 - 161.

[98] J.W. Xia, W.L. Zhan, B.W. Wei, et al. *The heavy ion cooler-storage-ring project (HIRFL-CSR) at Lanzhou*. Nuclear Instruments and Methods in Physics Research Section A, 2002, 488(1-2):11-25.

[99] W.L. Zhan, H.S. Xu, G.Q. Xiao, et al. *Progress in HIRFL-CSR*. Nuclear Physics A, 2010, 834(1-4):694c - 700c.

[100] Hu Shan Xu et al. *Accurate mass measurements of exotic nuclei with the CSRe in Lanzhou*. International Journal of Mass Spectrometry, 2013, **349-350**:162 - 171.

[101] H. Wollnik. *History of mass measurements in time-of-flight mass analyzers*. International Journal of Mass Spectrometry, 2013, 349-350:38-46.

[102] B. Schlitt, K. Beckert, F. Bosch et al. *Schottky mass spectrometry at the ESR: a novel tool for precise direct mass measurements of exotic nuclei*. Nuclear Physics A, 1997, 626(1-2):315 - 325.

[103] T. Radon, Th. Kerscher, B. Schlitt et al. *Schottky Mass Measurements of Cooled Proton-Rich Nuclei at the GSI Experimental Storage Ring*. Phys. Rev. Lett., 1997, **78**:4701.

[104] H. Poth. *Electron cooling: Theory, experiment, application*. Physics Reports, 1990, 196(3-4):135 -297.

[105] M. Hausmann, F. Attallah, K. Beckert et al. *First isochronous mass spectrometry at the experimental storage ring ESR*. Nuclear Instruments and Methods in Physics Research Section A, 2000, 446(3):569 - 580.

[106] M. Hausmann, J. Stadlmann, F. Attallah et al. *Isochronous Mass Measurements of Hot Exotic Nuclei*. Hyperfine Interaction, 2001, **132**:289-295.

[107] Sergey A. Litvinov. *Investigation of the Isochronous Mode of the Experimental Storage Ring (ESR) and the Collector Ring (CR). Decay Spectroscopy of Highly Charged Stored ^{140}Pr Ions at the FRS-ESR Facility*. PhD thesis, Justus-Liebig Universitat Giessen, March 2008.

[108] F. Bosch, Yu. A. Litvinov, and Th. Stöhlker. *Nuclear physics with unstable ions at storage rings*. Progress in Particle and Nuclear Physics, 2013, **73**: 84-140.

[109] H. Geissel, R. Knöbel, Yu. A. Litvinov et al. *A new experimental approach for isochronous mass measurements of short-lived exotic nuclei with the FRS-ESR facility*. Hyperfine Interactions, 2006, **173**:49-54.

[110] H. Geissel and Yu. A. Litvinov. *Precision experiments with relativistic exotic nuclei at GSI*. Journal of Physics G, 2005, **31**: 1779-1783.

[111] Y.M. Xing, Y.H. Zhang, R.J. Chen et al. *First Isochronous Mass Measurements with two Time-of-Flight Detectors at CSRe*. Phys. Scrip., 2015, **T166**: 014010.

[112] F. Nolden, P. Hülsmann, Yu.A. Litvinov et al. *A fast and sensitive resonant Schottky pick-up for heavy ion storage rings*. Nuclear Instruments and Methods in Physics Research Section A, 2011, 659(1):69 - 77.

[113] J. Bowman, R. Heffner. *A novel zero time detector for heavy ion spectroscopy*. Nuclear Instruments and Methods, 1978, 148(3):503 - 509.

[114] S. Saro, R. Janik, S. Hofmann et al. *Large size foil-microchannel plate timing detectors*. Nuclear Instruments and Methods in Physics Research Section A, 1996, **381**:520.

[115] Y.D. Zang, J.X. Wu, T.C. Zhao, et al. *Simulation and measurement of the resonant Schottky pickup*. Chinese Physics C, 2011, 35(12):1124.

[116] B. Mei, X.L. Tu, M. Wang et al. *A high performance Time-of-Flight detector applied to isochronous mass measurement at CSRe*. Nuclear Instruments and Methods in Physics Research Section A, 2010, 624(1):109 - 113.

[117] W. Zhang, X.L. Tu, M. Wang et al. *Time-of-flight detectors with improved timing performance for isochronous mass measurements at the CSRe*. Nuclear Instruments and Methods in Physics Research Section A, 2014, **756**: 1-5.

[118] Natalia Kuzminchuk-Feuerstein Nuclear Instruments and Methods in Physics Research Section A, 2016, **821**: 160–168.

[119] W. STARZECKI et al. *A COMPACT TIME-ZERO DETECTOR FOR MASS IDENTIFICATION OF HEAVY IONS*. Nuclear Instruments and Methods, 1982, **193**:71-74.

[120] F. Busch et al. *A position-sensitive transmission time detector*. Nuclear Instruments and Methods, 1979, **171**:71-74.

[121] C. W. Arnold et al. *Development of position-sensitive time-of-flight spectrometer for fission fragment research*. Nuclear Instruments and Methods in Physics Research A, 2014, **764**:53–58.

[122] K. Kosev et al. *A high-resolution time-of-flight spectrometer with tracking capabilities for fission fragments and beams of exotic nuclei*. Nuclear Instruments and Methods in Physics Research A, 2008, **594**:178 – 183.

[123] H. Bethe et al. Z. Phys., 1932 **76**: 293.

[124] H. Bethe et al. Handb. Phys., 1933 **24**: 273.

[125] Sternglass, E. J.. *Theory of Secondary Electron Emission by High-Speed Ions*. Phys. Rev., 1957, **108**:1-12.

[126] Bohr, Niels. *The penetration of atomic particles through matter*. I kommission hos E. Munksgaard, 1948, **18**.

[127] P. Ahlen, Steven. *Theoretical and experimental aspects of the energy loss of relativistic heavily ionizing particles. Rev. Mod. Phys., 1980,* **52***:121–173.*

[128] C. Scheidenberger, H.Geissel. Penetration of relativistic heavy ions through matter. *Nuclear Instruments and Methods in Physics Research B, 1998,* **135***:25-34.*

[129] Hans Geissel and Christoph Scheidenberger. Slowing down of relativistic heavy ions and new applications. *Nuclear Instruments and Methods in Physics Research Section B: Beam Interactions with Materials and Atoms, 1998,* **136–138***:114 - 124.*

[130] Bethe, HA. Julius Springer, Berlin, 1933.

[131] C. Loty et al. Acta Electronica., 1971, **14***:107.*

[132] N. Nankov et al. Wiss. Tech. Berichte FZR-423, 2005, **25***(Annual Report 2004).*

[133] http://www.simion.com

[134] H. Rothard et al. Nucl. Instr. and Meth. B, 1990, **48***:616-620.*

[135] H. Rothard et al. Phys. Rev. A, 1990, **41(5)***:2521.*

[136] H. Rothard et al. Target-thickness-dependent electron emission from carbon foils bombarded with swiftt highly charged heavy ions. *Phys. Rev. A, 1995,* **51(5)***:3066.*

[137] H. Rothard et al. Projectile- and charge-state dependent electron yields from ion penetration of solids as a probe of pre-equilibrium stopping power. *Phys. Rev. A, 1992,* **45***:3.*

[138] M. Jung, H. Rothard et al. Transport of electrons induced by highly charged Ni (74 MeV/u) and Cu (9.6 MeV/u) ions in carbon. A study of target-thickness dependent electron yields. *Phys. Rev. A, 1996,* **54***:5.*

[139] P. Koschar et al. Secondary electron yield as a probe of preequilibrium stopping power of heavy ions colliding with solids. *Phys. Rev. A, 1989,* **40***:7.*

[140] RoentDek GmbH; http://www.roentdek.com

[141] J. L. Wiza. Micro channel plate detectors. *Nucl. Instr. and Meth., 1979* **162***:587-601.*

[142] http://www.hamamatsu.com/

[143] http://www.photonis.com

[144] Jon Lapington. WSO Detector Workshop, Leicester, 2007.

[145] O.H.W. Siegmund et al. Cross strip imaging anodes for microchannel plate detectors. *IEEE Trans. Nucl. Sci., 2001* **48***: 430-434.*

[146] O.H.W. Siegmund et al. High resolution cross strip anodes for photon counting detectors. *Nuclear Instruments and Methods in Physics Research A, 2003* **504***: 177–181.*

[147] O.H.W. Siegmund et al. Nuclear Instruments and Methods in Physics Research A, 2009 **610***: 118-122.*

[148] Vallerga, J. et al. Astrophys Space Sci, 2009 **320***: 247-250.*

[149] S. KALBITZER et al. ON THE CHARGE DIVIDING MECHANISM IN POSITION SENSITIVE DETECTORS. *Nuclear Instruments and Methods, 1967* **56***: 301-304.*

[150] Davinder Siwal et al. Using pulse shape analysis to improve the position resolution of a resistive anode microchannel plate detector. *Nuclear Instruments and Methods in Physics Research A, 2015* **804***: 144–148.*

[151] M. Lampton et al. Low-distortion resistive anodes for two-dimensional position-sensitive MCP systems. *Review of Scientific Instruments, 1979* **50***: 1093.*

[152] P. Downie et al. Measurement Science and Technology, 1993 **4***: 1293.*

[153] Romualdo T. deSouza et al. Development of a high resolution position sensitive MCP-PMT detector. *Neutron and Photon Detector Workshop, 2012.*

[154] M. Lampton et al. Optimization of the Readout Electronics for Microchannel Plate Delay Line Anodes. *Proc. SPIE 4139, Instrumentation for UV/EUV Astronomy and Solar Missions, 2000.*

[155] Sobottka and Williams. IEEE , 1988 **TS-35***: 348.*

[156] M. Lampton et al. Multiple Hit Read-out of a Microchannel Plate Detector with a Three-Layer Delay-Line Anode. *IEEE Transactions on Nuclear Science, 2002* **49***: 2477 - 2483.*

[157] M. Lampton et al. Multiple Hit Read-out of a Microchannel Plate Detector with a Three-Layer Delay-Line Anode. *IEEE Transactions on Nuclear Science, 2002* **49***: 2477 - 2483.*

[158] M. Lampton et al. Multilayer anode with crossed serpentine delay lines for high spatial resolution readout of microchannel plate detectors. *Review of Scientific Instruments, 1996* **67***: 596.*

[159] M. B. WILLIAMS et al. High resolution two dimensional read-out of microchannel plates with large area delay lines. *IEEE Transactions, 1989* **36(1)***: 227–230.*

[160] M. B. WILLIAMS et al. Delay line read- out of microchannel plates in a prototype position-sensitive photomultiplier tube. *Nuclear Instruments and Methods in Physics Research Section A, 1991* **302(1)***: 105 – 112.*

[161] C. Martin et al. Wedge-and-strip anodes for centroid-finding position-sensitive photon and particle detectors. Review of Scientific Instruments, 1981 **52***: 1067.*

[162] G.W. Fraser. Nuclear Instruments and Methods in Physics Research, 1984 **221***: 115.*

[163] Jürgen Barnstedt. Advanced Practical Course Microchannel Plate Detectors, 2016

[164] T. Mizogawa et al. Nuclear Instruments and Methods in Physics Research A, 1997 **387***: 395.*

[165] Spezialelektronik GmbH; http://www.iseg-hv.de

[166] http://www.kaizuworks.co.jp

[167] https://www.ortec-online.com/products/electronics

[168] https://www.repic.co.jp/product/repic/product.html

[169] http://www.kagaku.com/hoshin/english.html

[170] Y. Hirao et al. Nucl. Phys. A, 1992 **538***: 541.*

[171] M. Kanazawa et al. Nucl. Phys. A, 2004 **746***: 393.*

[172] H. Kumagai et al. Nuclear Instruments and Methods in Physics Research B, 2013 **317***: 717–727.*

[173] N. Fukuda et al. Nuclear Instruments and Methods in Physics Research B, 2013 **317***: 323–332.*

[174] Y. Yamaguchi et al. Construction of rare-RI ring at RIKEN RI Beam Factory. *Nucl. INstrum. Methods B, 2013* **317***: 629-635.*

[175] Y. Yamaguchi et al. Fast-kicker system for rare-RI ring. *Phys. Scr. , 2015* **T166***:014056.*

[176] T. Yamaguchi et al. The challenge of precision mass measurements of short-lived exotic nuclei. *International Journal of Mass Spectrometer, 2013* **349-350***: 240-246.*

[177] F. Suzaki et al. Design study of a resonant Schottky pick-up for the Rare-RI Ring project. *Phys. Scr. , 2015* **T166***:014056.*

[178] Tomohiro Uesaka et al. The SHARAQ spectrometer. *Prog. Theor. Exp. Phys., 2012* **2012***:03C007.*

[179] K. Kimura et al. High-rate particle identification of high-energy heavy ions using a tilted electrode gas ionization chamber. *Nuclear Instruments and Methods in Physics Research A, 2005* **538***:608–614.*

[180] D. Nagae et al. Nucl. Instrum. Methods Phys. Res. B, 2013 **317***:640-643.*

[181] Y. Abe et al. JPS Conf. Proc., 2014 **1***:013059.*

[182] Y. Abe et al. Phys. Scr. , 2015 **T166***:014047.*

[183] M. Hausmann et al. Nucl. Instr. and Meth. in Phys. Res. A, 2000 **446***:569-580.*

[184] D.C. Carey et al. Advances in Imaging and Electron Physics, Elsevier Inc. , 2009 **157**.

[185] D.C. Carey et al. Harwood Academic Publisher, New York , 1987.

[186] H. Wollnik et al. Optics of charged particles. *Academic Press, Florida , 1987.*

[187] O. Kamigaito et al. Proceedings of IPAC2014, Dresden, Germany , 2014: MO-PRI082.

[188] FAIR: Facility for Antiproton and Ion Research, webpage: www.gsi.de/fair.

[189] J.C. Yang et al High Intensity heavy ion Accelerator Facility (HIAF) in China. *Nucl. Instr. and Meth. in Phys. Res. B, 2013* **317***:263–265.*

orbit

Appendix A

Principle of Isochronous Mass Spectrometry

A.1 Principle of Isochronous Mass Spectrometry (IMS) by the Rare-RI Ring

The revolution time T of a stored ion (m/q) with velocity v circulating in a storage ring with orbit length C is given as:

$$T = \frac{C}{v}. \tag{A.1}$$

By differentiation of Eq. A.1, we obtain:

$$dT = \frac{\delta T}{\delta C} dC + \frac{\delta T}{\delta v} dv = \frac{1}{v}\delta C - \frac{C}{v^2} dv. \tag{A.2}$$

and relative differential of T:

$$\frac{dT}{T} = \frac{1}{vT} dC + \frac{C}{v^2 T} dv = \frac{dC}{C} - \frac{dv}{v}. \tag{A.3}$$

With this relation one can already see that the revolution time depends on the relative change in circumference (hence the orbit in the ring) as well as on the relative change in velocity. The differences between the flight paths of the reference particle and the non-reference particle will be considered. In terms of accelerator physics the relative change of the orbit in a circular accelerator or storage ring is described with the so called momentum compaction factor α_p [183, 184, 186]. α_p is defined as:

$$\alpha_p = \frac{1}{C} \oint \frac{D(s)}{\rho} ds, \tag{A.4}$$

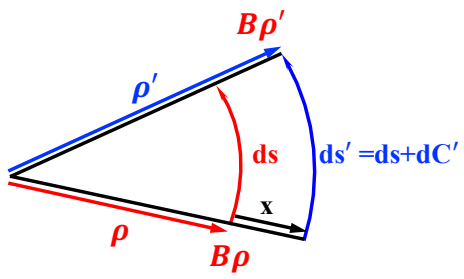

Fig. A.1 Schematic view of comparison of a central orbit trajectory with a shifted trajectory. The ion with the magnetic rigidity Bρ moves on the trajectory ds, while the ion with Bρ' = Bρ + d(Bρ) moves on the trajectory ds' = ds + dC'.

α_p characterizes the ratio between the relative change in the orbital length C and the relative change in the magnetic rigidity $B\rho$ (or relative momentum deviation) of the stored ions, which is nearly constant over the entire revolution frequency acceptance of the storage ring. The α_p can also be deduced from the dispersion function $D(s)$ of the ring. Here s denotes the coordinate along the reference orbit C_0, while ρ is the radius of the curvature of this reference orbit in the bending sections. with D(C′) being the dispersion from the central orbit at position C′ and ρ′ the deflection radius. The dispersion describes the dependency between a shift from the central orbit ρ′ relative to its momentum p′. Since the momentum of a confined particle in a ring depends on the magnetic rigidity of the central orbit Bρ and its change according to the shift from the orbit, the dispersion can be written as:

$$D(s) = -\frac{x(s)}{\Delta(B\rho)/B\rho)} \tag{A.5}$$

Figure A.1 illustrates that particles with central orbit (ρ) move along the trajectory ds while particles with an orbit ρ' $(\rho + x)$ move along a different trajectory ds′ $(ds + dC')$. The trajectory $ds + dC'$ belongs to the particle with magnetic rigidity of $B\rho'$ $(B\rho + d(B\rho))$. This also means that:

$$\frac{\rho}{(\rho + x)} = \frac{ds}{ds + dC'}, \tag{A.6}$$

and

$$\frac{\rho}{x(s)} = \frac{ds}{dC'}, \tag{A.7}$$

With these relations and knowing that $dC = \oint dL$ is the difference in the full revolution circumference, we can rewrite Eq. A.8 into:

$$\alpha_p = \frac{1}{C}\oint \frac{\rho'}{\delta(B\rho)/B\rho)}\frac{ds}{\rho} = \oint \frac{dC'}{\delta(B\rho)/B\rho)} = \frac{(dC/C)}{(d(B\rho)/B\rho)} = \frac{1}{\gamma^2} = \frac{1}{C}\oint \frac{D(s)}{\rho}\,ds, \tag{A.8}$$

Going back to equation Eq. A.3 and using Eq. A.8 we get:

$$\frac{dT}{T} = \alpha_p \frac{d(B\rho)}{B\rho)} - \frac{dv}{v}. \tag{A.9}$$

In mass measurements the magnetic rigidity is a measure for the mass-to-charge ratio and can be written for a magnetic dipole field in the relativistic case with momentum $p = \gamma m v$ as:

$$B\rho = \frac{P}{q} = \frac{\gamma m v}{q} = \frac{m}{q}\gamma\beta c. \tag{A.10}$$

With c the speed of light in vacuum, $\beta = v/c$, the relativistic Lorentz factor $\gamma = \beta^2)^{-1/2}$ and $\gamma\beta = \beta(1-\beta^2)^{-1/2} = \sqrt{(\gamma^2 - 1)}$. The total differential of Eq. A.10 is:

$$d(B\rho) = \frac{d(B\rho)}{d(\frac{m}{q})} d(\frac{m}{q}) + \frac{d(B\rho)}{d(\gamma\beta)} d(\gamma\beta) = \gamma\beta c \cdot d(\frac{m}{q}) + \frac{m}{q} c \cdot d(\gamma\beta). \tag{A.11}$$

Taking again the relative differential and using equation Eq. A.10 yields:

$$\frac{d(B\rho)}{B\rho} = \frac{d(\frac{m}{q})}{(\frac{m}{q})} + \frac{d(\gamma\beta)}{\gamma\beta}. \tag{A.12}$$

In a final step the last term $\frac{d(\gamma\beta)}{\gamma\beta}$ will be evaluated. Taking the total differential:

$$d(\gamma\beta) = \frac{d(\gamma\beta)}{d\beta} d\beta = (\frac{1}{\sqrt{1-\beta^2}} + \frac{\beta^2}{(1-\beta^2)^{3/2}}) d\beta = (\gamma + \beta^2\gamma^3) d\beta = \gamma(1 + (\gamma\beta)^2) d\beta. \tag{A.13}$$

and then using the relative differential:

$$\frac{d(\gamma\beta)}{\gamma\beta} = (1 + (\gamma\beta)^2)\frac{d\beta}{\beta} = (1 + \frac{\beta^2}{1-\beta^2})\frac{d\beta}{\beta} = (\frac{1}{1-\beta^2})\frac{d\beta}{\beta} = \gamma^2 \frac{d\beta}{\beta} \tag{A.14}$$

Combining equation Eq. A.12 with Eq. A.14 one gets:

$$\frac{d(B\rho)}{(B\rho)} = \frac{d(\frac{m}{q})}{(\frac{m}{q})} + \gamma^2 \frac{d\beta}{\beta}. \tag{A.15}$$

The beam frequency spread is related to its momentum spread via the so called frequency dispersion function or phase slip factor by:

$$\eta = \frac{1}{f}\frac{df}{\delta} = \frac{1}{\gamma^2} - \frac{1}{C}\frac{dC}{\delta} = \frac{1}{\gamma^2} - \frac{1}{{\gamma_t}^2}, \tag{A.16}$$

where $\delta = dp/p = d(B\rho)/B\rho$. Substitution of Eq. A.14 in equation Eq. A.9 with $d\beta/\beta = dv/v$ finally yields the dependency between revolution time T and the mass-to-charge ratio m/q:

$$\begin{aligned}\frac{dT}{T} &= \alpha_p\left(\frac{d(\frac{m}{q})}{(\frac{m}{q})} + \gamma^2\frac{d\beta}{\beta}\right) - \frac{dv}{v} \\ &= \alpha_p\frac{d(m/q)}{m/q} - \left(1 - \frac{\gamma^2}{\gamma_t^2}\right)\frac{dv}{v}.\end{aligned} \tag{A.17}$$

Using the so called transition point $\gamma_t = \frac{1}{\sqrt{\alpha_p}}$ from equation Eq. A.7, Eq. A.17 can be written for revolution time T or revolution frequency f as:

$$\frac{dT}{T} = -\frac{df}{f} = \frac{1}{\gamma_t^2}\frac{d(\frac{m}{q})}{(\frac{m}{q})} - \left(1 - \frac{\gamma^2}{\gamma_t^2}\right)\frac{dv}{v}, \tag{A.18}$$

The sign of the velocity dependent term $-(\eta\gamma^2)\frac{dv}{v}$ in Eq. A.18 depends on the sign of η and hence on the ratio $\gamma^2/\gamma_t^2 = \alpha_p\gamma^2$. η is positive for $\alpha_p\gamma^2 < 1$, i.e. $\gamma < \gamma_t$, and the revolution frequency increases with the increasing of particle energy. On the other hand, the revolution frequency f decreases for increasing particle energy ($\eta < 0$) if $\alpha_p\gamma^2 > 1$ (i.e. $\gamma > \gamma_t$). Due to this transition, the particle energy $E_t = \gamma_t mc_2$ for the reference particle, is called the transition energy of the accelerator or storage ring []. If the ring is operated at transition point, i.e. $\gamma > \gamma_t$ for the reference particle, then the frequency dispersion η vanishes. In this case, the revolution frequency does practically not depend on small changes of the particle energy (energy isochronous mode).

From Eq. A.15, the relative velocity β difference can be transformed to the magnetic rigidity $B\rho$ difference for a certain nucleus. Consequently, Eq. A.18 could be alternatively written as:

$$\frac{dT}{T} = -\frac{df}{f} = \frac{1}{\gamma^2}\frac{d(m/q)}{m/q} + \left(\frac{1}{\gamma_t^2} - \frac{1}{\gamma^2}\right)\frac{d(B\rho)}{B\rho} \tag{A.19}$$

Eq. A.18 and Eq. A.19 allows to connect the revolution times of known (reference) and unknown nuclei with their mass-to-charge ratio if the second term in Eq. A.18 vanishes. For the Schottky Mass Spectrometry the statistic and electron cooling leads to $dv/v \approx 10^{-7}$, which makes the second term negligible in a first order approximation. For the Isochronous Mass Spectrometry the second term is also cancelled, however this is not done with cooling but by tuning the ion optical parameter γ_t to be equal to the Lorentz factor γ of one selective m/q. During the experiments it is more practicable to set the ring to a fixed γ_t and change the

energy (and with it their Lorentz factor) of the particles injected into the ring until $\gamma = \gamma_t$ is reached.

The mass resolving power R after the cancellation of the second term is given by:

$$R = \frac{m}{dm} = \frac{1}{\gamma_t{}^2}\frac{T}{dT}, \tag{A.20}$$

A.1.1 Principle of orbit-IMS method at Rare-RI Ring

A new concept storage ring mass spectrometry, Rare-RI Ring, has been constructed at RIKEN RI Beam Factory (RIBF). The new scheme of IMS coupled with the individual injection method and velocity or $B\rho$ correction technique will achieve a mass accuracy on the order of 10^{-6}. Mass measurement with the Rare-RI Ring is based on the cyclotron frequency (f) or revolution time (T), which is expressed as:

$$f = \frac{1}{2\pi}\frac{Bq}{m} \tag{A.21}$$

and

$$T = 2\pi\frac{m}{Bq} \tag{A.22}$$

where m is mass , q is charge of the ion, and B is the magnetic field of the ring. The revolution time (T_0) of an ion with isochronous optics ($B = B_0\gamma$) is given by:

$$T = 2\pi\frac{m}{q}\frac{1}{B_0\gamma}, \tag{A.23}$$

and $\gamma = (1-\beta^2)^{-1/2}$ represents the relativistic factor and $\beta = v/c$ denotes the particle velocity relative to the velocity of light c. The relative uncertainty of the mass-to-charge ratio m_0/q_0 is:

$$\frac{\delta(\frac{m_0}{q_0})}{(\frac{m_0}{q_0})} = \frac{\delta T_0}{T_0} + \frac{\delta B_0}{B_0} \tag{A.24}$$

If we measure T_0 and B_0 with an accuracy of order 10^{-6}, we can determine the mass with an accuracy of order 10^{-6}. However, it is difficult to maintain and measure an isochronous field accurately. Therefore, we measure mass of the $\frac{m_1}{q_1}$ of target RI relative to that of a reference nucleus whose mass $\frac{m_0}{q_0}$ is precisely known. When the particle of interest with a mass-to-charge ratio of $\frac{m_1}{q_1}$ has the same momentum as that of a reference particle with a mass- to-charge ratio of $\frac{m_0}{q_0}$, the flight path length of these particles become identical in the

isochronous storage ring. Consequently, the following equations hold for these particles,

$$\begin{cases} \frac{m_0}{q_0}\gamma_0\beta_0 = \frac{m_1}{q_1}\gamma_1\beta_1 \\ \beta_0 T_0 = \frac{m_0}{q} T_1 \end{cases} \tag{A.25}$$

From these relations, the mass-to-charge ratio $\frac{m_1}{q_1}$ for the nucleus with unknown mass, for which the isochronism is not fulfilled, is expressed as:

$$\frac{m_1}{q_1} = \frac{m_0}{q_0}\frac{T_1}{T_0}\frac{\gamma_0}{\gamma_1} \tag{A.26}$$

Principle of velocity correction orbit-IMS method

By using the relation from Eq. A.25 to replace $\frac{\gamma_0}{\gamma_1}$ with $\sqrt{\frac{1-\beta_1^2}{1-(\frac{T_1}{T_0})^2{\beta_1}^2}}$, m_1/q_1 can be transformed to be as:

$$\frac{m_1}{q_1} = \frac{m_0}{q_0}\frac{T_1}{T_0}\sqrt{\frac{1-\beta_1^2}{1-(\frac{T_1}{T_0})^2{\beta_1}^2}} \tag{A.27}$$

The parameter K=$\sqrt{\frac{1-\beta_1^2}{1-(\frac{T_1}{T_0})^2{\beta_1}^2}}$ is defined as velocity correction factor.

The relative uncertainty for $\frac{m_1}{q_1}$ is given as:

$$\frac{\delta(\frac{m_1}{q_1})}{\frac{m_1}{q_1}} = \frac{\delta(\frac{m_0}{q_0})}{\frac{m_0}{q_0}} + \gamma_0^2\frac{\delta(\frac{T_1}{T_0})}{\frac{T_1}{T_0}} + k\frac{\delta\beta_1}{\beta_1} \tag{A.28}$$

where,

$$k = -\frac{{\beta_1}^2}{1-{\beta_1}^2} + (\frac{T_1}{T_0})^2\frac{{\beta_1}^2}{1-(\frac{T_1}{T_0})^2{\beta_1}^2} \tag{A.29}$$

The uncertainty of the mass-to-charge ratio, $\frac{m_1}{q_1}$, consists of three terms: the first term of Eq. A.28 is the uncertainty of the reference nuclear mass, and should be on the order of 10^{-6} or less. The second term is the uncertainty coming from an imperfection of the isochronism of the ring and the time resolution of the TOF detector. Even when the isochronism is perfectly tuned to the reference nucleus, isochronism for rare-RIs which is not satisfied, and usually will be slightly broken depending on the $\frac{\delta(m/q)}{m/q}$ relative to the reference. Therefore, the velocity measurement to compensate for variation in the third term in Eq. A.28 is essential. The value of k is on the order of 10^{-2} even if m/q differs from the reference nucleus

by 1% and gets smaller as the decreasing of $\frac{\delta(m/q)}{m/q}$. The third term is on the order of 10^{-6} as long as β_1 is measured with an uncertainty of 10^{-6}.

In principle, the velocity uncertainty parameter in Eq. A.29 can be derived as:

$$\begin{aligned}
&{\gamma_0}^2 - {\gamma_1}^2 \\
&= {\gamma_0}^2 - \frac{1}{1-{\beta_1}^2} = {\beta_0}^2{\gamma_0}^2 - \beta_1^2{\gamma_1}^2 \\
&= (\frac{T_1}{T_0})^2\frac{{\beta_1}^2}{1-(\frac{T_1}{T_0})^2{\beta_1}^2} - {\beta_1}^2{\gamma_1}^2 = (\frac{T_1}{T_0})^2\frac{{\beta_1}^2}{1-(\frac{T_1}{T_0})^2{\beta_1}^2} - \frac{{\beta_1}^2}{1-{\beta_1}^2} \\
&= k
\end{aligned} \tag{A.30}$$

Using Eq. A.30 to replace k in Eq. A.18, the following equation hold:

$$\begin{aligned}
&\frac{\delta(\frac{m_1}{q_1})}{\frac{m_1}{q_1}} - \frac{\delta(\frac{m_0}{q_0})}{\frac{m_0}{q_0}} \\
&= {\gamma_0}^2\frac{\delta(\frac{T_1}{T_0})}{\frac{T_1}{T_0}} + ({\gamma_0}^2 - {\gamma_1}^2)\frac{\delta\beta_1}{\beta_1} \\
&= {\gamma_0}^2(\frac{\delta(T_1)}{T_1} - \frac{\delta(T_0)}{T_0}) + ({\gamma_0}^2 - {\gamma_1}^2)\frac{\delta\beta_1}{\beta_1}
\end{aligned} \tag{A.31}$$

For a reference nucleus with m_0/q and target nucleus with m_1/q, the difference of the mass-to-charge ratio for the two nucleus $\frac{d(\frac{m}{q})}{(\frac{m}{q})}$ can be written as:

$$\frac{d(\frac{m}{q})}{(\frac{m}{q})} = \gamma_0^2\frac{dT}{T} + ({\gamma_0}^2 - {\gamma_1}^2)\frac{d\beta}{\beta}, \tag{A.32}$$

which is equivalent to the conventional principle expression Eq. A.18 for IMS with a velocity-β term.

Principle of momentum correction orbit-IMS method

By using the relation from Eq. A.25 to replace $\frac{\gamma_0}{\gamma_1}$ with $\sqrt{\frac{1-(\frac{T_0}{T_1})^2}{\left(\frac{\frac{m_0}{q_0}c}{(B\rho)_0}\right)^2}}$, m_1/q_1 can be transformed to be as:

$$\frac{m_1}{q_1} = \frac{m_0}{q_0}\frac{T_1}{T_0}\sqrt{\frac{1-(\frac{T_0}{T_1})^2}{\left(\frac{\frac{m_0}{q_0}c}{(B\rho)_0}\right)^2}} \tag{A.33}$$

The momentum P=$\sqrt{\frac{1-(\frac{T_0}{T_1})^2}{(\frac{m_0}{q_0}c)^2}}$ is defined as velocity correction factor.

The relative uncertainty for $\frac{m_1}{q_1}$ is given as:

$$\frac{\delta(\frac{m_1}{q_1})}{\frac{m_1}{q_1}} = \frac{\delta(\frac{m_0}{q_0})}{\frac{m_0}{q_0}} + \gamma_1^2 \frac{\delta(\frac{T_1}{T_0})}{\frac{T_1}{T_0}} + p\frac{\delta(B\rho)_0}{(B\rho)_0} \tag{A.34}$$

where,

$$p = \frac{(B\rho)_0^2(1-(\frac{T_1}{T_0})^2)}{(B\rho)_0^2(1-(\frac{T_1}{T_0})^2) + (\frac{m_0}{q_0}c)^2} \tag{A.35}$$

The mass-to-charge ratio m/q derived from the equation 1.32 and expressed as following:

$$m/q = \frac{B\rho}{\gamma\beta c} = \frac{B\rho}{\gamma L/TOF} = B\rho\sqrt{(\frac{TOF}{L})^2 - (\frac{1}{c})^2} \tag{A.36}$$

are utilized to deduce the p parameter and

$$(m/q)^2 = ((B\rho)/L)^2 TOF^2 - ((B\rho)/c)^2 = a_1(TOF)^2 - a_2 \tag{A.37}$$

can be used to calibrate the $B\rho$ and circumference of the reference orbit with several injected well-known masses together with their precisely measured revolution times in the storage ring. Alternatively, the Eq. A.33 and Eq. A.27 can be used to calibrate the velocity β and magnetic-rigidity (or momentum) $B\rho$ of the reference orbit, respectively on a order of 10^{-5} or better. The β and $B\rho$ calibration function can be expressed as:

$$\beta = \sqrt{\frac{\left[\frac{(\frac{m_1}{q_1})^2}{(\frac{m_0}{q_0})^2}(\frac{T_1}{T_0})^2 - 1\right]}{\left[1-\frac{T_1}{T_0})^2\right]}}(\frac{m_0}{q_0})c, \tag{A.38}$$

and

$$(B\rho)_0 = \sqrt{\frac{\left[\frac{(\frac{m_1}{q_1})^2}{(\frac{m_0}{q_0})^2}(\frac{T_1}{T_0})^2 - 1\right]}{\left[\frac{(\frac{m_1}{q_1})^2}{(\frac{m_0}{q_0})^2} - 1\right]}}. \tag{A.39}$$

The values of m_1/q_1 and m_0/q_0 can be from two well-known (or mass determined in our experiment) ion species (indicated as "0" and "1") with a relative precision on the order of $10^5 - 10^8$ or better. The T_0 and T_1 are measured revolution time on the order of 10^6.

The uncertainty of the mass-to-charge ratio by the momentum correction orbit-IMS method, $\frac{m_1}{q_1}$, also consists of three terms: the first term of Eq. A.34 is the uncertainty of the reference nuclear mass, and should be 10^{-6} or less. The second term is the uncertainty coming from an imperfection of the isochronism of the ring and the time resolution of the TOF detector. The momentum measurement to compensate for variation in the third term in Eq. A.28 is as important as and equivalent of velocity. The value of p is on the order of 10^{-2} even if m/q differs from the reference nucleus by 1% and gets smaller as the decreasing of $\frac{\delta(m/q)}{m/q}$. The third term is on the order of 10^{-6} as long as $(B\rho)_0$ is measured with an uncertainty of 10^{-6}.

In principle, the velocity uncertainty parameter in Eq. A.35 can be derived as:

$$\begin{aligned}
1-\frac{{\gamma_1}^2}{{\gamma_0}^2} &= {\gamma_1}^2(\frac{1}{{\beta_0}^2}-\frac{1}{{\beta_1}^2}) = \frac{\frac{{\gamma_0}^2}{{\gamma_1}^2}-1}{\frac{{\gamma_0}^2}{{\gamma_1}^2}} \\
&= \frac{{\beta_0}^2{\gamma_0}^2-\beta_1^2{\gamma_1}^2-1}{{\beta_0}^2{\gamma_0}^2-\beta_1^2{\gamma_1}^2} \\
&= \frac{1-\frac{{\beta_1}^2}{{\beta_0}^2}}{1-\frac{{\beta_1}^2}{{\beta_0}^2}+\frac{1}{{\beta_0}^2{\gamma_0}^2}} \\
&= \frac{1}{1+\frac{1}{{\beta_0}^2{\gamma_0}^2(1-(\frac{T_0}{T_1})^2)}} \\
&= \frac{(B\rho)_0^2(1-(\frac{T_1}{T_0})^2)}{(B\rho)_0^2(1-(\frac{T_1}{T_0})^2)+(\frac{m_0}{q_0}c)^2} \\
&= p
\end{aligned} \tag{A.40}$$

Using Eq. A.40 to replace p in Eq. A.34, the following equation hold:

$$\begin{aligned}
&\frac{\delta(\frac{m_1}{q_1})}{\frac{m_1}{q_1}}-\frac{\delta(\frac{m_0}{q_0})}{\frac{m_0}{q_0}} \\
&= {\gamma_0}^2\frac{\delta(\frac{T_1}{T_0})}{\frac{T_1}{T_0}}+(1-\frac{{\gamma_1}^2}{{\gamma_0}^2})\frac{\delta(B\rho)_0}{(B\rho)_0} \\
&= {\gamma_0}^2(\frac{\delta(T_1)}{T_1}-\frac{\delta(T_0)}{T_0})+(1-\frac{{\gamma_1}^2}{{\gamma_0}^2})\frac{\delta(B\rho)_0}{(B\rho)_0}
\end{aligned} \tag{A.41}$$

For a reference nucleus with m_0/q and target nucleus with m_1/q the difference of the mass-to-charge ratio for the two nucleus $\frac{d(\frac{m}{q})}{(\frac{m}{q})}$ can be written as:

$$\frac{d(\frac{m}{q})}{(\frac{m}{q})} = \gamma_0^2 \frac{dT}{T} + (1 - \frac{{\gamma_1}^2}{{\gamma_0}^2})\frac{(B\rho)}{(B\rho)} \tag{A.42}$$

which is equivalent to the conventional principle expression Eq. A.19 for IMS with a $B\rho$ term.

In summary, conventional storage ring mass spectrometry used for the accurate and precise determination of ion masses by the measurement of the differences between the revolution times/frequencies of different ion species depends on the methods of

1. Strong reduction of the velocity spread of all RIs by a correspondingly strong beam cooling technique, e.g. by electron cooling,
2. Operating the storage ring at transition point in a so-called isochronous mode,

to reduce the dispersion of second term in Eq. A.18 or Eq. A.19 as much as possible. For the formula deduction processes, we can get to know that this orbit-IMS method is a universal method for all storage rings. The IMS method with additional velocity or momentum measurement will help provide new insights into the high accuracy and precision mass measurements for a large range of momentum dispersion and exotic RIs with large amounts of big difference m/q far way from that of reference nucleus. The drawbacks of:

1. the investigation of electron-cooled ion beams is limited to longer-lived nuclei with half-lives down to the order of one second as caused by the required cooling time,
2. isochronous condition need to operate the storage ring at transition point, typically resulting in an unavoidably reduced momentum acceptance of the ring, and only a small number of different ion species can be stored simultaneously in this mode compared to normal operation conditions,

can be solved by measuring the revolution time/ frequency with additional velocity or momentum measurement by operating the storage ring in any optics, which we can treated as a long beam-line $B\rho$-TOF mass spectrometer.

For one species of ion, a certain ideal orbit C_i (i indicates the orbit number) corresponding to a certain velocity v_i of the ion with the corresponding revolution time T_i the following relationship holds,

$$C_i = T_i \cdot v_i, \tag{A.43}$$

From Eq. A.18 or Eq. A.19, and for one species of ions, the revolution time difference of the number i orbit from the reference orbit number 0 can be expressed as:

$$\frac{T_0 - T_i}{T_i} = -(1 - \frac{\gamma_i^2}{\gamma_t^2})\frac{v_0 - v_i}{v_i} = -(\frac{1}{\gamma_i^2} - \frac{1}{\gamma_t^2})\frac{B\rho_0 - B\rho_i}{B\rho_i} = (1 - \frac{\gamma_t^2}{\gamma_i^2})\frac{C_0 - C_i}{C_i}, \tag{A.44}$$

where $B\rho_i$, $B\rho_0$ are the corresponding magnetic rigidity of ions circulating at the number i orbit and reference orbit, respectively. Therefore, from Eq. A.44, The revolution time of ion at the number i orbit C_i can be corrected to the reference orbit revolution time T_0 with a orbit length of C_0:

$$T_0 = \frac{C_0}{v_0} = T_i + (1 - \frac{\gamma_t^2}{\gamma_i^2})\frac{C_0 - C_i}{C_i}T_i = T_i - (1 - \frac{\gamma_i^2}{\gamma_t^2})\frac{v_0 - v_i}{v_i}T_i = T_i - (\frac{1}{\gamma_i^2} - \frac{1}{\gamma_t^2})\frac{B\rho_0 - B\rho_i}{B\rho_i}T_i. \tag{A.45}$$

From Eq. A.45, we can know that with the TOF and additional velocity or momentum to reconstruct revolution times of all orbits in a storage to the reference orbit, which will minimize the revolution time distributions of all ion species, thus to result in a high accuracy and precision mass measurements of RIs of all momentum range and m/q range.

The detector developed in this work with high performance of timing resolution and good position sensitivity and resolution will installed for mass measurements, it will help built up the this method to achieve a high accuracy and precision mass measurements.

The Rare-RI Ring is designed to be an Isochronous Mass Spectrometer with individual injection and typically each time only one ion is injected and extracted after 2000 turns circulation. It is preferable to be operated in IMS mode with additional velocity or magnetic rigidity measurement for mass correction. The orbit-IMS method can be utilized in the existing storage rings CSRe and ESR, and will be also suitable for new storage ring line SRing at next generation facility HIAF in IMP and the CRing in FAIR at GSI in the future. Possibly, the normal optical operation can be realized in these storage rings for high precision mass measurements.

A.2 Magnets and Isochronous field of the Rare-RI Ring

The Rare-RI Ring consists of 24 dipole magnets as shown in Fig. 2.2[182, 174]. Four dipole magnets form one sector and six sectors make up the whole ring. The dipole magnets to be used were originally used in a heavy-ion storage ring, TARN-II, at the Institute of Nuclear Study, University of Tokyo. Each dipole magnet causes 15° bending with a bending radius of 4.045 m. Each sector has a straight section of 4.02 m. The circumference of the ring

is 60.3507 m There are two ways of achieving a first-order isochronous field. One is the installation of an edge angle (ε) in the magnet of sector; the other is the installation of an n-value in the magnets of sector. If $n = 0$ (homogeneous magnetic field), to achieve the first-order isochronous field, ε can be given by

$$tan(\varepsilon) = \frac{(R\phi + S) - R\phi\gamma^2}{(R\phi + S) - R\phi\gamma^2 + 2R\gamma^2 tan(\phi/2)} tan(\phi/2) \tag{A.46}$$

where $R, S, and\ \phi$ are the radius of the central orbit in the magnetic sector, the length of straight section along the central orbit, and the bending angle, respectively []. For the case of $\varepsilon = 0$, to achieve the first-order isochronous field, the n-value to fulfill the isochronous condition is given as:

$$n = 1 - \gamma^2 \frac{R\phi}{(R\phi + S)} \tag{A.47}$$

Besides, we obtain a radial gradient value of magnetic field from the following equation:

$$\frac{\partial B_z}{\partial r} \frac{1}{B_0} = \frac{n}{R}. \tag{A.48}$$

The radial gradient of the magnetic field comes from each sector consists of four dipole magnets which has fixed edge angle 7.5°.

The isochronous magnetic field is formed using 10 trim coils equipped to 12 bending magnets (in the two outer dipoles among the four dipoles in each magnetic sector)[182, 174, 175]. Every trim coil consists of a one-turn coil, which is made of a 6×6 mm^2 hollow conductor. The achieved isochronism is about 2×10^{-6} in the region of ±50 mm in the radial direction which cover the acceptance of the ring.

The magnets are most important parts of the Rare-RI Ring system (see Fig. 2.2). The main specification of the dipole magnets, quadrupole magnets, septum magnets, and the kicker magnets are listed in Tab. A.1, A.2, A.3, A.4.

Table A.1 Main parameters of dipole magnet

parameters	dipole
type	laminated
bending angle	15°
bending radius	4.045 m
useful aperture	80 × 440 mm
maximum field	1.7 T
in gap coil current (maximum)	3000 A
number of coil turns	40

Table A.2 Main parameters of quadrupole magnets

parameters	quadrupole
type	laminated
bore Radius	50 mm
pole length	600 mm
max. Field Gradient	18 T/m
coil current (max.)	1000 A
maximum filed at pole tip	0.6 T

Table A.3 Main parameters of septum magnet

parameters	Septum 1	Septum 2
type	lumped	lumped
bending angle	12.7°	5.3°
pole length	1.117 m	1.202 m
pole gap	45 mm	45 mm
central orbit radii	5.05 m	13 m
magnetomotive force	42600 AT	16600 AT
maximum field in gap	1.19 T	0.464 T
coil current (max.)	2130 A	2075 A
number of coil turns	20	8

Table A.4 Main parameters of kicker magnet

parameters	kicker
Number of cell	13
Length of cell	25 mm
Characteristic impedance	12.5 Ω
Capacitance	350 pF/cell
Inductance	100 nH
Maximum current	3000 A/35 kV
Aperture	160 mm × 40 mm

Appendix B

Specifications and Properties of MCPs & Storage, Handling and Operation of MCP

B.1 Rectangular type chevron MCP

B.1.1 Specifications and properties of rectangle-type MCP

Table B.1 Specifications of MCP

PHYSICAL CHARACTERISTICS OF MCPS	SPECIFICATIONS
Quality Dimensions:	Two Segments of 95.00mmx42.00mm Minimum Each
Center-to-Center Spacing:	12um Nominal
Pore Size:	10um Nominal
Bias Angle:	$8^{\circ} \pm 1^{\circ}$
Bias Angle Orientation:	Parallel to Shorter Sides
Open Area Ratio:	55% Minimum
Test/Inspection Level:	Detection Quality
ELECTRICAL CHARACTERISTICS OF DETECTOR	SPECIFICATIONS
Electron Gain@2400$Volts$ Maximum:	1 x 10^7 Minimum
Bias Current Range @2400$Volts$:	20 – 200 Microamps (For Reference Only)
Resistance:	6 – 60 Megohms
Dark Count:	Best Efforts Only
Pulse Height Distribution:	200% FWHM
Maximum Specified Operating Voltage (Across MCPs):	2400$Volts$

Electrical characteristics are measured at the optimum MCP operating voltage (the lowest bias voltage required to attain the specified values). Unmasked edges of MCPs can produce elevated and unpredictable levels of noise and self-emissions up to 1mm in from the edge. The Chevron detector assembly contains four Detection Quality Advanced Performance Long-Life Micro-Channel Plates, configured in two parallel Chevron sets, mounted

in stainless steel, alumina, and PEEK hardware. There will be up to 7mm of non-quality area that may self-emit (cause noise), between the two Chevron quality areas. Photonics USA lacks the test equipment to identify where self-emissions are occurring on the output, and therefore dark count shall not be constrained. The built in anode will be a one-dimensional Resistive Anode Encoder with contacts on the shorter ends. The detector assembly is non-bakeable. Detection Quality detector assemblies are intended for use in applications where image quality is not critical. These economical devices are used as signal detectors and amplifiers and are typically used in applications such as time-of-flight mass spectrometry, residual gas analysis (RGA), or point source detectors.

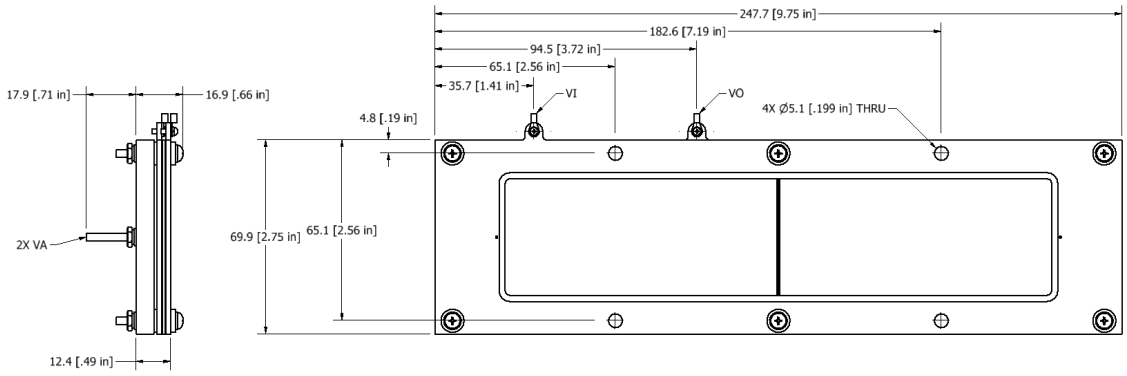

Fig. B.1 Mechanical Dimensions (from Photonics USA, INC.)

B.2 Circle type chevron MCP

The Micro-Channel Plate (MCP) detector with delay-line anode is a device for single particle/photon counting, giving information on the position of each particle/photon and its impact time with high precision. It uses an electronic read-out scheme employing fast timing amplifiers, timing discriminators and digitizers. It operates under ultra-high vacuum and requires high voltage supplies.

This detector system is modular and com in different sizes and versions.

1. **Typical performance:**

   position resolution: <0.1mm

   overall linearity: 0.3 mm

   temporal resolution: <0.2 ns

   rate capability: 1 MHz

   multi-hit dead time: 10-20 ns

2. **Typical characteristics of the detector assembly:**

   Height above a mounting Flange: about 100 mm (adjustable)

   Mounting Diameter: 94/144/196/246 mm

   Operating Temperature Range: -50 to 70 $^{\circ}C$

   Operating Pressure: $< 2 * 10^{-6}$ mbar

   Baking Temperature: 150 $^{\circ}C$ Maximum

   Electron Gain @ 2400 Volts*: 10^{7} Minimum

Table B.2 Specifications and properties of Circle-type MCPs for delay-line detector (bought from RoentDek and manufactured by PHOTONIS).

MCP mechanical properties	MCP I			MCP II		
Outer diameter	127 mm			127 mm		
Minimum quality area	120 mm			120 mm		
Channel diameter	25 μm			25 μm		
Center to Center	32 μm			32 μm		
Thickness	1.5 mm			1.5 mm		
L/D ratio	60:1			60:1		
Bias Angle	19°			19°		
Solid glass border	No, rimless			No, rimless		
Open area ratio	63%			63%		
	MCP I			MCP II		
MCP electrical properties	voltage	Bias current (μA)	Gain	voltage	Bias current (μA)	Gain
	900 V	48.0	4.8E+03	900 V	42.0	4.2E+03
	1200 V	62.0	24E+05	1200 V	54.0	2.2E+05

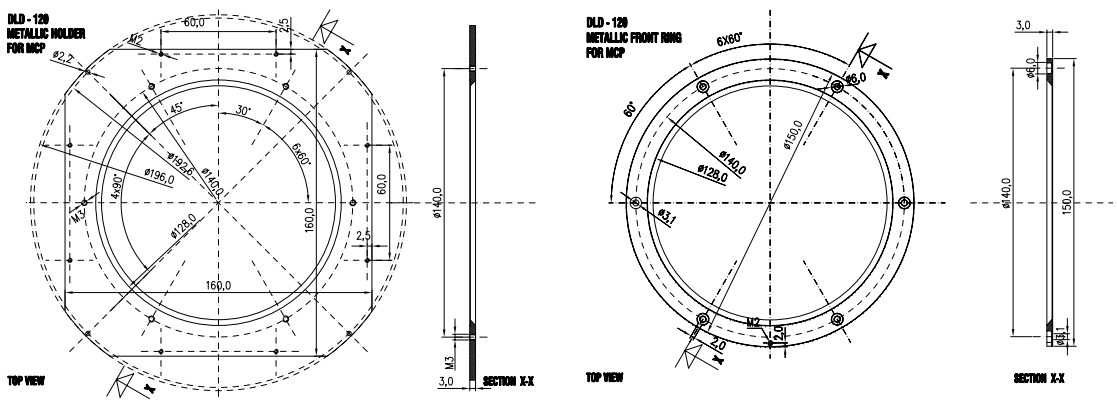

(a) (b)

Fig. B.2 (a) Metallic holder for MCP. (b) Metallic front ring for MCP (120 mm in diameter).

B.3 Storage, Handling and Operation of Micro-channel Plates (from PHOTONIS)

Microchannel Plates (MCP) and MCP-based devices must be adequately stored to ensure proper performance and longevity. This procedure details proper storage techniques. Any deviation from the recommended storage procedures will void the warranty of PHOTONICS.

1. **STORAGE**

   Because of their structure and the nature of the materials used in manufacture, care must be taken when handling or operating MCPs. The following precautions are strongly recommended: Containers in which microchannel plates are shipped are not suitable for storage periods exceeding the delivery time. Upon delivery to the customer's facility, microchannel plates must be transferred to a suitable long term storage medium.

   (a) ***The most effective long-term storage environment for an MCP is an oil free vacuum of at least*** 10^{-4} ***Torr***. When stored in vacuum, the parts can be removed from their aluminum vacuum storage bags,

   (b) While vacuum storage is strongly recommended, a continuously purged dry box which utilizes a dry inert gas, such as argon or nitrogen, can be used for storage for up to several weeks. In this case it is critical that the part remain in its sealed aluminum vacuum storage bag while in the purged dry box.

   (c) Desicator type cabinets which utilize silica gel or other solid dessicants to remove moisture have been proven unacceptable.

2. **HANDLING**

   (a) Shipping containers should be opened only under class 100 Laminar flow clean-room conditions.

   (b) Personnel should always wear clean, talc-free, class 100 clean-room compatible, vinyl gloves when handling MCPs. No physical object should come in contact with the active area of the wafer. The MCP should be handled by its solid glass border using clean, degreased tools fabricated from stainless steel, Teflon or other ultra-high vacuum-compatible materials. Handling MCPs with triceps should be limited to trained, experienced personnel.

   (c) MCPs without solid glass border should be handled very carefully with great care taken to contact the outer edges of the plate only.

   (d) MountingPad^{TM} MCP's should be contacted only at the mounting pads.

   (e) All ion barrier MCPs should be placed in their containers with the ion barrier facing down.

(f) The MCP should be protected from exposure to particle contamination. Particles which become affixed to the plate can be removed by using a single-hair brush and an ionized dry nitrogen gun.

(g) The MCP should be mounted only in fixtures designed for this purpose. Care should be taken due to electrical potentials involved.

(h) ***CAUTION***: Voltages must not be applied to the device while at atmospheric pressure. ***Pressure should be*** 10^{-5} ***Torr*** $\simeq 1.33 \times 10^{-3} pa$ ***or lower at the microchannel plate before applying voltage***. Otherwise, damaging ion feedback or electrical breakdown will occur.

3. **OPERATION**

(a) A dry-pumped or well-trapped/diffusion-pumped operating environment is desirable.

(b) A poor vacuum environment will most likely shorten MCP life or change MCP operating characteristics.

(c) ***A pressure of*** 10^{-6} ***Torr or better is preferred***. Higher pressure can result in high background noise due to ion feedback.

(d) MCPs may be vacuum baked to a temperature of 380 °C (no voltage applied).

(e) MCPs with standard bias currents (non-EDR MCP's) may be operated at a maximum temperature of 350 °C. Contact PHOTONIS Technical Service to determine maximum operating temperature for MCPs with the EDR option.

When a satisfactory vacuum has been achieved, voltages may be applied. It is recommended that this be done slowly and carefully. Current measuring devices in series with power supplies aid in monitoring MCP behavior. Voltage drop across the meter should be taken into consideration when calculating the applied voltage.

1. ***Voltage should be applied to the MCP in 100 volt steps***. If current is being monitored, no erratic fluctuations should appear. If fluctuations do appear, damage or contamination should be suspected and the voltage should be turned off. The assembly should then be inspected before proceeding.

2. Maximum voltage that may be applied across a single MCPs is:

(a) L/D 40:1 is 1000 volts.

(b) L/D 60:1 is 1200 volts

(c) L/D 80:1 is 1400 volts

3. Higher potentials may result in irreversible damage.

Appendix C

Dimensions

Dimensions of detector system

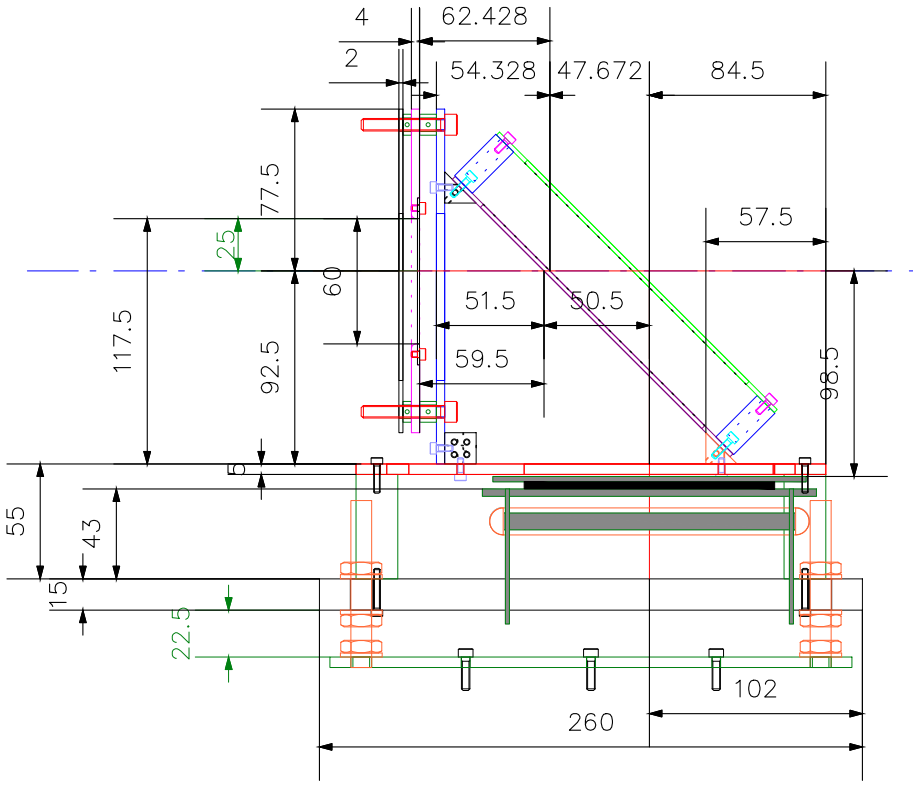

Fig. C.1 Dimensions of the BMP/TOF detector with circular MCPs.

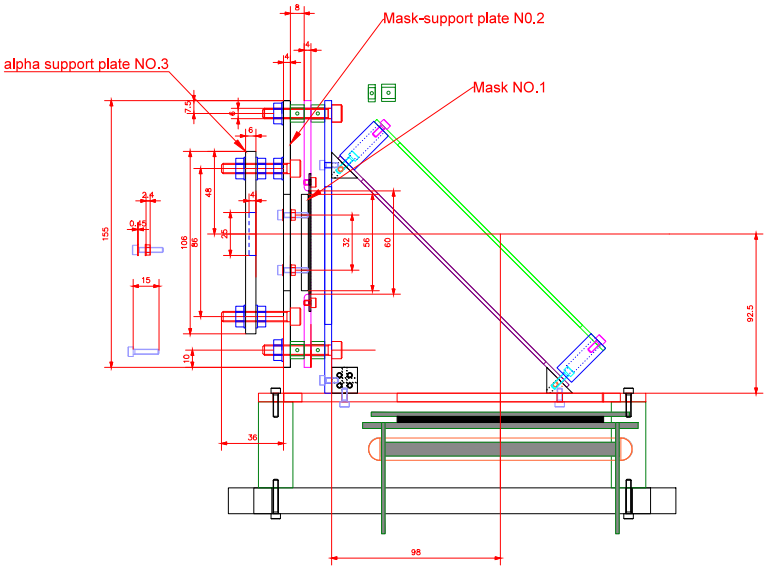

Fig. C.2 The schematic assembly diagram of the new mask system.

Appendix D

Analysis of m/q resolution by beam-line detectors

The mass-to-charge ratio in an accelerator system can be described as:

$$m/q = \frac{B\rho}{\gamma\beta c} = \frac{B\rho}{\gamma L/TOF} = B\rho\sqrt{(\frac{TOF}{L})^2 - (\frac{1}{c})^2} = B\rho\sqrt{(\frac{1}{\beta})^2 - (\frac{1}{c})^2} \tag{D.1}$$

For fully stripped ions, the Q equal to the proton number Z.

$$\left(\frac{\Delta(m/q)}{m/q}\right)^2 = \left(\frac{\Delta(B\rho)}{B\rho}\right)^2 + \gamma^4(\frac{\Delta\beta}{\beta})^2 \tag{D.2}$$

The momentum B□:

$$B\rho = (B\rho)_0(1+\delta) \tag{D.3}$$

with a relative deviation of:

$$\frac{\Delta(B\rho)}{B\rho} = \frac{\Delta\delta}{1+\Delta\delta} \sim \Delta\delta \tag{D.4}$$

If a particle is tansported from F3 to F6, the $\delta = \frac{\delta(B\rho)}{B\rho}$ can be expressed as:

$$\delta = [(a|a)x_{F6} - (x|x)x_{F3} - (x|a)a_{F6} - (a|x)x_{F3}]/det \tag{D.5}$$

where $det = (x|d)(a|a) - (x|a)(a|d) = 75.4 \cdot 1.12 - 0.9 \cdot 3.97 = 80.875$. (for ms03: 75.4 *mm*/%, for ms02: 98 *mm*/%) The deviation of momentum dispersion from detector measurements can be written as:

$$(\Delta\delta)^2 = [(a|a)^2(\Delta X_{F6})^2 + (a|a)^2(x|x)^2 + (x|a)^2(a|x)^2(\Delta X_{F3})^2 + (x|a)^2(\Delta a_{F6})^2]/det^2, \tag{D.6}$$

and reduced to be:

$$(\Delta\delta)^2 = [1.2544(\Delta X_{F6})^2 + 1.016(\Delta X_{F3})^2 + 0][\%^2]/(80.875)2 \tag{D.7}$$

As BigRIPS PPAC has a reported position resolution $\sigma < 0.5$ mm (Position resolution σ : 0.35 - 0.46 mm) for heavy ions, thus resulting in:

$$\Delta X^2 = \Delta X_{F3}^2 = \Delta X_{F6}^2 =\sim 0.12\,mm^2\,to\,0.21\,mm^2 \tag{D.8}$$

By taking the ΔX of 0.2 mm, with a beam of Bρ= 4.848 Tm, $\gamma \sim 1.18$, $\beta \sim 0.5$, central particle of ^{78}Ge, the $B\rho$ measurement resolution can be described as:

$$\frac{\Delta(B\rho)}{B\rho} = 0.00694[\%], TOF = L/(\beta c) \tag{D.9}$$

With F3 pla: $\sim$ 30 ps; TOF: $\sim$ 500 - 570 ns, taking 550 ns, (S0 timing detector σ: 200ps, TOF F3S0: $\sim$ 202 ps, relative resolution: 4 x 10^{-4}); the relative resolution of:

$$\left(\frac{\Delta(m/q)}{m/q}\right)^2 = \left(\frac{\Delta(B\rho)}{B\rho}\right)^2 + \gamma^4(\frac{\Delta\beta}{\beta})^2 = 0.0000694^2 + 0.000364^2 = (3.70x10^{-4})^2, \tag{D.10}$$

in total TOF resolution 200 ps case.

With assumption of: S0 timing detector σ :40 ps, TOF F3S0: 50 ps, corresponding to resolution: 9.09 x 10^{-5}=0.0091%. In MS3 TOF (F3S0) resolution ~230-250 ps, with a relative resolution ~(0.000418, 0.000454), therefore, the m/q resolution measured by beam-line detectors can reach a relative resolution of:

$$\left(\frac{\Delta(m/q)}{m/q}\right)^2 = \left(\frac{\Delta(B\rho)}{B\rho}\right)^2 + \gamma^4(\frac{\Delta\beta}{\beta})^2 = 0.0000694^2 + 0.000091^2 = (9.10x10^{-5})^2, \tag{D.11}$$

in total TOF resolution 50 ps case.

Publication List

1. Title: Development of Mirror-type MCP Detectors for Mass Measurements at the Rare-RI Ring

   Z. Ge et al., JPS Conference Proceedings, The 10th International Conference on Nuclear Physics at Storage Rings (STORI'17)

2. Title: Simulation and design of a large area position sensitive TOF MCP detector at the Rare RI Ring

   Z. Ge et al., RIKEN Accel. Prog. Rep. 50 (2017) 187

3. Title: Online results for the injection ion optics of the Rare RI Ring

   Z. Ge et al., RIKEN Accel. Prog. Rep. 49 (2016) 180

4. Title: Beam production of 18Ne with in-flight method for alpha scattering at CRIB

   N.N. Duy et al., Nuclear Inst. and Methods in Physics Research, A 897 (2018) 8–13

5. Title: Application of isochronous mass spectrometry for the study of angular momentum population in projectile fragmentation reactions

   X. L. Tu et al., PHYSICAL REVIEW C 95, 014610 (2017) 1-6

6. Title: An improvement of isochronous mass spectrometry: Velocity measurements using two time-of-flight detectors

   P. Shuai et al., Nuclear Instruments and Methods in Physics Research B 376 (2016) 311–315

7. Title: Time and Position-sensitive Foil-MCP Detector for high-precision Mass Measurements at the Rare-RI Ring

   Z.Ge et al., To be submitted to Nuclear Instruments and Methods in Physics Research A